



Special Issue Reprint

China Water Forum 2024

Edited by
Qiting Zuo, Fuqiang Wang, Jiaqi Zhai, Xiuyu Zhang, Dunxian She, Lei Zou,
Rong Gan and Zengliang Luo

mdpi.com/journal/water



China Water Forum 2024

China Water Forum 2024

Guest Editors

Qiting Zuo

Fuqiang Wang

Jiaqi Zhai

Xiuyu Zhang

Dunxian She

Lei Zou

Rong Gan

Zengliang Luo



Basel • Beijing • Wuhan • Barcelona • Belgrade • Novi Sad • Cluj • Manchester

Guest Editors

Qiting Zuo
Zhengzhou University
Zhengzhou
China

Fuqiang Wang
North China University of
Water Resources and Electric
Power
Zhengzhou
China

Jiaqi Zhai
China Institute of Water
Resources and Hydropower
Research
Beijing
China

Xiuyu Zhang
North China University of
Water Resources and Electric
Power
Zhengzhou
China

Dunxian She
Wuhan University
Wuhan
China

Lei Zou
Chinese Academy of Sciences
Beijing
China

Rong Gan
Zhengzhou University
Zhengzhou
China

Zengliang Luo
China University of
Geosciences
Wuhan
China

Editorial Office

MDPI AG
Grosspeteranlage 5
4052 Basel, Switzerland

This is a reprint of the Special Issue, published open access by the journal *Water* (ISSN 2073-4441), freely accessible at: https://www.mdpi.com/journal/water/special_issues/FRL3085503.

For citation purposes, cite each article independently as indicated on the article page online and as indicated below:

Lastname, A.A.; Lastname, B.B. Article Title. <i>Journal Name</i> Year , Volume Number, Page Range.
--

ISBN 978-3-7258-6057-9 (Hbk)

ISBN 978-3-7258-6058-6 (PDF)

<https://doi.org/10.3390/books978-3-7258-6058-6>

© 2025 by the authors. Articles in this book are Open Access and distributed under the Creative Commons Attribution (CC BY) license. The book as a whole is distributed by MDPI under the terms and conditions of the Creative Commons Attribution-NonCommercial-NoDerivs (CC BY-NC-ND) license (<https://creativecommons.org/licenses/by-nc-nd/4.0/>).

Contents

About the Editors	vii
 Qiting Zuo, Fuqiang Wang, Jiaqi Zhai, Xiuyu Zhang, Dunxian She, Lei Zou, et al. A Review of China's Water Security Issues: Insights from the Special Issue of China Water Forum 2024 Reprinted from: <i>Water</i> 2025 , 17, 2733, https://doi.org/10.3390/w17182733	
	1
 Jing Zhao, Hanting Li, Zhiying Liu, Yaoqing Jiang and Wenbin Mu Water Saving and Carbon Reduction (CO ₂) Synergistic Effect and Their Spatiotemporal Distribution Patterns Reprinted from: <i>Water</i> 2025 , 17, 1847, https://doi.org/10.3390/w17131847	
	6
 Pingyu Lv, Sidong Zeng, Xin Liu and Linhan Yang Changes in Streamflow Pattern and Complexity in the Whole Yangtze River Basin Reprinted from: <i>Water</i> 2024 , 16, 2467, https://doi.org/10.3390/w16172467	
	29
 Qiang Wang, Fang Yang, Xiaozhang Hu, Peng Hou, Yin Zhang, Pengjun Li and Kairong Lin Multi-Model Comparison in the Attribution of Runoff Variation across a Humid Region of Southern China Reprinted from: <i>Water</i> 2024 , 16, 1729, https://doi.org/10.3390/w16121729	
	49
 Yongxiao Ren, Xiaoxiao Lai, Jiawei Wang, Ronggui Li, Shenshen Li, Xingyu Yan, et al. Simulation of Heavy Metal Removal in Irrigation Water Using a Shell-Derived Biochar-Integrated Ecological Recycled Concrete Reprinted from: <i>Water</i> 2024 , 16, 3646, https://doi.org/10.3390/w16243646	
	69
 Yihan Dong, Yifan Han, Xu Han, Yaoxuan Chen and Yuanzheng Zhai Sewage Vertical Infiltration Introduced Polygenic Multipollutants into Groundwater Reprinted from: <i>Water</i> 2024 , 16, 2305, https://doi.org/10.3390/w16162305	
	81
 Qianqian Wang, Fang Yang, Haiqing Liao, Weiying Feng, Meichen Ji, Zhiming Han, et al. Seasonal Variations of Ice-Covered Lake Ecosystems in the Context of Climate Warming: A Review Reprinted from: <i>Water</i> 2024 , 16, 2727, https://doi.org/10.3390/w16192727	
	98
 Yuqian Yao, Yang Xiao, Peng Hou and Shuqin Li Evaluating the Influence of Water Quality on Clogging Behavior in Drip Irrigation Emitters: A CT Imaging Study Reprinted from: <i>Water</i> 2025 , 17, 1065, https://doi.org/10.3390/w17071065	
	115
 Jichang Yang, Yuncong Lu, Zhiqiang Zhang, Jieru Wei, Jiandong Shang, Chong Wei, et al. A Deep Learning Method Coupling a Channel Attention Mechanism and Weighted Dice Loss Function for Water Extraction in the Yellow River Basin Reprinted from: <i>Water</i> 2025 , 17, 478, https://doi.org/10.3390/w17040478	
	132

About the Editors

Qiting Zuo

Qiting Zuo is a Professor and Doctoral Supervisor at the School of Water Conservancy and Transportation, Zhengzhou University. He serves as the Dean of the Yellow River Ecological Protection and Regional Coordinated Development Institute, Director of the Water Science Research Center, and Director of the Henan International Joint Laboratory for Water Cycle Simulation and Water Environmental Protection, all at Zhengzhou University. He also holds academic positions, including Vice President of the Chinese Society of Natural Resources, Vice Chairman of the Chinese Committee of the International Water Resources Association, and Co-Chairman of the UK-China Association for Resources and Environment (UK-CARE). The team he leads has been recognized by the Ministry of Education as a “National Huang Danian-Style Teacher Team in Higher Education.” His research focuses on water resources and the water environment. He has received 12 provincial and ministerial-level science and technology awards, published 21 academic monographs, and authored over 560 academic papers. He has been recognized for having one of China’s 100 Most Influential Domestic Academic Papers and is the founder of the discipline of Human–Water Relationship Science. His research findings have been applied to major national needs, including ecological civilization construction, national water network construction, water conservancy modernization, water-saving society construction, the strictest water resources management system, water disaster prevention and control, smart water conservancy, dual-carbon goals, high-quality development, and new quality productive forces.

Fuqiang Wang

Fuqiang Wang has a Ph.D. in Engineering and is a Professor and Doctoral Supervisor at the North China University of Water Resources and Electric Power, where he currently serves as Executive Dean of the Yellow River Research Institute. He serves as Discipline Leader of Eco-Hydraulic Engineering in Henan Province, Academic and Technical Leader of the Henan Provincial Department of Education, Director of the Provincial First-Class Undergraduate Program in Water Affairs Engineering, and Director of the Henan Provincial Research Center for Watershed Ecological Protection and Restoration Engineering. He also holds several national and professional appointments, including Deputy Director of the Water Resources Committee of the Chinese Society of Natural Resources, and Member of the Basin Development Strategy Committee, Youth Working Committee, and Environmental and Ecological Engineering Committee of the Chinese Hydraulic Engineering Society and the Chinese National Committee on Large Dams. He has been recognized as a Leading Talent in Scientific and Technological Innovation of Central China, Outstanding Young Innovator of Henan Province, High-Level Talent of Henan Province, Innovative University Faculty Member of Henan Province, and Henan Provincial Model Teacher. His research focuses on watershed ecohydrological effects and water security, water resources planning and management, and aquatic ecosystem protection and restoration. He has presided over more than 30 major research projects, including key programs supported by the National Natural Science Foundation of China (NSFC) and the National Key Research and Development Program of China. He has published over 100 peer-reviewed papers, authored 7 scholarly monographs, and holds 18 authorized national invention patents. In addition, he has contributed to 3 national or industrial standards and received 6 provincial and ministerial-level awards for scientific and technological innovation.

Jiaqi Zhai

Jiaqi Zhai is a Senior Engineer and Master's Supervisor at the China Institute of Water Resources and Hydropower Research. His main research focuses on the development and application of distributed water cycle models (WACMs), watershed water resource assessment and evolution prediction, agricultural water-saving potential evaluation, and regional drought assessment. He has received 8 provincial and ministerial-level science and technology awards, published 6 academic monographs, and authored 57 academic papers. Additionally, he holds 23 authorized invention patents and 7 software copyrights. Four of his technologies have been included in the *Key Promotion Guide for Advanced Practical Water Conservancy Technologies*, and one has been selected for the *National Mature and Applicable Water-Saving Technologies*. He has also contributed to the compilation of 2 national standards, 1 industry standard, and 3 local standards. His research findings have been applied to major national needs, including the construction of the national water network, the development of a water-saving society, the strictest water resources management system, groundwater overexploitation control in North China, and the "Four Waters and Four Determinations" water governance strategy.

Xiuyu Zhang

Xiuyu Zhang is a Professor, Doctor of Engineering, and Doctoral Supervisor at North China University of Water Resources and Electric Power. He holds the titles of Distinguished Teacher in Henan Province and Director of the First-Class Discipline Construction Office of the university. Additionally, he serves in multiple academic organizations, including a Council Member of the Teaching Research Branch of the China Association of Higher Education, a Council Member of the Higher Education Branch of the China Water Resources Education Association, a Member of the Water Resources Professional Committee of the Chinese Society of Natural Resources, a Member of the Watershed Development Strategy Professional Committee of the Chinese Hydraulic Engineering Society, a Member of the Teaching Guidance Committee for Ordinary Higher Education Institutions of Henan Province, and Expert of the Henan Provincial Hydraulic Engineering Society. His research and teaching focus on integrated watershed resource management, efficient utilization of regional water resources, water disaster prevention, and risk management. He has won numerous academic and educational awards, including a National Second-Class Teaching Achievement Award, a National First-Class Teaching Achievement Award, and a Second-Class Teaching Achievement Award in water resources-related disciplines, as well as two Special Awards, three First-Class Awards, and one Second-Class Award for Higher Education Teaching Achievements in Henan Province. He has published over 60 academic papers and presided over more than 20 research projects, including major public welfare scientific and technological projects in Henan Province, general projects of the Henan Provincial Natural Science Foundation, and key scientific and technological projects in Henan Province.

Dunxian She

Dunxian She is a Professor and Doctoral Supervisor at the School of Water Resources and Hydropower Engineering, Wuhan University. He serves as the Deputy Director of Hubei Key Laboratory of Water System Science for Sponge City Construction at Wuhan University. He also holds academic positions, including being a Member of the Chinese Society of Natural Resources and the Chinese National Commission for the International Association of Hydrological Sciences. His research focuses on climate change and extreme hydrological events. He has authored over 100 academic papers in *Nature Cities*, *Water Resources Research*, *Water Research*, *Agricultural and Forest Meteorology*, etc.

Lei Zou

Lei Zou holds a Ph.D. in Engineering and is an Associate Professor at the Institute of Geographic Sciences and Natural Resources Research, Chinese Academy of Sciences, as well as a Master's Supervisor. He also serves as the Deputy Secretary General of the Water Resources Professional Committee of the Chinese Society of Natural Resources. His research focuses on watershed water cycle system modeling and its response to environmental changes. He has published over 80 academic papers, been granted 20 invention patents, and has coauthored three monographs. He has led several research projects, including a key project of the National Key R&D Program and a sub-project under the National Natural Science Foundation of China. His research achievements were selected among the "Top 10 Research Advances in Geographical Science in China (2023)" and the "Top 10 Scientific and Technological Advances in Ecological Environment in China (2023)".

Rong Gan

Rong Gan is an associate professor and doctoral supervisor at the School of Water Conservancy and Transportation, Zhengzhou University. She also serves as the Deputy Secretary-General of the Water Resources Professional Committee of the Chinese Society of Natural Resources. Her main research and teaching areas are hydrology, water resources, and water environment. She has led three national-level projects, including for the National Key Research and Development Program of China and the National Natural Science Foundation of China, as well as two provincial and ministerial-level projects. She received two excellent scientific paper awards from the Education Department of Henan Province and two awards for achievements in water conservancy technology progress in Henan Province. She has published over 50 academic papers and participated in the publication of 5 academic monographs and textbooks, and she is the supervisor of outstanding graduation theses in Henan Province.

Zengliang Luo

Zengliang Luo is a Professor and Doctoral Supervisor at the School of Geography and Information Engineering, China University of Geosciences (Wuhan). He serves as the Deputy Secretary-General of the Water Resources Professional Committee of the Chinese Society of Natural Resources, and a Member of the Water Resources Management and Conservation Committee of the Chinese Committee of the International Water Resources Association (CWRA). His research focuses on Hydrology and Water Resources, including remote sensing data analysis of water cycle variables, the development and application of distributed hydrological models, and data assimilation of water cycle variables using remote sensing. His work also covers theoretical methods for water balance closure and changes in terrestrial hydrological processes influenced by climate change and human activities. He has authored over 60 academic papers published in journals such as *Water Resources Research*, *Agricultural and Forest Meteorology*, *Hydrology and Earth System Sciences*, the *Journal of Hydrology*.

Editorial

A Review of China's Water Security Issues: Insights from the Special Issue of China Water Forum 2024

Qiting Zuo ^{1,2}, Fuqiang Wang ³, Jiaqi Zhai ⁴, Xiuyu Zhang ³, Dunxian She ⁵, Lei Zou ⁶, Rong Gan ¹
and Zengliang Luo ^{7,8,*}

¹ School of Water Conservancy and Transportation, Zhengzhou University, Zhengzhou 450001, China; zuoqt@zzu.edu.cn (Q.Z.); ganrong168@163.com (R.G.)

² Yellow River Institute for Ecological Protection & Regional Coordinated Development, Zhengzhou University, Zhengzhou 450001, China

³ College of Water Resources, North China University of Water Resources and Electric Power, Zhengzhou 450045, China; wangfuqiang@ncwu.edu.cn (F.W.); zhangxiuyu@ncwu.edu.cn (X.Z.)

⁴ China Institute of Water Resources and Hydropower Research (IWHR), Beijing 100038, China; jiaqizhai@163.com

⁵ School of Water Resources and Hydropower Engineering, Wuhan University, Wuhan 430072, China; shedunxian@whu.edu.cn

⁶ Institute of Geographic Sciences and Natural Resources Research, Chinese Academy of Sciences, Beijing 100101, China; zoulei@igsrr.ac.cn

⁷ School of Geography and Information Engineering, China University of Geosciences, Wuhan 430074, China

⁸ Engineering Research Center of Natural Resource Information Management and Digital Twin Engineering Software, Ministry of Education, Wuhan 430074, China

* Correspondence: luozengliang@cug.edu.cn

1. Introduction

Affected by global climate change and rapid socio-economic development, China, along with many other countries worldwide, faces a series of water security issues, such as water shortages, flood disasters, and water-related ecological and environmental problems. To address these challenges, China has adopted a range of measures, including a most stringent water resource management system, the South-to-North Water Diversion Project, and the River Chief System. Nevertheless, due to the complexity of water security issues, effective management is difficult to achieve in the short term, and interdisciplinary research provides important support.

To facilitate a better understanding of China's water security issues, a series of academic exchanges have been organized by us, including the well-known "China Water Forum," which focuses on discussing solutions to China's water challenges; the "Water Science Development Forum," which aims to promote the multidisciplinary integration of water science with other relevant disciplines in addressing China's water issues; and the "Water Science Lectures," an open, shared, and non-profit public lecture series.

The Editorial Department of the *Water* Journal cooperates with the "China Water Forum", the "Water Science Development Forum", and the "Water Science Lectures" to establish a series of Special Issues. At present, at least one Special Issue is planned each year. The Special Issue established in 2024, "China Water Forum 2024", has concluded, and the new Special Issue for 2025, namely "China Water Forum 2025", has commenced. A total of eight papers were accepted for the Special Issue "China Water Forum 2024." Based on the papers published in this Special Issue, we summarize China's water security status and issues to facilitate readers' understanding of the relevant research progress.

Four themes were proposed in "China Water Forum 2024":

- (1) Climate change and hydrology.

- (2) Water problems and human–water relationship control.
- (3) Water environment and ecology.
- (4) Water information technology and modeling.

2. Summary of Water Security Issues in China Based on Special Issue Publications

The eight published papers in this Special Issue examine China's water issues from different perspectives. They are divided into three categories based on their research themes: Category A, "Water Resource Management and Integrated Governance" (Contributions 1–3); Category B, "Rivers and Lakes Water Ecology and Water Pollution" (Contributions 4–6); and Category C, "Irrigation Technology and Water Use Efficiency" (Contributions 7,8).

For Category A, "Water Resource Management And Integrated Governance", Contribution (1) employs a non-radial directional distance function (NDDF) model to quantitatively assess provincial water saving and carbon reduction performance during 2000–2021, measures synergistic effects, and examines the spatiotemporal evolution of key indicators. The results show that synergistic performance consistently surpassed standalone measures, with most regions demonstrating accelerating synergistic enhancement over time. Contribution (2) uses the Hurst coefficient, Mann–Kendall nonparametric test, streamflow pattern indices, and sample entropy (SampEn) analyses to investigate the streamflow pattern of the Yangtze River basin at annual, monthly, and daily timepoints. The results reveal that streamflow complexity increases from upstream to downstream along the main reach, and the monthly streamflow shows significant trends in the dry and wet seasons. Contribution (3) analyzes the impact of climate change and human activities on the runoff of the Ganjiang River Basin using various models with different spatiotemporal scales and complexities. The results indicate that climate change is the main driving factor leading to runoff variation in the Ganjiang River Basin, accounting for 60.07% to 82.88% of the runoff change. Therefore, future studies should focus on developing more integrated and adaptive models to better understand the complex interactions between climate change, human activities, and water resource management, and explore innovative strategies for enhancing water security and sustainability.

For Category B, "Rivers and Lakes Water Ecology and Water Pollution", Contribution (4) formulates three types of eco-recycled concrete (ERC) by integrating shell-derived biochar with recycled aggregates and evaluates their efficacy in treating polluted water with heavy metals. Their results show that biochar addition significantly enhances the continuous porosity and water permeability of the concrete and substantially improves its adsorption capacity of heavy metals. Contribution (5) conducts a controlled laboratory experiment and combines it with long-term field monitoring to determine the main hydro-biogeochemical processes of polygenic multipollutants and their secondary pollutants in groundwater. The results indicate that the redox environment and the gradient change in pH are the most critical controlling factors for the evolution of pollutants. Contribution (6) systematically reviews 1141 articles on seasonal frozen lakes from 1991 to 2021, discussing the seasonal variations and control conditions of ice-covered lakes. The review shows that the ice-cover period is shortening, lake evaporation is increasing, and planktonic organisms are responding to global climate change with earlier spring blooming.

For Category C, "Irrigation Technology and Water Use Efficiency", Contribution (7) investigates the distribution and accumulation of clogging substances within drip irrigation emitters under three water conditions (saline water, Yellow River water, and a mixture of both). The results show that the use of blended water can effectively alleviate clogging and enhance drip irrigation efficiency. Contribution (8) proposes a network structure, the SE-Attention-Residual-Unet (SE-ResUnet), for water extraction tasks in the Yellow River

Basin. The results demonstrate that the strategy combining an attention mechanism and a weighted loss function significantly improves the effectiveness of neural network models in water extraction tasks.

3. Discussion and Suggestions

According to the aforementioned research findings and current progress in the field, we further summarize the water security issues in China as follows:

(I) The uneven spatiotemporal distribution of water resources, driven by multiple factors, is a fundamental cause of water security challenges. From a climatic perspective, most regions of China are influenced by the monsoon climate, with precipitation primarily concentrated in summer and autumn, while relatively low levels in winter and spring create temporal imbalances in water availability. Furthermore, variability in the onset and retreat of the summer monsoon leads to substantial interannual and regional differences in precipitation, further intensifying the uneven spatiotemporal distribution of water resources. From a geographical perspective, China's vast territory and complex topography, combined with pronounced gradients in distance from the sea, result in marked regional disparities in precipitation and runoff. In general, water resources exhibit the pattern of "more in the east and less in the west, more in the south and less in the north" [1]. The southern regions are predominantly humid or semi-humid, with abundant rainfall, whereas the northern regions are mainly semi-arid or arid, with limited precipitation. In addition, anthropogenic influences cannot be ignored. Population growth and industrial–agricultural development have continuously increased water demand, while water waste and pollution have worsened, further aggravating the imbalance in water resource distribution [2].

To address the uneven spatiotemporal distribution of water resources, a comprehensive and coordinated strategy is essential. On the one hand, cross-basin water diversion projects, such as the South-to-North Water Diversion Project, can effectively transfer water from resource-abundant regions to water-deficient areas, thereby mitigating chronic water shortages in northern China. Concurrently, it is vital to strengthen water resource assessment and planning, enhance reservoir operation to regulate runoff and seasonal fluctuations, improve water supply reliability during dry periods, and minimize water losses during flood seasons. On the other hand, greater emphasis should be placed on raising public awareness of water conservation and further strengthening the rigid water resource constraint index system to ensure sustainable management and efficient utilization.

(II) China continues to face challenges related to aquatic ecological degradation and water pollution. While rapid industrialization and urbanization have driven substantial economic growth, they have simultaneously imposed severe pressures on aquatic ecosystems. For example, in certain regions of China, the overexploitation of water resources—such as groundwater extraction in the North China Plain—has altered the natural regulatory functions of aquatic systems. In addition, the discharge of industrial wastewater, agricultural non-point source pollution, and untreated domestic sewage persists in some areas, leading to eutrophication and severe river pollution. These challenges not only undermine ecological stability but also pose considerable risks to public health and the long-term sustainability of economic development.

To mitigate aquatic ecological degradation and water pollution, a comprehensive strategy integrating systemic governance, source control, and ecological restoration is essential. Current priorities in water resource protection and environmental governance include strengthening river rehabilitation, restoring the natural morphology of rivers, and enhancing their water conveyance capacity [3]. Furthermore, ecological restoration initiatives—such as afforestation and wetland rehabilitation—should be advanced to improve the self-purification capacity of aquatic systems. Equally important is the comprehen-

sive regulation and control of pollution sources across multiple sectors. In the industrial sector, emission standards should be upgraded, clean production practices and circular economy models promoted, and the discharge of toxic and hazardous substances strictly controlled. In agriculture, emphasis should be placed on adopting ecological farming methods, applying precision fertilization and pesticide technologies, and improving the utilization of livestock and poultry waste to effectively reduce non-point source pollution. In urban areas, efforts should focus on strengthening sewage collection systems, improving the treatment efficiency of wastewater treatment plants—particularly regarding nitrogen and phosphorus removal—and increasing the reuse of reclaimed water. At the same time, it is imperative to strengthen the water environment monitoring network [4].

(III) The contradiction between water resource supply and demand remains prominent. The uneven spatial and temporal distribution of water resources, combined with growing demand driven by economic and social development, has intensified this imbalance [5]. Water resources in the Yangtze River Basin and southern regions account for more than 80% of the national total, whereas the northern region possesses less than 20% but supports over 60% of the national population and cultivated land. This disparity has led to persistent water scarcity in northern China. With the accelerating processes of urbanization and industrialization, the contradiction between water supply and demand has become increasingly acute.

Under the framework of the water management principle of “prioritizing water conservation, achieving spatial balance, pursuing systematic governance, and advancing with dual efforts,” the key to addressing China’s supply–demand contradictions and safeguarding water security lies in the implementation of systematic and comprehensive measures [6]. Enhancing the efficiency of water resource utilization is particularly crucial in agriculture, industry, and urban domestic sectors [7]. In agriculture, the large-scale adoption of efficient irrigation technologies such as drip and sprinkler systems, adjustment of cropping structures, selection of drought-resistant crops, and implementation of precision irrigation management are essential. In industry, water conservation requires technological upgrading, increased reuse rates of water resources, and the promotion of water-efficient industries. In urban areas, efforts should focus on the widespread use of water-saving appliances, reduction in pipeline leakage, promotion of reclaimed water reuse technologies, and strengthening of the public awareness of water conservation. Equally important is the optimization of water resource allocation and the rational layout of water supply systems. Within the context of inter-basin water transfers, the construction and management of projects such as the South-to-North Water Diversion Project should be optimized to meet supply demands while carefully considering ecological impacts. Strengthening integrated river basin management is also indispensable, ensuring coordinated regulation of water volume, water quality, and aquatic ecosystems across regions [8]. By improving water-use efficiency, optimizing allocation, protecting aquatic ecosystems, advancing institutional reforms, and fostering scientific and technological innovation, sustainable water resource management can be achieved, thereby providing a strong safeguard for China’s long-term economic and social development.

Author Contributions: Conceptualization and writing—original draft, Q.Z. and Z.L.; writing—review and editing, F.W., J.Z., X.Z., D.S., L.Z. and R.G. All authors have read and agreed to the published version of the manuscript.

Acknowledgments: The authors acknowledge the contributions of all authors of the eight papers in this Special Issue.

Conflicts of Interest: The authors declare no known conflicts of interest.

List of Contributions

1. Zhao, J.; Li, H.; Liu, Z.; Jiang, Y.; Mu, W. Water Saving and Carbon Reduction (CO₂) Synergistic Effect and Their Spatiotemporal Distribution Patterns. *Water* **2025**, *17*, 1847. <https://doi.org/10.3390/w17131847>.
2. Lv, P.; Zeng, S.; Liu, X.; Yang, L. Changes in Streamflow Pattern and Complexity in the Whole Yangtze River Basin. *Water* **2024**, *16*, 2467. <https://doi.org/10.3390/w16172467>.
3. Wang, Q.; Yang, F.; Hu, X.; Hou, P.; Zhang, Y.; Li, P.; Lin, K. Multi-Model Comparison in the Attribution of Runoff Variation across a Humid Region of Southern China. *Water* **2024**, *16*, 1729. <https://doi.org/10.3390/w16121729>.
4. Ren, Y.; Lai, X.; Wang, J.; Li, R.; Li, S.; Yan, X.; Liu, J.; Song, S. Simulation of Heavy Metal Removal in Irrigation Water Using a Shell-Derived Biochar-Integrated Ecological Recycled Concrete. *Water* **2024**, *16*, 3646. <https://doi.org/10.3390/w16243646>.
5. Dong, Y.; Han, Y.; Han, X.; Chen, Y.; Zhai, Y. Sewage Vertical Infiltration Introduced Polygenic Multipollutants into Groundwater. *Water* **2024**, *16*, 2305. <https://doi.org/10.3390/w16162305>.
6. Wang, Q.; Yang, F.; Liao, H.; Feng, W.; Ji, M.; Han, Z.; Pan, T.; Feng, D. Seasonal Variations of Ice-Covered Lake Ecosystems in the Context of Climate Warming: A Review. *Water* **2024**, *16*, 2727. <https://doi.org/10.3390/w16192727>.
7. Yao, Y.; Xiao, Y.; Hou, P.; Li, S. Evaluating the Influence of Water Quality on Clogging Behavior in Drip Irrigation Emitters: A CT Imaging Study. *Water* **2025**, *17*, 1065. <https://doi.org/10.3390/w17071065>.
8. Yang, J.; Lu, Y.; Zhang, Z.; Wei, J.; Shang, J.; Wei, C.; Tang, W.; Chen, J. A Deep Learning Method Coupling a Channel Attention Mechanism and Weighted Dice Loss Function for Water Extraction in the Yellow River Basin. *Water* **2025**, *17*, 478. <https://doi.org/10.3390/w17040478>.

References

1. Wang, K.; Li, B.; Shang, F.; Han, J.; Wu, X.; Huang, Y. Progress and Challenges of Water Ecological Environment Protection from the Perspective of Three Waters Overall Planning. *J. Basic Sci. Eng.* **2025**, *33*, 111–121.
2. Shi, X.; Li, C.; Yu, Z. Evaluating the comprehensive water resources utilization level in China: Dynamic distribution analysis and spatial convergence insights. *PLoS ONE* **2025**, *20*, e0319150. [CrossRef] [PubMed]
3. Geissen, V.; Mol, H.; Klumpp, E.; Umlauf, G.; Nadal, M.; van der Ploeg, M.; van de Zee, S.E.A.T.M.; Ritsema, C.J. Emerging pollutants in the environment: A challenge for water resource management. *Int. Soil Water Conserv. Res.* **2015**, *3*, 57–65. [CrossRef]
4. Ji, Y. Status and Treatment Model of Water Resources Pollution in the Yellow River Basin of China. *Nat. Environ. Pollut. Technol.* **2017**, *16*, 783–788.
5. Yin, Y.; Wang, L.; Wang, Z.; Tang, Q.; Piao, S.; Chen, D.; Xia, J.; Conradt, T.; Liu, J.; Wada, Y.; et al. Quantifying water scarcity in northern China within the context of climatic and societal changes and south-to-north water diversion. *Earth's Future* **2020**, *8*, e2020EF001492. [CrossRef]
6. Wang, X.; Zhang, J.; Gao, J.; Shahid, S.; Xia, X.; Geng, Z.; Tang, L. The new concept of water resources management in China: Ensuring water security in changing environment. *Environ. Dev. Sustain.* **2018**, *20*, 897–909. [CrossRef]
7. Song, S.; Fang, L.; Yang, J.; Zhou, R.; Bai, G.; Qiu, Y. The spatial-temporal matching characteristics of water resources and socio-economic development factors: A case study of Guangdong Province. *Water* **2024**, *16*, 362. [CrossRef]
8. Zhu, Q.; Cao, Y. Research on provincial water resources carrying capacity and coordinated development in China based on combined weighting TOPSIS model. *Sci. Rep.* **2024**, *14*, 12497. [CrossRef] [PubMed]

Disclaimer/Publisher's Note: The statements, opinions and data contained in all publications are solely those of the individual author(s) and contributor(s) and not of MDPI and/or the editor(s). MDPI and/or the editor(s) disclaim responsibility for any injury to people or property resulting from any ideas, methods, instructions or products referred to in the content.

Article

Water Saving and Carbon Reduction (CO₂) Synergistic Effect and Their Spatiotemporal Distribution Patterns

Jing Zhao, Hanting Li *, Zhiying Liu, Yaoqing Jiang and Wenbin Mu

Water Conservancy Engineering Department, School of Water Resources, Longzihu Campus, North China University of Water Resources and Electric Power, Zhengzhou 450046, China; zhaojing19870515@163.com (J.Z.); 19555717151@163.com (Z.L.); 16634861011@163.com (Y.J.); muwenbin@ncwu.edu.cn (W.M.)

* Correspondence: lihanting0612@163.com

Abstract: Under the dual constraints of rigid water resource management systems and China's "dual carbon" national strategy, water resource management authorities face pressing practical demands for the coordinated governance of water conservation and carbon dioxide emission reduction. This study comprehensively compiles nationwide data on water supply/consumption, energy use, water intensity, and CO₂ emissions across Chinese provinces. Employing a non-radial directional distance function (NDDF) model with multiple inputs and outputs, we quantitatively assess provincial water saving and carbon reduction performance during 2000–2021; measure synergistic effects; and systematically examine the spatiotemporal evolution, correlation patterns, and convergence trends of three key indicators: standalone water saving performance, standalone carbon reduction performance, and their synergistic performance—essentially addressing whether “1 + 1 > 2” holds true. Furthermore, we analyze the spatial convergence and clustering characteristics of synergistic effect across regions, delving into the underlying causes of inter-regional disparities in water–carbon synergy. Key findings reveal the following: ① Temporally, standalone water saving and carbon reduction performance generally improved, though the water saving metrics initially declined before stabilizing into sustained growth, ultimately outpacing carbon reduction gains. Synergistic performance consistently surpassed standalone measures, with most regions demonstrating accelerating synergistic enhancement over time. Nationally, water–carbon synergy exhibited early volatile declines followed by steady growth, though the growth rate gradually decelerated. ② Spatially, high-value synergy clusters migrated from the western to eastern regions and the northern to southern zones before stabilizing geographically. The synergy effect demonstrates measurable convergence overall, yet with pronounced regional heterogeneity, manifesting a distinct “high southeast–low northwest” agglomeration pattern. Strategic interventions should prioritize water–carbon nexus domains, leverage spatial convergence trends and clustering intensities, and systematically unlock synergistic potential.

Keywords: water saving and carbon reduction synergistic effect; non-radial directional distance function model (NDDF); synergistic effect quantification model; performance indicators; spatial analysis

1. Introduction

1.1. Research Background and Significance

Currently, global warming caused by greenhouse gas emissions from human activities has become a severe common challenge for the development of all humanity. The concentration of carbon dioxide in the atmosphere continues to rise year by year, triggering a

series of climate issues and causing significant changes in the reserves of various resources essential for human survival.

The latest climate report from the United Nations Intergovernmental Panel on Climate Change (IPCC) states that to limit global warming to 1.5 °C, the world must reduce carbon emissions by 40% by 2030 and achieve net-zero emissions by 2050. Without immediate action, the carbon budget for staying within the 1.5 °C threshold is projected to be exhausted within the next decade.

As the world's largest developing country, China is still in a phase of rapid development, where socioeconomic progress continues to demand substantial consumption of water resources and carbon-intensive mineral resources. In 2020, China's carbon dioxide emissions accounted for 31.9% of the global emissions [1]. On 22 September 2020, President Xi Jinping explicitly stated at the 75th United Nations General Assembly that China aims to peak its carbon dioxide emissions before 2030 and strive to achieve carbon neutrality before 2060. The IPCC technical report points out that climate change will have a significant impact on freshwater resources, and the uneven spatial and temporal distribution of water resources will exacerbate the world's water resource problems, leading to increasingly prominent contradictions between water supply and demand. In October 2019, General Secretary Xi Jinping visited the Yellow River and held a symposium on ecological protection and high-quality development in the Yellow River Basin. He pointed out that “we must adhere to the principle of using water to determine cities, land, people, and production, take water resources as the biggest rigid constraint, plan population, urban, and industrial development reasonably, and resolutely curb unreasonable water demand”. In 2019, the National Development and Reform Commission and the Ministry of Water Resources issued and implemented the National Water Conservation Action Plan, and in 2024, the Ministry of Water Resources organized the preparation of the National Water Conservation Medium-and-Long-Term Plan (2025–2035), both indicating that water conservation has risen to the national strategic level. Compared to 2014, with China's GDP nearly doubling in 2023, the overall water consumption remains stable at 610 billion cubic meters. The water consumption per CNY 10,000 of GDP and industrial added value have decreased by 41.7% and 55.1%, respectively, indicating a significant water saving effect. The achievement of the “dual carbon” goal is closely related to the conservation and utilization of water resources. With the establishment of the “dual carbon” goal, the comprehensive benefit evaluation that considers both “water conservation” and “carbon reduction” is no longer limited to the ecological environment field, but should take into account the rapid economic and social development and the sustainable utilization of resources.

The energy sector serves as the primary arena for achieving carbon peak and carbon neutrality in China, with energy-related carbon emissions accounting for approximately 88% of the nation's total CO₂ emissions. In 2022, China's CO₂ emissions per unit of GDP reached 6.6 tons per USD 10,000, significantly exceeding both the global average and the levels of major Western developed economies. From 2010 to 2022, China's per capita cumulative CO₂ emissions amounted to around 133 tons, surpassing the global average of 67 tons and France's 123 tons, yet remaining below the figures for Australia (352 tons), Canada (337 tons), the EU (195 tons), the United States (386 tons), and the UK (162 tons), reflecting the country's ongoing efforts and challenges in balancing economic growth with decarbonization goals [2]. To achieve carbon peak and carbon neutrality while ensuring energy security, a dual strategy of implementing “subtraction” through energy conservation and emission reduction on the consumption side and executing “addition” by expanding non-fossil energy on the supply side must be adopted, with both approaches being closely intertwined with water resources. On the consumption side, saving 1 ton of coal reduces water consumption by 2 tons and cuts CO₂ emissions by 2.5 tons [3], while conserving

1 kWh of electricity saves 4 L of water and reduces CO₂ emissions by 0.997 kg. On the supply side, scaling up non-fossil energy requires substantial water inputs—producing 1 m² of silicon wafers consumes 65 L of purified water, manufacturing a 156 mm × 156 mm photovoltaic cell requires 27 L, and assembling a module with 60 cells needs 34 L. Given that global energy production accounts for about 15% of the total water withdrawals (IEA estimate), the strong synergy between water usage and CO₂ emissions in energy systems becomes evident.

Under the dual strategic pressures of “water conservation priority” and “carbon neutrality,” China’s water resource management authorities face urgent practical needs for the coordinated governance of water conservation and carbon emission reduction. The synergistic management of water and CO₂ represents both a critical proposition for China’s high-quality development and national security and an imperative requirement under the constraints of resource scarcity and climate change. Currently, the intrinsic mechanisms linking water resource development/utilization with carbon emissions remain unclear, including several pressing practical questions: Does synergy exist between water conservation and carbon reduction? If so, what form does it take? Could the combined effect of coordinated water–carbon management yield greater benefits than the sum of separate water saving and emission reduction efforts (i.e., $1 + 1 > 2$)? What are the regional disparities in water–carbon synergy performance? What factors drive these differences?

To address these questions, this study introduces a non-radial directional distance function (NDDF) model capable of handling multiple inputs and outputs. Through this framework, we conduct a comprehensive evaluation of provincial water conservation and carbon reduction performance across China from 2000 to 2021. The analysis includes horizontal and vertical comparisons between standalone water–carbon management and coordinated water–carbon governance. By constructing a synergy quantification model, we examine the spatiotemporal evolution patterns of standalone water conservation, standalone carbon reduction, and their synergistic effect. Furthermore, we investigate the spatial correlation and clustering characteristics of the synergistic effects across provinces and regions, delving into the underlying causes behind the observed regional disparities in water–carbon synergy performance.

1.2. Research Progress at Domestic and International Levels

The theory of synergistic effect originates from the concept of co-benefits, which was proposed to demonstrate that measures taken to reduce greenhouse gas emissions can simultaneously decrease the generation of other pollutants [4]. The concept of “co-benefits” was first formally introduced in the IPCC Third Assessment Report. Synergistic effect, also known as synergistic interactions, refers to the phenomenon where the combined effect of multiple components working together exceeds the sum of their individual effects—essentially achieving a “ $1 + 1 > 2$ ” outcome. Scholars have conducted extensive research on co-benefit assessment, yielding substantial findings. However, these studies have primarily focused on the domains of atmospheric pollutants and greenhouse gas emissions reduction, examining various scales from global [5,6] to national [7] and regional levels [8], and spanning different sectors including power generation [9], steel production [10], cement manufacturing [11], and transportation [12]. Previous studies have predominantly employed methods such as numerical simulation, correlation analysis, regression analysis, and marginal abatement cost assessment to evaluate the synergistic effect of pollution reduction and carbon mitigation across different countries and industries. While numerical simulation proves highly valuable for predicting policy implementation outcomes, its results represent simulated or projected values under assumed policy targets, lacking retrospective analysis based on historical data [13]. Correlation analysis has provided

empirical references for identifying efficient synergistic emission reduction strategies, yet its evaluation results remain simulation values estimated based on engineering technical parameters [14,15]. The methodological limitations of regression analysis, constrained by its single-dependent-variable framework, permit only an isolated assessment of either pollution abatement or carbon mitigation synergies, fundamentally precluding an integrated evaluation of their combined effects. While extant studies have primarily focused on end-of-pipe solutions, China's dual advancement of water-efficient societal development and low-carbon transition necessitates a paradigm shift toward production-embedded mitigation strategies—particularly through energy mix optimization, economic model transformation, and resource productivity enhancement—which are proving indispensable for achieving systemic water–carbon synergy effect that transcends conventional pollution control approaches [16]. Moreover, production factors such as capital, labor, and energy exhibit certain degrees of substitutability, which collectively influence the operation of the entire economic system [17]. Therefore, the assessment methodology for water saving and carbon reduction synergies should adopt a total-factor productivity perspective to comprehensively evaluate their synergistic effects.

Research on synergistic effects has gradually extended to the water–carbon nexus, though such studies remain in the early developmental stage. The entire process of water resource utilization—including extraction, transportation, and wastewater treatment—consumes substantial energy and generates CO₂ emissions. For instance, Wakeel et al.'s study on energy consumption in urban water systems across countries revealed that China's municipal water supply requires 0.29 kWh of energy per cubic meter [18], while wastewater treatment consumes 0.25 kWh per cubic meter. Sowby et al. evaluated water supply-related CO₂ emissions across ten major U.S. cities [19], showing that supplying one cubic meter of water produces 21–560 g of CO₂ emissions, and that water conservation could reduce annual emissions by 1200–65,000 metric tons per city. Valek et al. quantified the water–energy nexus in Mexico City [20], demonstrating the feasibility of reducing water supply to decrease both energy consumption and CO₂ emissions. A considerable number of domestic studies have focused on the synergistic effects of pollution reduction and carbon emission reduction. For instance, Gu et al. [21], based on data from nine wastewater treatment plants in China, found that treating one cubic meter of domestic sewage requires 13.38 L of water and generates 0.23 kg of carbon dioxide emissions. Zhao et al. identified water systems as a major source of carbon emissions [22]. Zhu et al. noted that urban water systems account for 12% of the total urban carbon emissions during operation [23]. Meanwhile, numerous studies on the “water–carbon nexus” have been conducted from the “water–energy–carbon (WEC) nexus” perspective for discussion. Throughout the energy production chain—including coal mining and power generation—water resources play indispensable roles in cleaning and cooling processes. Notably, both energy production/consumption and wastewater treatment processes represent two primary sources of CO₂ emissions [24,25], meaning intensive emission reduction measures in resource- and energy-intensive industries can significantly influence both water usage and carbon emissions [26]. Jin et al. evaluated the synergistic effect between energy conservation and water saving [3], demonstrating that energy-saving measures in the energy sector can yield significant water conservation benefits. Their study quantified that energy conservation in the sector achieved water savings of $12.40 \times 10^8 \text{ m}^3$, while water conservation measures resulted in energy savings equivalent to 1.12×10^6 tons of standard coal. Industrial restructuring generates both push and pull effects, leading to coordinated changes in water usage and CO₂ emissions [27]. Additionally, the development and utilization of hydropower causes transformations in both energy mix and water source composition, which in turn impacts CO₂ emission levels [28]. Li et al. demonstrated that

expanding China's wind power capacity to 200 GW could reduce carbon intensity by 23% while conserving 800 million m³ of water [29]. Zhang et al.'s assessment of the water–carbon nexus in China's thermal power sector revealed that adopting air-cooled units would increase CO₂ emissions by 24.3–31.9 million tons but reduce water consumption by 832–942 million m³ [30]. Feng et al. further quantified that transitioning from coal to low-carbon renewable energy generation could achieve over 79% reduction in CO₂ emissions and more than 50% decrease in water usage [31]. The existing research has consistently demonstrated significant synergies between water consumption and CO₂ emissions in industrial production processes [32]. Tan et al. identified a significant synergistic effect between water conservation and carbon reduction [33]. Zhao et al. quantified water use per unit of CO₂ emission, confirming substantial water–carbon synergy [34]. Zhang et al.'s analysis of the water–energy–carbon nexus in the steel industry revealed that energy-saving measures simultaneously reduce both water use and emissions [35]. Some scholars have also explored the synergistic effects of water conservation and carbon reduction through the lens of the water–carbon coupling relationship. For example, Yang et al. analyzed the trends in industrial water use and CO₂ emissions in the Yangtze River Delta region. They employed the coupling coordination degree and the LMDI (Logarithmic Mean Divisia Index) decomposition method to quantify the effects of coordinated water conservation and carbon reduction efforts [36]. These findings collectively prove that water conservation effectively reduces CO₂ emissions, while decarbonization processes conserve water, enabling the concurrent achievement of dual water saving and emission reduction objectives.

Although some initial explorations into the synergistic effects of water conservation and carbon reduction have been undertaken, the existing research still has significant limitations. Studies on the synergistic effects of water conservation and carbon reduction across different regions and industry sectors within the entire socioeconomic system remain relatively scarce. There has been no examination of the synergistic effects of water conservation and carbon reduction from a full-factor perspective. Water conservation and performance improvement can be seen as two sides of the same coin. However, few studies have evaluated the synergistic effects of water conservation and carbon reduction from a performance perspective. The spatiotemporal distribution characteristics are still unclear, and the convergence and divergence trends remain to be revealed.

2. Synergy Effect Evaluation Methods

The current literature classifies energy–environmental performance measurement methods into two categories: single-factor indicators and total-factor indicators [37]. Single-factor indicators exhibit inherent limitations as they fail to account for input substitution effects between energy and other production factors such as capital and labor [38]. Within the neoclassical production theory framework, total-factor energy–environmental productivity measures that incorporate capital and other input factors have consequently gained widespread development and application. The production process yields not only desirable outputs but also inevitably generates undesirable by-products simultaneously. It is precisely this capability to jointly evaluate both desirable and undesirable outputs that has made distance function methodology the predominant approach for measuring total-factor energy–environmental productivity. However, the conventional approach requires the proportional scaling of both desirable and undesirable outputs. To reconcile this inherent conflict, Chung et al. developed the directional distance function (DDF) model [39]. The DDF's key advantage lies in its ability to simultaneously increase desirable outputs while decreasing undesirable outputs within the production possibility set. Nevertheless, the DDF maintains a restrictive assumption of strictly proportional changes—requiring equiv-

alent rates of expansion for desirable outputs and contraction for both input factors and undesirable outputs, which may induce “slack bias” [40]. To address this limitation, the non-radial directional distance function (NDDF) was subsequently developed, relaxing the rigid proportionality assumptions and allowing for non-uniform adjustments [41].

The NDDF (non-radial directional distance function) is a non-parametric efficiency evaluation model based on the Data Envelopment Analysis (DEA) framework, primarily used to measure the efficiency performance of decision-making units (DMUs) in multi-input and multi-output systems. This model significantly improves upon the traditional directional distance function (DDF) by constructing the production frontier through linear programming and defining the efficiency value of DMU as the “directional distance” to the frontier, thereby reflecting their potential for improvement. The NDDF model allows for the simultaneous consideration of input reduction and output expansion, supporting non-radial adjustments, which means that different variables can be optimized at different proportions without any restrictions on the direction and proportion of increase or decrease for each element, making it more flexible in dealing with complex multi-input and multi-output systems.

The article constructs a quantitative model based on the perspective of emission reduction performance, fully reflecting all factor attributes of the production process, introducing water resources variables, constructing a non-radial distance function (NDDF), considering the synergistic effect of two parameters, and measuring the performance of water resource conservation and carbon dioxide emissions. By comparing the changes in emission performance under separate water saving, separate carbon reduction, and water saving and carbon reduction synergistic scenarios, a quantitative evaluation method for water saving and carbon reduction synergistic effect is constructed from the perspective of performance, providing methodological support for evaluating water saving and carbon reduction synergistic effect.

2.1. NDDF Model Construction

We assume that there are $i = 1, 2, \dots, N$ regions as basic decision-making units (DMUs) with a total of $t = 1, 2, \dots, T$ periods. Each region inputs factors for production in each period, resulting in expected output accompanied by unexpected output. This production technology can be represented by P . In this article, considering the dual goals of water conservation and carbon reduction, input factors are set to include capital (K), labor (L), energy consumption (E_1), and water usage (E_2). The expected output is measured using GDP (G), while unexpected output includes water consumption (W) and carbon dioxide emissions (C). Drawing inspiration from Zhou et al., a non-radial distance function is constructed [42]:

$$\vec{ND}(K, L, E_1, E_2, G, W, C; g) = \sup \left\{ w^T \beta : ((K, L, E_1, E_2, Y, W, C) + g \cdot \text{diag}(\beta)) \in P \right\} \quad (1)$$

The relaxation vector $\beta = (\beta_K, \beta_L, \beta_{E_1}, \beta_{E_2}, \beta_G, \beta_W, \beta_C)^T \geq 0$ is the ratio of expansion and reduction in each input–output variable, $w = (w_K, w_L, w_{E_1}, w_{E_2}, w_G, w_W, w_C)^T$ represents the weight of each input–output, and $g = (g_K, g_L, g_{E_1}, g_{E_2}, g_G, g_W, g_C)$ is the direction vector, representing the direction of the expected output expansion and the direction of the input and unexpected output reduction.

The linear programming equation for solving the non-radial distance function is as follows:

$$\begin{aligned}
 \vec{ND}(K, L, E_1, E_2, G, W, C; g) = & \max w_K \beta_K + w_L \beta_L + w_{E_1} \beta_{E_1} + w_{E_2} \beta_{E_2} + w_G \beta_G + w_W \beta_W + w_C \beta_C \\
 \text{s.t. } & \sum_{i=1}^N \sum_{t=1}^T \lambda_{i,t} K_{i,t} \leq K + \beta_K g_K, \sum_{i=1}^N \sum_{t=1}^T \lambda_{i,t} L_{i,t} \leq L + \beta_L g_L \\
 & \sum_{i=1}^N \sum_{t=1}^T \lambda_{i,t} E_{1i,t} \leq E_1 + \beta_{E_1} g_{E_1}, \sum_{i=1}^N \sum_{t=1}^T \lambda_{i,t} E_{2i,t} \leq E_2 + \beta_{E_2} g_{E_2} \\
 & \sum_{i=1}^N \sum_{t=1}^T \lambda_{i,t} G_{i,t} \geq G + \beta_G g_G, \sum_{i=1}^N \sum_{t=1}^T \lambda_{i,t} W_{i,t} = W + \beta_W g_W, \sum_{i=1}^N \sum_{t=1}^T \lambda_{i,t} C_{i,t} = C + \beta_C g_C \\
 & \lambda_{i,t} \geq 0, i = 1, 2, \dots, N, t = 1, 2, \dots, T \\
 & \beta_K, \beta_L, \beta_{E_1}, \beta_{E_2}, \beta_G, \beta_W, \beta_C \geq 0
 \end{aligned} \tag{2}$$

The optimal solution β can be obtained by solving Equation (2). Its connotation is to maximize the expected output and minimize the unexpected output, and the relative importance of the maximum and minimum objectives is characterized by the weight vector w .

2.2. Model Parameters and Weight Settings

In accordance with the orientation of the research objectives, to explore how decision-making units (DMUs) can optimize their output structure under a given level of input, the weights of the input variables are set to 0. This aligns with the “Fixed-input, Variable-output” research paradigm and helps focus the analysis on the potential for efficiency improvement on the output side. While maintaining the theoretical rigor of the model, by fixing the input factors, the focus is more on changes in output rather than adjustments in input. This also effectively simplifies the complexity of the model, making it easier to understand and apply.

In sustainability assessment, economic benefits and environmental impacts are irreplaceable. Therefore, setting equal weights (1:1) for desirable outputs (economic benefits) and undesirable outputs (environmental impacts) ensures that the model does not presuppose a value judgment prioritizing economic or environmental goals. This approach prevents the assessment from leaning towards one aspect and avoids evaluation bias introduced by subjective preferences. It also aligns with the OECD’s (2008) principle of policy assessment neutrality.

Taking the case of individual water conservation as an example, the direction vector and weight vector are set as follows:

$$\begin{cases} g = (-K, -L, -E_1, -E_2, G, -W, 0) \\ w^T = (0, 0, 0, 0, \frac{1}{2}, \frac{1}{2}, 0) \end{cases} \tag{3}$$

Similarly, the direction vector and weight vector for the coordinated situation of individual carbon reduction, water conservation, and carbon reduction are as follows:

$$\begin{cases} g = (-K, -L, -E_1, -E_2, G, 0, -C) \\ w^T = (0, 0, 0, 0, \frac{1}{2}, 0, \frac{1}{2}) \end{cases} \tag{4}$$

$$\begin{cases} g = (-K, -L, -E_1, -E_2, G, -W, -C) \\ w^T = (0, 0, 0, 0, \frac{1}{2}, \frac{1}{4}, \frac{1}{4}) \end{cases} \tag{5}$$

Below is an example of the synergistic effect of water conservation and carbon reduction. The weight coefficients and direction vectors are input into the NDDF linear programming equation to obtain the synergistic effect linear programming problem. The

optimal solution of the relaxation variable β is solved according to different situations to construct performance indicators.

$$\begin{aligned}
 \vec{ND}(K, L, E, G, W, C; g) = & \max \left(\frac{1}{2}\beta_G + \frac{1}{4}\beta_W + \frac{1}{4}\beta_C \right) \\
 \text{s.t. } & \sum_{i=1}^N \sum_{t=1}^T \lambda_{i,t} K_{i,t} \leq K(1 - \beta_K), \sum_{i=1}^N \sum_{t=1}^T \lambda_{i,t} L_{i,t} \leq L(1 - \beta_L), \\
 & \sum_{i=1}^N \sum_{t=1}^T \lambda_{i,t} E_{1i,t} \leq E_1(1 - \beta_{E_1}), \sum_{i=1}^N \sum_{t=1}^T \lambda_{i,t} E_{2i,t} \leq E_2(1 - \beta_{E_2}) \\
 & \sum_{i=1}^N \sum_{t=1}^T \lambda_{i,t} G_{i,t} \geq G(1 + \beta_G), \sum_{i=1}^N \sum_{t=1}^T \lambda_{i,t} W_{i,t} = W(1 - \beta_W), \sum_{i=1}^N \sum_{t=1}^T \lambda_{i,t} C_{i,t} = C(1 - \beta_C) \\
 & \lambda_{i,t} \geq 0, i = 1, 2, \dots, N, t = 1, 2, \dots, T \\
 & \beta_K, \beta_L, \beta_{E_1}, \beta_{E_2}, \beta_G, \beta_W, \beta_C \geq 0
 \end{aligned} \tag{6}$$

The relaxation variables for separate water saving and carbon reduction can be solved in the same way, and will not be repeated here.

2.3. Construction of Performance Indicators

In order to more intuitively reflect the individual water conservation, carbon reduction, and the synergistic effect of the two, based on solving the relaxation variable and referring to existing literature [32], the efficiency improvement ratio based on DEA measurement is introduced, and two performance indicators, Water Conservation Performance Index (WEPI) and Carbon Reduction Performance Index (CEPI), are introduced. Their calculation formulas are as follows:

$$WEPI = \frac{G/W}{(G + \beta_G G)/(W - \beta_W W)} = \frac{1 - \beta_W}{1 + \beta_G} \tag{7}$$

$$CEPI = \frac{G/C}{(G + \beta_G G)/(C - \beta_C C)} = \frac{1 - \beta_C}{1 + \beta_G} \tag{8}$$

In the formula, WEPI is the ratio of the expected output under actual unit water consumption to the expected output under potential unit water consumption, and CEPI is the ratio of the expected output under actual unit CO₂ emissions to the expected output under potential CO₂ emissions. Obviously, the sizes of both are between 0 and 1. The larger the value, the higher the energy performance and the expected output per unit of energy consumption; β_G is the expansion ratio of regional gross domestic product (G) when the decision-making unit performs efficiency improvement, β_W is the reduction ratio of water consumption when the decision-making unit performs efficiency improvement, and β_C is the reduction ratio of CO₂ emissions when the decision-making unit performs efficiency improvement.

2.4. Quantitative Model for Synergistic Effect of Water Saving and Carbon Reduction

Based on the measured water saving and carbon reduction performance, a coupled coordination model is constructed to characterize the synergistic effect of the two. Following the approach of Tian Yun et al., the coupling degree D is first calculated using the following formula [43]:

$$D = 2\sqrt{W \times C} / (W + C) \tag{9}$$

In the formula, W is the water saving performance indicator calculated in the previous text, and C is the carbon reduction performance indicator. Based on this, a quantitative model for synergistic effect is further constructed, as shown in formula (10).

$$\begin{cases} S = \sqrt{D \times T} \\ T = \alpha W + \beta C \end{cases} \quad (10)$$

In the formula, S represents the synergistic effect of water conservation and carbon reduction, T is the comprehensive development evaluation index of water conservation performance and carbon reduction performance, α and β are undetermined indices, and $\alpha + \beta = 1$. Both reflect the contribution of water conservation and carbon reduction to collaborative development. Considering the equal status of water conservation and carbon reduction, the values of α and β are evenly divided into 0.5.

2.5. Analysis of Spatial Convergence and Aggregation

Convergence analysis is employed to examine whether variables tend toward a stable state over time. In this study, σ -convergence is utilized to reflect the dispersion degree of the research variables, analyzing and testing the spatial convergence of synergistic effect at the interprovincial level. The calculation formula is as follows:

$$\sigma = \frac{\sqrt{\frac{1}{n-1} \sum_{i=1}^n (S_{i,t} - \bar{S}_t)^2}}{\bar{S}_t} \quad (11)$$

In the formula, n is the number of provinces, $S_{i,t}$ is the synergy effect of the i -th province in year t , and \bar{S}_t is the average interprovincial synergy effect in year t . The criterion for determination is as follows: if $\sigma_{t+1} < \sigma_t$, it indicates the presence of σ -convergence (i.e., regional disparities are diminishing); if $\sigma_{t+1} > \sigma_t$, it signifies σ -divergence.

To thoroughly investigate the spatial clustering patterns of water saving and carbon reduction synergy effect across China's provincial regions, this study employs the Local Moran's I index to identify spatial autocorrelation characteristics. The core methodology involves calculating the similarity degree between each spatial unit and its neighboring units, thereby determining the existence of significant spatial associations and revealing high-value or low-value clustering patterns. The calculation formula for the Local Moran's I index is as follows:

$$\begin{aligned} I_i &= \frac{(S_i - \bar{S})}{\text{Var}(S)} \sum_{j=1}^n \omega_{ij} (S_j - \bar{S}) \\ \text{Var}(S) &= \frac{1}{n} \sum_{i=1}^n (S_i - \bar{S})^2 \end{aligned} \quad (12)$$

The output indicators of the Local Moran's I index include Local Moran's I, Z-Score, PValue, and COType. The clustering area and abnormal area are distinguished by the positive and negative values of Local Moran's I. When the value of Local Moran's I is positive, it is displayed as a clustering area, otherwise it is an abnormal area. The absolute value of Z-Score can reflect the randomness of regional spatial patterns, and the larger its absolute value, the more significantly the spatial pattern (clustering or anomaly) of the observed values deviates from the random distribution. Using PValue to define the significance of spatial patterns, the smaller the value, the more significant the spatial pattern is considered. COType refers to the four types of spatial patterns, namely High High Cluster (H-H), Low Low Cluster (L-L), High Low Outlier (H-L), and Low High Outlier (L-H), representing hot spot areas, cold spot areas, and outlier areas, respectively.

2.6. Data Source and Explanation

This paper selects panel data from 30 provinces in China (excluding Xizang, Hong Kong, Macao, and Taiwan), mainly based on the following considerations: First, ensure the availability and consistency of data. The availability and refinement of provincial data are relatively high, which can more accurately account for carbon emissions, water resource consumption, and energy use. Secondly, the selected 30 provinces cover the three major economic belts of eastern, central, and western China, with spatial representativeness and accounting for over 95% of the country's land area and over 99% of the total population. They can comprehensively reflect the commonalities and differences in the coordinated development of water conservation and carbon reduction in different regions of China.

This article selects a time span from 2000 to 2021 to maintain data continuity and avoid the impact of missing or interrupted data on research results, which is beneficial for more accurate analysis of long-term trends and intrinsic relationships between variables; At the same time, a longer time span covering multiple economic cycles can more comprehensively reflect the changes in the input–output efficiency of the economic system in different states, which helps to analyze in depth the long-term structural factors and short-term random factors that affect production efficiency, thus providing a basis for formulating more scientific and reasonable policies and management measures.

The water consumption data used in the article are sourced from the “Water Resources Bulletin” of various provinces over the years, the labor and economic output data are sourced from the “National Economic and Social Development Bulletin” of various provinces over the years, and the capital stock data of each province is sourced from the “Statistical Yearbook”. Among them, the capital stock input factor is based on 2005 as the initial year. This article refers to Zhang Jun's perpetual inventory method to calculate the capital stock [44], and the specific calculation formula is as follows:

$$x_1^t = (1 + \delta)x_1^{t-1} + I^t \quad (13)$$

In the formula: x_1 is the capital stock in year t ; I is the investment for year t ; and δ is the depreciation rate of fixed assets.

3. Result Analysis

3.1. Comparison of Individual Water Conservation and Carbon Reduction with Collaborative Performance

The national WEPI is 0.061. From 2001 to 2002, WEPI showed a decline, and from 2002 to 2021, it showed a continuous upward trend, increasing from 0.015 in 2002 to 0.103 in 2021, an increase of 5.9 times. WEPI fluctuated slightly from 2018 to 2019, possibly due to the “National Water Conservation Action Plan” jointly released by the National Development and Reform Commission and the Ministry of Water Resources in 2019, which was guided by “policy guidance, market orientation, and innovation drive”, proposing measures such as establishing and improving incentive mechanisms, strengthening social capital investment, supporting water conservation service enterprises, and promoting the development of water conservation industries, further promoting water conservation work throughout society.

The average CEPI is 0.052. In the early stage, due to the initial stage of carbon reduction work, the effects of policies and measures have not yet fully manifested, and their changes have tended to stabilize. After 2003, CEPI maintained an upward trend, and the rate of increase has increased since 2010, with a growth rate of 89.0%. It may be due to the National Development and Reform Commission's release of the “Notice on Launching Carbon Emission Trading Pilot Work” in 2011, which initiated the pilot

work of carbon emission trading. In 2020, China proposed the “dual carbon” goal, and in 2021, the national carbon emission trading market was launched and put into operation. Through market mechanisms, enterprises were incentivized to reduce carbon emissions, increasing carbon reduction efforts and thus promoting further improvement in carbon reduction performance. The temporal variation characteristics of individual water-saving and individual carbon reduction performance are shown in Figure 1.

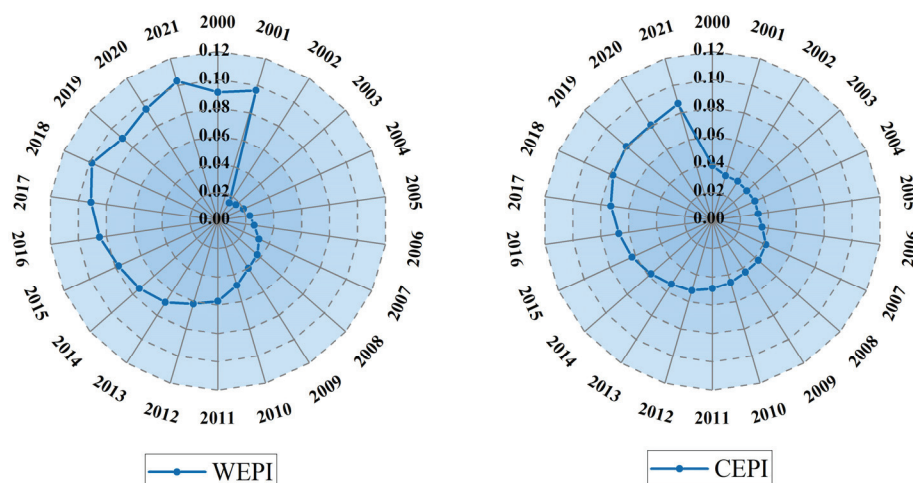


Figure 1. Time-varying graphs of individual water saving and carbon reduction performance.

To comprehensively consider the “individual” performance and “collaborative” performance, the sum of the water saving performance and carbon reduction performance in the collaborative water saving and carbon reduction state is defined as collaborative performance, i.e., “1 + 1”. The sum of the water saving performance in the individual water saving state and the carbon reduction performance in the individual carbon reduction state is defined as individual performance. The changes in individual and collaborative performance in China and seven major regions are shown in Figure 2. From 2000 to 2021, at the national level, both individual and collaborative performance showed an overall upward trend, indicating a significant improvement in water conservation and carbon reduction over time. At the same time, the collaborative performance value is generally higher than the sum of individual performance, and collaborative performance has obvious advantages compared to individual performance. Moreover, the growth rate of collaborative performance in the later stage is relatively fast, with less volatility, showing a more stable growth trend.

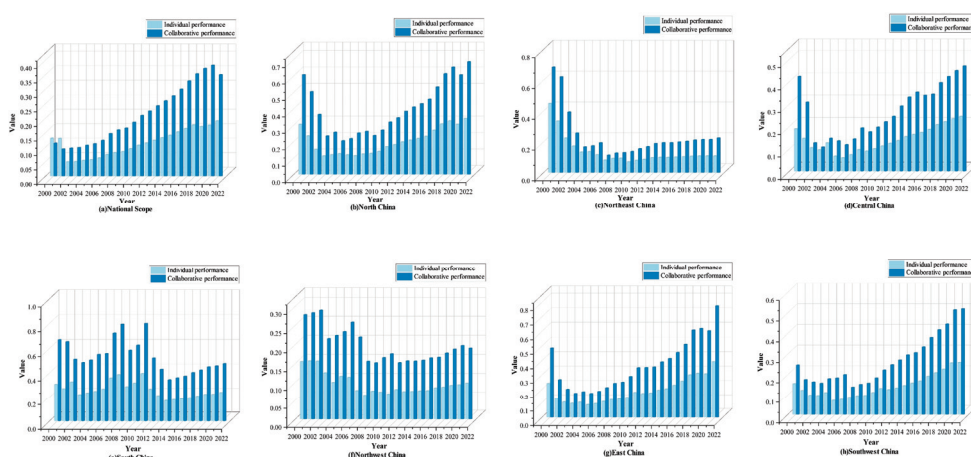


Figure 2. Individual and collaborative performance.

The “collaborative” performance in all the regions of the country is greater than the sum of the “individual” performance, that is, “1 + 1 > 2” exists, and there is a characteristic of first fluctuation and then stability. Over time, the improvement of collaborative performance in most regions is greater than that in the initial stage. The growth rate in North China increased from 62.7% to 101.8%, Northeast China increased from 52.7% to 109.1%, East China increased from 79.4% to 98.1%, Southwest China increased from 58.9% to 100.6%, and Northwest China increased from 72.6% to 95.4%, achieving an improvement in collaborative performance growth. The collaborative promotion of water conservation and carbon reduction work can more effectively integrate and optimize the allocation of related resources, fully tap into the potential of resources, achieve the dual goals of water conservation and carbon reduction, and improve resource utilization efficiency and work efficiency.

3.2. Temporal Evolution of Water Saving and Carbon Reduction Synergistic Effect

The synergistic effect quantification model further yields the water saving and carbon reduction synergy values. At the national level, the average synergy effect reached 0.231. Due to imperfect coordination mechanisms and the ongoing exploration of policies and technical measures during the initial stage, the synergy effect experienced significant fluctuations, dropping sharply from 0.244 in 2000 to 0.149 in 2002. From 2002 to 2018, it showed continuous and rapid growth, increasing from 0.149 to 0.216, demonstrating a visible synergistic effect. Although the growth rate slightly slowed from 2018 to 2021, it maintained an upward trend. The temporal evolution of the synergy effect at both national and regional levels is illustrated in Figure 3.

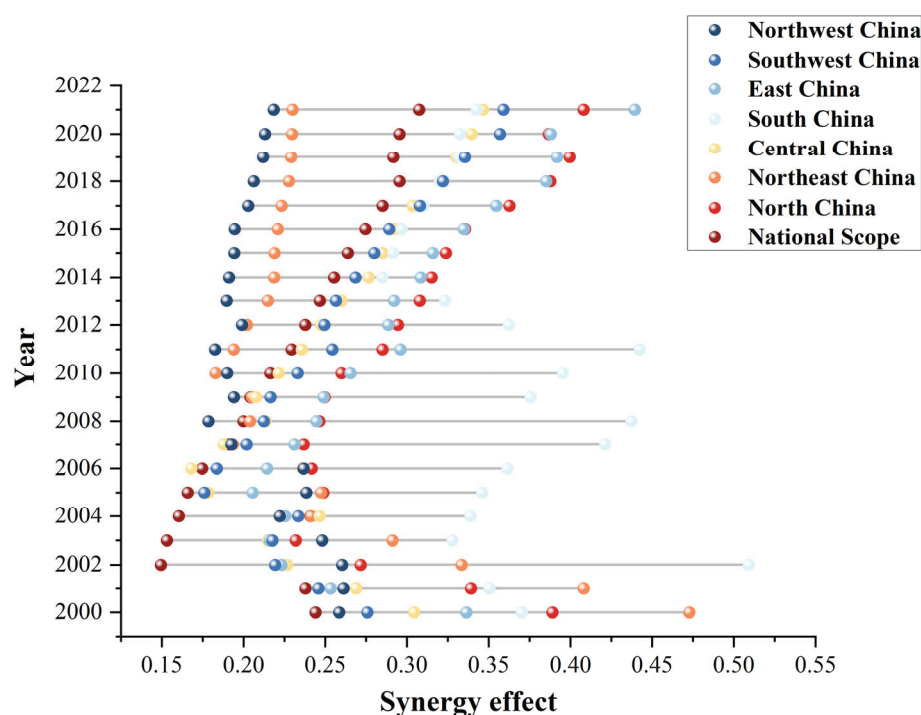


Figure 3. The evolution of water saving and carbon reduction synergistic effect at the national and regional levels.

During the period 2000–2021, significant synergistic effects were observed across all the regions, exhibiting an overall trend of initial decline followed by growth, which aligns with the evolutionary pattern of national-level water saving and carbon reduction synergy effect.

During 2000–2007, Northeast China experienced significant synergy effect fluctuations characterized by an initial sharp decline followed by stabilization, attributable to delayed economic restructuring that maintained the dominance of energy- and water-intensive heavy industries, resulting in high resource consumption, slow improvements in water-use efficiency, and persistently high carbon emission intensity. Other regions demonstrated distinct patterns: North, East, Central, and Southwest China all showed short-term fluctuating declines before achieving remarkable growth at rates of 75.9%, 113.8%, 106.2%, and 104.0%, respectively, with East China exhibiting the most pronounced synergy enhancement driven by robust development in high-tech industries and modern services. Northwest China followed a similar but more moderate trajectory of initial decline followed by gradual recovery.

At the provincial level, provinces generally showed a downward trend during 2001–2007, while exhibiting a basically stable growth trend during 2007–2020 with only a few exceptions.

The synergy values of municipalities directly under the central government such as Beijing, Tianjin, and Shanghai maintained continuous and rapid growth, while coastal economic powerhouses like Jiangsu, Zhejiang, and Fujian showed steady growth in synergy effect, all surpassing the national average. Among major economic provinces, Shandong's synergy value increased from 0.156 in 2001 to 0.306 in 2020, and although Guangdong's synergy value fluctuated, it generally remained at a relatively high level. Provinces with active development in economy, technology, and other aspects including Hebei, Jiangxi, Hainan, Guangxi, and Yunnan saw varying degrees of increase in their synergy values. In recent years, the state has increased policy support and financial investment in the central and western regions, driving significant growth in synergy effect in key western areas like Chongqing and Sichuan. However, Liaoning, Jilin, and Heilongjiang experienced fluctuating declines to varying degrees, and as resource-based provinces, Shanxi and Inner Mongolia showed more obvious downward trends, with their final synergy values being lower than the national average. The evolution process of synergistic effects among 30 provinces and cities is shown in Figure 4.

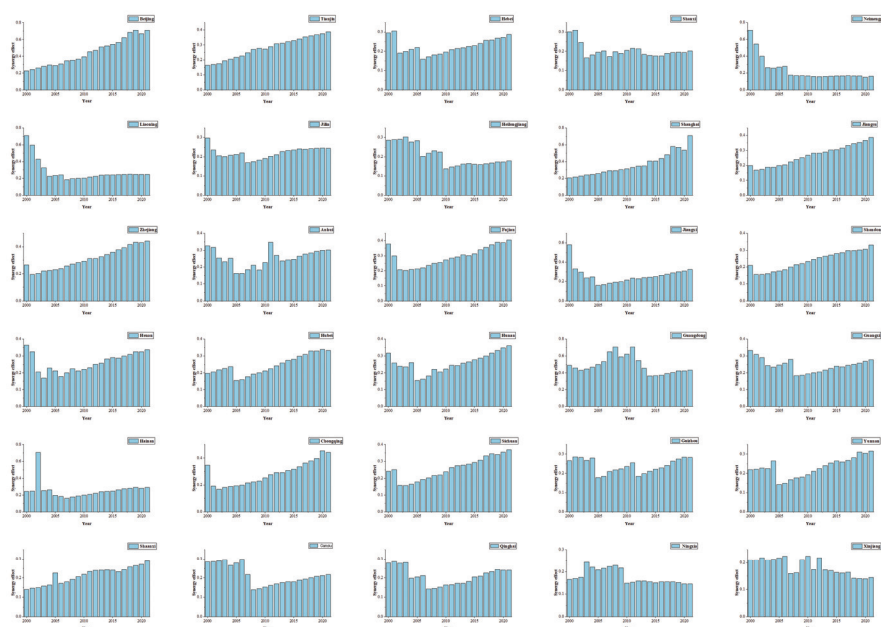


Figure 4. Evolution of synergistic effect across 30 provinces and municipalities.

3.3. Spatial Distribution Patterns of Water Saving and Carbon Reduction Synergistic Effect

At the regional level, Northwest China's arid climate and water scarcity have resulted in relatively higher difficulty and cost for water conservation, coupled with the region's heavy reliance on high-carbon fossil fuels like coal in its energy mix, leading to substantial carbon emissions from energy consumption. These factors collectively constrain the water-carbon synergy, yielding a below-average synergistic effect of 0.213. While Northeast China's synergy effect (0.247) exceeds the national average, it remains comparatively lower than other regions. In contrast, East China (0.294), North China (0.307), and South China (0.358) demonstrate significantly better performance in achieving water saving and carbon reduction synergies.

The synergistic effect values of each province/municipality in key years are shown in Figure 5. From 2001 to 2007, the distribution of synergistic effect underwent significant changes, with high-value areas shifting from the western to eastern regions and from the northern to southern parts of China. Between 2013 and 2020, the disparities both within the northern regions and between the northern and southern regions gradually narrowed, indicating a stabilization trend in the spatial distribution of synergistic effect values.

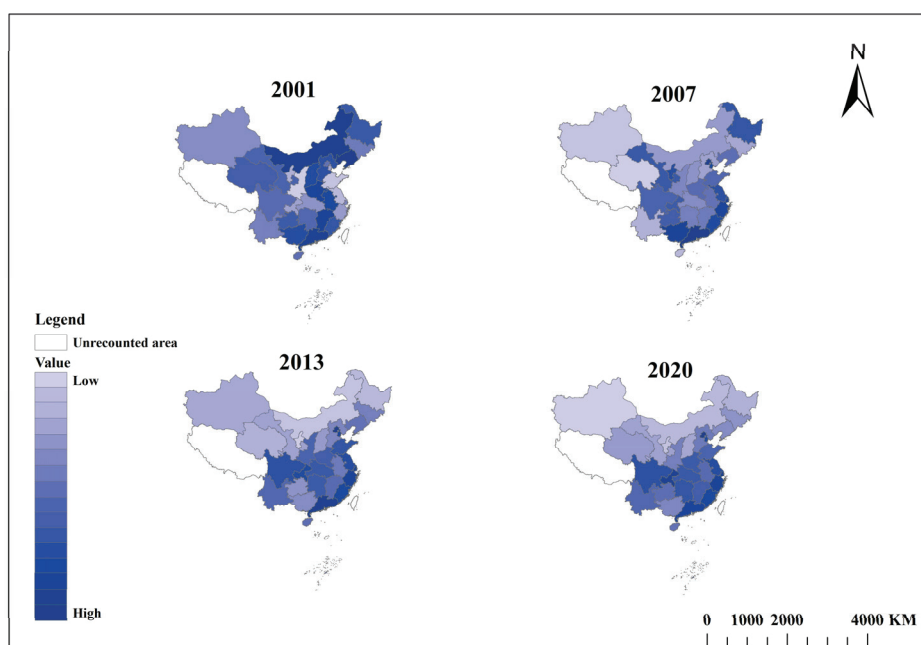


Figure 5. Synergistic effect values by province/municipality in key years.

Overall analysis reveals distinct spatial patterns in synergistic effect: The southern provinces generally demonstrate higher values with faster growth rates, while the performance gaps among the high-performing southern regions have progressively narrowed. In contrast, the northern regions like Inner Mongolia and Shanxi showed initially elevated but ultimately stagnant synergy values with limited growth momentum. Regional disparities persist between the eastern and western areas, with the coastal eastern provinces transitioning from single-pole dominance (led by Guangdong and Shanghai) to multi-center collaboration, while the western provinces exhibit growing divergence. Spatially, the high-value clusters of synergistic effect have systematically shifted from the northern to southern regions, developing a “southern acceleration and polarization versus northern structural lock-in” dynamic over time. This evolution has stabilized into a clear spatial pattern characterized by “higher values in southern and eastern regions versus lower values in northern and western areas”.

3.4. Convergence of Water Saving and Carbon Reduction Synergistic Effect

Due to significant disparities in regional resource endowments and production conditions, coupled with divergent development trajectories, this study quantitatively analyzes the convergence characteristics of water saving and carbon reduction synergistic effects. As illustrated in Figure 6, the σ convergence index demonstrates an 11.5% decline at the national level, decreasing from 0.462 in 2000 to 0.409 in 2021, indicating an overall reduction in interprovincial disparities. However, this convergence process exhibits a distinctive three-phase pattern: (1) rapid convergence phase, (2) fluctuating rebound phase, and (3) platform adjustment phase. The analysis reveals stronger convergence tendencies during the earlier stages, while accelerated economic development in the later periods has gradually amplified spatial heterogeneity among provinces, leading to weakened convergence effects.

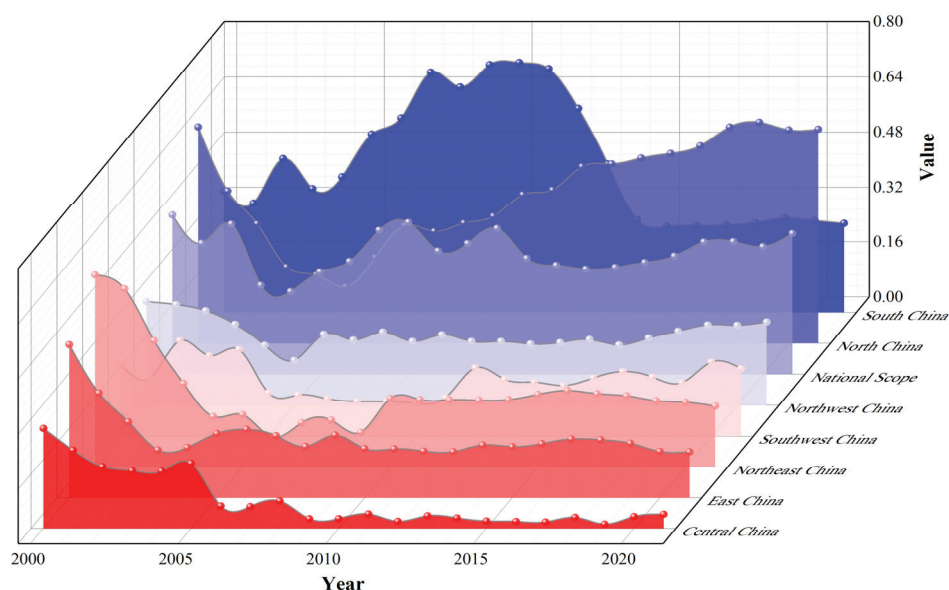


Figure 6. Temporal trends of spatial convergence indices at national and regional levels.

The convergence characteristics across regions exhibit distinct temporal patterns. In North China and South China, the convergence shows relatively large fluctuations. The σ trend in North China resembles the national pattern, demonstrating a U-shaped rebound—initially decreasing then significantly increasing, indicating pronounced late-stage divergence. Notably, North China recorded the highest σ value nationwide in 2021, with the smallest overall reduction between initial and final periods at just 1.01%. South China displays an inverted U-shaped pattern: early σ values fluctuated upward due to the coexistence of Guangdong's export-driven economic recovery and Guangxi's lower efficiency, peaking at 0.727 in 2008, which reflected substantial intra-regional disparities and significant divergence among provinces. Subsequently, the values gradually stabilized, demonstrating Guangdong's leading and radiating effects. Northwest China shows relatively gradual convergence, with the σ values changing from 0.301 in 2000 to 0.242 in 2021, a 19.6% decrease. Southwest China exhibits weak convergence trends, with the values decreasing by 5.8%. Northeast China, East China, and Central China demonstrate better convergence outcomes with notable spatial convergence. Their σ value reductions reach 68.2%, 69.8%, and 85.7%, respectively. Central China achieved the nation's lowest σ value at 0.028 in 2009 and maintained stability after 2013, reflecting development level convergence among provincial units in the region. Northeast China shows a fluctuating decline with somewhat prominent volatility, while East China's convergence σ values display a stepwise decreasing pattern.

3.5. Spatial Aggregation Characteristics of Water Saving and Carbon Reduction Synergistic Effect

The convergence analysis reveals the temporal variation of overall disparities but fails to capture local interdependencies among spatial units. The Local Moran's I index was employed to examine spatial clustering, further identifying whether high-value or low-value spatial agglomerations exist. Overall, Figure 7 clearly demonstrates significant spatial clustering characteristics of water saving and carbon reduction synergistic effects across China's provinces. When provinces with a high synergistic effect are surrounded by other high-value provinces, distinct "high-high" clusters emerge; conversely, when low-value provinces are bordered by other low-value provinces, clear "Low-Low" clusters form. As shown in Figure 7, the "high-high" clusters are predominantly distributed in the eastern and southeastern coastal regions, primarily encompassing Fujian and Jiangxi provinces, establishing positive spatial autocorrelation and serving as exemplary models. In contrast, the northwestern regions, mainly Qinghai and Xinjiang provinces, exhibit "low-low" clustering patterns. Although their synergistic effect remains relatively underdeveloped, they similarly demonstrate positive spatial autocorrelation. Notably, the analysis reveals no "high-low" or "low-high" clusters, indicating the absence of significant spatial outliers.

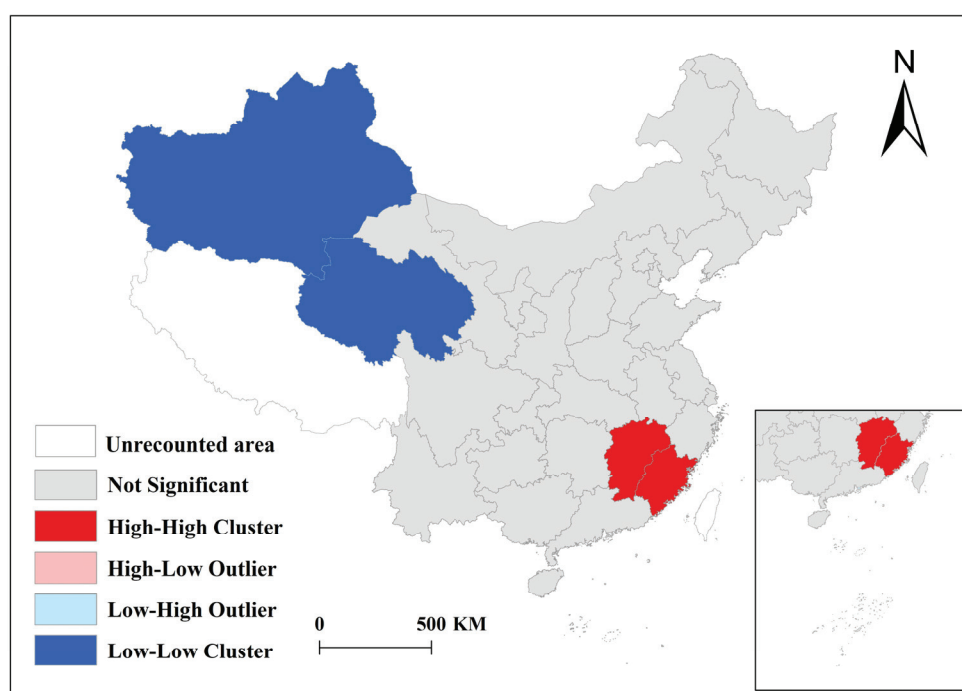


Figure 7. Local Moran's I map of synergy effect.

Among these regions, Fujian and Xinjiang exhibit relatively strong spatial autocorrelation, with Local Moran's I values of 0.648 and 0.490, respectively, indicating high similarity in attribute values with their neighboring areas. Jiangxi and Qinghai demonstrate weaker but still statistically significant local spatial clustering, with Local Moran's I values of 0.170 and 0.192. The Z-Scores for Fujian (2.096), Jiangxi (1.956), Qinghai (1.603), and Xinjiang (1.696) all exceed the threshold of 1.6, effectively ruling out the possibility of random spatial clustering. Furthermore, the p -values for these provinces range between 0.015 and 0.046 (all below 0.05), providing additional confirmation of statistically significant spatial aggregation patterns.

4. Discussion

4.1. Why Is “1 + 1 > 2”? Are There Significant Differences Among Different Regions?

According to the calculation results presented above, the characteristic of “1 + 1 > 2” is reflected at both the national and regional levels. At the national level, the collaborative performance is 87.1% higher than the individual performance. Among all the regions, the South China region has the highest growth rate of collaborative performance compared to individual performance, reaching 106.3%, which is far above the national average level. The main reason is that considering the dual goals of water saving and carbon reduction in a coordinated manner can integrate resources, achieve optimal allocation, and maximize the utilization efficiency. It can also promote technological complementarity and innovation, improve policy implementation efficiency, realize economies of scale, and share risks, thereby achieving more efficient water saving and carbon reducing effects.

Although the collaborative performance values of all the regions are generally higher than the individual performance values, there are differences in the collaborative performance values and growth rates among different regions. Among them, the North China, South China, and East China regions have higher collaborative performance values. The North China region shows the most significant trend of first decreasing and then increasing. The South China region, with its vibrant market economy, has frequent fluctuations in its collaborative performance value. Meanwhile, technological progress and innovation provide support for the improvement of performance values, resulting in a steady increase in its collaborative performance value since 2016. The East China region, with its developed economy and a high degree of opening up, can attract more external resources and cooperation opportunities. Its performance growth started earlier and is relatively faster. The sharing of resources and complementary advantages within the region promotes the synchronous improvement of collaborative performance, making the collaborative performance values of the Central China and Southwest China regions relatively synchronized. The collaborative performance values of the Northeast and Northwest regions are relatively low. The Northeast region, which underwent industrial structure adjustment in the early stage, experienced a significant decline in its collaborative performance value. The Northwest region, with its weak economic foundation and relatively slow technological progress, and a relatively stable policy environment, shows stable and slow growth in its collaborative performance.

4.2. Why Does the Synergistic Effect Exhibit a Spatially Clustered Distribution of “High in the Southeast and Low in the Northwest” Across Different Regions?

The σ -convergence analysis in this study reveals the temporal variation characteristics of spatial disparities among China’s regions. The seven major regions of China can be classified into three categories: significant convergence regions, slow convergence regions, and divergent regions. Specifically, Northeast China, East China, and Central China exhibit notable spatial convergence, with provincial development levels gradually aligning, categorizing them as significant convergence regions. Northwest China shows a relatively slow convergence trend, while Southwest China demonstrates weak convergence, reflecting a lag in balanced development and thus classifying them as slow convergence regions. In contrast, South China recorded the highest nationwide divergence value during the mid-term period, indicating significant disparities among its provinces, whereas North China experienced a marked increase in divergence in later stages, reflecting widening intra-regional differences—both regions are thus identified as divergent regions.

Recognizing that a single convergence indicator may obscure spatial heterogeneity, this study incorporates the Local Moran’s I Index for spatial clustering analysis to identify the significance of regional spatial aggregation patterns. Fujian and Jiangxi exhibit high-high

clustering characteristics, indicating a high degree of similarity with neighboring provinces in the observed variables. In contrast, Qinghai and Xinjiang display low–low clustering features, reflecting their low-level consistency with adjacent regions. Notably, no “high–low” or “low–high” outlier clusters were detected, suggesting that spatial correlations between provinces and their surrounding areas are primarily characterized by coordinated variation rather than significant disparities.

Since the convergence analysis and agglomeration analysis reflect the different concepts of “whether the differences are narrowing” and “whether there is spatial dependence”, respectively, by considering the results of both analyses, it is found that although the Northeast and Central China regions show convergence in space, they have not formed local high-/low-value clusters, which to some extent reflects the characteristics of homogeneous development. However, the Northwest region shows agglomeration without convergence due to the existence of growth polarization.

The agglomeration characteristics of the synergistic effect among provinces and cities nationwide show significant spatial differences in the clustering of high and low values. This spatial distribution pattern is shaped by the combined influence of various factors, including natural conditions and resource endowments, economic development and industrial layout, population density and urbanization levels, and geographical location and external cooperation. In other words, it is driven by the triple forces of “nature, economy, and policy.” The high-value agglomeration (H-H) in the southeast is the result of the combined effects of favorable natural conditions, high economic levels, and strong policy and technological support. In contrast, the low-value agglomeration (L-L) in the northwest is constrained by resource shortages, extensive industrial practices, and lagging technology.

Water saving and carbon reduction synergy effect, as a key pathway to achieving the dual-carbon goals, is not only subject to the rigid constraints of water resource distribution but also relies on the transformation momentum provided by regional economic development levels. It is essential to explore the consistency between the synergy effect and the spatial distribution of water resources and economic benefits:

(1) Partial Consistency and Significant Exceptions with Water Resource Distribution

High Synergy–High Water Resources Areas: Southern provinces such as the Yangtze River Delta (Jiangsu, Zhejiang) and the Pearl River Delta (Guangdong) have abundant water resources (Yangtze and Pearl River basins) and high synergy effect values.

Low Synergy–Low Water Resources Areas: The arid northwestern region (Xinjiang, Qinghai, Ningxia) has scarce water resources and long-term lowest synergy effect values nationwide.

High Synergy–Low Water Resources Areas: Municipalities directly under the central government like Beijing and Shanghai have water scarcity but maintain a high synergy effect through inter-regional water transfer and policy advantages.

Low Synergy–High Water Resources Areas: Some southwestern provinces (e.g., Yunnan, Guizhou) have abundant water resources but relatively low synergy effect values, indicating that water resources are not the sole determinant of the synergy effect.

(2) High Consistency with Economic Benefit Distribution

High Synergy–High Economic Effect Areas: Eastern coastal economic powerhouses (Guangdong, Jiangsu, and Zhejiang) lead in both synergy effect and economic level. Economic agglomeration effects promote the cross-regional flow of resources, technology, and talent. The high value-added industries (finance and technology) in municipalities (Beijing and Shanghai) further reinforce the mutual enhancement of the economy and synergy.

Low Synergy–Low Economic Effect Areas: Economically lagging regions in the northwest (Qinghai and Xinjiang) and southwest (Guizhou) generally have low synergy effect

values. Their weak economic foundations result in insufficient demand and capacity for collaboration.

4.3. Policy Implications

- (1) Formulating regionally differentiated policies based on heterogeneous synergistic effects

For regions with high synergistic effects (e.g., Beijing, Shanghai, and Guangdong), policies should further leverage their leading role in driving innovation resource spillover to neighboring areas, thereby enhancing regional collaborative development. In contrast, regions with low synergistic effects (e.g., Ningxia, Xinjiang, and Qinghai) require strengthened infrastructure development, optimized industrial layouts, and targeted policy support to attract talent and capital, ultimately improving their regional coordination capacity.

- (2) Targeting clustered regions as strategic breakthroughs, this study proposes differentiated approaches to enhance synergistic effect.

For high–high clusters (e.g., Fujian and Jiangxi), policy priorities should strengthen regional connectivity and amplify spillover effects through technology diffusion, talent mobility, and data-sharing platforms, thereby transforming spontaneous coordination into strategic pivots, while guarding against “siphon effects” that may excessively drain neighboring resources; for low–low clusters (e.g., Qinghai and Xinjiang), key measures include ecological value conversion, precision industrial upgrading, and cross-regional compensation mechanisms (e.g., “Western Water–Eastern Carbon” bilateral compensation) to break path dependence.

- (3) Focusing on key influencing factors to strengthen the convergence trend of synergistic effect

The convergence of water–carbon synergy is affected by technological maturity and compatibility, economic scale and industrial structure, natural and social conditions, and inter-regional cooperation. To enhance this convergence, multidimensional interventions are required across technology, policy, economics, and social dimensions. Technologically, priority should be given to developing integrated systems like photovoltaic drip irrigation and wastewater energy recovery, combined with digital platforms for dynamic resource allocation optimization. Policy-wise, it is crucial to design water–carbon bundled indicators and link water rights with carbon trading markets. Concurrently, water–carbon coupling models should be established to evaluate policy effectiveness while actively incorporating international best practices. Through data transparency, policy flexibility, and equity safeguards, the water–carbon synergy can evolve from fluctuation to stable convergence, achieving dual environmental and economic benefits.

4.4. Research Prospects

This study has preliminarily explored the comparative relationship between individual and collaborative water saving and carbon reduction performance at the national and provincial levels, the characteristics of changes in synergistic effect, and their spatial distribution. It aims to provide a scientific basis for formulating more effective water saving and carbon reduction policies. The future research directions and prospects are as follows:

- (1) Focus on intra-regional differences and explore effective models of collaborative water saving and carbon reduction efforts in different types of cities. There are significant differences in economic development levels, industrial structures, resource endowments, and environmental carrying capacities across regions, all of which can affect the performance of water saving and carbon reduction initiatives. Therefore, future research could analyze the collaborative effects of water saving and carbon

reduction efforts based on different types of cities (such as industrial cities, tourist cities, and agricultural cities) and summarize effective models of collaborative water saving and carbon reducing efforts for different types of cities.

- (2) Conduct a systematic analysis of the specific driving factors behind the changes in the synergistic effect of water saving and carbon reduction efforts. The changes in synergistic effects are influenced by a variety of factors, including policy orientation, technological progress, public awareness, and market mechanisms. Future research can identify the key driving factors affecting the changes in synergistic effects through both quantitative and qualitative analyses, and explore how these factors interact with each other to jointly influence the synergistic effect of water saving and carbon reduction efforts.
- (3) Compare domestic and international management cases. By comparing successful cases of water saving and carbon reduction efforts both domestically and internationally, summarize the experiences and lessons learned in collaborative management from different countries and regions. Conduct comparative analyses in terms of policy design, implementation process, and effectiveness evaluation, and distill experiences and practices that can be referenced in China, providing new ideas and insights for China's collaborative management of water saving and carbon reduction efforts.

5. Conclusions

Based on water saving and carbon reduction performance data at the national and regional levels from 2000 to 2021, this study systematically analyzed the temporal evolution patterns, spatial distribution characteristics, and convergence trends of the synergy effect, and explored its driving mechanisms and policy implications. The main conclusions are as follows:

- (1) The collaborative performance is significantly better than the individual performance, showing the characteristic of “ $1 + 1 > 2$ ”.

At the national level, both the collaborative and individual performances in water saving and carbon reducing efforts show an upward trend. The average collaborative performance (0.212) is significantly higher than the individual performance (0.114). Moreover, the increase in collaborative performance is more pronounced in most regions, which reflects the high efficiency of collaborative promotion in integrating resources and achieving dual goals.

- (2) The temporal evolution of the synergistic effect in most provinces and cities shows a trend of fluctuating upward.

Nationally, although the synergistic effect value initially fluctuated significantly, it has been on a continuous upward trend since 2002, with the growth rate stabilizing after 2018. In different regions, from 2000 to 2021, the synergistic effect was significantly present and exhibited a similar evolution trend of first decreasing and then increasing as the national synergistic effect of water saving and carbon reduction efforts.

- (3) At the national level, the spatial convergence of the synergistic effect shows a “three-stage” change trend, and the convergence changes in different regions have different characteristics.

From 2001 to 2007, there were significant spatial distribution changes in the synergistic effect values, with high values shifting from the west to the east and from the north to the south. Between 2013 and 2020, the distribution of synergistic effect values tended to stabilize. Analyzing the spatial convergence of the synergistic effect at the national level, the provinces initially showed strong convergence, but later, with the rapid economic development, the spatial differences among different provinces gradually increased, and

the convergence gradually weakened. Considering the regions separately, East China and Central China achieved the best convergence results (with a reduction of over 68%), while North China and South China showed significant differentiation, and Northwest China had slow convergence.

- (4) The spatial agglomeration distribution of the synergistic effect shows the characteristic of being “high in the southeast and low in the northwest.”

The southeastern coastal areas (such as Fujian and Jiangxi), with their developed economies, advanced technologies, and strong policy coordination, form a “high–high” agglomeration with significant demonstration effects. The northwestern regions (such as Qinghai and Xinjiang), constrained by resource shortages and extensive industrial practices, show a “low–low” agglomeration.

Supplementary Materials: The following supporting information can be downloaded at: <https://www.mdpi.com/article/10.3390/w17131847/s1>, This article has Additional Materials and they are presented in the Supplementary. Supplementary File: Water consumption.xlsx, Labor force.xlsx, GDP.xlsx, Energy consumption (water usage).xlsx, Energy consumption (10,000 tons of standard coal).xlsx.

Author Contributions: Conceptualization, J.Z.; methodology, H.L.; software, Z.L.; validation, Y.J. and W.M.; formal analysis, H.L.; investigation, J.Z.; resources, Z.L.; data curation, Y.J.; writing—original draft preparation, J.Z.; writing—review and editing, H.L.; visualization, H.L.; supervision, W.M.; project administration, J.Z. All authors have read and agreed to the published version of the manuscript.

Funding: This study was supported by the National Key Research and Development Program [2023YFC3206802].

Data Availability Statement: Data are contained within the article and Supplementary Materials.

Acknowledgments: We are grateful to the reviewers and the editor for their constructive suggestions, which have helped us a lot in improving the quality of the paper.

Conflicts of Interest: The authors declare no conflicts of interest.

References

1. Liu, Z.; Deng, Z.; Zhu, B.Q.; Ciais, P.; Davis, S.J.; Tan, J.G.; Andrew, R.M.; Boucher, O.; Arous, S.B.; Canadell, J.G.; et al. Global patterns of daily CO₂ emissions reductions in the first year of COVID-19. *Nat. Geosci.* **2022**, *15*, 615–620. [CrossRef]
2. Hu, Q.F.; Chen, J.; Wang, H.J.; Su, X.; Zhang, G.R.; Liu, L. Synergistic Development of Water-saving and Energy under the Dual-carbon Goals. *China Water Resour.* **2024**, *15*, 39–44.
3. Jin, Y.; Tang, X.; Feng, C.Y.; Mikael, H. Energy and water conservation synergy in China: 2007–2012. *Resour. Conserv. Recycl.* **2017**, *127*, 206–215. [CrossRef]
4. Ayres, R.U.; Walter, J. The greenhouse effect: Damages costs and abatement. *Environ. Resour. Econ.* **1991**, *1*, 237–270. [CrossRef]
5. Scovronick, N.; Budolfson, M.; Dennig, F.; Erickson, F.; Fleurbaey, M.; Peng, W.; Socolow, R.H.; Spears, D.; Wagner, F. The impact of human health co-benefits on evaluations of global climate policy. *Nat. Commun.* **2019**, *10*, 2095. [CrossRef]
6. Huang, X.Y.; Srikrishnan, V.; Lamontagne, J.; Keller, K.; Peng, W. Effects of global climate mitigation on regional air quality and health. *Nat. Sustain.* **2023**, *6*, 1054–1066. [CrossRef]
7. Wang, P.; Lin, C.K.; Wang, Y. Location-specific co-benefits of carbon emissions reduction from coal-fired power plants in China. *Nat. Commun.* **2021**, *12*, 6948. [CrossRef]
8. Wang, T.Y.; Jiang, Z.; Zhao, B.; Gu, Y.; Liou, K.N.; Kalandiyur, N.; Zhang, D.; Zhu, Y.F. Health co-benefits of achieving sustainable net-zero greenhouse gas emissions in California. *Nat. Sustain.* **2020**, *3*, 597–605. [CrossRef]
9. Tong, D.; Geng, G.N.; Zhang, Q.; Cheng, J.; Qin, X.Y.; Hong, C.P.; He, K.B.; Davis, S.J. Health co-benefits of climate change mitigation depend on strategic power plant retirements and pollution controls. *Nat. Clim. Change* **2021**, *11*, 1077–1083. [CrossRef]
10. Wang, Y.H.; Wen, Z.G.; Lv, X.J.; Tao, Y.A.; Zhu, J.M. The spatial heterogeneity of synergy and trade-off linkages between carbon and air pollutant mitigations in China’s steel industry. *J. Clean. Prod.* **2023**, *418*, 138166. [CrossRef]

11. Tan, Q.; Wen, Z.G.; Chen, J.J. Goal and technology path of CO₂ mitigation in China's cement industry: From the perspective of co-benefit. *J. Clean. Prod.* **2016**, *114*, 299–313. [CrossRef]
12. Shi, X.H.; Huang, Z.N.; Dai, Y.T.; Du, W.Y.; Cheng, J.P. Evaluating emission reduction potential and co-benefits of CO₂ and air pollutants from mobile sources: A case study in Shanghai, China. *Resour. Conserv. Recycl.* **2024**, *202*, 107347. [CrossRef]
13. Zhong, L.; Liu, X.S.; Ao, J.F. Spatiotemporal dynamics evaluation of pixel-level gross domestic product, electric power consumption, and carbon emissions in countries along the belt and road. *Energy* **2022**, *239*, 121841. [CrossRef]
14. Yu, S.; Zhang, S.; Zhang, Z.J.; Huo, Y.Z.; Liu, T.K. Evaluation of the synergistic control effect of atmospheric pollutants and greenhouse gases during the 14th Five Year Plan period in Beijing. *J. Environ. Sci.* **2022**, *42*, 499–508. [CrossRef]
15. Tang, X.B.; Zhang, Y.; Cao, L.Z.; Zhang, J.M.; Chen, X.H. The spatiotemporal characteristics and impact mechanism analysis of the synergistic effect of pollution reduction and carbon reduction in China. *Environ. Sci. Res.* **2022**, *35*, 2252–2263. [CrossRef]
16. Zhang, C.; Shi, D.; Li, P.F. Potential benefits of implementing inter provincial carbon emissions trading in China. *Financ. Trade Econ.* **2017**, *38*, 93–108.
17. Steinbuks, J.; Narayanan, B.G. Fossil Fuel Producing Economies Have Greater Potential for Industrial Interfuel Substitution. *Energy Econ.* **2015**, *47*, 168–177. [CrossRef]
18. Wakeel, M.; Chen, B.; Hayat, T.; Alsaedi, A.; Ahmad, B. Energy consumption for water use cycles in different countries: A review. *Appl. Energy* **2016**, *178*, 868–885. [CrossRef]
19. Sowby, R.B.; Capener, A. Reducing carbon emissions through water conservation: An analysis of 10 major U.S. cities. *Energy Nexus* **2022**, *7*, 100094. [CrossRef]
20. Valek, A.M.; Sušnik, J.; Grafakos, S. Quantification of the urban water-energy nexus in México City, México, with an assessment of water-system related carbon emissions. *Sci. Total Environ.* **2017**, *590*, 258–268. [CrossRef]
21. Gu, Y.F.; Dong, Y.N.; Wang, H.T.; Arturo, K.; Xu, J.; Thomas, C.; Li, F.T. Quantification of the water, energy and carbon footprints of wastewater treatment plants in China considering a water–energy nexus perspective. *Ecol. Indic.* **2016**, *60*, 402–409. [CrossRef]
22. Zhao, R.Q.; Yu, J.; Xiao, L.G.; Sun, J.; Luo, H.L.; Yang, W.J.; Chuai, X.W.; Jiao, S.X. Research on Carbon Emissions of Urban Water Systems Based on the Correlation of “Water-Energy-Carbon”. *J. Geogr. Sci.* **2021**, *76*, 3119–3134.
23. Zhu, Y.X. Research on Energy Consumption Evaluation Method for the Whole Process of Social Water Cycle. Master's Thesis, China Institute of Water Resources and Hydropower Research, Beijing, China, 2017.
24. Lee, M.; Keller, A.A.; Chiang, P.C.; Den, W.; Wang, H.T.; Hou, C.H.; Wu, J.; Wang, X.; Yan, J.Y. Water-energy nexus for urban water systems: A comparative review on energy intensity and environmental impacts in relation to global water risks. *Appl. Energy* **2017**, *205*, 589–601. [CrossRef]
25. Shrestha, E.; Ahmad, S.; Johnson, W.; Shrestha, P.; Batista, J.R. Carbon footprint of water conveyance versus desalination as alternatives to expand water supply. *Desalination* **2011**, *280*, 33–43. [CrossRef]
26. Yang, W.Q.; Zhao, R.Q.; Zhang, Z.P.; Xiao, L.G.; Cao, L.H.; Wang, S.; Yang, Q.L. Research on Carbon Water Footprint Efficiency of Different Industries in Henan Province. *J. Nat. Resour.* **2019**, *34*, 92–103.
27. Yan, M.Y. Research on China's Industrial Structure Optimization Based on “Dual Peaks of Water and Carbon”. Master's Thesis, China University of Petroleum, Beijing, China, 2020. [CrossRef]
28. Ni, H.Z.; Zhao, J.; Peng, X.J.; Chen, G. Estimating the economic impact of large hydropower projects: A dynamic multi-regional computable general equilibrium analysis. *Water Policy* **2022**, *24*, 1343–1365. [CrossRef]
29. Li, X.; Feng, K.S.; Siu, Y.L.; Hubacek, K. Energy-water nexus of wind power in China: The balancing act between CO₂ emissions and water consumption. *Energy Policy* **2012**, *45*, 440–448. [CrossRef]
30. Zhang, C.; Anadon, L.D.; Mo, H.; Zhao, Z.N.; Liu, Z. Water-carbon trade-off in China's coal power industry. *Environ. Sci. Technol.* **2014**, *48*, 11082–11089. [CrossRef]
31. Feng, K.S.; Hubacek, K.; Siu, Y.L.; Li, X. The energy and water nexus in Chinese electricity production: A hybrid life cycle analysis. *Renew. Sustain. Energy Rev.* **2014**, *39*, 342–355. [CrossRef]
32. Ye, C.X.; Zhong, R.D.; Chen, X.H.; Jin, H.Y. Simulation of the strategic evolution process and interactions between stakeholders in water trading and carbon trading. *J. Hydrol.* **2023**, *616*, 128787. [CrossRef]
33. Tan, Q.L.; Liu, Y.; Zhang, X.P. Stochastic optimization framework of the energy-water-emissions nexus for regional power system planning considering multiple uncertainty. *J. Clean. Prod.* **2020**, *281*, 124470. [CrossRef]
34. Zhao, J.; Duan, J.J.; Han, Y.P.; Gao, F. Correlation between carbon emissions and water consumption in different industries in China: Spatial and temporal distribution characteristics and driving factors. *J. Clean. Prod.* **2023**, *427*, 139196. [CrossRef]
35. Zhang, Q.; Wang, X.Z.; Xu, L.S.; Shen, J.L. Coupling Relationship and Analysis of Steel Process Resources Energy Carbon Emissions. *Steel* **2020**, *55*, 103–114. [CrossRef]
36. Yang, R.P.; Wang, T.; Yang, L.; Li, L.P.; Wang, M. Research on Collaborative Promotion of Water Conservation and Carbon Reduction in the Industrial Sector of the Yangtze River Delta Region. *Environ. Sci. Res.* **2024**, *12*, 2622–2631.36. [CrossRef]
37. Li, L.B.; Hu, J.L. Ecological total-factor energy efficiency of regions in China. *Energy Policy* **2012**, *46*, 216–224. [CrossRef]

38. Lin, B.Q.; Liu, H.X. Is foreign trade conducive to improving energy and environmental efficiency? Taking China's industrial sector as an example. *J. Econ. Res.* **2015**, *50*, 127–141.
39. Chung, Y.H.; Fare, R.; Grosskopf, S. Productivity and Undesirable Outputs: A Directional Distance Function Approach. *J. Environ. Manag.* **1997**, *51*, 229–240. [CrossRef]
40. Fukuyama, H.; Weber, W.L. A directional slacks-based measure of technical inefficiency. *Socio-Econ. Plan. Sci.* **2008**, *43*, 274–287. [CrossRef]
41. Zhang, N.; Choi, Y. Total-factor carbon emission performance of fossil fuel power plants in China: A metafrontier non-radial Malmquist index analysis. *Energy Econ.* **2013**, *40*, 549–559. [CrossRef]
42. Zhou, P.; Ang, B.W.; Wang, H. Energy and CO₂ Emission Performance in Electricity Generation: A Non-radial Directional Distance Function Approach. *Eur. J. Oper. Res.* **2012**, *221*, 625–635. [CrossRef]
43. Tian, Y.; Lin, Z.J. Coupling and Coordination of Agricultural Carbon Emission Efficiency and Economic Growth in Chinese Provinces. *China Popul. Resour. Environ.* **2022**, *32*, 13–22.
44. Zhang, J.; Zhang, Y. Re estimation of China's capital stock K. *Econ. Res. J.* **2003**, *7*, 35–43+90.

Disclaimer/Publisher's Note: The statements, opinions and data contained in all publications are solely those of the individual author(s) and contributor(s) and not of MDPI and/or the editor(s). MDPI and/or the editor(s) disclaim responsibility for any injury to people or property resulting from any ideas, methods, instructions or products referred to in the content.

Article

Changes in Streamflow Pattern and Complexity in the Whole Yangtze River Basin

Pingyu Lv ^{1,2,3}, Sidong Zeng ^{2,*}, Xin Liu ² and Linhan Yang ²¹ College of Mechanical and Vehicle Engineering, Chongqing University, Chongqing 400044, China² Chongqing Institute of Green and Intelligent Technology, Chinese Academy of Sciences, Chongqing 400714, China; yanglinhan@cigit.ac.cn (L.Y.)³ Water-Environment Monitoring Center for the Upper Reach of Changjiang, Changjiang Water Resource Commission, Chongqing 400020, China

* Correspondence: zengsidong@cigit.ac.cn

Abstract: The assessment of streamflow patterns and their complexity variations across multiple timescales within river basins is a crucial aspect of water resource management and policy formulation. In this study, the Hurst coefficient, Mann–Kendall nonparametric test method, streamflow pattern indices, and sample entropy (SampEn) analyses were used to investigate the streamflow pattern in the whole Yangtze River basin at annual, monthly, and daily scales. The results show that with the increase in the time resolution, the streamflow shows more complex changing characteristics and streamflow changes more obviously on the monthly timescale than on the annual one. The annual mean streamflow decreases only in some of the tributaries, while the monthly streamflow shows significant increasing trends in the dry season and significant decreasing trends in the late wet season in almost the whole basin. Results also show that the minimum extreme streamflow indices increase in almost the whole basin. The maximum indices show decreasing trends in most of the tributaries and the Yichang gauge in the main reach. The streamflow complexity in the tributaries is higher and the complexity increases from upstream to downstream along the main reach in the basin. Along the main reach, the average SampEn increases downstream of the reach with values of 0.05, 0.07, 0.10, 0.12, 0.14, and 0.14 at Shigu, Pingshan, Cuntan, Yichang, Hankou, and Datong, respectively. These findings are helpful for understanding the hydrological characteristics and water resource management in the Yangtze River basin.

Keywords: streamflow indices; different timescales; complexity analysis; Yangtze River basin

1. Introduction

Streamflow is a major path linking land and ocean for water, energy, and nutrients, which plays an important role in the natural water cycle and ecosystem health [1–3]. Streamflow changes could affect water resource availability and the biogeochemical processes in river systems [4]. The maintenance of environmental streamflow for natural water bodies is essential for sustainable ecosystem services [5]. Meanwhile, rivers are also important habitats for human survival and development. Hydrological regime changes could have significant effects on water supply, irrigation, flood control and electric power production [6,7]. Investigating streamflow index changes is especially important for understanding hydrological mechanisms and water resource management.

Many studies have shown that streamflow around the world has been affected both by climate change and human activities in the past and will be affected by them in the future, which has received much attention [8–10]. For example, Zhang et al. found that streamflow decreases mainly in northern China and the upper reaches of the Yangtze and the Pearl River basins and significant decreasing streamflow was found in the Yellow River, the Liaohe River, and the Haihe River basins in China [11]. The characteristics of streamflow, including changing trends, abrupt points, complexity, etc., are often diversified

over different time scales [12–14], and are also different between upstream and downstream areas in a certain basin, especially for the large basins [15,16]. As far as we know, policy makers are continuously seeking to know more about the characteristics of streamflow index changes under changing environments for different management purposes. For example, water supply management departments focus on the spatiotemporal variations in water resources on monthly or annual scales, while emergency management departments urgently need to obtain the runoff changes and the regional flood composition over a short duration for flood control. Hence, it is necessary to find the potential hydrological characteristics and their spatiotemporal variations over different scales in a river basin.

The Yangtze River basin (YRB), the world's third largest river basin, spans 19 provinces and includes the eastern, central, and western economic zones of China. Fluctuations in the streamflow of the Yangtze River have a profound impact on both the local socio-economic landscape and the ecological environment. For example, the severe drought that hit the middle and lower reaches of Yangtze in 2011 caused water levels to drop to historic lows, severely affecting agricultural irrigation, urban water supply, and navigation safety [17]. Understanding streamflow patterns at multiple timescales is essential for monitoring water resources and making adaptive management strategies to mitigate impacts on agriculture, socioeconomics, and nature. Previous studies showed that the streamflow along the main reach of the Yangtze River has experienced significant changes in recent decades due to environmental factors and human activities, indicating that the discharge series are non-stationary [18,19]. Jiang et al. [20] showed that streamflow increased in the headwater of the YRB, while it had little influence downstream. Gao et al. [21] indicated that flow regime changes vary in different seasons in the upper reaches of the Yangtze River; annual streamflow decreased in the period from 1961 to 2008, while autumn streamflow evidently decreased after the 1980s. Zhang et al. [22] showed a significant increase in streamflow in the middle of the Yangtze River by analyzing the streamflow indices at three stations, namely Yichang, Hankou, and Datong. Previous studies have also analyzed hydrological characteristics and their changes caused by the operation of the Three Gorges Dam in the lower reaches of the Yangtze River, showing that the water level and discharge significantly increase during most months from January to March and significantly decrease from August to November, and the date of the start of the dry season has been advanced in the lower reach [23,24]. Recently, some studies have also investigated the spatial distribution and dynamic changes in streamflow complexity in the middle and lower reaches of the Yangtze River using six gauges along the main reach showing an obvious spatial difference and an increasing trend [24]. However, according to our literature research, previous studies are mainly focused on the streamflow changes in certain subregions or the mainstream of the Yangtze River and analyses over multiple temporal scales are also scarce. The Yangtze River, China's longest river, exhibits pronounced differences in terrain and climatic conditions across its upper, middle, and lower reaches. With an enormous annual flow volume of approximately $9600 \times 10^8 \text{ m}^3$, it contributes a significant 36% to China's total river flow [25], underscoring its pivotal role in water resource management, agriculture, and flood control. Analyzing streamflow at daily, monthly, and annual scales provides a comprehensive view of temporal variations, encompassing extremes, intra-annual distribution patterns, and total water resource availability, respectively. This multi-scale investigation deepens our understanding of hydrological dynamics, facilitates adaptation to climate change, and informs precise, adaptive, and science-based strategies for water management. So, the comprehensive analysis of streamflow changes in the whole Yangtze River basin at different spatiotemporal scales is still required.

In order to better understand the characteristics of streamflow index changes in the YRB, a trend analysis, an abrupt analysis, and a complexity analysis are conducted for streamflow at different timescales from upstream to downstream in the YRB using the most recent dataset during 1960–2018. The main objectives of this study are as follows: (1) to investigate the annual and monthly water yield changes, (2) to quantify extreme changes

in streamflow over the past year, and (3) to analyze the streamflow complexity across the whole Yangtze River basin.

2. Study Area and Data

2.1. Description of the Study Area

The Yangtze River basin (YRB), depicted in Figure 1, spans latitudes 25° N to 35° N and longitudes 91° E to 122° E, encompassing a vast drainage area of 1.80 million square kilometers, representing 18.8% of China's total landmass. As China's longest river at approximately 6300 km, the YRB stretches from the Qinghai–Tibet Plateau to the East China Sea, traversing a remarkable elevation drop of 6600 m. The basin's geography is diverse, with the upper reaches extending from its source to Yichang, covering 4504 km and a drainage area of 1 million km², dominated by mountainous terrain. Conversely, the middle reaches, stretching from Yichang to Hukou, span 955 km and feature primarily fluvial plains, with a drainage area of 0.68 million km². The lower reaches, extending from Hukou to the river's estuary, encompass 938 km and a drainage area of 0.12 million km². Climate-wise, the majority of the YRB experiences a subtropical monsoon climate, contributing to its status as a region of abundant precipitation. Specifically, the average annual precipitation is approximately 1126.7 mm [26], though there are notable variations. The source area receives roughly 400 mm of the annual precipitation, while most other regions within the basin experience between 800 and 1600 mm. This uneven spatial distribution of precipitation, decreasing from southeast to northwest, is attributed to the interplay of local circulation patterns and topography. The YRB's complex terrain and climate and significant river flows require the study of river flows at daily, monthly, and annual scales. This research deepens the understanding of hydrological dynamics, supports adaptation to climate change, and guides precise, adaptive, science-based water management strategies.

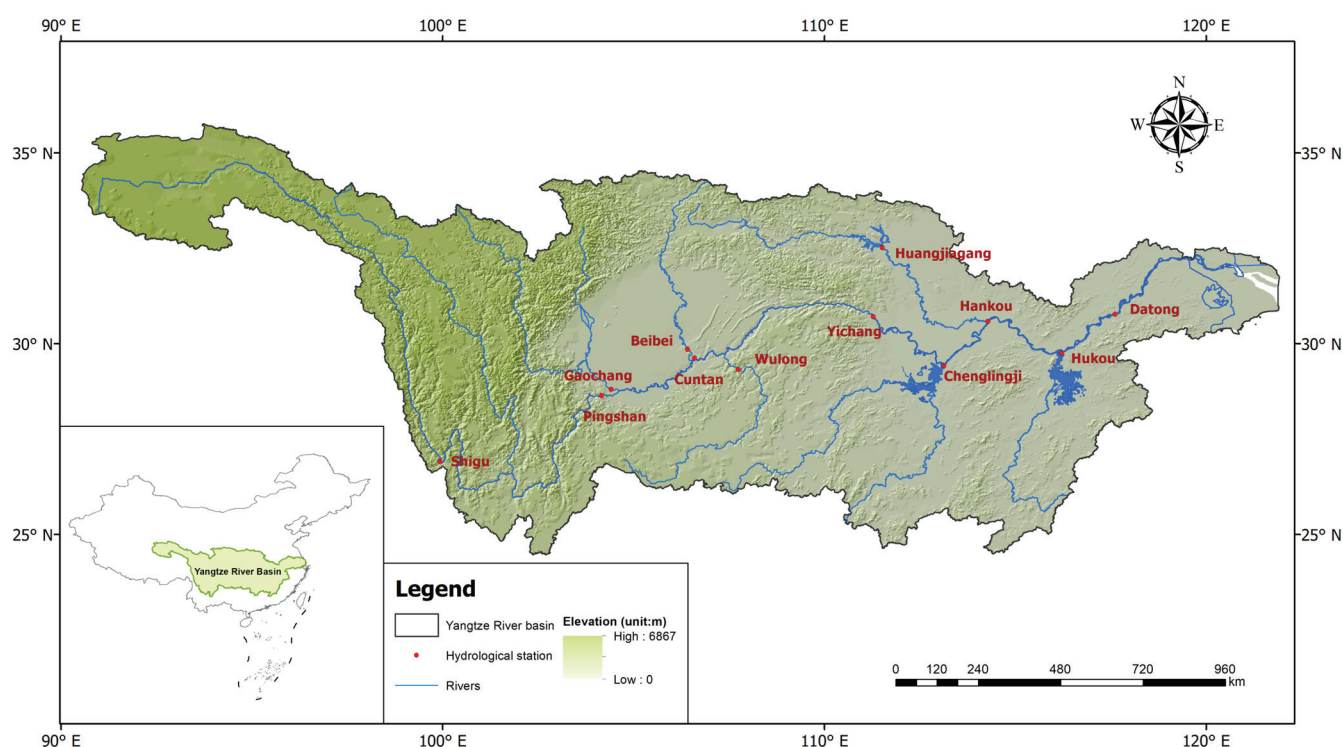


Figure 1. The Yangtze River basin and the location of the hydrological stations.

2.2. Streamflow Data

Daily streamflow data from 1960 to 2018 from 12 hydrological stations—Gaochang, Beibei, Wulong, Chenglingji, Hukou, Huangjiagang, Shigu, Pingshan, Cuntan, Yichang, Hankou, and Datong (Figure 1)—covering the YRB were used in this study, and were ob-

tained from the Hydrological Bureau of the Ministry of Water Resources and the Changjiang Water Resources Commission, China. The 12 gauges represent the streamflow characteristics of the mainstream and tributaries in the whole river basin. The details of each gauge, including the station name, river basin, and the catchment area, are shown in Table 1.

Table 1. The hydrological stations used in this study.

Station ID	Name	River Basin	Catchment Area (10 ⁴ km ²)	Time Series
1	Gaochang	Minjiang River basin	13.54	1960~2018
2	Beibei	Jialingjiang River basin	15.61	1960~2018
3	Wulong	Wujiang River basin	8.3	1960~2018
4	Chenglingji	Dongting Lake basin	26.28	1960~2018
5	Hukou	Poyang Lake basin	16.22	1960~2018
6	Huangjiagang	Hanjiang River basin	9.52	1960~2018
7	Shigu	Upper Jinshajiang River basin	21.42	1960~2018
8	Pingshan	Jinshajiang River basin	48.51	1960~2018
9	Cuntan	Yangtze mainstream	86.66	1960~2018
10	Yichang	Yangtze mainstream	100.55	1960~2018
11	Hankou	Yangtze mainstream	148.80	1960~2018
12	Datong	Yangtze mainstream	170.54	1960~2018

3. Methods

3.1. Alteration Change Method

In this study, the Hurst coefficient method was firstly used to judge whether a series alteration existed and the degree of the alteration. If there was an alteration, the Mann–Kendall test, moving T-test method, and the Mann–Kendall–Sneyers test were used to perform a detailed analysis on trends and abrupt points in the sequence.

The Hurst coefficient method [27,28] can be used to determine if there is an alteration and the alteration degree. According to the value of H , we can observe three cases. When H equals 0.5, it means that this is a random series. When H is greater or less than 0.5, it indicates a future trend that is the same or opposite to the present trend, showing whether there is a positive continuous effect or reverse continuous effect. Moreover, the more H deviates from 0.5 indicates a larger alteration degree. In this study, the rescaled range analysis (R/S analysis) method, which is commonly used, was selected to calculate the Hurst coefficient H by following the steps below.

Considering a time series $\{X(t)\}$, $t = 1, 2, \dots$, for any positive integer $t \geq 1$, the mean series is defined as

$$\bar{X}_t = \frac{1}{\tau} \sum_{i=1}^{\tau} X(t), \tau = 1, 2, \dots, n \quad (1)$$

The cumulative deviation $\varsigma(t)$ is given as

$$\varsigma(t, \tau) = \sum_{u=1}^t [X(u) - \bar{X}_\tau], 1 \leq t \leq \tau \quad (2)$$

The range R is calculated via

$$R(\tau) = \max_{1 \leq t \leq \tau} \varsigma(t, \tau) - \min_{1 \leq t \leq \tau} \varsigma(t, \tau), \tau = 1, 2, \dots, n \quad (3)$$

The standard deviation S is

$$S(\tau) = \left\{ \frac{1}{\tau} \sum_{t=1}^{\tau} [X(t) - \bar{X}_\tau]^2 \right\}^{\frac{1}{2}}, \tau = 1, 2, \dots, n \quad (4)$$

For a given sequence,

$$R(\tau)/S(\tau) = (c\tau)^H, \ln[R(\tau)/S(\tau)] = H(\ln c + \ln \tau) \quad (5)$$

According to the observation results, the least squares method was used to calculate the parameter c and the Hurst coefficient H . The relationship between the fractional Brownian motion correlation function and the Hurst coefficient H is shown as follows.

$$C(t) = -\frac{E[B_H(-t)B_H(t)]}{E[B_H(t)]^2} = 2^{2H-1} - 1 \quad (6)$$

The correlation function value $C(t)$ is tested by using the statistical test method. Under the given significance level α , where $C(t)$ is less than the critical value r_α , the long-term correlation is not evident. Where $C(t)$ is larger than the critical value r_α , the sequence alteration is evident. The alteration and its degree are determined as shown in Table 2, based on the Hurst coefficient of the hydrological sequence and its grade interval of alteration.

Table 2. Classification of alteration degree.

Correlation Function C(t)	Hurst Coefficient H	Alteration Degree
$0 \leq C(t) < r_\alpha$	$0.5 \leq H < h_\alpha$	No alteration
$r_\alpha \leq C(t) < r_\beta$	$h_\alpha \leq H < h_\beta$	Weak alteration
$r_\beta \leq C(t) < 0.6$	$h_\beta \leq H < 0.839$	Medium alteration
$0.6 \leq C(t) < 0.8$	$0.839 \leq H < 0.924$	Strong alteration
$0.8 \leq C(t) \leq 1.0$	$0.924 \leq H \leq 1.0$	Huge alteration

Due to the advantages without particular underlying distributions [29], the Mann–Kendall (M–K) nonparametric test method [30,31] has been widely used to detect hydrological changing trends. In our study, the autocorrelation of the selected streamflow sequences was eliminated via the pre-whitening method [32], as a higher autocorrelation may lead to a larger error in the M–K trend analysis [33]. A positive M–K statistics Z indicates an increasing trend, while a negative Z indicates a decreasing trend. More details of the M–K trend test can be found in Mann [30] and Kendall’s [31] work.

The abrupt changes in streamflow sequences were detected using the moving t -test method and the Mann–Kendall–Sneyers test [34] in this study. Within the t -test, the original series was divided into two subsequences; if there is an obvious difference detected between the mean value of the two subsequences exceeding a certain significant level, it indicates that the time sequence has a point of alteration.

The non-parametric Mann–Kendall–Sneyers test is widely employed to identify abrupt changes in climatic factors and streamflow time series [35,36]. Given a time series of data represented by x_1, \dots, x_n , the methodology involved calculating t_k , the cumulative sum of m_i , where m_i is the cumulative count of instances where a later value in the series is greater than its preceding value.

$$t_k = \sum_{i=1}^k m_i \quad (2 \leq k \leq n) \quad (7)$$

Under the assumption of random independence among the data points in the time series, the mean and variance of the statistic can be derived as specified in the relevant equations.

$$\overline{t_k} = E(t_k) = k(k-1)/4 \quad (8)$$

$$Var(t_k) = \frac{k(k-1)(2k+5)}{72} \quad (9)$$

To obtain the statistic U_{BK} , the streamflow data time series was rearranged in reverse order, and the calculations analogous to those in Equations (7)–(9) were repeated, with the initial condition $UB1$ set to 0. At a predetermined significance level, if the U_{FK} and U_{BK}

curves intersected within the confidence interval, the point of intersection was designated as the theoretical abrupt change point.

$$U_{FK} = \frac{(t_k - \bar{t}_k)}{\sqrt{\text{Var}(t_k)}} \quad (10)$$

3.2. Streamflow Pattern Indices

Using the daily streamflow data spanning from 1960 to 2018, collected by 12 hydrological gauges distributed across the YRB, we calculated annual and monthly runoff series for each site to capture water yield variations across different time scales. Given the YRB's propensity for flooding, as evidenced by the extreme floods recorded in 1954, 1998, 2010, and 2020, extreme floods remain a primary concern in our study. To comprehensively analyze these extreme flood events, we have selected several indicators that capture both the magnitude and duration of peak flows and low flows. Specifically, for extremely high streamflow, we have chosen the annual maximum daily streamflow (MAX1), annual maximum 3-day streamflow (MAX3), annual maximum 7-day streamflow (MAX7), and annual maximum 15-day streamflow (MAX15). These indicators have been chosen for two primary reasons: Firstly, they effectively reflect the changing characteristics of flood peaks and flood volumes, providing crucial insights into the severity and duration of extreme flooding events. Secondly, they align with the data series commonly used in China for designing flood control measures and managing flood risks, thereby ensuring that our findings can inform practical strategies for flood prevention and mitigation. Additionally, given the significance of dry season streamflow for maintaining riverine ecosystems, we have also included indicators of extremely low flow: the annual minimum daily streamflow (MIN1), annual minimum 3-day streamflow (MIN3), annual minimum 7-day streamflow (MIN7), and annual minimum 15-day streamflow (MIN15).

3.3. Streamflow Complexity Indices

Streamflow complexity is defined as the variability and uncertainty of streamflow and could reflect the dynamic structure of streamflow. In this study, the sample entropy (SampEn) analysis, initially proposed by Richman and Moorman [37], was utilized to quantify the complexity of streamflow. SampEn, which is a modification of the approximate entropy, has been employed to measure the complexity of time series data, where larger entropy values indicate a higher degree of complexity. The method is advantageous in that it is less dependent on the length of the data and demonstrates relative consistency across a broader range of parameter values [37,38]. SampEn has been used to characterize the complexity of hydrological time series in several recent studies [39–41].

For a certain time series $\{x(1), x(2), \dots, x(N)\}$, SampEn is calculated as follows:
Create an m -dimension vector:

$$X_m(i) = \{x(i), x(i+1), \dots, x(i+m-1)\}, i = 1, 2, \dots, N-m+1 \quad (11)$$

Define the distance between $X_m(i)$ and $X_m(j)$:

$$d[X_m(i), X_m(j)] = \max\{|x(i+k) - x(j+k)|\}, k = 0, 1, \dots, m-1 \quad (12)$$

Given a tolerance criterion r , count the $d[X_m(i), X_m(j)]$ that are smaller than r . The function $C_i^m(r)$ and the average similarity $C^m(r)$ are defined as

$$C_i^m(r) = \{\text{the number of } d[X_m(i), X_m(j)] < r\} / (N-m) \quad (13)$$

$$C^m(r) = \sum C_i^m(r) / (N-m+1) \quad (14)$$

where $i = 1, 2, \dots, N-m+1$.

Change the dimension to $m + 1$ and repeat the above steps to calculate $C^{m+1}(r)$. The $SampEn(m, r, N)$ of a time series can be defined as follows:

$$SampEn(m, r, N) = -\ln[C^{m+1}(r)/C^m(r)] \quad (15)$$

SampEn, an index of complexity in time series analysis, employs the variables m (embedding dimension) and r (tolerance) [39] to quantify the conditional probability that two sequences, similar within r for at least m consecutive points, will remain similar at their $(m + 1)$ th point. The choice of m determines the minimum sequence length for a similarity assessment, impacting sensitivity to pattern complexity. Meanwhile, r sets the maximum allowed difference for sequence similarity, balancing between capturing fine details and ensuring sufficient matches. SampEn excludes self-matches and considers only the first $N - m$ vectors, facilitating the evaluation of short-term pattern predictability in time series dynamics.

4. Results

4.1. Changes in Inter-Annual and Intra-Annual Streamflow

Figure 2 shows the annual mean streamflow changes at the 12 gauges in the Yangtze River basin. The results indicate that the annual mean flow shows decreasing trends at most of the gauges including Gaochang, Beibei, Wulong, Pingshan, Cuntan, and Yichang in the upper stream and Chenglingji, Huangjiagang, and Hankou in the lower basin. The streamflow shows increasing trends only in Shigu in the upper stream and Hukou and Datong in the middle and lower reaches (Table 3).

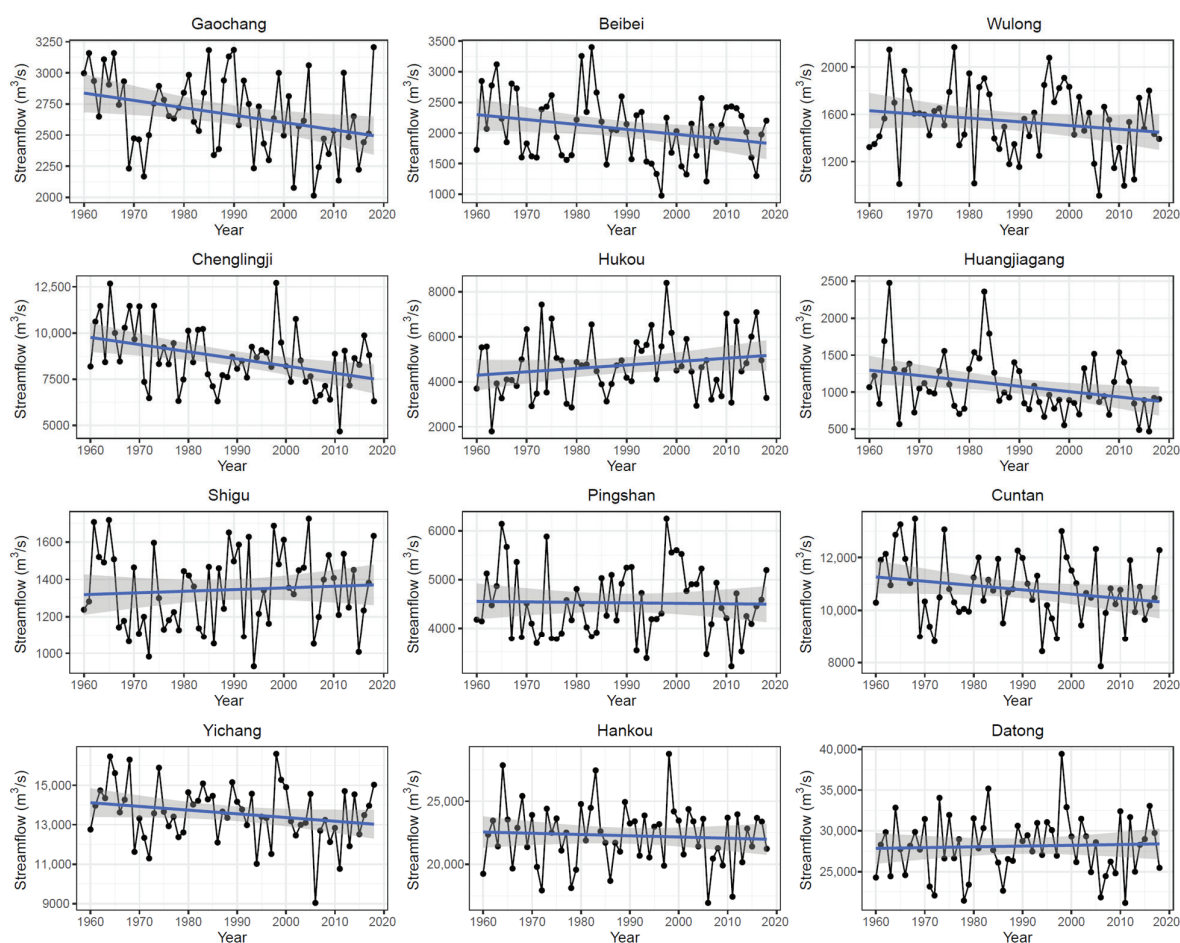


Figure 2. The changes of annual mean flow at the 12 gauges in the Yangtze River basin. (The black lines and dots are the annual average streamflow, and the blue lines are the linear trends).

Table 3. Changing characteristics of annual mean streamflow.

Station ID	Name	Changing Trend (10 ⁸ m ³ /y)	Z _c	Significance Level ¹	Hurst	Alteration Degree ²	Abrupt Point
1	Gaochang	−1.86	−2.18	**	0.75	++	1969
2	Beibei	−2.54	−1.66	*	0.71	+	1994
3	Wulong	−0.99	−1.20	-	0.68	+	2005
4	Chenglingji	−12.19	−2.71	***	0.73	++	1971
5	Hukou	4.75	1.31	-	0.64	-	-
6	Huangjiagang	−2.28	−1.70	*	0.73	++	1991
7	Shigu	0.28	0.58	-	0.70	+	1967
8	Pingshan	−0.31	0.16	-	0.66	-	-
9	Cuntan	−5.11	−1.43	-	0.68	+	1969
10	Yichang	−5.93	−1.62	-	0.65	-	-
11	Hankou	−3.10	−0.51	-	0.60	-	-
12	Datong	3.00	0.29	-	0.63	-	-

Notes: ¹ in this study, the significance level α is set to be 0.01, 0.05, and 0.1 and the corresponding values of $Z_{1-\alpha/2}$ are 2.32, 1.96, and 1.64. ***, **, and * indicate significance levels of 0.01, 0.05, and 0.1, respectively; - means significance exceeds 0.1. ² ++ and + indicate medium alteration and weak alteration, respectively. - means no alteration according to the Hurst coefficient method.

Table 3 shows the results of the trend analysis based on the Mann–Kendall test. The results show that the changes in trends are significant at Gaochang ($\alpha = 0.05$) in the Minjiang River, Beibei ($\alpha = 0.1$) in the Jialingjiang River in the upper stream and Chenglingji ($\alpha = 0.01$) in Dongting Lake and Huangjiagang ($\alpha = 0.1$) in the Hanjiang River in the middle reach. However, there are no obvious changes in trends at Wulong in the Wujiang River, Hukou in Poyang Lake and the gauges along the main reach.

The abrupt point analysis is also shown in Table 3. From the results, we can see there are changes in Gaochang (abrupt point at 1969), Beibei (abrupt point at 1994), Wulong (abrupt point at 2005), Shigu (abrupt point at 1967), and Cuntan (abrupt point at 1969) in the upper stream and Chenglingji (abrupt point at 1971) and Huangjiagang (abrupt point at 1991) in the middle reach. The other gauges, including Hukou in Poyang Lake and Pingshan, Yichang, Hankou, and Datong along the main reach, indicate no obvious alterations according to the Hurst coefficient method.

Figure 3 and Table 4 show the trends and abrupt point detection results of the monthly streamflow in the 12 gauges based on the Mann–Kendall test. In the upper reach, the Gaochang gauge in the Minjiang River shows significant increasing trends from January to April and significant decreasing trends from July to November. Table 4 shows that the changes are also moderate to significant from January to March, in June and July, and from September to December. The abrupt point analysis shows similar points in the dry season, while the changes are different in the flood season. The Beibei gauge representing the runoff changes in the Jialingjiang River shows increasing trends from January to March and decreasing trends in September and October (Figure 3). The abrupt point analysis shows that there was no change from June to August, while the changes are small to moderate in other months. The abrupt point analysis also shows similar points after 2000 in the dry season, while the changes occurred around 1970 and 1980 in the flood season. The Wulong gauge at the outlet of the Wujiang River shows significant increasing trends from January to March and decreasing trends in May, October, and November. The results of change detection show that there are no changes in April and November. The abrupt points are in 2001 from January to March and around 1980 (May and August), 1990 (September and October) and after 2004 (June, July, and December).

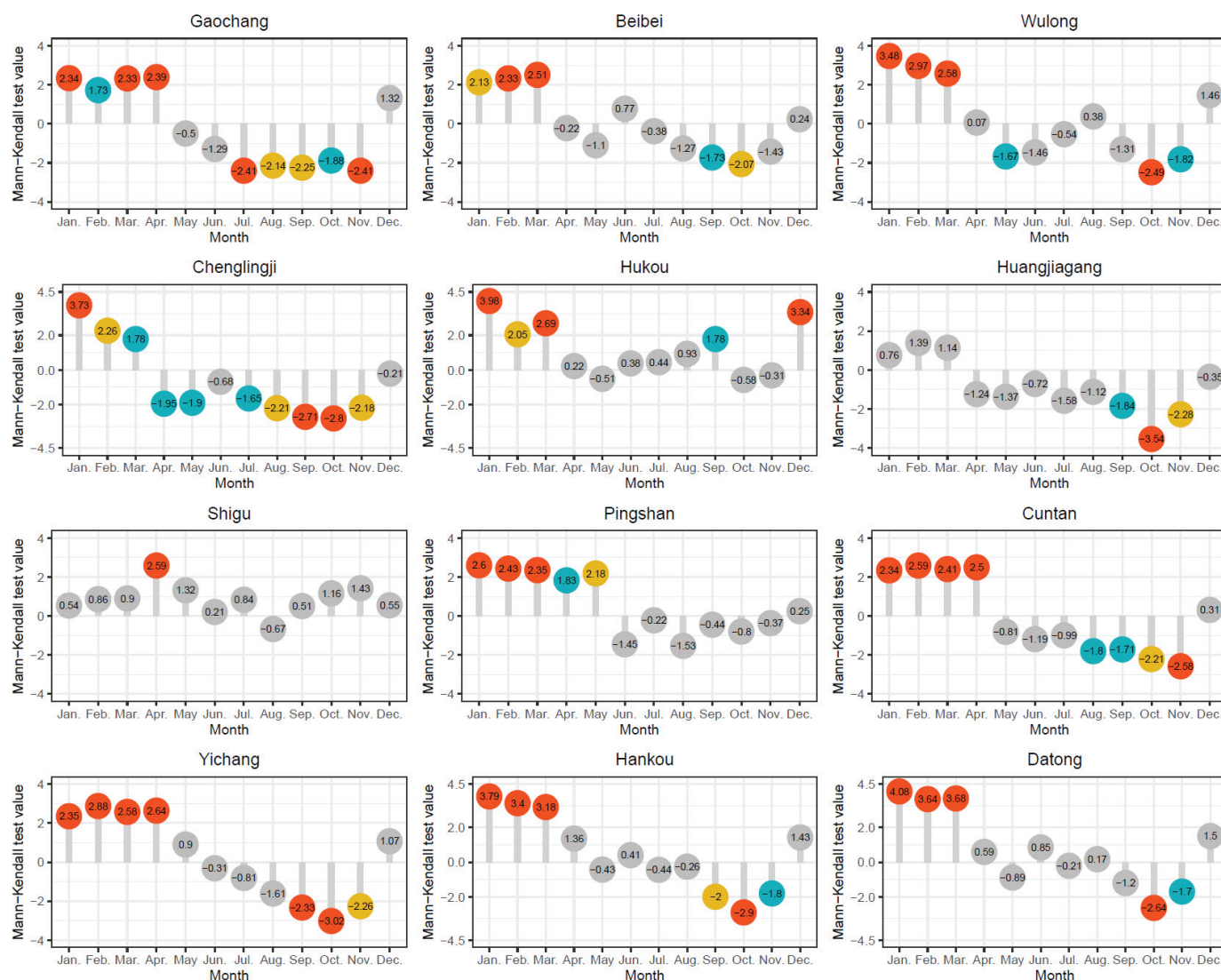


Figure 3. The monthly streamflow changing trends of the gauges in the Yangtze River basin (the red, yellow and green dots indicate that the changing trends exceed the significance levels α of 0.01, 0.05, and 0.1, respectively, while the gray means no obvious trends).

In the middle stream of the YRB, the data at the Chenglingji gauge in Dongting Lake indicate increasing trends from January to March and decreasing trends in April, May, and June until November. The results show that changes occur in most months except April, June, and August. The abrupt points in January, February, and March occur in 1990, 1982, and 1980, and the abrupt points in the remaining months are all in the 1970s. The Hukou gauge in Poyang Lake shows increasing trends in January to March, September, and October, while in the other months, there are no obvious trends. The abrupt point in 1973 in March and April and in the 1980s and 1990s during the other months exhibit changes. The data from the Huangjiagang gauge representing the streamflow of the Hanjiang river indicate significant decreasing trends in autumn exceeding the significance level of 0.1, while in the other months, there are no obvious trends. The changes are obvious throughout the year except for September, with an abrupt point in the 1970s in winter and spring and in the 1980s, 1990s and 2010s, in summer and autumn.

Table 4. Abrupt detection of monthly mean streamflow in the Yangtze River basin.

Station ID	Name	Abrupt Detection	January	February	March	April	May	June	July	August	September	October	November	December
1	Gaochang	Alteration degree	+++	+++	++	-	-	+	++	-	++	++	++	++
2	Beibei	Abrupt point	2011	2011	2011	-	-	2006	1986	-	2005	1995	1970	2011
		Alteration degree	++	++	++	++	+	-	-	-	++	++	+	++
3	Wulong	Abrupt point	2004	2004	2004	1970	1969	-	-	-	1986	1976	1970	2011
		Alteration degree	++	++	++	-	++	+	+	+	++	+	-	+
4	Chenglingji	Abrupt point	2001	2001	2001	-	1978	2005	2004	1979	1990	1990	-	2011
		Alteration degree	++	++	+	-	++	-	+	-	++	++	++	+
5	Hukou	Abrupt point	1990	1982	1980	-	1979	-	1971	-	1970	1976	1971	1971
		Alteration degree	+	-	+	+	-	-	+	++	++	+	-	++
6	Huangjiagang	Abrupt point	1983	-	1973	1973	-	-	1989	1992	1991	1980	-	1993
		Alteration degree	++	++	+	+	++	+	+	+	-	++	++	++
7	Shigu	Abrupt point	1972	1971	1974	1970	1971	1995	1995	2014	-	1987	1986	1971
		Alteration degree	++	++	++	+	++	-	-	-	++	+	++	+
8	Pingshan	Abrupt point	1980	1981	1981	1978	1967	-	-	-	1967	1985	1987	1980
		Alteration degree	+++	+++	+++	++	-	-	-	-	-	-	-	-
9	Cuntan	Abrupt point	2013	2013	2013	2013	-	-	-	-	-	-	-	-
		Alteration degree	+++	+++	+++	-	-	-	-	-	++	++	-	++
10	Yichang	Abrupt point	2013	2013	2013	-	-	-	-	-	1991	1994	-	2014
		Alteration degree	+++	+++	+++	+	++	-	++	-	++	+++	-	++
11	Hankou	Abrupt point	2010	2010	2011	2013	2012	-	2001	-	2002	2002	-	2014
		Alteration degree	+++	+++	++	-	++	-	+	-	-	++	-	+
12	Datong	Abrupt point	1995	1989	1989	-	1978	-	2001	-	-	1996	-	2013
		Alteration degree	++	++	++	-	+	-	+	-	++	++	+	-
		Abrupt point	1995	1989	1989	-	1978	-	2004	-	2011	1997	1991	-

Notes: +++, ++, and + indicate strong, medium, and weak alterations, respectively. - means no alteration according to the Hurst coefficient method.

In the upper stream of the main reach, there are no obvious trends in most months except for in April at the Shigu gauge. The results show that the changes are clear in spring, autumn, and winter, and the abrupt points occur around the 1980s and 1970s. At the Pingshan gauge, the results show that streamflow increases significantly from January to May, while the trends are not obvious from June to December. The changes are significant from January to March and moderate in April, while in the other months, there are no alterations. The abrupt points in the four months are the same in 2013. At the Cuntan gauge, the streamflow increases significantly from January to April and decreases significantly from August to November. From the results of the abrupt point detection, the alterations occur mostly in the dry season, and the abrupt point is around 2013 from December to March and in early 1990 in autumn. At the Yichang gauge, the streamflow shows increasing trends from January to April and significant decreasing trends from September to November. The changes are clear in most months, and the abrupt points are after 2010 in spring and winter and around 2002 in autumn. The results show that streamflow increases significantly from January to March in the middle and lower reaches of the mainstream at the Hankou and Datong gauges. The streamflow decreases significantly from September to November at Hankou, while at the Datong gauge, the streamflow decreases only in October and November. The changes in the streamflow at the Hankou and Datong gauges are similar from January to August with the same abrupt point, while the changes are clear in October and December at the Hankou gauge and in September, October, and November at the Datong gauge.

4.2. Changes in Extreme Streamflow Indices

The minimum and maximum streamflow at 1 day, 3 days, 7 days, and 15 days were selected, and then, the changing characteristics were analyzed in the range of 1960–2018, as shown in Figure 4 and Table 5. In the upper stream of the Yangtze River basin, the maximum streamflow indices at the Gaochang gauge show significant decreasing trends, while the minimum streamflow indices show no significant increasing trends. The abrupt point detection shows the minimum and maximum streamflow indices exhibit medium to strong changes, and the abrupt points are around 2010 and 2000, respectively. At the Beibei gauge, only the minimum 1-day and 3-day flows show significant decreasing trends. From the results of the abrupt point detection, the changes are clear for all the streamflow indices. The abrupt point is in 1991 for the 1-day and 3-day minimum streamflow and in 2008 for the 7-day and 15-day minimum flows. The abrupt point for the 1-day, 3-day, 7-day, and 15-day maximum streamflow is in 1990. For the Wulong station, the minimum streamflow indices all show significant increasing trends, while the maximum streamflow indices all show decreasing trends. The changes are clear for the maximum streamflow, and the abrupt point is in 2004, while the minimum streamflow shows no change.

In the middle stream of the Yangtze River basin, significant increasing and decreasing trends were detected for the minimum and maximum streamflow indices, respectively. The abrupt point detection shows that the extreme flow indices all change, and the abrupt points are in 2007 for the 1-day minimum flow, 2012 for the 3-day to 15-day minimum flows, and 2000 for the maximum flow indices. At the Hukou gauge, the minimum streamflow indices increase significantly, while the maximum flow indices show no obvious decreasing trends. The results also show that the minimum streamflow indices exhibit an abrupt change in 1992, while the change is only obvious for the 7-day maximum streamflow in 2000. For the Huangjiagang gauge, the annual minimum 1-day streamflow increases, and the maximum streamflow indices all show significantly decreasing trends. The abrupt point detection results show that the minimum streamflow indices clearly change around early 1970, and the maximum streamflow indices change in 1985.

In the mainstream of the Yangtze river, the Shigu and Pingshan gauges in the upper reach show no change in trends for extreme flows except for the 15-day minimum flow at Pingshan, while the changes are clear for the minimum streamflow indices, with the abrupt point in 1988 and 2014 for the two gauges. At the Cuntan gauge, the minimum

streamflow for 1 day, 3 days, 7 days, and 15 days increases significantly, and changes are also significant, with the abrupt point in 2000. However, the maximum streamflow indices show no obvious changes at the Cuntan gauge. In the middle and lower reaches of the mainstream, the results show that the minimum streamflow indices are all increasing at the Yichang, Hankou, and Datong gauges, and the changes are all very significant, with abrupt points in 2009, 2000, and 2000, respectively. For the maximum streamflow, the indices decrease significantly only at the Yichang gauge, while there are no obvious trends for the Hankou and Datong gauges. The results of the abrupt point detection show that all maximum streamflow indices at the Yichang, Hankou, and Datong gauges change, and the abrupt points are in 2006, 2006, and 2000, respectively.

To further investigate the changes in the extreme flows, the annual minimum and maximum streamflow before and after the abrupt points were analyzed, as shown in Table 6. The results show that annual minimum streamflow increases in all the gauges except for Beibei in the Jialingjiang River. The biggest increase in the annual minimum streamflow occurs at the Huangjiagang gauge at about 96.3%, followed by the Yichang gauge at about 68.2%, and the Hukou gauge at about 59.5%. In the upper reach of the Yangtze River, the annual minimum streamflow increases downstream of the main reach from 5.2% to 35.2% but decreases at Cuntan, as indicated by the reduction at the Beibei gauge. In the middle and lower reaches, the annual minimum streamflow decreases downstream of the main reach from 68.2% to 30.9%. Meanwhile, the results also show that the monthly minimum streamflow occurs one or two months after it occurs in the main reach.

The results show the annual maximum streamflow decreases after the changing point. In the upper stream, it decreases by about 28.1%, 21.1%, and 34.2% at the Gaochang, Beibei, and Wulong gauges, respectively, while in the middle stream, it decreases by about 14.7%, 13.7%, and 61.3% at Chenglingji, Hukou, and Huangjiagang, respectively. In the middle and lower main reaches of the Yangtze River, the annual maximum streamflow decreases downstream of the main reach from 23.4% to 9.0%. The monthly maximum streamflow shows no obvious changes.

Table 5. Abrupt detection of extreme streamflow in the Yangtze River basin.

Station ID	Name	Abrupt Detection	MIN1	MIN3	MIN7	MIN15	MAX1	MAX3	MAX7	MAX15
1	Gaochang	Alteration degree	++	++	+++	+++	++	++	++	++
		Abrupt point	2012	2012	2012	2011	2004	1998	1998	1996
2	Beibei	Alteration degree	+++	++	++	+	+	+	++	++
		Abrupt point	1991	1991	2008	2008	1990	1990	1990	1990
3	Wulong	Alteration degree	-	-	-	-	++	++	++	++
		Abrupt point					2004	2004	2004	2004
4	Chenglingji	Alteration degree	++	++	++	++	+	+	++	++
		Abrupt point	2007	2012	2012	2012	2000	2000	2000	2000
5	Hukou	Alteration degree	++	++	++	++	-	-	+	-
		Abrupt point	1992	1992	1992	1992			2000	
6	Huangjiagang	Alteration degree	++	++	++	++	++	++	++	++
		Abrupt point	1974	1971	1971	1971	1985	1985	1985	1985
7	Shigu	Alteration degree	+	+	++	++	-	-	-	-
		Abrupt point	1988	1988	1988	1988				
8	Pingshan	Alteration degree	+++	+++	+++	+++	-	-	-	-
		Abrupt point	2014	2014	2014	2014				
9	Cuntan	Alteration degree	+++	+++	+++	+++	-	-	-	-
		Abrupt point	2000	2000	2000	2000				
10	Yichang	Alteration degree	+++	+++	+++	+++	++	++	+	+
		Abrupt point	2009	2009	2009	2009	2006	2006	2006	2006
11	Hankou	Alteration degree	+++	+++	+++	+++	++	++	++	++
		Abrupt point	2000	2000	2000	2000	2006	2006	2006	2006
12	Datong	Alteration degree	+++	+++	+++	+++	++	++	++	++
		Abrupt point	2000	2000	2000	2000	2000	2000	2000	2000

Notes: +++, ++, and + indicate strong, medium, and weak alterations, respectively. - means no alteration according to the Hurst coefficient method.

Table 6. Changing characteristics of annual minimum and maximum streamflow.

Station ID	Name	Annual Minimum Flow					Annual Maximum Flow				
		Before Abrupt		After Abrupt		Change Percentage	Before Abrupt		After Abrupt		Change Percentage
		Streamflow	Most Frequently Occurs	Streamflow	Most Frequently Occurs		Streamflow	Most Frequently Occurs	Streamflow	Most Frequently Occurs	
1	Gaochang	574	2	744	5	29.6%	16,519	8	11,876	7	−28.1%
2	Beibei	327	2	256	2	−21.7%	24,677	7	19,458	7	−21.1%
3	Wulong	-	-	-	-	-	12,370	6	8137	6	−34.2%
4	Chenglingji	1408	1	1751	1	24.4%	28,298	7	24,126	7	−14.7%
5	Hukou	−3994	9	−1601	7	59.9%	15,995	6	13,806	6	−13.7%
6	Huangjiagang	203	2	399	12	96.3%	10,337	7	3996	7	−61.3%
7	Shigu	368	2	387	2	5.2%	-	-	-	-	-
8	Pingshan	1253	3	1694	1	35.2%	-	-	-	-	-
9	Cuntan	2653	3	3210	2	21.0%	-	-	-	-	-
10	Yichang	3436	2	5781	12	68.2%	49,161	7	37,662	7	−23.4%
11	Hankou	6525	2	9078	12	39.1%	54,767	7	48,300	7	−11.8%
12	Datong	8383	2	10,974	1	30.9%	60,518	7	55,042	7	−9.0%

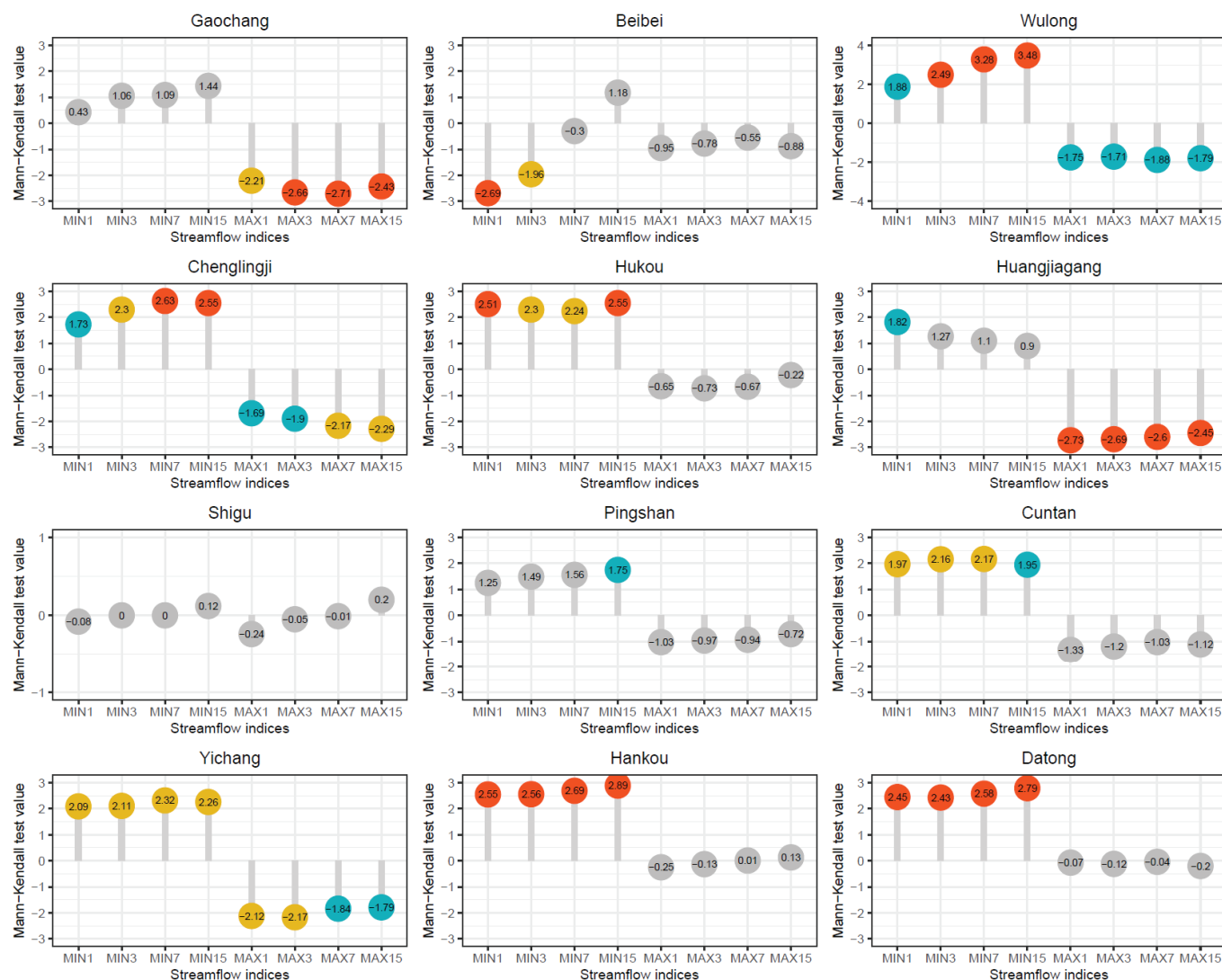


Figure 4. The extreme streamflow changing trends of the gauges in the Yangtze River basin based on the Mann-Kendall trend test method (the meaning of the red dots, yellow dots, green dots, and gray dots are same as in Figure 3).

4.3. Streamflow Complexity Change Analysis

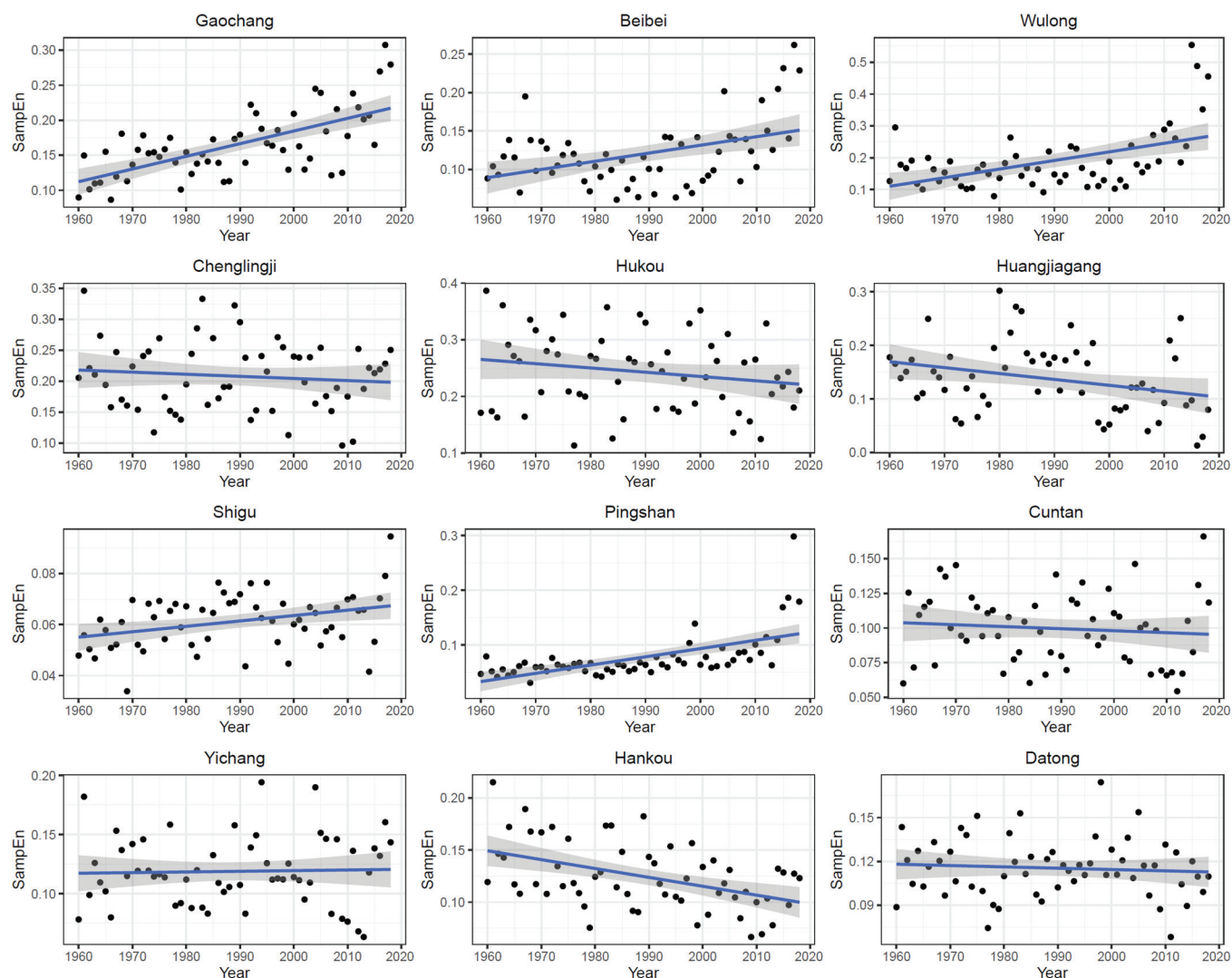
The changing characteristics of the sample entropy (SampEn) in the YRB are shown in Table 7. In the upper stream, the average SampEn is 0.17, 0.11, and 0.19 at Gaochang, Beibei, and Wulong, respectively. In the middle stream of the basin, the SampEn is higher, with values of 0.21, 0.25, and 0.17 at Chenglingji, Hukou, and Huangjiagang, respectively. Along the main reach, the average SampEn increases downstream of the reach, with values of 0.05, 0.07, 0.10, 0.12, 0.14, and 0.14 at Shigu, Pingshan, Cuntan, Yichang, Hankou, and Datong, respectively.

Figure 5 and Table 7 illustrate that the SampEn shows increasing trends at Gaochang, Beibei, and Wulong in the upper stream of the basin, and the trends are obvious at Gaochang and Wulong according to the Mann-Kendall test. However, the SampEn decreases at Chenglingji, Hukou, and Huangjiagang in the middle stream of the basin. Along the main reach of the Yangtze River, the SampEn shows obvious increasing trends at Shigu and Pingshan in the upper stream, while there are no obvious decreasing or increasing trends at the Cuntan and Yichang gauges. In the middle and lower reaches, the SampEn decreases significantly at Hankou, and the decreasing trend is not obvious at Datong.

Table 7. Changing characteristics of the streamflow complexity.

Station ID	Name	SampEn	Z _c	Significance Level ¹	Hurst	Alteration Degree ²	Abrupt Point
1	Gaochang	0.17	2.38	***	0.84	+++	2010
2	Beibei	0.11	1.36	-	0.81	++	2013
3	Wulong	0.19	1.65	*	0.83	++	2010
4	Chenglingji	0.21	−0.50	-	0.59	-	-
5	Hukou	0.25	−1.56	-	0.60	-	-
6	Huangjiagang	0.17	−1.44	-	0.81	++	1998
7	Shigu	0.05	2.18	**	0.68	+	1974
8	Pingshan	0.07	1.73	*	0.82	++	2012
9	Cuntan	0.10	−1.11	-	0.69	+	1978
10	Yichang	0.12	0.13	-	0.58	-	-
11	Hankou	0.14	−2.83	***	0.74	++	1977
12	Datong	0.14	−0.63	-	0.63	-	-

Notes: ^{1,2} the meanings are same as in Table 1. ***, **, and * indicate significance levels of 0.01, 0.05, and 0.1, respectively; - means significance exceeds 0.1. +++, ++ and + indicate strong alteration, medium alteration and weak alteration, respectively. - means no alteration according to the Hurst coefficient method.

**Figure 5.** The streamflow complexity changes during 1960–2018 at the 12 gauges in the Yangtze River basin.

The abrupt point detection results in Table 7 show that changes are moderate to significant at most of the gauges, and they are not clear in Chenglingji, Hukou, Yichang,

and Datong. In the upper stream, the changes are moderate at Beibei and Wulong and significant at Gaochang, with an abrupt point around 2010. In the middle stream of the basin, the changes are moderate at Huangjiagang, and the abrupt point is in 1998. Along the main reach of the Yangtze River, the changes are clear at Shigu (abrupt in 1974), Pingshan (abrupt in 2012), Cuntan (abrupt in 1978), and Hankou (abrupt in 1977).

5. Discussion

The spatiotemporal characteristics of the streamflow indices vary over different time scales from upstream to downstream in the Yangtze River basin from 1960 to 2018, as seen from the results above. On the annual time scale, the mean streamflow shows significant decreasing trends in only some of the tributaries of the Yangtze River such as the Minjiang River, Jialingjiang River, Dongting Lake, and Hanjiang River, and the change is also moderate only in the Minjiang River, Dongting Lake, and Hanjiang River. However, the annual mean streamflow shows no significant trends along the main reach from upstream to downstream. The annual streamflow changes are directly related to the precipitation and evapotranspiration changes. Previous studies have shown that precipitation increases mainly in the eastern Tibet Plateau and the middle and lower Yangtze River basin, like Poyang Lake and decreases in the region of the Minjiang River, Jialingjiang River, Wujiang River and Hanjiang River. For the whole basin, precipitation increased and then decreased from 1960 to 2015. Meanwhile, the evapotranspiration decreased slightly in the Yangtze River basin according to the previous research. A warming–wetting trend is detected in the southeastern and northwestern regions, while there is a warming–drying trend in the middle regions of the basin [42].

However, on the monthly time scale, the streamflow shows significant increasing trends in the dry season, especially from January to March, at most of the gauges in the whole basin, and the change detection results show similar characteristics at each gauge. In the late wet season, the streamflow shows significant decreasing trends at most of the gauges. Particularly, streamflow decreases significantly in the flood season from July to November. The streamflow is noted to have passively increased from January to March, a phenomenon that is likely attributed to the melting of snowpacks and the enhanced precipitation in upstream regions [43,44] driven by seasonal shifts in weather patterns. The passive increase in minimum streamflow may be a consequence of altered precipitation patterns, enhanced evaporation rates due to climate change, or the cumulative effect of water management strategies. Similarly, the decrease in maximum streamflow from July to September could be attributed to changes in runoff generation mechanisms, dam operations, and water diversions [45]. A possible reason for this is the large number of reservoirs in the basin used to store water in the wet season and subsequently supply water in the dry season, which reduces the streamflow in the wet season and increases it in the dry season. Another reason may be the decreasing precipitation in the wet season and increasing precipitation in the dry season. Jiang et al. [46] found significant changes in many monthly precipitation datasets collected between 1961 and 2000. Gemmer et al. [47] reported that a statistically significant negative trend can be found in September over the Yangtze River basin, especially in the middle region. Along the main reach, the streamflow decreases in the flood season from August to November at the Cuntan gauge, indicating a decreasing inflow at the Three Gorges Dam; however, the streamflow decreases only in September, October, and November in the Yichang gauge due to regulation by the Three Gorges Dam. Additionally, the reduction degree reduces at Hankou and Datong in the middle and lower reaches. The abrupt change points of the monthly streamflow are similar in the dry season, while they are more complex in the wet season, which indicates the more complex effects of climate change and human activities on the streamflow in the wet season.

Over the daily time scale, the minimum extreme streamflow indices show increasing trends in most of the tributaries, while the maximum extreme streamflow indices show decreasing trends in the Minjiang River, Wujiang River, Dongting Lake and Hanjiang

River. The results also show that the minimum streamflow occurs one or two months in advance along the main reach, while the maximum streamflow mainly occurs in June and July. As we know, the changes in extreme streamflow can be related to reservoir regulation and extreme precipitation. Guan et al. [48] showed that maximum 1-day and 5-day precipitation and maximum consecutive dry days have all increased significantly. Li et al. [49] showed that the extreme precipitation intensities and the frequency of extreme precipitation have significantly increased. Lü et al. [50] reported that 73% of the stations exhibited rising trends in annual maximum 1-day precipitation and the June–July–August seasonal maximum 1-day precipitation, with the most pronounced increases in the Yangtze River basin. From these previous studies, we can infer that the extreme streamflow changes are directly caused by reservoir regulation, which increases the ecological environmental flow in the dry season. It should be noted that the minimum 1-day and 3-day streamflow indices show decreasing trends at the Beibei gauge in the Jialingjiang River. Along the main reach of the Yangtze River, the minimum extreme streamflow indices show increasing trends from upstream to downstream, while the maximum extreme streamflow indices show significant decreasing trends only in the Yichang gauge due to the Three Gorges Dam.

The sample entropy (SampEn) values, indicating the streamflow complexity in the river basin, show an increasing trend from upstream to downstream in the main reach, and the SampEn values in the tributaries are generally higher than those in the main-stream [51]. As we know, a higher SampEn value means a more complex river system. In the upper stream of the main reach, the streamflow complexity is lower due to the lower impact of human activities, climate, and underlying surface conditions. From upstream to downstream, as the runoff of the tributaries flows into the main reach, the complexity increases due to the combined effects of human activities like reservoir regulation, human consumption, land use change, and climate change [52]. The higher SampEn values in the tributaries indicate that the streamflow is more unpredictable and complex on the regional scale in the Yangtze River basin. The results also show that the sample entropy in the Dongting and Poyang lakes is higher than that at all the other sites, which may be due to the complex water exchange between the Yangtze River and the Dongting and Poyang lakes, determined by both the flow and water level of the Yangtze main reach and the two lakes [53]. The data show that the SampEn values increase in the upper stream and decrease in the lower stream of the basin both in the main reach and tributaries. A possible reason for this is the increasing anthropic effects caused by the construction of large-scale hydraulic projects [54].

Although the spatiotemporal characteristics of the streamflow indices across the Yangtze River basin are detected in this study, a more reasonable quantitative analysis of the contributions of climate change and human activities to changes in different streamflow indices over various time scales should be conducted in our following studies. For instance, an analysis of the effects of climate change and human activities on streamflow on a monthly scale could help improve the efficiency of water resource regulation, and a quantitative analysis of factors impacting the streamflow on a daily scale could be useful for flood control. Consequently, this could lead to a better understanding of the main influencing factors and hydrological process mechanisms, providing more scientific support for water resource management in the river basin.

6. Conclusions

In this study, changes in the streamflow indices have been investigated from upstream to downstream in the whole Yangtze River basin over different time scales. The changing characteristics of the annual and monthly extreme minimum and maximum streamflow and streamflow complexity have been studied. The annual mean streamflow shows significant decreasing trends in only some of the tributaries, while it shows no significant trends along the main reach from upstream to downstream. The monthly streamflow shows significant increasing trends in the dry season, especially from January to March, and significant

decreasing trends in the late wet season at most of the gauges. The abrupt change points of the monthly streamflow are similar in the dry season, while they are more complex in the wet season in the basin. The minimum extreme streamflow indices show increasing trends almost over the whole basin, while the maximum extreme streamflow indices show decreasing trends in most of the tributaries and only at the Yichang gauge in the main reach. The streamflow changes are more complex in the tributaries than those in the main reach. In addition, the complexity increases from upstream to downstream along the main reach in the basin. These findings can help us to understand the hydrological characteristics in the Yangtze River basin.

Author Contributions: P.L.: conceptualization, writing—original draft, review and editing. S.Z.: conceptualization, writing—original draft, review and editing. X.L.: investigation, visualization. L.Y.: writing—review and editing. All authors have read and agreed to the published version of the manuscript.

Funding: This study was funded by the Youth Innovation Promotion Association, CAS (2021385).

Data Availability Statement: The data are unavailable due to privacy or ethical restrictions.

Conflicts of Interest: The authors declare that they have no known competing financial interests or personal relationships that could have appeared to influence the work reported in this paper.

References

1. Kennard, M.J.; Pusey, B.J.; Olden, J.D.; Mackay, S.J.; Stein, J.L.; Marsh, N. Classification of natural flow regimes in Australia to support environmental flow management. *Freshw. Biol.* **2010**, *55*, 171–193. [CrossRef]
2. Sun, T.; Feng, M.L. Multistage analysis of hydrologic alterations in the Yellow River, China. *River Res. Appl.* **2013**, *29*, 991–1003. [CrossRef]
3. Mishra, P.; Chiphang, N.; Bandyopadhyay, A.; Bhadra, A. Process-based eco-hydrological modeling in an Eastern Himalayan watershed using RHESSys. *Model. Earth Syst. Environ.* **2021**, *7*, 2553–2574. [CrossRef]
4. Ju, X.; Wang, Y.; Wang, D.; Wu, J.; Tao, Y.; Qiu, R. Impacts of climate change on hydrological regimes in the Jinsha River Basin, China. *Authorea* **2020**. [CrossRef]
5. Zhao, C.; Yang, S.; Liu, J.; Liu, C.; Hao, F.; Wang, Z.; Zhang, H.; Song, J.; Mitrovic, S.M.; Lim, R.P. Linking fish tolerance to water quality criteria for the assessment of environmental flows: A practical method for streamflow regulation and pollution control. *Water Res.* **2018**, *141*, 96–108. [CrossRef] [PubMed]
6. Lee, J.; Jung, C.; Kim, S.; Kim, S. Assessment of Climate Change Impact on Future Groundwater-Level Behavior Using SWAT Groundwater-Consumption Function in Geum River Basin of South Korea. *Water* **2019**, *11*, 949. [CrossRef]
7. Corobov, R.; Ene, A.; Trombitsky, I.; Zubcov, E. The Prut River under Climate Change and Hydropower Impact. *Sustainability* **2021**, *13*, 66. [CrossRef]
8. Heerspink, B.P.; Kendall, A.D.; Coe, M.T.; Hyndman, D.W. Trends in streamflow, evapotranspiration, and groundwater storage across the Amazon Basin linked to changing precipitation and land cover. *J. Hydrol. Reg. Stud.* **2020**, *32*, 100755. [CrossRef]
9. Liu, S.; Shi, H.; Niu, J.; Chen, J.; Kuang, X. Assessing future socioeconomic drought events under a changing climate over the Pearl River basin in South China. *J. Hydrol. Reg. Stud.* **2020**, *30*, 100700. [CrossRef]
10. Wang, H.; Sun, F.; Liu, W. Characteristics of streamflow in the main stream of Changjiang River and the impact of the Three Gorges Dam. *Catena* **2020**, *189*, 104498. [CrossRef]
11. Zhang, Q.; Singh, V.P.; Sun, P.; Chen, X.; Zhang, Z.; Li, J. Precipitation and streamflow changes in China: Changing patterns, causes and implications. *J. Hydrol.* **2011**, *410*, 204–216. [CrossRef]
12. Wang, W.; Vrijling, J.K.; van Gelder, P.H.; Ma, J. Testing for nonlinearity of streamflow processes at different timescales. *J. Hydrol.* **2006**, *322*, 247–268. [CrossRef]
13. Ma, Z.; Kang, S.; Zhang, L.; Tong, L.; Su, X. Analysis of impacts of climate variability and human activity on streamflow for a river basin in arid region of northwest China. *J. Hydrol.* **2008**, *352*, 239–249. [CrossRef]
14. Yao, L.; Libera, D.A.; Kheimi, M.; Sankarasubramanian, A.; Wang, D. The Roles of Climate Forcing and Its Variability on Streamflow at Daily, Monthly, Annual, and Long-Term Scales. *Water Resour. Res.* **2020**, *56*, e2020WR027111. [CrossRef]
15. Teutschbein, C.; Grabs, T.; Karlsen, R.H.; Laudon, H.; Bishop, K. Hydrological response to changing climate conditions: Spatial streamflow variability in the boreal region. *Water Resour. Res.* **2015**, *51*, 9425–9446. [CrossRef]
16. Diop, L.; Yaseen, Z.M.; Bodian, A.; Djaman, K.; Brown, L. Trend analysis of streamflow with different time scales: A case study of the upper Senegal River. *ISH J. Hydraul. Eng.* **2018**, *24*, 105–114. [CrossRef]
17. Sun, Z.; Zhu, X.; Pan, Y.; Zhang, J.; Liu, X. Drought evaluation using the GRACE terrestrial water storage deficit over the Yangtze River Basin, China. *Sci. Total Environ.* **2018**, *634*, 727–738. [CrossRef]
18. Zhang, Q.; Xu, C.-Y.; Zhang, Z.; Chen, Y.D.; Liu, C.-L.; Lin, H. Spatial and temporal variability of precipitation maxima during 1960–2005 in the Yangtze River basin and possible association with large-scale circulation. *J. Hydrol.* **2008**, *353*, 215–227. [CrossRef]

19. Wei, W.; Chang, Y.; Dai, Z. Streamflow changes of the Changjiang (Yangtze) River in the recent 60 years: Impacts of the East Asian summer monsoon, ENSO, and human activities. *Quat. Int.* **2014**, *336*, 98–107. [CrossRef]
20. Jiang, C.; Zhang, L.; Tang, Z. Multi-temporal scale changes of streamflow and sediment discharge in the headwaters of Yellow River and Yangtze River on the Tibetan Plateau, China. *Ecol. Eng.* **2017**, *102*, 240–254. [CrossRef]
21. Gao, B.; Yang, D.; Zhao, T.; Yang, H. Changes in the eco-flow metrics of the Upper Yangtze River from 1961 to 2008. *J. Hydrol.* **2012**, *448–449*, 30–38. [CrossRef]
22. Zhang, Q.; Liu, C.; Xu, C.-Y.; Xu, Y.; Jiang, T. Observed trends of annual maximum water level and streamflow during past 130 years in the Yangtze River basin, China. *J. Hydrol.* **2006**, *324*, 255–265. [CrossRef]
23. Tian, J.; Chang, J.; Zhang, Z.; Wang, Y.; Wu, Y.; Jiang, T. Influence of Three Gorges Dam on Downstream Low Flow. *Water* **2019**, *11*, 65. [CrossRef]
24. Wang, Y.; Tao, Y.; Sheng, D.; Zhou, Y.; Wang, D.; Shi, X.; Wu, J.; Ma, X. Quantifying the change in streamflow complexity in the Yangtze River. *Environ. Res.* **2020**, *180*, 108833. [CrossRef] [PubMed]
25. Zhang, D.; Hong, H.; Zhang, Q.; Li, X. Attribution of the changes in annual streamflow in the Yangtze River Basin over the past 146 years. *Theor Appl Clim.* **2015**, *119*, 323–332. [CrossRef]
26. Xiao, Z.; Shi, P.; Jiang, P.; Hu, J.; Qu, S.; Chen, X.; Chen, Y.; Dai, Y.; Wang, J. The Spatiotemporal Variations of Runoff in the Yangtze River Basin under Climate Change. *Adv. Meteorol.* **2018**, *2018*, 5903451. [CrossRef]
27. Xie, P.; Chen, G.C.; Lei, H.F. Hydrological alteration analysis method based on Hurst coefficient. *J. Basic Sci. Eng.* **2009**, *17*, 32–39. (In Chinese)
28. Du, H.; Xia, J.; Zeng, S.; She, D.; Liu, J. Variations and statistical probability characteristic analysis of extreme precipitation events under climate change in Haihe River Basin, China. *Hydrol. Process.* **2014**, *28*, 913–925. [CrossRef]
29. Ahmad, I.; Zhang, F.; Tayyab, M.; Anjum, M.N.; Zaman, M.; Liu, J.; Farid, H.U.; Saddique, Q. Spatiotemporal analysis of precipitation variability in annual, seasonal and extreme values over upper Indus River basin. *Atmos. Res.* **2018**, *213*, 346–360. [CrossRef]
30. Mann, H.B. Nonparametric tests against trend. *Econometrica* **1945**, *13*, 245–259. [CrossRef]
31. Kendall, M.G. *Rank Correlation Methods*; Griffin: London, UK, 1975.
32. Burn, D.H.; Hag Elnur, M.A. Detection of hydrologic trends and variability. *J. Hydrol.* **2002**, *255*, 107–122. [CrossRef]
33. Yue, S.; Wang, C.Y. Applicability of prewhitening to eliminate the influence of serial correlation on the Mann-Kendall test. *Water Resour. Res.* **2002**, *38*, 4-1–4-7. [CrossRef]
34. Sneyers, R. *Sur l'analyse Statistique des Series D'observations*; OMM Note Technique; Organization Météorologique Mondiale: Geneve, Switzerland, 1975.
35. Demaree, G.R.; Nicolis, C. Onset of sahelian drought viewed as a fluctuation-induced transition. *Q. J. R. Met. Soc.* **1990**, *116*, 221–238.
36. Moraes, J.M.; Pellegrino, G.Q.; Ballester, M.V.; Martinelli, L.A.; Victoria, R.L.; Krusche, A.V. Trends in hydrological parameters of a southern Brazilian watershed and its relation to human induced changes. *Water Resour. Manag.* **1998**, *12*, 295–311. [CrossRef]
37. Richman, J.S.; Moorman, J.R. Physiological time-series analysis using approximate entropy and sample entropy. *American journal of physiology. Heart Circ. Physiol.* **2000**, *278*, H2039–H2049. [CrossRef] [PubMed]
38. Dai, Y.; He, J.; Wu, Y.; Chen, S.; Shang, P. Generalized entropy plane based on permutation entropy and distribution entropy analysis for complex time series. *Phys. A Stat. Mech. Its Appl.* **2019**, *520*, 217–231. [CrossRef]
39. Xavier, S.F.A.; da Silva Jale, J.; Stosic, T.; dos Santos, C.A.C.; Singh, V.P. An application of sample entropy to precipitation in Paraíba State, Brazil. *Theor Appl Clim.* **2019**, *136*, 429–440. [CrossRef]
40. Zhang, L.; Li, H.; Liu, D.; Fu, Q.; Li, M.; Faiz, M.A.; Khan, M.I.; Li, T. Identification and application of the most suitable entropy model for precipitation complexity measurement. *Atmos. Res.* **2019**, *221*, 88–97. [CrossRef]
41. Ma, W.; Kang, Y.; Song, S. Analysis of Streamflow Complexity Based on Entropies in the Weihe River Basin, China. *Entropy* **2019**, *22*, 38. [CrossRef]
42. Cui, L.; Wang, L.; Lai, Z.; Tian, Q.; Liu, W.; Li, J. Innovative trend analysis of annual and seasonal air temperature and rainfall in the Yangtze River Basin, China during 1960–2015. *J. Atmos. Sol.-Terr. Phys.* **2017**, *164*, 48–59. [CrossRef]
43. Zhang, Y.; Hao, Z.; Xu, C.Y.; Lai, X. Response of melt water and rainfall runoff to climate change and their roles in controlling streamflow changes of the two upstream basins over the Tibetan Plateau. *Hydrol. Res.* **2020**, *51*, 272–289. [CrossRef]
44. Li, H.; Wang, W.; Fu, J.; Wei, J. Spatiotemporal heterogeneity and attributions of streamflow and baseflow changes across the headstreams of the Tarim River Basin, Northwest China. *Sci. Total Environ.* **2023**, *856*, 159230. [CrossRef]
45. Huang, A.; Gao, G.; Yao, L.; Yin, S.; Li, D.; Do, H.X.; Fu, B. Spatiotemporal variations of inter-and intra-annual extreme streamflow in the Yangtze River Basin. *J. Hydrol.* **2024**, *629*, 130634. [CrossRef]
46. Jiang, T.; Kundzewicz, Z.W.; Su, B. Changes in monthly precipitation and flood hazard in the Yangtze River Basin, China. *Int. J. Climatol.* **2008**, *28*, 1471–1481. [CrossRef]
47. Gemmer, M.; Jiang, T.; Su, B.; Kundzewicz, Z.W. Seasonal precipitation changes in the wet season and their influence on flood/drought hazards in the Yangtze River Basin, China. *Quat. Int.* **2008**, *186*, 12–21. [CrossRef]
48. Guan, Y.; Zheng, F.; Zhang, X.; Wang, B. Trends and variability of daily precipitation and extremes during 1960–2012 in the Yangtze River Basin, China. *Int. J. Climatol.* **2017**, *37*, 1282–1298.

49. Li, X.; Zhang, K.; Gu, P.; Feng, H.; Yin, Y.; Chen, W.; Cheng, B. Changes in precipitation extremes in the Yangtze River Basin during 1960–2019 and the association with global warming, ENSO, and local effects. *Sci. Total Environ.* **2021**, *760*, 144244. [CrossRef] [PubMed]
50. Lü, M.; Wu, S.-J.; Chen, J.; Chen, C.; Wen, Z.; Huang, Y. Changes in extreme precipitation in the Yangtze River basin and its association with global mean temperature and ENSO. *Int. J. Climatol.* **2018**, *38*, 1989–2005. [CrossRef]
51. Sun, F.; Xu, C.Y. Analysis of streamflow changes in the Yangtze River basin, China, using the sample entropy method. *Hydrol. Process.* **2010**, *24*, 2513–2523.
52. Wang, H.; Xu, C.Y. The impact of climate change and human activities on streamflow in the Yangtze River basin. *Hydrol. Sci. J.* **2011**, *56*, 909–919.
53. Liu, J.; Yang, Z.F. Analysis of the complex water exchange between the Yangtze River and its adjacent lakes using MODIS data. *Remote Sens.* **2013**, *5*, 6618–6637.
54. Chen, Z.; Xu, K. Impact of large-scale hydraulic projects on the hydrological regime of the Yangtze River. *Water Int.* **2015**, *40*, 566–578.

Disclaimer/Publisher’s Note: The statements, opinions and data contained in all publications are solely those of the individual author(s) and contributor(s) and not of MDPI and/or the editor(s). MDPI and/or the editor(s) disclaim responsibility for any injury to people or property resulting from any ideas, methods, instructions or products referred to in the content.

Article

Multi-Model Comparison in the Attribution of Runoff Variation across a Humid Region of Southern China

Qiang Wang^{1,2,3,4}, Fang Yang^{2,3,4}, Xiaozhang Hu^{2,3,4}, Peng Hou^{2,3,4}, Yin Zhang^{2,3,4}, Pengjun Li⁵ and Kairong Lin^{1,*}

¹ School of Civil Engineering, Sun Yat-Sen University, Guangzhou 510275, China; q.wang0718@whu.edu.cn

² Pearl River Water Resources Research Institute, Pearl River Water Resources Commission, Guangzhou 510611, China

³ Key Laboratory of the Pearl River Estuary Regulation and Protection of Ministry of Water Resources, Guangzhou 510611, China

⁴ Key Laboratory of Water Security Guarantee in Guangdong-Hong Kong-Macao Greater Bay Area of Ministry of Water Resources, Guangzhou 510611, China

⁵ State Key Laboratory of Water Resources and Hydropower Engineering Science, Wuhan University, No. 8 Donghu South Road, Wuhan 430072, China

* Correspondence: linkr@mail.sysu.edu.cn

Abstract: The natural hydrological cycle of basins has been significantly altered by climate change and human activities, leading to considerable uncertainties in attributing runoff. In this study, the impact of climate change and human activities on runoff of the Ganjiang River Basin was analyzed, and a variety of models with different spatio-temporal scales and complexities were used to evaluate the influence of model choice on runoff attribution and to reduce the uncertainties. The results show the following: (1) The potential evapotranspiration in the Ganjiang River Basin showed a significant downward trend, precipitation showed a significant upward trend, runoff showed a nonsignificant upward trend, and an abrupt change was detected in 1968; (2) The three hydrological models used with different temporal scales and complexity, GR1A, ABCD, DTVGM, can simulate the natural distribution of water resources in the Ganjiang River Basin; and (3) The impact of climate change on runoff change ranges from 60.07% to 82.88%, while human activities account for approximately 17.12% to 39.93%. The results show that climate change is the main driving factor leading to runoff variation in the Ganjiang River Basin.

Keywords: runoff response; climate change; human activities; hydrological model; elasticity coefficient; Ganjiang River Basin

1. Introduction

Climate change and human activities have changed the natural characteristics of the hydrological processes, the spatio-temporal distribution of precipitation and surface water resources, and the basin is now facing a series of increasing extreme hydro-climatic issues such as floods and droughts [1–3]. The variability of water resources under a changing environment presents pressing challenges for the planning and management of water resources, which is also a prominent research topic. As the most important indicator of water resources, runoff is not only distributed by human activities, but is also very sensitive to climate change. It is a comprehensive result of climate and human activities [4]. Therefore, in order to further understand the process of hydrological cycle, it is important to distinguish the impacts of climate change and human actions on runoff.

Currently, almost all processes in the water cycle are directly or indirectly affected by climate change and human activities to varying degrees. Temperature and precipitation are the most critical meteorological elements affecting the water cycle. Runoff is mainly replenished by precipitation and consumed by evapotranspiration, which is highly affected

by temperature. As reported by the IPCC [1], global surface temperature in the first two decades of the 21st century was 0.99 °C higher than 1850–1900, and global precipitation had a faster speed of increase since the 1980s. On the one hand, rising temperature will accelerate the melting of glaciers and snowpack, increasing runoff. On the other hand, rising temperature will change evapotranspiration and reduce runoff [5]. The influence of human activities on runoff can be classified into two aspects: one involving the manipulation of reservoirs and gates to store and redirect runoff, thereby altering its seasonal distribution; and the other entailing the modification of underlying surface conditions to influence the processes of runoff generation and concentration. Recently, the increasing frequency and intensity of human activities had a significant impact on hydrological processes. Gao and Ruan [6] pointed out that human activities were the dominate factor, accounting for 87.20% of the relative contribution rate, while climate change only contributed 12.80% in the middle reaches of Huaihe River Basin, China. Ni et al. [7] considered the influence of the underlying surface on runoff, and estimated that the contributions of the underlying surface, precipitation and potential evaporation were 64.22%, 20.09% and 15.69% in the Yellow River source areas of China, respectively. Similarly, Hu et al. [8] analyzed the relative contribution of human activities that exceeded 100%, while that of climate change was between −14.25% and −5.43% in the Amu Darya River Basin.

There exist three primary approaches for runoff attribution analysis: empirical statistics, paired catchment comparisons, and hydrological modelling methods [9]. The empirical statistics method, is mostly employed in establishing a relationship between runoff and meteorological variables, which can be linear or nonlinear [10,11]. Although this method is simple to implement and only requires runoff and meteorological data, it lacks adequate physical mechanisms and is highly sensitive to input values. The paired catchment method involves the comparison of hydrological processes in a minimum of two neighboring catchments that share similar climatic and geographical attributes (area, topography, vegetation, soil, etc.) [12,13]. However, it is hard to find a catchment with similar hydroclimatic characteristics for a unique catchment, especially for medium and large-sized catchments, which limits the widespread application of this method [14]. The third approach involves the utilization of hydrological models to distinguish the influence of climate change and human actions on runoff. The hydrological model is usually composed of a series of functions with various parameters, which can describe a variety of hydrological processes in detail [15]. Among these three methods, the hydrological modelling method is more comprehensive than the others, and a series of hydrological models have been applied in a large number of studies, such as the SWAT (Soil and Water Assessment Tool) [16,17], VIC (Variable infiltration Capacity) [18], XAJ (Xin'anjiang model) [19], TOPMODEL (topography-based hydrological model), DTVGM (Distributed Time Variant Gain Model) [20,21], SWIM (Soil and Water integrated Model) [6], and Budyko coupled hydrothermal equilibrium equation [7,8,11].

Due to the variations in model structures, complexities, process representations, and parameters among different hydrological models, there is a consistent presence of significant uncertainties in the results obtained from hydrological modeling [22]. A large number of efficient numerical techniques have been employed in evaluating the impact of parameter uncertainties, while the uncertainties arising from model structures resulting from the simplification of hydrological processes have received comparatively less attention [23]. Consequently, the selection of a hydrological model can exert a significant influence on the analysis of runoff attribution, thereby introducing substantial uncertainties into the obtained results. At present, the quantitative assessment of the response of runoff to climate change and human activities mostly adopts a single attribution method, which fails to consider the uncertainties of the assessment results brought by model or method choice, and the attribution analysis using multiple attribution methods to verify each other still needs to be further strengthened. This study focuses on quantitatively evaluating and separating the influence of meteorological elements and human activities on runoff changes in a humid area of southern China, Ganjiang River Basin (GRB). The primary

purposes of this study are to (1) analyze the trends and mutations of meteorological and hydrological series in the GRB, (2) quantify the contributions of climate change and human activities to the runoff changes, and (3) analyze the influence of model choice on the runoff attribution analysis. This study serves as a reference for local authorities, decision-makers, and researchers in understanding the driving mechanisms of hydrological processes in a changing environment. The findings will significantly contribute to establishing a scientific foundation for practical water resource management and future planning in the GRB.

2. Study Area and Data

2.1. Study Area

The Ganjiang River, spanning a main river length of 823 km, is the largest river in Jiangxi province of China and also one of the eight major tributaries of the Yangtze River. The Ganjiang River Basin (GRB), located between 113°30' and 116°40' E and 24°29' and 29°21' N, encompasses a total area of 80,948 km² above the Waizhou hydrological station, accounting for approximately 48.5% of the area of Jiangxi province (Figure 1). The topography exhibits diversity, ranging from hills in the southern region to alluvial plains in the northeastern region; mountains constitute around 50%, hills account for about 30%, and plains make up roughly 20%. Elevation varies between −105 and 2128 m above sea level. Annual precipitation in this basin amounts to an average of 1626.8 mm with an annual average evaporation rate of approximately 1550 mm. The average temperature is about 18 °C. Summer is the warmest season, accompanied by heavy rainfall, the plum rain precipitation is the most concentrated from April to June, and typhoon-type heavy rainfall occurs from July to September, resulting in significant seasonal variations in streamflow.

2.2. Data

The daily precipitation data of 36 rainfall gauges in and around the GRB from 1956 to 2018 were collected, along with the daily meteorological elements (precipitation, temperature, relative humidity, etc.) of 9 meteorological gauges for the same period. The gauge distribution was relatively uniform, providing a rough representation of temporal and spatial changes in meteorological and hydrological variables within the basin. Some missing data were interpolated by establishing a regression relationship with the corresponding meteorological variable sequences of adjacent gauges. Daily and monthly streamflow data at the Waizhou hydrological station were obtained from the Hydrology Bureau of Jiangxi province for calibration and validation in hydrological models. Due to the limited availability of measured evapotranspiration over long periods, potential evapotranspiration was estimated using the Penman–Monteith method recommended by the Food and Agriculture Organization of the United Nations (FAO). Basic geographic datasets, including digital elevation model (DEM), land cover, and soil type data, were collected from the Resource and Environmental Science Data Center of the Chinese Academy of Sciences. Previous studies have confirmed that all the data used in this study are reliable and suitable for driving hydrological models [24–26]. The location and gauge distribution of the GRB are shown in Figure 1.

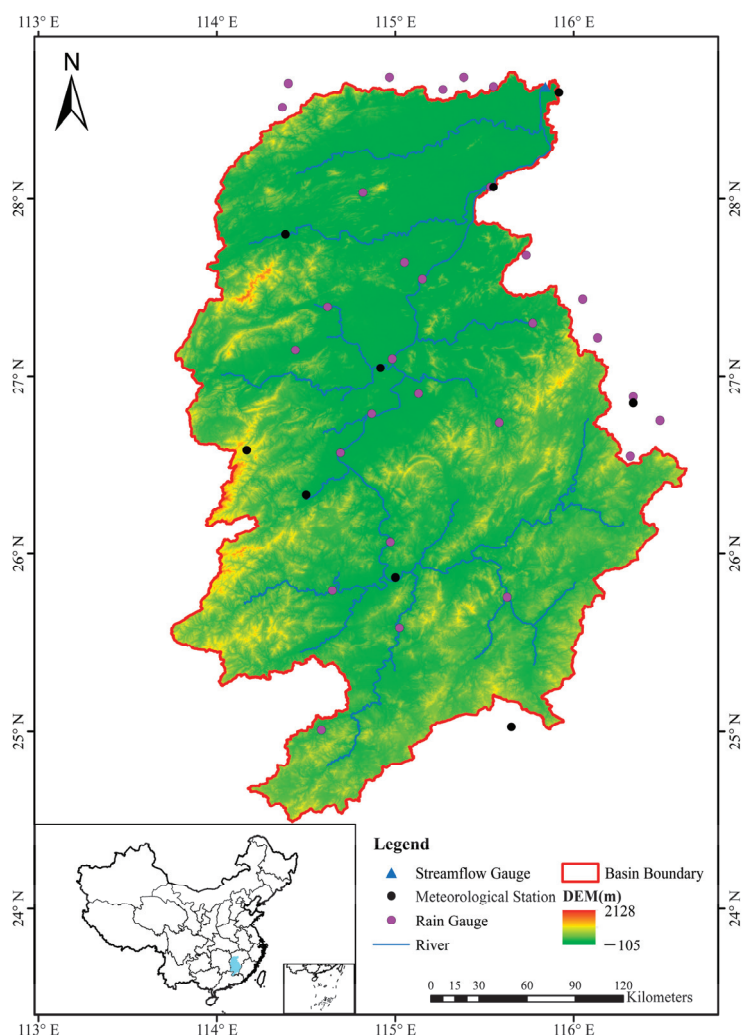


Figure 1. The location of the Ganjiang River Basin (GRB) and corresponding rain gauges, meteorological stations and streamflow gauge.

3. Methodology

3.1. Trend and Mutation Analysis

In this study, the Mann–Kendall (M-K) method was employed to detect trends and abrupt changes in precipitation, evapotranspiration, and runoff time series. The M-K method is a nonparametric statistical test that serves as a robust and reliable approach for trend detection. Consequently, it has been recommended by the World Meteorological Organization (WMO) for examining time series trends in meteorology, hydrology, and environmental science fields. The calculated statistic index Z from the M-K method is utilized to indicate the magnitude of the trend: $Z > 0$ represents an increasing trend; $Z < 0$ signifies a decreasing trend; and $Z = 0$ indicates no discernible trend detected. While the M-K method can only identify statistically significant trends but not their slopes, this study assumes linearity in trends as a quantification of temporal change. To determine the slope of time series unaffected by outliers or data errors, Sen's slope method was employed. Additionally, an abrupt change test is conducted using a critical value at the 95% significance level.

3.2. Hydrological Model

In order to analyze the influence of model choice on runoff attribution analysis, three hydrological models with different complexities and temporal scales, are selected to simulate streamflow. The GR1A model is an annual-scale hydrological model with a simple

structure, the ABCD model is a monthly scale hydrological model with a more complex structure, while the DTVGM model is a daily scale hydrological model with the most complex structure. Additionally, the first two models are lumped hydrological models, while the DTVGM is a distributed hydrological model. A detailed description of these three models is given as follows.

3.2.1. GR1A Model

The GR1A model, developed at Cemagref at the end of 1980s, is an annual runoff simulation model [27,28]. The GR1A model adopts a simplified and aggregated framework, taking into account the influence of dynamic storage and preceding precipitation conditions. This model is characterized by a concise mathematical equation featuring only one parameter, as shown in Equation (1).

$$Q_k = P_k \left\{ 1 - \frac{1}{\left[1 + \left(\frac{0.7P_k + 0.3P_{k-1}}{X \cdot PET_k} \right)^2 \right]^{0.5}} \right\}, \quad (1)$$

where Q_k and PET_k are simulated streamflow and average potential evapotranspiration of the year k ; P_k and P_{k-1} are the basin average precipitation of the year k and $k - 1$; X is the only parameter of this model to be optimized. The GR1A model indirectly characterizes the impact of initial soil water storage on runoff through the antecedent precipitation P_{k-1} . The optimized model parameter X exhibits a median value of 0.7, with a 90% probability confidence interval ranging from 0.13 to 3.5.

3.2.2. ABCD Model

The ABCD model, originally proposed by Thomas [29], is a physics-based, lumped, and nonlinear watershed model. The monthly streamflow in this model is determined by the inputs of monthly precipitation and potential evapotranspiration. In this model, the catchment storage is divided into soil water and groundwater compartments (Figure 2). Precipitation is partitioned into actual evapotranspiration, surface runoff, and soil water recharge processes. The total runoff consists of both surface runoff and baseflow released from groundwater. The physical interpretation and range of parameters are listed in Table 1.

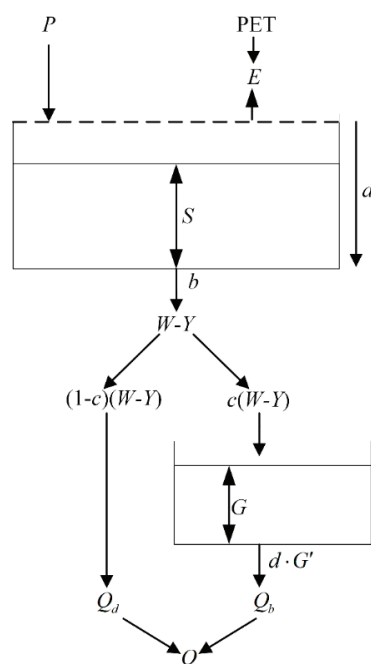


Figure 2. Model structure of the ABCD model.

Table 1. Physical interpretation and range of ABCD model parameters.

Parameter	Physical Interpretation	Range
a	The propensity of runoff occurs before the soil is fully saturated	[0, 1]
b	Upper soil water storage capacity(mm)	[100, 1000]
c	Groundwater recharge coefficient	[0, 1]
d	Groundwater runoff recession constant	[0, 1]

3.2.3. DTVGM Model

The Distributed Time Variant Gain Model (DTVGM), developed by Xia et al. [30], is a physics-based, distributed and nonlinear watershed hydrological model. The distinguishing feature of the DTVGM model lies in its incorporation of soil moisture as a crucial link between runoff generation and flow routing processes. Moreover, this model has a relatively parsimonious model structure and limited free parameters to describe the rainfall–runoff processes. Consequently, the DTVGM model has demonstrated successful applications in many basins in China with satisfactory results [31–34]. Therefore, this model was selected to simulate streamflow process of the GRB.

3.2.4. Model Calibration

The hydrological model contains many parameters that will affect hydrological simulation results. The optimized model has better potential to characterize the conditions and processes of hydrological systems [35]. In this study, the Shuffled Complex Evolution–University of Arizona (SCE-UA) optimization algorithm, developed by Duan et al. [36], is used for the parameter calibration of these three hydrological models. Three different indices were selected to evaluate model performance in this study, including the Nash–Sutcliffe efficiency (NSE) [37], regression coefficient of determination (R^2), and relative error (Bias) [38]. The detailed calculation formulas of NSE, R^2 and Bias are shown as follows.

$$NSE = 1 - \frac{\sum_{i=1}^n (Q_{i,obs} - Q_{i,sim})^2}{\sum_{i=1}^n (Q_{i,obs} - \overline{Q_{obs}})^2}, \quad (2)$$

$$R^2 = \frac{\sum_{i=1}^n (Q_{i,obs} - \overline{Q_{obs}})(Q_{i,sim} - \overline{Q_{sim}})}{\sqrt{\sum_{i=1}^n (Q_{i,obs} - \overline{Q_{obs}})^2 \sum_{i=1}^n (Q_{i,sim} - \overline{Q_{sim}})^2}}, \quad (3)$$

$$Bias = \frac{\sum_{i=1}^n (Q_{i,sim} - Q_{i,obs})}{\sum_{i=1}^n Q_{i,obs}} \times 100\%, \quad (4)$$

where n is the number of samples, $Q_{i,sim}$ and $Q_{i,obs}$ are the simulated and observed streamflow values, respectively, $\overline{Q_{obs}}$ and $\overline{Q_{sim}}$ are their mean values, respectively. The model performance criteria were provided by Moriasi et al. [38] and Krause et al. [39].

3.3. Attribution of Runoff Changes

3.3.1. Hydrological Model Method

The quantitative separation of climate change and human activities can be mathematically formulated as follows.

$$\Delta Q = Q_L - Q_N, \quad (5)$$

$$\Delta Q_C = Q_M - Q_N, \quad (6)$$

$$\Delta Q_H = \Delta Q - \Delta Q_C, \quad (7)$$

$$F_C = \frac{\Delta Q_C}{\Delta Q} \times 100\%, \quad (8)$$

$$F_H = \frac{\Delta Q_H}{\Delta Q} \times 100\%, \quad (9)$$

where ΔQ represents the disparity between average streamflow during reference period (Q_N) and average streamflow during changed period (Q_L); Q_M is the simulated natural streamflow under changed period; ΔQ_C and ΔQ_H indicate the changes in streamflow attributed to climate change and human activities, respectively; and F_C and F_H represent the relative contribution rates of climate change and human activities on runoff variation, correspondingly.

3.3.2. Climatic Elastic Coefficient Method

In recent years, the Budyko framework has gained significant popularity in runoff attribution analysis due to its concise physical mechanism. Within this framework, it is assumed that the long-term hydro-meteorological characteristics of a basin adhere to the balance of water and energy. Actual evapotranspiration (E) primarily depends on both the atmospheric water supply (P) and the land surface's evapotranspiration capacity (PET). As a result, actual evapotranspiration can be expressed as a function of aridity index ϕ .

$$E = f\left(\frac{\text{PET}}{P}\right) \cdot P = f(\phi) \cdot P, \quad (10)$$

where ϕ is the aridity index, $\phi = \frac{\text{PET}}{P}$; $f(\cdot)$ is the Budyko function. On the year or multi-year scale, the alteration in water storage within a watershed may be insignificant, therefore the water balance between runoff (Q) and climate variables (P and E) can be expressed as:

$$Q = P - E, \quad (11)$$

As pointed by Donohue et al. [40], the runoff change caused by climate change could be described as:

$$\frac{\Delta Q_C}{Q} = \varepsilon_P \frac{\Delta P}{P} + \varepsilon_{PET} \frac{\Delta \text{PET}}{\text{PET}}, \quad (12)$$

where ε_P and ε_{PET} are the climate elasticity coefficient to express the sensitivity of Q to P and PET. ε_P and ε_{PET} are defined as:

$$\varepsilon_P = \lim_{\frac{\Delta P}{P} \rightarrow 0} \frac{\Delta Q/Q}{\Delta P/P} = \frac{\partial Q}{\partial P} \times \frac{P}{Q} = 1 + \frac{\phi f'(\phi)}{1 - f(\phi)}, \quad (13)$$

$$\varepsilon_{PET} = \lim_{\frac{\Delta \text{PET}}{\text{PET}} \rightarrow 0} \frac{\Delta Q/Q}{\Delta \text{PET}/\text{PET}} = \frac{\partial Q}{\partial \text{PET}} \times \frac{\text{PET}}{Q} = -\frac{\phi f'(\phi)}{1 - f(\phi)}, \quad (14)$$

$$\varepsilon_P + \varepsilon_{PET} = 1, \quad (15)$$

As shown in Equations (13) and (14), different forms of the Budyko function would obtain different elasticity coefficients. With the advancement of the Budyko framework, numerous Budyko functions have been employed in describing the relationship between water and energy. Therefore, four frequently utilized Budyko functions are used in this study, as listed in Table 2.

Table 2. Four frequently utilized forms of $f(\phi)$ and $f'(\phi)$ functions based on the Budyko hypothesis.

Reference	$f(\phi)$	$f'(\phi)$
Schreiber [41]	$1 - e^{-\phi}$	$e^{-\phi}$
Ol'Dekop [42]	$\phi \tanh\left(\frac{1}{\phi}\right)$	$\tanh\left(\frac{1}{\phi}\right) - \frac{4}{\left[\phi \left(e^{-\frac{1}{\phi}} + e^{\frac{1}{\phi}}\right)\right]^2}$
Budyko [43]	$\left[\phi \tanh\left(\frac{1}{\phi}\right) (1 - e^{-\phi})\right]^{0.5}$	$0.5 \left[\phi \tanh\left(\frac{1}{\phi}\right) (1 - e^{-\phi})\right]^{-0.5} \left[\left(\tanh\left(\frac{1}{\phi}\right) - \frac{\text{sech}^2\left(\frac{1}{\phi}\right)}{\phi} \right) (1 - e^{-\phi}) + \phi \tanh\left(\frac{1}{\phi}\right) e^{-\phi} \right]$
Turc-Pike [44]	$(1 + \phi^{-2})^{-0.5}$	$\frac{1}{\left[\phi^3 \left(1 + \left(\frac{1}{\phi}\right)^2\right)^{1.5}\right]}$

4. Results and Discussion

4.1. Trends of Hydro-Meteorological Variables

Figure 3 provides the series of annual potential evapotranspiration, precipitation and runoff in the GRB. The M-K method and Sen's slope method were utilized to analyze the trend of annual precipitation, potential evapotranspiration, and runoff series, with the results presented in Table 3. The annual potential evapotranspiration series of the GRB generally showed a downward trend, with a decreasing rate of 0.91 mm/year. The Z value of potential evapotranspiration estimated by the M-K method was -2.16 , which shows that the potential evapotranspiration series presented a downward trend, and the trend was significant (0.05 significance level). The precipitation and runoff series in the GRB showed an overall upward trend, with a rising rate of 3.21 mm/year and 1.75 mm/year, respectively. The precipitation had a slightly significant upward trend with 0.10 significance level, while the upward trend of runoff was not significant.

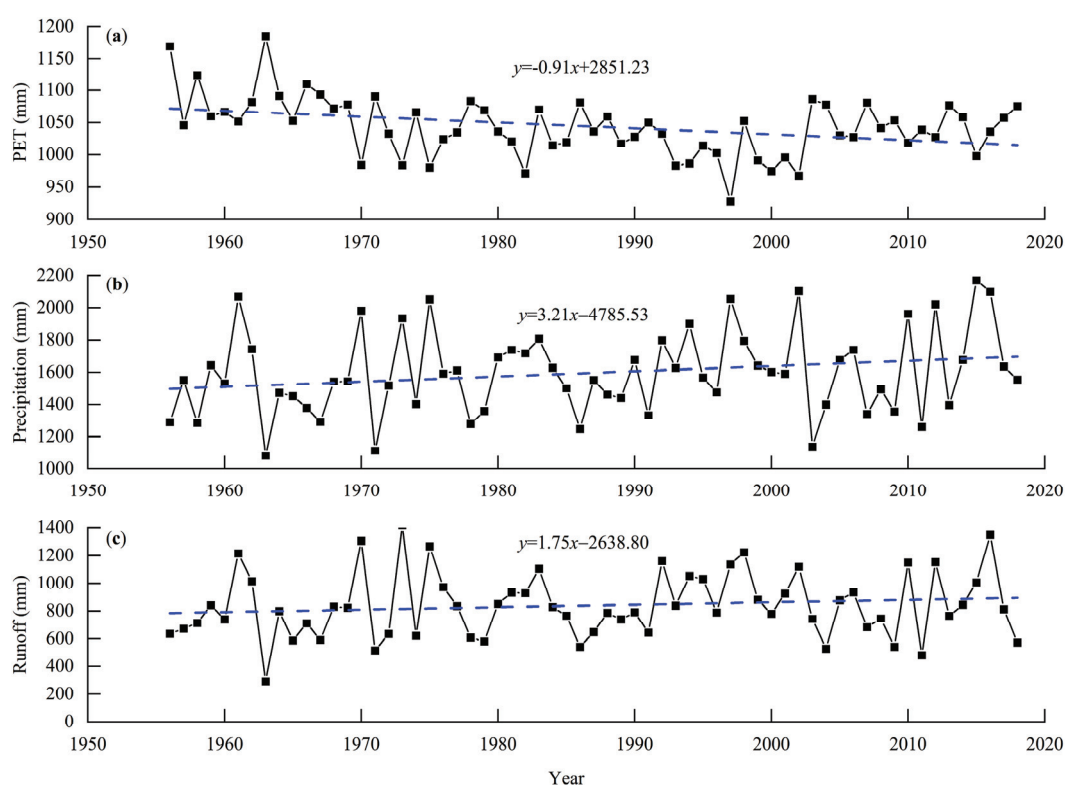


Figure 3. The time series of hydro-climatic variables in Ganjiang River Basin ((a) potential evapotranspiration; (b) precipitation; (c) runoff). The black square lines are observed values, and the best-fit lines estimated by the OLS (ordinary least square) method are the blue dotted lines.

Table 3. Variations of hydro-climatic series before and after the abrupt change point in the GRB.

Variable	Z	Significance	Sen's Slope	Average Value/mm		Change Rate/%
				1956–1968	1969–2018	
PET	-2.61	**	-0.89	1092.64	1031.01	-5.64
P	1.67	*	2.96	1487.12	1624.58	9.24
Q	1.15	ns	1.98	742.09	865.71	16.66

Note: ** Significant at $p < 0.05$; * significant at $p < 0.1$; ns indicates there is no significant trend.

As shown in Figure 4, the M-K mutation test exhibited more than one mutation point, and the moving-T test was used to divide the reference period and the changed period. Consequently, the GRB changed abruptly in the year of 1968; a similar result was obtained by using the standard normal homogeneity test (SNHT) and other studies by

Lei et al. [45], Fan et al. [46] and Zhang et al. [47]. Taking 1968 as the critical time point, the whole sequence is divided into the reference period (1956–1968) and the changed period (1969–2018), and the influence of climate change and human activities on runoff is quantitatively analyzed (Table 3). Compared with the reference period, the annual potential evapotranspiration in the changed period decreased by 5.64%, while the annual precipitation and annual runoff increased by 9.24% and 16.66%, respectively.

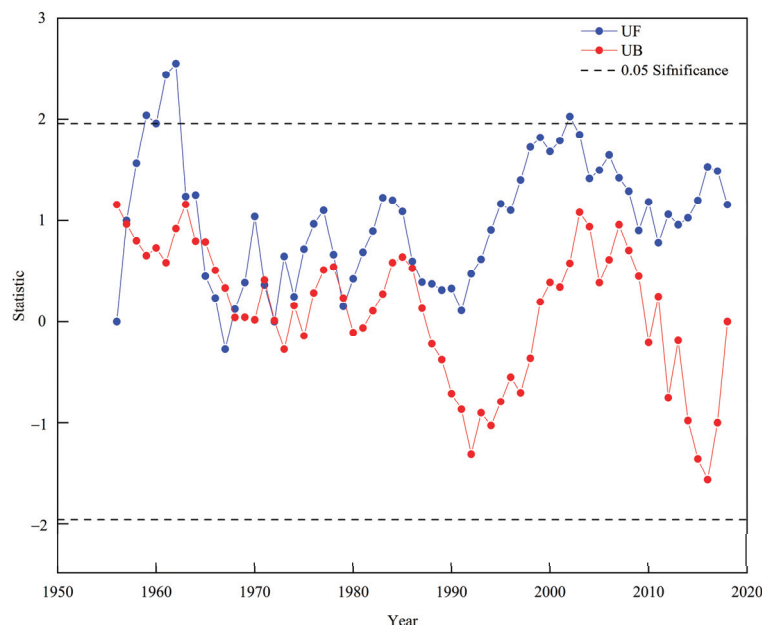


Figure 4. The mutation point detection of runoff series at Waizhou station.

4.2. The Calibration and Validation of Hydrological Models

This study employed three hydrological models, each characterized by distinct temporal scales and complexities. Due to the limited duration of the annual precipitation, potential evapotranspiration, and runoff series in the reference period (1956–1968), the entire hydro-meteorological datasets for that period were employed for parameter calibration in the GR1A model. Utilizing the SCE-UA optimization algorithm [48], the parameter of the GR1A model was calibrated, resulting in an optimized parameter X of 0.79. Figure 5 shows the simulated and observed annual runoff processes for the reference period (1956–1968), demonstrating a general agreement. The NSE and R^2 values of the GR1A model were both 0.83, and the Bias was 1.76%. The simulation results demonstrated the applicability of the GR1A model for simulating runoff variations in the GRB.

When using ABCD and DTVGM models for runoff simulations, the reference period was divided into two periods: calibration (1956–1962) and validation (1963–1968) periods. The SCE-UA algorithm was used to calibrate the ABCD model with NSE and R^2 as the objective functions, and the optimized parameter values were $a = 0.94$, $b = 548.42$, $c = 0.16$ and $d = 0.34$. Table 4 lists the simulation accuracy evaluation of the ABCD model in the calibration and validation periods, and Figure 6 shows the monthly runoff simulated by the ABCD model. The ABCD model obtained NSE of 0.86 and 0.92, R^2 of 0.87 and 0.92, and Bias of -1.96% and 3.44% in the calibration and validation periods, respectively. The strong agreement between the simulated and observed monthly runoff during both calibration and validation periods, as shown in Figure 6, indicates that the ABCD model was highly effective in simulating monthly runoff in the GRB.

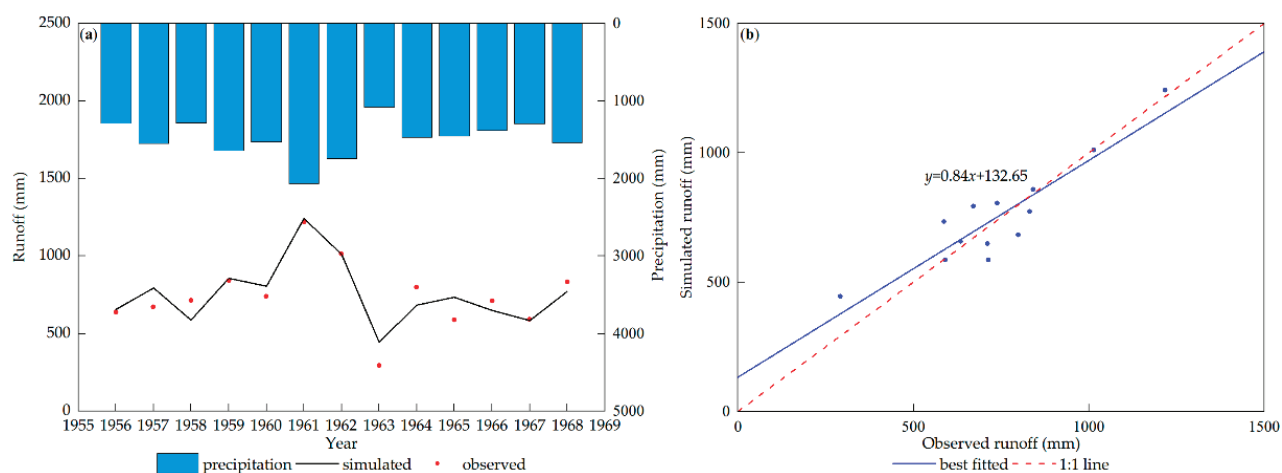


Figure 5. Comparison between simulated runoff and observed runoff at Waizhou station during 1955–1968 by using GR1A model, for (a) runoff processes and (b) scatter curve chart.

Table 4. Model performance evaluation of ABCD model.

Period	Statistical Metrics		
	NSE	R^2	Bias
Calibration period (1956–1962)	0.86	0.87	−1.96%
Validation period (1963–1968)	0.92	0.92	3.44%

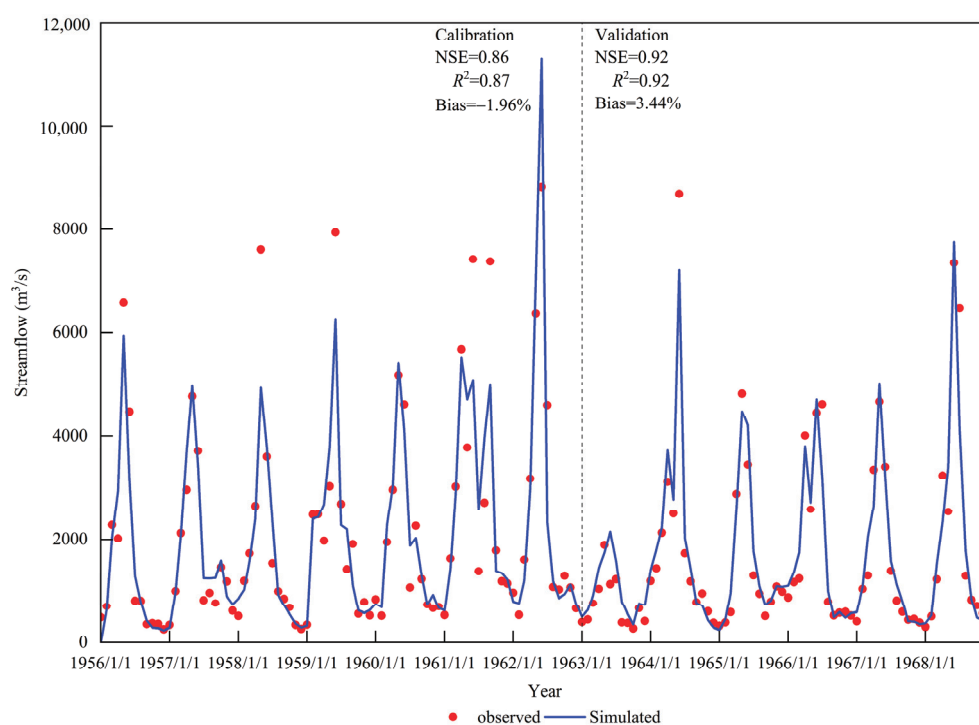


Figure 6. Comparison between simulated runoff and observed runoff and curve chart at Waizhou station during 1955–1968 by using ABCD model.

The optimized parameters of the DTVGM model are presented in Table 5, while Table 6 demonstrates the evaluation of simulation accuracy for this model. Both the calibration and validation periods exhibit NSE and R^2 values exceeding 0.95, accompanied by Bias values of −1.25% and 3.85%, respectively. Figure 7 illustrates a strong agreement between

simulated and measured runoff throughout calibration and validation periods, thereby validating the effectiveness of the DTVGM model.

Table 5. The description of the parameters of the DTVGM model and the optimal values.

Parameter	Physical Interpretation	Optimal Value
g_1	Surface runoff generation parameter	0.06
g_2	Surface runoff generation parameter	0.47
g_3	Subsurface runoff generation parameter	0.22
Nashn	Unit hydrograph shape parameter	2.93
Nashk	Unit hydrograph scale parameter	1.86
kgg	The recession parameter of groundwater storage	0.80

Table 6. Model performance evaluation of the DTVGM model.

Period	Statistical Metrics		
	NSE	R^2	Bias
Calibration period (1956–1962)	0.95	0.95	−1.25%
Validation period (1963–1968)	0.95	0.96	3.85%

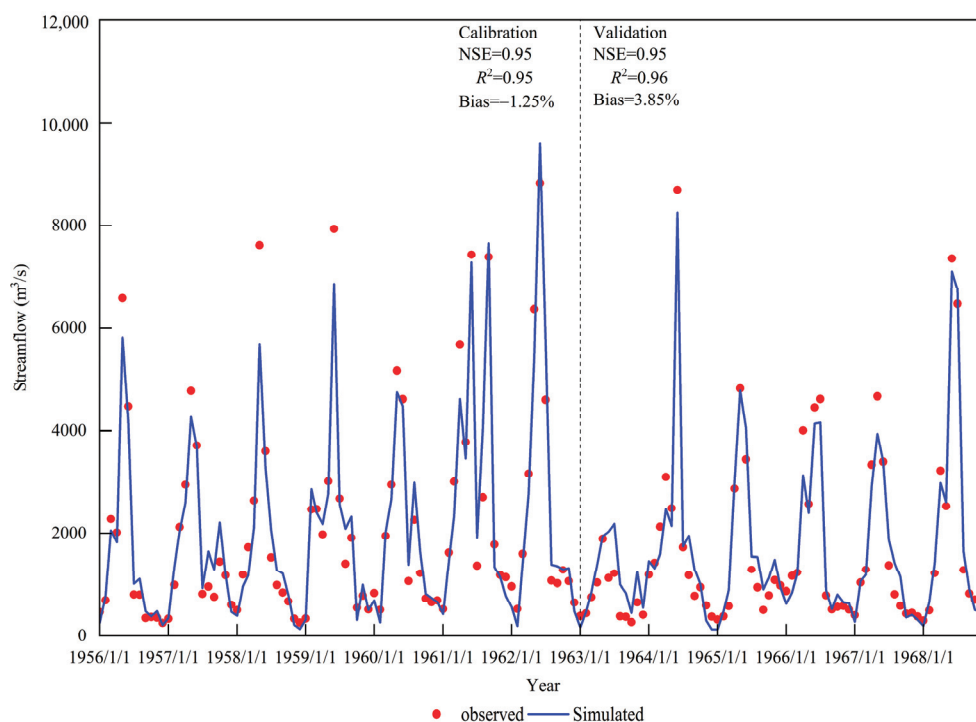


Figure 7. Comparison between simulated runoff and observed runoff and curve chart at Waizhou station during 1955–1968 by using the DTVGM model.

4.3. Contributions of Climate Change and Human Activities to Runoff Change

4.3.1. Climate Elasticity Coefficient Analysis

The climate elastic coefficient method to quantitatively separate the influence of climate change and human activities is mainly carried out on a multi-year scale. As the most important input variable of the Budyko formulas, the aridity index of the GRB is 0.65. The elastic coefficient of runoff to precipitation was calculated as listed in Table 7. The elastic coefficients of runoff to precipitation were 1.63, 1.57, 1.61, and 1.59 for four different Budyko functions, which meant that the runoff would increase 1.63 mm, 1.57 mm, 1.61 mm, and 1.59 mm with a unit increase in precipitation. Similarly, the runoff would change −0.63 mm, −0.57 mm, −0.61 mm, and −0.59 mm with a unit increase in potential evapotranspiration.

In addition, although different forms of the Budyko function were applied in this study, the elastic coefficients obtained by different formulas were very close. The average elastic coefficients of runoff to precipitation and potential evapotranspiration were 1.60 and -0.60 , respectively. The choice of the Budyko function had a relatively small impact on the runoff attribution analysis results, while the aridity index was more sensitive to the results.

Table 7. Separating the effects of climate change and human activities by climate elasticity method.

Period	Variable	Budyko Equation				Mean
		Schreiber	Ol'dekop	Budyko	Turc-Pike	
1969–1979	ε_P	1.63	1.57	1.61	1.59	1.60
	ε_{PET}	-0.63	-0.57	-0.61	-0.59	-0.60
	$\Delta Q_C/\text{mm}$	107.50	102.00	104.89	103.30	104.42
	$\Delta Q_H/\text{mm}$	21.94	27.44	24.55	26.14	25.02
	$F_C/\%$	83.05	78.80	81.03	79.81	80.67
	$F_H/\%$	16.95	21.20	18.97	20.19	19.33
	$\Delta Q_C/\text{mm}$	108.78	103.05	106.06	104.40	105.57
	$\Delta Q_H/\text{mm}$	-37.83	-32.10	-35.11	-33.46	-34.62
1980–1989	$F_C/\%$	74.20	76.25	75.13	75.73	75.30
	$F_H/\%$	25.80	23.75	24.87	24.27	24.70
1990–1999	$\Delta Q_C/\text{mm}$	215.16	204.79	210.23	207.24	209.35
	$\Delta Q_H/\text{mm}$	-2.07	8.30	2.86	5.85	3.74
	$F_C/\%$	99.05	96.10	98.66	97.25	98.25
	$F_H/\%$	0.95	3.90	1.34	2.75	1.75
2000–2009	$\Delta Q_C/\text{mm}$	78.38	73.78	76.20	74.87	75.81
	$\Delta Q_H/\text{mm}$	-32.64	-28.05	-30.46	-29.14	-30.07
	$F_C/\%$	70.60	72.46	71.44	71.99	71.60
	$F_H/\%$	29.40	27.54	28.56	28.01	28.40
2010–2018	$\Delta Q_C/\text{mm}$	253.10	242.41	248.02	244.94	247.12
	$\Delta Q_H/\text{mm}$	-90.94	-80.24	-85.86	-82.77	-84.95
	$F_C/\%$	73.57	75.13	74.29	74.74	74.42
	$F_H/\%$	26.43	24.87	25.71	25.26	25.58
1969–2018	$F_C/\%$	80.28	79.82	80.24	80.01	80.17
	$F_H/\%$	19.72	20.18	19.76	19.99	19.83

Then, the changed period was divided into five decades, including 1969–1979, 1980–1989, 1990–1999, 2000–2009, 2010–2018, and the contribution rates of climate change and human activities in each decade were estimated in Table 7 and Figure 8. For the whole changed period, the contribution rates estimated by four different Budyko formulas were almost the same, with the average contribution rate of climate change and human activities 80.17% and 19.83%, respectively. Among the five decades, the contribution rate of climate change during 1990–1999 was the highest, with a value of 98.25%, while the values of other decades were around 70–80%. Based on the climate elastic coefficient method, climate change was the main factor affecting runoff change in the GRB.

4.3.2. Hydrological Simulation Analysis

The runoff process of the changed period was simulated by using the calibrated GR1A, ABCD and DTVGM models, as shown in Figure 9. The three model evaluation indices for assessing the applicability of three hydrological models are shown in Table 8. Compared with the reference period, GR1A and DTVGM models had a relatively worse performance with a lower NSE and R^2 , while ABCD models showed the same performance with an NSE of 0.91 and R^2 of 0.92. These values of the three hydrological models were all within a reasonable range and reached a satisfactory level based on Moriasi et al. [38].

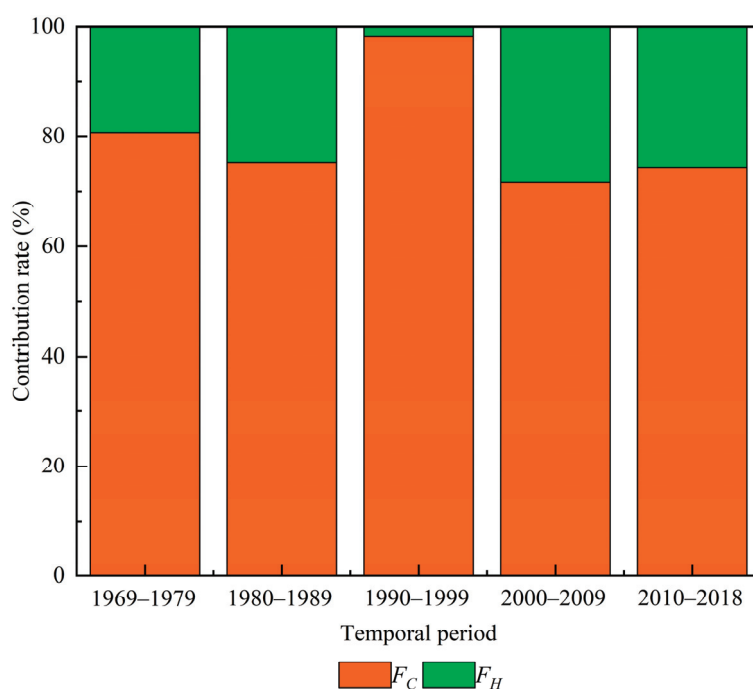


Figure 8. Relative contribution rate of runoff to climate change and human activities estimated by climate elasticity coefficient analysis.

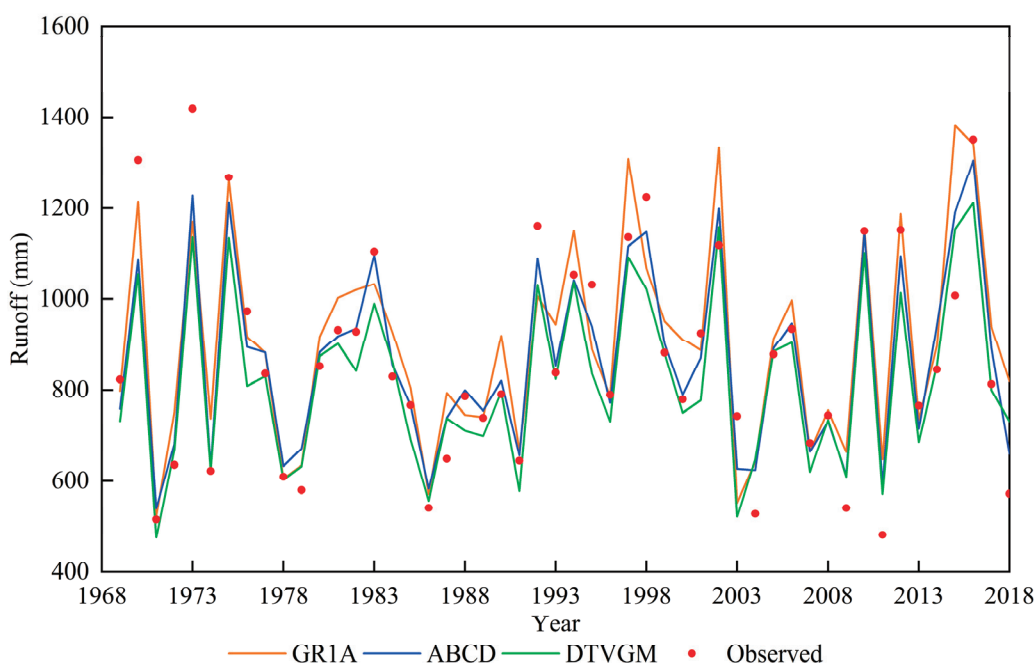


Figure 9. Comparison of annual streamflow with simulated streamflow obtained by different hydrological models during the changed period.

Based on the hydrological simulation method, the influence of climate change and human activities on the runoff change were quantitatively distinguished, as shown in Table 9. There were significant variations in the detected contribution rates among different hydrological models. Within the three models, the impact of climate change on runoff varied from 60.07% to 82.88%, whereas human activities accounted for a range of 17.12% to 39.93%. The respective average values were 74.40% and 25.60%, respectively. The contribution rate results indicated that the impact of climate change on runoff change is

higher than that of human activities, which is consistent with the results of the climatic elastic coefficient method. However, the ranges of the contribution rate estimated by hydrological models were wider than those estimated by Budyko formulas, indicating greater uncertainties.

Table 8. The statistical metrics of three hydrological models for the annual runoff simulation of changed period.

Model	Statistical Metrics		
	NSE	R ²	Bias
GR1A	0.75	0.78	4.36%
ABCD	0.91	0.92	0.24%
DTVGM	0.80	0.85	−4.99%

Table 9. Separating the effects of climate change and human activities by hydrological simulating method.

Period	Variable	Hydrological Model			Mean
		GR1A	ABCD	DTVGM	
1969–1979	$\Delta Q_C/\text{mm}$	121.15	95.69	48.69	88.51
	$\Delta Q_H/\text{mm}$	8.29	33.74	80.74	40.93
	$F_C/\%$	93.60	73.93	37.62	68.38
	$F_H/\%$	6.40	26.07	62.38	31.62
1980–1989	$\Delta Q_C/\text{mm}$	113.79	91.43	44.52	83.24
	$\Delta Q_H/\text{mm}$	−42.84	−20.48	26.43	−12.30
	$F_C/\%$	72.65	81.70	62.75	72.37
	$F_H/\%$	27.35	18.30	37.25	27.63
1990–1999	$\Delta Q_C/\text{mm}$	227.14	191.98	140.77	186.63
	$\Delta Q_H/\text{mm}$	−14.05	21.11	72.32	26.46
	$F_C/\%$	94.17	90.09	66.06	83.44
	$F_H/\%$	5.83	9.91	33.94	16.56
2000–2009	$\Delta Q_C/\text{mm}$	90.08	53.51	18.70	54.10
	$\Delta Q_H/\text{mm}$	−44.34	−7.78	27.04	−8.36
	$F_C/\%$	67.01	87.31	40.89	65.07
	$F_H/\%$	32.99	12.69	59.11	34.93
2010–2018	$\Delta Q_C/\text{mm}$	269.39	206.95	160.85	212.40
	$\Delta Q_H/\text{mm}$	−107.22	−44.79	1.32	−50.23
	$F_C/\%$	71.53	82.21	99.19	84.31
	$F_H/\%$	28.47	17.79	0.81	15.69
1969–2018	$F_C/\%$	80.23	82.88	60.07	74.40
	$F_H/\%$	19.77	17.12	39.93	25.60

The average relative contribution rates of climate change and human activities over five decades are given in Figure 10. Among these five decades, the contribution rates of climate change during 1990–1999 and 2010–2018 were the highest, with values of 84.44% and 84.31%, while the values of other decades ranged between 65% and 73%. Contribution rates of climate change estimated by climate elasticity coefficient and hydrological model analysis were 80.17% and 74.40%, respectively. Both methods identified climate change as the main factor influencing runoff changes. However, the contribution rate of human activities detected by the hydrological simulation method was higher than that detected by the elastic coefficient method, and the two methods identified different periods as the most sensitive to climate change.

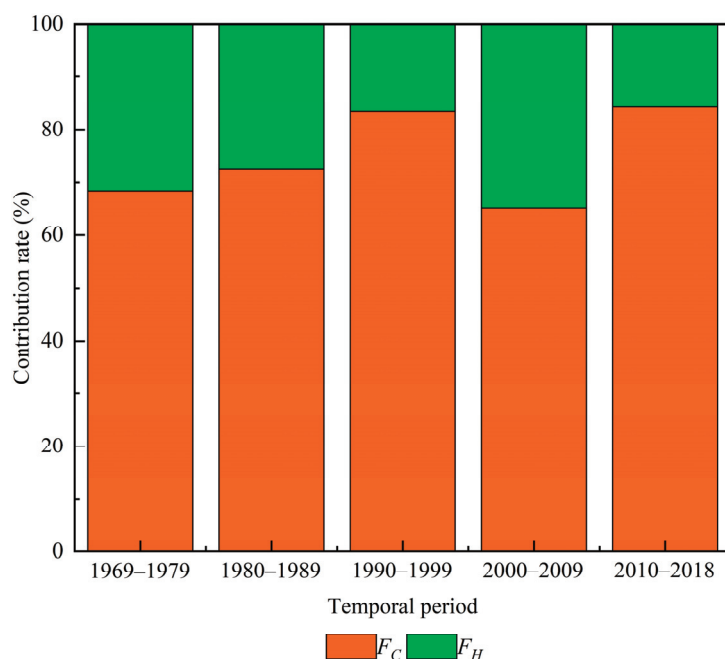


Figure 10. The average relative contribution rates of runoff to climate change and human activities are estimated by hydrological simulation analysis.

The contribution rates of climate change and human activities estimated by different hydrological models are shown in Figure 11. The contribution rate of each factor estimated by the three hydrological models was significantly different. Among three hydrological models, the GR1A model identified 1969–1979 and 1990–1999 as the most sensitive periods to climate change, with contribution rates larger than 90%, while the ABCD model determined that 1990–1999 and 2000–2009 were more sensitive to climate change, with contribution rates of 90.09% and 87.31%. In contrast, the DTVGM model tended to overestimate the contribution rate of human activities. The influence of human activities was more prominent in the periods of 1969–1979 and 2000–2009, with contribution rates of 62.38% and 59.11%, while climate change was most significant in 2010–2018, with a contribution rate as high as 99.19%.

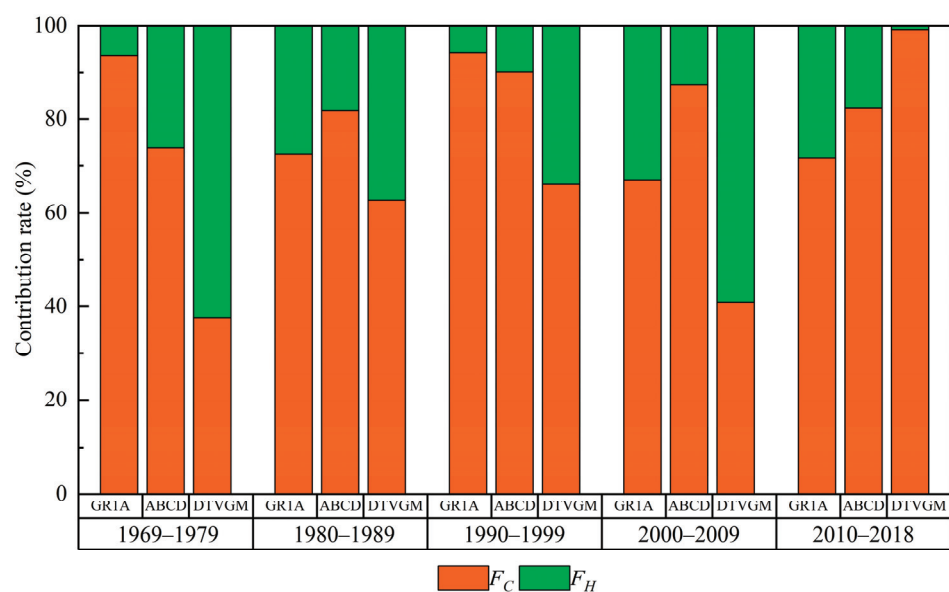


Figure 11. The contribution rates of climate change and human activities are estimated by different hydrological models.

4.4. Discussion

Climate change and human activities play important roles in runoff variation, especially in tropical and subtropical areas. However, these two factors would cause different impacts on hydrological processes in different study areas. For example, Ni et al. [7] highlighted that human activities predominantly influence runoff in the source area of the Yellow River, while Wang et al. [49] concluded that climate change was the main factor for runoff change in the delta area of the Yangtze River. This difference could be attributed to the basin characteristics of study areas (size, soil types, slope, etc.) and the spatio-temporal heterogeneity of climate change and human activities.

For the GRB, climate change, especially in the form of precipitation and temperature changes, was the main factor causing runoff change according to previous results in Section 4.3, which is consistent with the conclusion of Guo et al. [50], Lei et al. [45], Ye et al. [51] and Fan et al. [46], while Liu et al. [52] found the influence of reservoir construction on the runoff change was more significant. Runoff attribution results for the GRB obtained by different studies are listed in Table 10, and the contribution rates of climate change and human activities vary significantly among different studies. Currently, water reservoir construction and land use/cover change are the two primary ways to alter runoff. Based on the reservoir construction report from Jiangxi Province, a large number of medium and small-sized reservoirs were constructed from the 1950s to the 1970s with agricultural irrigation the primary purpose. Subsequently, several large and medium-sized reservoirs primarily for power generation were built after the 1980s. Today, there are 13 large reservoirs, 120 medium-sized reservoirs, and 3678 small reservoirs in the GRB. These reservoirs predominantly influence the annual runoff distribution process by storing excess water during the wet season and releasing it during the dry seasons. Consequently, these reservoirs have a significant influence on the annual runoff distribution but have little influence on the inter-annual variability of runoff. Furthermore, there have been substantial land use/cover changes in the GRB. From the 1950s to the 1980s, forest coverage dropped from 40.1% to 31.5%. However, since the 1980s, the implementation of afforestation and forest restoration projects has led to a remarkable increase in forest coverage, surpassing 60%. This considerable increase in vegetation can reduce runoff during the flood seasons and enhance it during dry seasons. Additionally, following the initiation of the Reform and Opening Policy, China's urbanization has developed rapidly, with significant changes taking place in the underlying surface of cities. Rapid urbanization has contributed to an increase in surface runoff and a reduction in evapotranspiration, consequently decreasing river streamflow. As pointed out by Zhang et al. [47], the increase in streamflow caused by urbanization would offset the decrease caused by afforestation. Therefore, despite extensive human activities over nearly six decades within the GRB, the overall impact of human activities on runoff is still less significant than that of climate change.

Table 10. Comparison of runoff attribution results of the GRB estimated by different studies.

Model	Period		Contribution Rate		Reference
	Reference Period	Changed Period	$F_C/\%$	$F_H/\%$	
Budyko framework	1956–1968	1969–2018	80.17	19.83	Section 4.3.1
ABCD	1956–1968	1969–2018	80.23	19.77	Section 4.3.2
GR1A	1956–1968	1969–2018	82.88	17.12	Section 4.3.2
DTVGM	1956–1968	1969–2018	60.07	39.93	Section 4.3.2
Linear regression	1960–1987	1988–2015	90.71	9.29	[45]
Budyko framework	1960–1969	1970–2007	73.91	26.09	[51]
AWBM	1955–1969	1970–2009	61.00	39.00	[47]
Linear regression	1970–1993	1994–2015	82.72	17.28	[53]
Budyko framework	1955–1991	1992–2017	95.54	4.46	[54]

Various uncertainties affect the model performance and the runoff attribution results, including data sources, methods and temporal periods. In this study, the choice of the

hydrological model is a significant source of uncertainty in separating impacts. As shown in Table 7, different formulas yielded almost the same results, indicating that the choice of the Budyko formula is not sensitive to the runoff attribution results. However, selecting an appropriate hydrological model can greatly affect the results, as shown in Table 10. The Budyko framework constructs a relatively simple relationship between precipitation, actual evapotranspiration and potential evapotranspiration. Although a series of Budyko formulas have been proposed, these formulas are relatively simple, with only one or two key parameters. Therefore, the input is more sensitive to the results when using Budyko formulas. In contrast, the simulation results of the hydrological model are mainly dominated by inputs, model structure and model parameters. The runoff attribution results obtained by different hydrological models would vary obviously. The choice of hydrological model plays an important role in the separation of climate change and human activities on runoff. It is worth noting that higher complexity in a hydrological model does not necessarily translate to more reliable and accurate simulation. More complex models typically involve numerous parameters and require additional inputs, leading to challenges such as parameter identification difficulties and uncertainties [55]. A recommended approach to account for these uncertainties is to run different models, compare results using different methods, and subsequently obtain a more accurate and acceptable runoff attribution analysis.

5. Conclusions

In this study, the impacts of climate change and human activities on runoff variations are quantitatively evaluated based on hydrological simulation and the Budyko framework. Their individual contributions are separated by multiple attribution methods in different periods. Results show that annual potential evapotranspiration has significantly decreased, annual precipitation has slightly increased, and annual runoff has no significant change. The reference period and changed period are detected and the abrupt year is 1968. Three hydrological models simulate the daily runoff well in the GRB, with NSE and R^2 being larger than 0.8. The average contributions of climate change and human activities are 80.17% and 19.83%, by using the climate elasticity method. Similar results are obtained through hydrological simulation analysis, with the average contributions of climate change and human activities being 74.40% and 25.60%, respectively. Therefore, climate change plays a dominant role in runoff variations. The different Budyko formulas have a small impact on the runoff attribution analysis, while different hydrological models might cause dramatic deviation. In order to reduce the uncertainties caused by different data sources, model structures and model parameters, the more accurate way is to assemble multiple models and compare their results for runoff attribution analysis.

The impact of climate change and human activities on runoff process and basin hydrological characteristics are complex owing to it is associated with multiple factors and processes. Furthermore, the impact of human activities on runoff can be divided into fast impact(reservoirs, water diversion projects) and slow impact(land use and land cover changes), while the impacts of these two changes were not clearly distinguished in this study. Therefore, how to quantitatively distinguish the impact of different types of human activities and meteorological elements on the runoff process and understand the impact mechanism of climate change and human activities on basin hydrological processes are important areas for further research.

This study highlights the influence of model choice on the runoff attribution analysis. The outcomes will help provide a scientific basis for practical water resource management and planning of the GRB in the future and will be beneficial to decision-makers in improving the evolutionary characteristics and understanding the driving mechanisms of hydrological processes in a changing environment.

Author Contributions: Conceptualization, Q.W., X.H. and K.L.; methodology, Q.W., F.Y. and P.H.; software, F.Y. and X.H.; validation, P.H., P.L. and Y.Z.; formal analysis, Y.Z. and P.L.; investigation, Q.W.; data curation, P.L.; writing—original draft preparation, Q.W. and K.L. All authors have read and agreed to the published version of the manuscript.

Funding: This research was supported by the National Key Research and Development Program of China (No. 2022YFC3202200, No. 2021YFC3001000, No. 2022YFC3002903), Guangdong Basic and Applied Basic Research Foundation (No. 2023A1515110764, No. 2023B1515040028), Guangdong Provincial Bureau of Hydrology (No. 440001-2023-10716) and Water Conservancy Youth Talent Development Funding Project (Research on multi-objective collaborative scheduling of gate-pump groups in the Guangdong Hong Kong Macao Greater Bay Area).

Data Availability Statement: Data will be made available on request.

Acknowledgments: The authors' gratitude is extended to the China Meteorological Administration (CMA) for providing precipitation and temperature data. The authors gratefully acknowledged the valuable comments and suggestions given by the editors and the anonymous reviewers.

Conflicts of Interest: The authors declare no conflicts of interest.

References

1. Masson-Delmotte, V.; Zhai, P.; Pirani, A.; Connors, S.L.; Péan, C.; Berger, S.; Caud, N.; Chen, Y.; Goldfarb, L.; Gomis, M.I.; et al. *Climate Change 2021: The Physical Science Basis. Contribution of Working Group I to the Sixth Assessment Report of the Intergovernmental Panel on Climate Change*; Cambridge University Press: Cambridge, UK, 2021; Volume 2, p. 2391.
2. Tellman, B.; Sullivan, J.A.; Kuhn, C.; Kettner, A.J.; Doyle, C.S.; Brakenridge, G.R.; Erickson, T.A.; Slayback, D.A. Satellite Imaging Reveals Increased Proportion of Population Exposed to Floods. *Nature* **2021**, *596*, 80–86. [CrossRef] [PubMed]
3. Zhao, R.; Wang, H.; Chen, J.; Fu, G.; Zhan, C.; Yang, H. Quantitative Analysis of Nonlinear Climate Change Impact on Drought Based on the Standardized Precipitation and Evapotranspiration Index. *Ecol. Indic.* **2021**, *121*, 107107. [CrossRef]
4. Huntington, T.G. Evidence for Intensification of the Global Water Cycle: Review and Synthesis. *J. Hydrol.* **2006**, *319*, 83–95. [CrossRef]
5. Barnett, T.P.; Adam, J.C.; Lettenmaier, D.P. Potential Impacts of a Warming Climate on Water Availability in Snow-Dominated Regions. *Nature* **2005**, *438*, 303–309. [CrossRef] [PubMed]
6. Gao, C.; Ruan, T. The Influence of Climate Change and Human Activities on Runoff in the Middle Reaches of the Huaihe River Basin, China. *J. Geogr. Sci.* **2018**, *28*, 79–92. [CrossRef]
7. Ni, Y.; Lv, X.; Yu, Z.; Wang, J.; Ma, L.; Zhang, Q. Intra-Annual Variation in the Attribution of Runoff Evolution in the Yellow River Source Area. *Catena* **2023**, *225*, 107032. [CrossRef]
8. Hu, Y.; Duan, W.; Chen, Y.; Zou, S.; Kayumba, P.M.; Sahu, N. An Integrated Assessment of Runoff Dynamics in the Amu Darya River Basin: Confronting Climate Change and Multiple Human Activities, 1960–2017. *J. Hydrol.* **2021**, *603*, 126905. [CrossRef]
9. Zeng, F.; Ma, M.G.; Di, D.R.; Shi, W.Y. Separating the Impacts of Climate Change and Human Activities on Runoff: A Review of Method and Application. *Water* **2020**, *12*, 2201. [CrossRef]
10. Zhang, C.; Zhang, B.; Li, W.; Liu, M. Response of Streamflow to Climate Change and Human Activity in Xitiaoxi River Basin in China. *Hydrol. Process.* **2014**, *28*, 43–50. [CrossRef]
11. Zhang, H.; Xu, W.; Xu, X.; Lu, B. Responses of Streamflow to Climate Change and Human Activities in a River Basin, Northeast China. *Adv. Meteorol.* **2017**, 1023821. [CrossRef]
12. Zhang, S.; Yang, Y.; McVicar, T.R.; Yang, D. An Analytical Solution for the Impact of Vegetation Changes on Hydrological Partitioning Within the Budyko Framework. *Water Resour. Res.* **2018**, *54*, 519–537. [CrossRef]
13. Brown, A.E.; Zhang, L.; McMahon, T.A.; Western, A.W.; Vertessy, R.A. A Review of Paired Catchment Studies for Determining Changes in Water Yield Resulting from Alterations in Vegetation. *J. Hydrol.* **2005**, *310*, 28–61. [CrossRef]
14. Seibert, J.; McDonnell, J.J. Land-Cover Impacts on Streamflow: A Change-Detection Modelling Approach That Incorporates Parameter Uncertainty. *Hydrol. Sci. J.—J. Des. Sci. Hydrol.* **2010**, *55*, 316–332. [CrossRef]
15. Sood, A.; Smakhtin, V. Global Hydrological Models: A Review. *Hydrol. Sci. J.* **2015**, *60*, 549–565. [CrossRef]
16. Zuo, D.; Xu, Z.; Yao, W.; Jin, S.; Xiao, P.; Ran, D. Assessing the Effects of Changes in Land Use and Climate on Runoff and Sediment Yields from a Watershed in the Loess Plateau of China. *Sci. Total Environ.* **2016**, *544*, 238–250. [CrossRef] [PubMed]
17. Mehdi, B.; Ludwig, R.; Lehner, B. Evaluating the Impacts of Climate Change and Crop Land Use Change on Streamflow, Nitrates and Phosphorus: A Modeling Study in Bavaria. *J. Hydrol. Reg. Stud.* **2015**, *4*, 60–90. [CrossRef]
18. Su, T.; Miao, C.; Duan, Q.; Gou, J.; Guo, X.; Zhao, X. Hydrological Response to Climate Change and Human Activities in the Three-River Source Region. *Hydrol. Earth Syst. Sci.* **2023**, *27*, 1477–1492. [CrossRef]
19. Guo, Y.; Fang, G.; Xu, Y.-P.; Tian, X.; Xie, J. Identifying How Future Climate and Land Use/Cover Changes Impact Streamflow in Xinanjiang Basin, East China. *Sci. Total Environ.* **2020**, *710*, 136275. [CrossRef] [PubMed]
20. Wang, G.; Xia, J.; Chen, J. Quantification of Effects of Climate Variations and Human Activities on Runoff by a Monthly Water Balance Model: A Case Study of the Chaobai River Basin in Northern China. *Water Resour. Res.* **2009**, *45*, W00A11. [CrossRef]

21. Hou, J.; Ye, A.; You, J.; Ma, F.; Duan, Q. An Estimate of Human and Natural Contributions to Changes in Water Resources in the Upper Reaches of the Minjiang River. *Sci. Total Environ.* **2018**, *635*, 901–912. [CrossRef]
22. Moran-Tejeda, E.; Zabalza, J.; Rahman, K.; Gago-Silva, A.; Lopez-Moreno, J.I.; Vicente-Serrano, S.; Lehmann, A.; Tague, C.L.; Beniston, M. Hydrological Impacts of Climate and Land-Use Changes in a Mountain Watershed: Uncertainty Estimation Based on Model Comparison. *Ecohydrology* **2015**, *8*, 1396–1416. [CrossRef]
23. Rojas, R.; Kahunde, S.; Peeters, L.; Batelaan, O.; Feyen, L.; Dassargues, A. Application of a Multimodel Approach to Account for Conceptual Model and Scenario Uncertainties in Groundwater Modelling. *J. Hydrol.* **2010**, *394*, 416–435. [CrossRef]
24. Zhang, L.; Lu, J.; Chen, X.; Liang, D.; Fu, X.; Sauvage, S.; Perez, J.M.S. Stream Flow Simulation and Verification in Ungauged Zones by Coupling Hydrological and Hydrodynamic Models: A Case Study of the Poyang Lake Ungauged Zone. *Hydrol. Earth Syst. Sci.* **2017**, *21*, 5847–5861. [CrossRef]
25. Wang, Q.; Xia, J.; Zhang, X.; She, D.; Liu, J.; Li, P. Multi-Scenario Integration Comparison of CMADS and TMPA Datasets for Hydro-Climatic Simulation over Ganjiang River Basin, China. *Water* **2020**, *12*, 3243. [CrossRef]
26. Wang, Q.; Xia, J.; She, D.; Zhang, X.; Liu, J.; Zhang, Y. Assessment of Four Latest Long-Term Satellite-Based Precipitation Products in Capturing the Extreme Precipitation and Streamflow across a Humid Region of Southern China. *Atmos. Res.* **2021**, *257*, 105554. [CrossRef]
27. Mouelhi, S. Vers Une Chaîne Cohérente de Modèles Pluie-Débit Conceptuels Globaux Aux pas de Temps Pluriannuel, Annuel, Mensuel et Journalier. Doctoral Dissertation, ENGREF, Paris, France, 2003.
28. Perrin, C.; Michel, C.; Andréassian, V. *A Set of Hydrological Models*; John Wiley & Sons, Inc.: Hoboken, NJ, USA, 2013; pp. 493–509. [CrossRef]
29. Thomas, H.A., Jr. *Improved Methods for National Water Assessment, Water Resources Contract: WR15249270*; Harvard Water Resources Group: Cambridge, MA, USA, 1981. [CrossRef]
30. Xia, J.; Wang, G.; Lv, A. A Research on Distributed Time Variant Gain Modeling. *ACTA Geogr. Sin. Ed.* **2003**, *58*, 789–796.
31. Ning, L.; Xia, J.; Zhan, C.; Zhang, Y. Runoff of Arid and Semi-Arid Regions Simulated and Projected by CLM-DTVGM and Its Multi-Scale Fluctuations as Revealed by EEMD Analysis. *J. Arid Land* **2016**, *8*, 506–520. [CrossRef]
32. Cai, M.; Yang, S.; Zeng, H.; Zhao, C.; Wang, S. A Distributed Hydrological Model Driven by Multi-Source Spatial Data and Its Application in the Ili River Basin of Central Asia. *Water Resour. Manag.* **2014**, *28*, 2851–2866. [CrossRef]
33. Xia, J.; Wang, Q.; Zhang, X.; Wang, R.; She, D. Assessing the Influence of Climate Change and Inter-Basin Water Diversion on Haihe River Basin, Eastern China: A Coupled Model Approach. *Hydrogeol. J.* **2018**, *26*, 1455–1473. [CrossRef]
34. Song, Z.; Xia, J.; Wang, G.; She, D.; Hu, C.; Hong, S. Regionalization of hydrological model parameters using gradient boosting machine. *Hydrol. Earth Syst. Sci.* **2022**, *26*, 505–524. [CrossRef]
35. Asgari, M.; Yang, W.; Lindsay, J.; Tolson, B.; Dehnavi, M.M. A Review of Parallel Computing Applications in Calibrating Watershed Hydrologic Models. *Environ. Model. Softw.* **2022**, *151*, 105370. [CrossRef]
36. Duan, Q.; Ajami, N.K.; Gao, X.; Sorooshian, S. Multi-Model Ensemble Hydrologic Prediction Using Bayesian Model Averaging. *Adv. Water Resour.* **2007**, *30*, 1371–1386. [CrossRef]
37. Nash, J.E.; Sutcliffe, J.V. River Flow Forecasting Through Conceptual Models Part I—a Discussion of Principles. *J. Hydrol.* **1970**, *10*, 282–290. [CrossRef]
38. Moriasi, D.N.; Arnold, J.G.; Van Liew, M.W.; Bingner, R.L.; Harmel, R.D.; Veith, T.L. Model Evaluation Guidelines for Systematic Quantification of Accuracy in Watershed Simulations. *Trans. ASABE* **2007**, *50*, 885–900. [CrossRef]
39. Krause, P.; Boyle, D.P.; Bäse, F. Comparison of Different Efficiency Criteria for Hydrological Model Assessment. *Adv. Geosci.* **2005**, *5*, 89–97. [CrossRef]
40. Donohue, R.J.; Roderick, M.L.; McVicar, T.R. Assessing the Differences in Sensitivities of Runoff to Changes in Climatic Conditions across a Large Basin. *J. Hydrol.* **2011**, *406*, 234–244. [CrossRef]
41. Schreiber, P. Über Die Beziehungen Zwischen Dem Niederschlag Und Der Wasserführung Der Flüsse in Mitteleuropa. *Z. Meteorol* **1904**, *21*, 441–452.
42. Ol'Dekop, E.M. On Evaporation from the Surface of River Basins. *Trans. Meteorol. Obs.* **1911**, *4*, 200.
43. Budyko, M.I. *Evaporation under Natural Conditions*; Gidrometeorizdat: Leningrad, Russia, 1963.
44. Pike, J.G. The Estimation of Annual Run-off from Meteorological Data in a Tropical Climate. *J. Hydrol.* **1964**, *2*, 116–123. [CrossRef]
45. Lei, X.; Gao, L.; Wei, J.; Ma, M.; Xu, L.; Fan, H.; Li, X.; Gao, J.; Dang, H.; Chen, X. Contributions of Climate Change and Human Activities to Runoff Variations in the Poyang Lake Basin of China. *Phys. Chem. Earth Parts A/B/C* **2021**, *123*, 103019. [CrossRef]
46. Fan, H.; He, H.; Xu, L.; Zhang, R.; Jiang, J. Simulation and Attribution Analysis Based on the Long-Short-Term-Memory Network for Detecting the Dominant Cause of Runoff Variation in the Lake Poyang Basin. *J. Lake Sci.* **2023**, *33*, 866–878.
47. Zhang, Q.; Liu, J.; Singh, V.P.; Gu, X.; Chen, X. Evaluation of Impacts of Climate Change and Human Activities on Streamflow in the Poyang Lake Basin, China. *Hydrol. Process.* **2016**, *30*, 2562–2576. [CrossRef]
48. Duan, Q.; Sorooshian, S.; Gupta, V.K. Optimal Use of the SCE-UA Global Optimization Method for Calibrating Watershed Models. *J. Hydrol.* **1994**, *158*, 265–284. [CrossRef]
49. Wang, Q.; Xu, Y.; Xu, Y.; Wu, L.; Wang, Y.; Han, L. Spatial Hydrological Responses to Land Use and Land Cover Changes in a Typical Catchment of the Yangtze River Delta Region. *Catena* **2018**, *170*, 305–315. [CrossRef]

50. Guo, L.; Mu, X.; Hu, J.; Gao, P.; Zhang, Y.; Liao, K.; Bai, H.; Chen, X.; Song, Y.; Jin, N. Assessing Impacts of Climate Change and Human Activities on Streamflow and Sediment Discharge in the Ganjiang River Basin (1964–2013). *Water* **2019**, *11*, 1679. [CrossRef]
51. Ye, X.; Zhang, Q.; Liu, J.; Li, X.; Xu, C. Distinguishing the Relative Impacts of Climate Change and Human Activities on Variation of Streamflow in the Poyang Lake Catchment, China. *J. Hydrol.* **2013**, *494*, 83–95. [CrossRef]
52. Liu, G.; Qi, S.; Zhu, J.; Xiong, M.; Wang, D. Quantitative Estimation of Runoff Changes in Ganjiang River, Lake Poyang Basin under Climate Change and Anthropogenic Impacts. *J. Lake Sci.* **2016**, *28*, 682–690. (In Chinese)
53. Hu, W.; Zheng, M. Water and Sediment Changes in the Ganjiang River Basin of China since 1970 and Its Attribution Analysis. *Mt. Res.* **2021**, *39*, 821–829. (In Chinese)
54. Liu, W.; Hua, H.; Zhang, J.; Wang, J.; Wang, Y.; Liu, L. Attribution Identification of Runoff Variation in Ganjiang River Basin Based on Budyko Hypothesis. *Pearl River* **2022**, *43*, 90–97. (In Chinese)
55. Chang, Y.; Wu, J.; Jiang, G.; Kang, Z. Identification of the Dominant Hydrological Process and Appropriate Model Structure of a Karst Catchment through Stepwise Simplification of a Complex Conceptual Model. *J. Hydrol.* **2017**, *548*, 75–87. [CrossRef]

Disclaimer/Publisher’s Note: The statements, opinions and data contained in all publications are solely those of the individual author(s) and contributor(s) and not of MDPI and/or the editor(s). MDPI and/or the editor(s) disclaim responsibility for any injury to people or property resulting from any ideas, methods, instructions or products referred to in the content.

Article

Simulation of Heavy Metal Removal in Irrigation Water Using a Shell-Derived Biochar-Integrated Ecological Recycled Concrete

Yongxiao Ren ^{1,2}, Xiaoxiao Lai ^{1,2}, Jiawei Wang ^{1,2}, Ronggui Li ³, Shenshen Li ⁴, Xingyu Yan ¹, Jing Liu ^{1,*} and Shuai Song ^{5,*}

¹ Environment Research Institute, Shandong University, Qingdao 266237, China; 202200210105@mail.sdu.edu.cn (Y.R.); 202200210090@mail.sdu.edu.cn (X.L.); 202220210072@mail.sdu.edu.cn (J.W.); 202312992@mail.sdu.edu.cn (X.Y.)

² School of Environmental Science and Engineering, Shandong University, Qingdao 266237, China

³ School of Electrical Engineering, Shandong University, Jinan 250100, China; 202200210094@mail.sdu.edu.cn

⁴ School of Software, Shandong University, Jinan 250100, China

⁵ School of Civil Engineering, Qingdao University of Technology, Qingdao 266520, China

* Correspondence: liu_jing@email.sdu.edu.cn (J.L.); songshuai@qut.edu.cn (S.S.)

Abstract: Water pollution intensifies water scarcity and poses a significant threat to ecosystems and human health. Construction waste generated by rapid urbanization also imposes a considerable burden on the environment. Fortunately, a large portion of this waste can be efficiently converted into recycled aggregates and reused in various fields including environmental remediation. In this study, three types of eco-recycled concretes (ERC) (Control-ERC, Biochar-ERC-1, and Biochar-ERC-2) were formulated by integrating shell-derived biochar with recycled aggregates. The porosity and water permeability of these concretes were characterized, and their efficacy evaluated in treating polluted water with six primary heavy metals (HMs), i.e., cadmium (Cd), chromium (Cr), arsenic (As), manganese (Mn), lead (Pb), and copper (Cu). Biochar addition significantly enhanced the continuous porosity and water permeability of the concrete, and substantially enhanced its adsorption capacity of HMs. Specifically, Biochar-ERCs removed over 90% of As, Cd, and Mn, and achieved a removal rate exceeding 60% for other HMs, surpassing the performance of Control-ERC. This study not only lays a solid foundation for the wide application of Biochar-ERCs in the field of environmental protection and remediation, but also provides strong technical support and practical examples for advancing the circular economy model of converting waste into resources while addressing the challenge of global water scarcity.

Keywords: construction waste; coarse aggregate; ecological recycled concrete; heavy metals; adsorption; biochar

1. Introduction

Water stress, exacerbated by improper usage, environmental pollution, and climate change, poses significant threats to both the natural environment and human health [1,2]. The extensive use of water for irrigation has led to severe water scarcity. Even when water is available for irrigation, it is often insufficient or contaminated, thereby adversely affecting the yields and the quality of agricultural production [3]. Furthermore, polluted irrigation water can contaminate soil, leading to long-lasting detrimental effects on the ecosystem and human health [4]. Pollution by heavy metals (HMs) in the environment is a major concern due to their non-degradability and potential toxicity to both ecosystems and humans [5]. The regeneration of clean water is a lengthy process through the natural water cycle, which has been further complicated and hindered by human activities [6]. Therefore, reusing treated wastewater or used water is imperative, which necessitates effective technologies for water pollution control and treatment. However, the high initial concentrations of HMs and the costs associated with these technologies require a considerable investment

to improve the quality of treated wastewater to a level for direct reuse in irrigation or landscaping. Among the conventional and innovative technologies, adsorption stands out as one of the most efficient methods for removing HMs from wastewater [7].

Biochar, characterized by its large specific surface-area-to-volume ratio, abundant pore space, high carbon content, and various surface functional groups, has emerged as a novel material with widespread applications in environmental remediation. It has proven to be effective in soil quality improvement, pollutant removal, carbon sequestration, and emission reduction [8,9]. This versatile material can be produced from a wide range of raw materials, including plant residues and organic solid waste [10,11], in alignment with the prevalent global resource policy that advocates conservation and reuse. Similarly, concrete, an important component in construction projects, is produced in large quantities, leading to the emergence of recycled concrete as a sustainable alternative [12]. Recycled concrete is obtained from previously used concrete, such as construction waste. Its reprocessing and reuse significantly mitigate resource wastage, facilitate concrete recycling, and propel the advancement of green environmental protection [13]. Furthermore, it aids in reducing land contamination, adsorbs HMs ions, and plays a pivotal role in environmental restoration [14]. By incorporating biochar and other materials with a multi-void structure into recycled concrete, the adsorption performance of pollutants is enhanced, thus augmenting the environmental remediation efficacy of the concrete. This approach exemplifies the principle of *utilizing waste to manage waste* [15,16], thereby promoting a sustainable and eco-friendly solution. The addition of biochar to the concrete production process not only minimizes the requirement for clinker in cement production process but also reduces the carbon dioxide (CO₂) emissions associated with clinker fabrication. Furthermore, biochar, distinguished by its high porosity and extensive specific surface area, exhibits the potential to sequester atmospheric CO₂ within the concrete structure [17,18]. High-strength lightweight concrete, formulated using biochar aggregate derived from kitchen waste digestate, effectively reduces the carbon emission of construction materials [19]. In addition, biochar enhances multiple critical properties of concrete, including compressive strength, flexural strength, and split tensile strength [13,20]. Moreover, biochar produced from lignocellulosic biomass in conjunction with sustainable eco-permeable concrete formulated with modified corn cob coarse aggregate has been shown to improve water retention within concrete [19,21], thereby significantly enhancing the strength and durability of the eco-concrete. The integration of biochar into concrete not only facilitates the recycling of concrete but also promotes the utilization of straw and organic solid waste as the sources of biochar. Furthermore, this combination demonstrates remarkable removal efficiency for manganese (Mn), nitrate (NO₃⁻), total phosphorus (TP), and organic pollutants [22], which enhances the environmental remediation effectiveness of both concrete and biochar. At present, the integration of marine-derived biochar with recycled concrete for environmental remediation is still in the stage of technical exploration and initial application. This composite can improve the elastic recovery characteristics and durability of biochar within the cementitious environment [23]. The incorporation of carbon dioxide (CO₂)-storing algal biomass and biochar with concrete effectively reduces CO₂ emissions while effectively adsorbing HM ions and reducing their contents [24,25]. Additionally, the combination of marine sediments with concrete not only reduces carbon emissions and enhances the immobilization of HMs, but also offers potential economic benefits for the treatment and utilization of oceanic sediments [26]. By investigating the application of marine-derived biomass, such as shells, in combination with concrete, this study endeavors to ascertain its efficacy in removing HMs from irrigation water. Consequently, it introduces a novel and sustainable solution for environmental remediation. This innovative method leverages the natural properties of marine biomass and recycled concrete to provide a cost-effective and eco-friendly solution addressing HM contamination in irrigation water, ultimately contributing to the preservation and enhancement of our natural environment.

2. Materials and Methods

2.1. Preparation of Experimental Materials

2.1.1. Preparation of Shell-Derived Biochar

The raw-material shells were collected from the beach at Binhai Park in Qingdao City, Shandong Province, China. These shells were then washed thoroughly with tap water 5 times, baked at 105 °C for 2 h, and subsequently subjected to crushing treatment. After this pretreatment, the shells were accurately weighed and placed into a muffle furnace (OTF-1200X-III-S, China). They were purged with nitrogen for 10 min, pyrolyzed at 900 °C for 2 h, and allowed to cool. The resultant material was then ground and passed through a sieve with a mesh size of 10,000. The fine particles were collected and stored in a dry place for later use. A scanning electron microscope (SEM, ZEISS Crossbeam 550, Germany) was used to examine the surface morphology and structure of the biochar.

2.1.2. Production of Eco-Recycled Concrete with Shell-Derived Biochar

In this study, three groups of eco-recycled concrete (ERC) blocks were prepared, namely Control-ERC, Biochar-ERC-1 and Biochar-ERC-2, with three blocks in each group. The raw materials used for the preparation of these concrete blocks included coarse aggregate sourced from construction waste and biochar derived from marine shell. The specific raw material ratios were as follows: 16.6 parts of cement (Shandong Shanshui Cement Group Limited, China); 76.6 parts of recycled aggregate; 0, 0.3, and 0.6 parts of marine-sourced shell-derived biochar, respectively, for Control-ERC, Biochar-ERC-1, and Biochar-ERC-2; 0.4 parts of reinforcing agent; and 6.0 parts of water. Coarse aggregate particles were sized in the range of 5–10 mm. During the mixing process, the aggregate, cement, and reinforcing agent (Zhejiang Kamiao Technology Co., Ltd., China) were placed first, followed by the addition of deionized water. Except for the control group, which did not contain shell-derived biochar, the other two groups incorporated 0.3 and 0.6 mass portions of shell-derived biochar, respectively. During molding, the molds (100 mm × 100 mm × 100 mm) were coated with mold release agent (Quanzhou Osle Industrial Materials Co., Ltd., China), filled with pounded and smoothed concrete, and wrapped with plastic film. The concrete blocks were then cured in the molds for 24 h before being demolded, rewrapped, and placed for an additional week to complete the concrete preparation. Procedural details of producing the concrete can be found in our previous study [16].

2.1.3. Water Permeability and Porosity Characterization of the Eco-Recycled Concrete

The water permeability coefficients of the three types of ERCs were measured using the constant head method [27], and three replicate blocks from each group were selected for the experiments. The experimental configuration is depicted in Figure 1a. First, the space between the test block and the square cylinder unit was sealed using sealing mud. The square cylinder unit was then placed in the drum unit. Water was then introduced, and the flow rate was adjusted to attain the desired head height. The difference in water level was measured with a straightedge and recorded as H. The water temperature (T) was also monitored. A timing duration of 60 s was set, during which a collection bucket was used to collect the water exiting from the outlet.

The permeability coefficient can be expressed by Equation (1):

$$k_T = \frac{Q \times L}{A \times H \times t} \quad (1)$$

where the k_T (mm/s) is the water permeability coefficient of the block when the water temperature is T °C; Q (mm³) is the volume of water seeping out at time t; L (mm) is the thickness of the concrete block; A (mm²) is the upper surface area of the concrete block; H (mm) is the water level difference; and t (s) is the time duration.

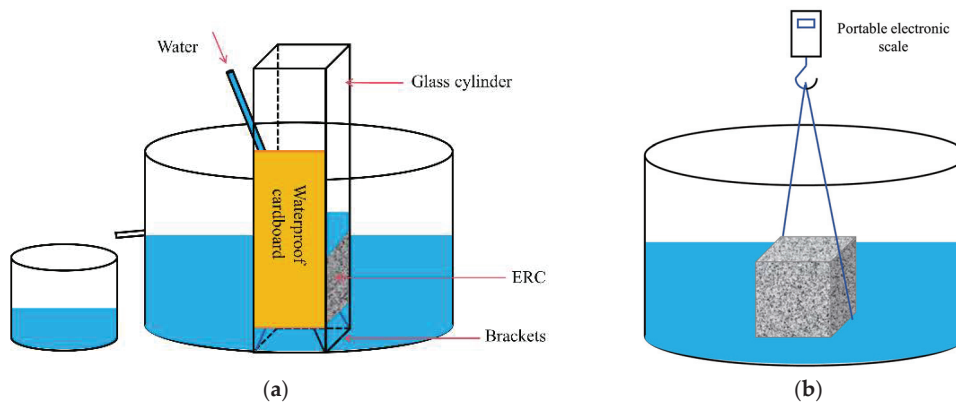


Figure 1. (a) Experimental configuration for measuring the permeability coefficient of the ERCs made with recycled aggregates and shell-derived biochar; (b) diagram of measuring the continuous porosity of the ERCs.

After conducting the permeability coefficient experiments, continuous porosity tests of the concrete blocks were performed. At the conclusion of the permeability coefficient experiment, the test block was securely tied with a rope and submerged in a bucket of water, making sure that the test block was completely submerged without touching the bottom, as illustrated in Figure 1b. The submerged test block was then weighed using a handheld electronic scale to obtain M_1 . The continuous porosity of the test block was calculated using the following Equation (2):

$$C_{\text{void}} = \left[1 - \frac{M_2 - M_1}{\rho V} \right] \times 100\% \quad (2)$$

where C_{void} (%) is the continuous porosity; M_1 (g) is the weight of the concrete block when submerged in water; M_2 (g) is the dry weight of the concrete block; ρ (g/cm^3) is the density of water; and V (cm^3) is the volume of the concrete block.

2.2. Simulation of Wastewater Filtration Process with the Concrete

2.2.1. Simulated Wastewater Preparation

A simulated wastewater effluent (SWW) was prepared with HM concentrations set to the maximum permissible emission concentrations stipulated in the People's Republic of China's Integrated Wastewater Discharge Standard [28]. Specifically, the concentrations were set as follows: lead (Pb) at 1.0 mg/L, cadmium (Cd) at 0.1 mg/L, chromium (Cr) at 1.5 mg/L, arsenic (As) at 0.5 mg/L, Mn at 2.0 mg/L, and copper (Cu) at 0.5 mg/L. These concentrations were achieved through the preparation of a solution composed of $\text{Pb}(\text{NO}_3)_2$, CdCl_2 , $\text{K}_2\text{Cr}_2\text{O}_7$, $\text{Na}_2\text{HAsO}_4 \cdot 7\text{H}_2\text{O}$, $\text{MnCl}_2 \cdot 4\text{H}_2\text{O}$, $\text{CuCl}_2 \cdot 2\text{H}_2\text{O}$, and deionized water.

2.2.2. Filtration Experiments Using ERCs for SWW

A simulated irrigation canal, in the form of an open reactor, was designed to evaluate the filtration efficiency of HMs using ERCs within agricultural irrigation systems. The experimental setup mainly consists of 4 parts, including an acrylic support plate, a partition plate, water purification tank with an ERC block, and purified water tank, as illustrated in Figure 2. The open-top reactor, the partition plate, and the purification water tank were constructed using gold-crystal super-white glass with a thickness of 6 mm. All the external dimensions of each component are illustrated in Figure 2. Three replicate ERC blocks of each type were selected for conducting the parallel experiments to ensure the reliability and reproducibility of the results.

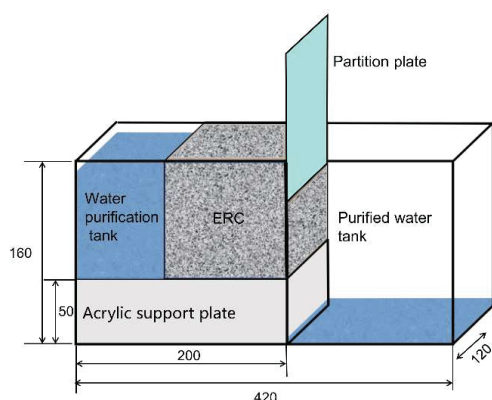


Figure 2. Schematic diagram of the filtration open-top reactor (dimension unit is mm).

The SWW was slowly introduced into the reactor from the left side of the device. After all of the SWW had been introduced into the device, it was allowed to react for 2 min. Following this period, the partition was then removed to enable the entire volume of the SWW to pass through the ERC block and into the tank on the right side.

The conductivity, pH, and dissolved oxygen (DO) of the SWW before and after filtration were monitored. Samples were collected and acidified using 2% nitric acid, and the concentrations of the HMs (Pb, Cd, Cr, As, Mn, Cu, etc.) in the samples were determined by inductively coupled plasma mass spectrometry (ICP-MS) to determine the adsorption of HMs by the ERCs.

The strengths of concrete blocks were tested with an electro-hydraulic servo universal testing machine after the filtration experiment. The elemental composition was analyzed with SEM-EDS (energy-dispersive spectrometer) with aggregates from crushed concrete blocks.

2.3. Statistical Analysis

One-way ANOVA was used to assess the differences in the adsorption capacity of different ERCs for HM ions in the SWW. The data were presented as mean \pm standard deviation, with $n = 3$ replicates. A statistically significant difference between groups was indicated by a p value of less than 0.05. All statistical analyses were conducted in R (R4.2.2) and figures were produced using the package ggplot2.

3. Results and Discussion

3.1. Characterization of Shell-Derived Biochar

SEM analysis indicated that the particle size of the shell-derived biochar varied from less than 1 μm to 5 μm , and exhibited irregular shapes and morphologies (Figure 3), which could be attributed to the inherent characteristics of the shell material and the pyrolysis process conditions used for their production. This variability in particle size and shape can influence the biochar's surface area, porosity, and overall performance of biochar-integrated ERCs.

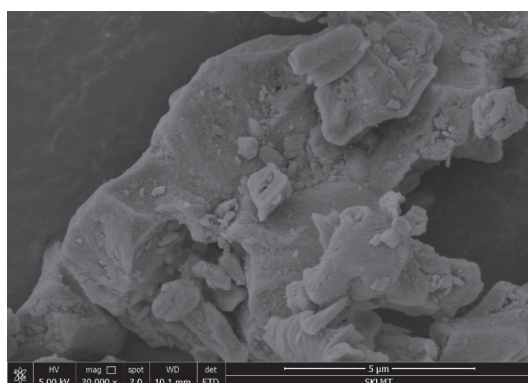


Figure 3. SEM analysis of the shell-derived biochar.

3.2. Characterization of ERCs

The surface morphology of the ERC blocks, as depicted in Figure 4, was captured using a high-resolution scanning device. The image displays a porous structure formed by relatively uniform recycled aggregates with biochar incorporated within, facilitating water permeability and enhancing pollutant absorption capabilities. Table 1 summarizes the fundamental physical characteristics of ERCs.



Figure 4. Surface morphology of the ERC.

Table 1. Physical characterization of the concrete blocks made with recycled aggregates and shell-derived biochar.

Concrete Blocks	Mass (g)	Dimension (cm)	Density (g/cm ³)	Permeability Coefficients (mm/s)	Continuous Porosity (%)	Strength (MPa)
Control-ERC	1676.67 ± 20.82	10 × 10 × 10	1.68	19.42 ± 0.14	33.83 ± 1.76	5.64
Biochar-ERC-1	1590 ± 26.46		1.59	23.08 ± 0.76	37.83 ± 0.58	6.53
Biochar-ERC-2	1606.67 ± 20.82		1.61	26.34 ± 0.80	37.17 ± 1.26	5.10

3.2.1. Permeability Coefficients

Water permeability is the main characteristic for evaluating the performance of pervious concrete [23]. The one-way ANOVA analysis indicate that there was a significant difference in the permeability coefficients of the three types of concrete ($p < 0.01$) (Table 1, Figure 5a). The additions of biochar with 0.3 and 0.6 mass portions significantly increased the permeability coefficients of the concrete by 18.85% and 35.63%, respectively, in comparison to Control-ERC. The correlation between the addition of biochar and the permeability coefficients of the concrete indicate that this coefficient increases linearly as the amount of biochar incorporated increases within a specific range (Figure 5b).

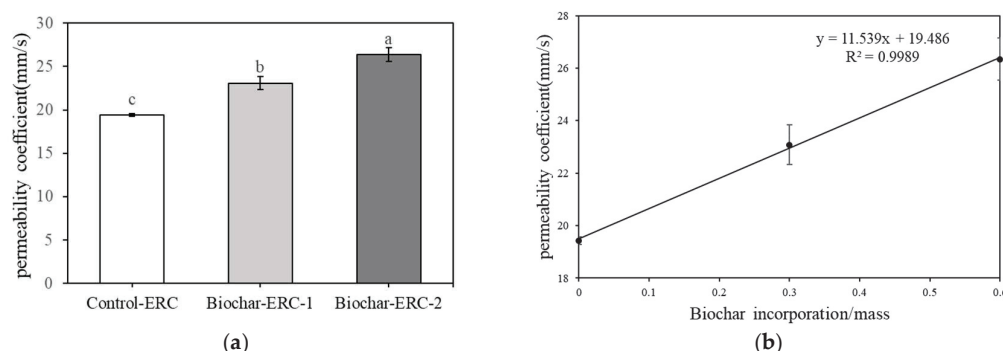


Figure 5. (a) Permeability coefficient of ERCs; (b) correlation between water permeability coefficient of ERCs and the amount of biochar addition. Note: Letters a–c in (a) denote statistical comparisons between groups; a significant difference is considered when two groups do not share common letters ($p < 0.05$).

3.2.2. Continuous Porosity

Closely related with the permeability performance, the continuous porosity of the concrete was also significantly increased by the admixture of the biochar in the ERCs ($p < 0.05$) (Table 1, Figure 6). However, the continuous porosity in the two biochar-integrated ERC groups did not show a significant difference. Generally, the porosity of pervious concrete is primarily controlled by the macropores formed between aggregates, which are largely determined by the particle size and distribution of the aggregates and have minimal direct correlation with additives such as cement and biochar [29]. Therefore, it is postulated that the porous structure of biochar may exert a certain influence on the porosity of pervious concrete, potentially enhancing its macroporous structure and thereby increasing the porosity of pervious concrete, but only to a certain extent.

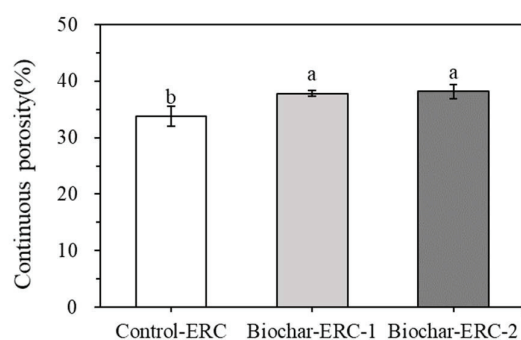


Figure 6. Continuous porosity of ERCs. Note: Letters a–b denote statistical comparisons between groups; a significant difference is considered when two groups do not share common letters ($p < 0.05$).

3.2.3. Strength of the Concrete

There is no significant difference in the strengths among the three types of concrete (Table 1), which proves a consistent manufacturing process. Moreover, the concrete strength can be tailored to meet specific application purposes and life expectancy based on more realistic requirements.

3.3. Adsorption Performance of HM Ions from SWW with the ERCs

Before the filtration, the concentrations of the six HMs in the SWW were determined to be As 355.01 $\mu\text{g/L}$, Cd 79.51 $\mu\text{g/L}$, Cr 3262.70 $\mu\text{g/L}$, Mn 2353.99 $\mu\text{g/L}$, Pb 551.74 $\mu\text{g/L}$, and Cu 549.11 $\mu\text{g/L}$, respectively (Figure 7). The measured concentrations of most HMs in the simulated wastewater effluent were approximate to their nominal concentrations, but a difference was exhibited for some HMs because of the chemical reactions within the system. For example, Pb^{2+} precipitated with $\text{Cr}_2\text{O}_5^{2-}$. After the filtration process, the

concentrations of all these HMs were significantly decreased in the SWW and met the standard for irrigation water quality in China [30], except that of Cr (Table 2). These results indicate that ERCs possess significant efficacy in absorbing most of these HMs from water. Chromium is extensively used in textile dyes and mordants, plating, pigments, alloying, etc., covering many walks of life [31]. However, removing Cr from wastewater is very challenging due to its rapid transformation between multiple oxidation states ranging from -2 to $+6$ [32]. This complexity is compounded by the fact that Cr can coexist in up to eleven different species in water [33]. Consequently, eliminating Cr from wastewater using a solitary technique is a formidable task. To date, various technologies have been developed to remove Cr from wastewater, encompassing physicochemical technology, electrochemical technology, and advanced oxidation technology. The method proposed in this study falls under the category of physicochemical technology, and it can involve multiple filtration stages or a filtration system to further reduce Cr concentrations and ensure compliance with the aforementioned standards.

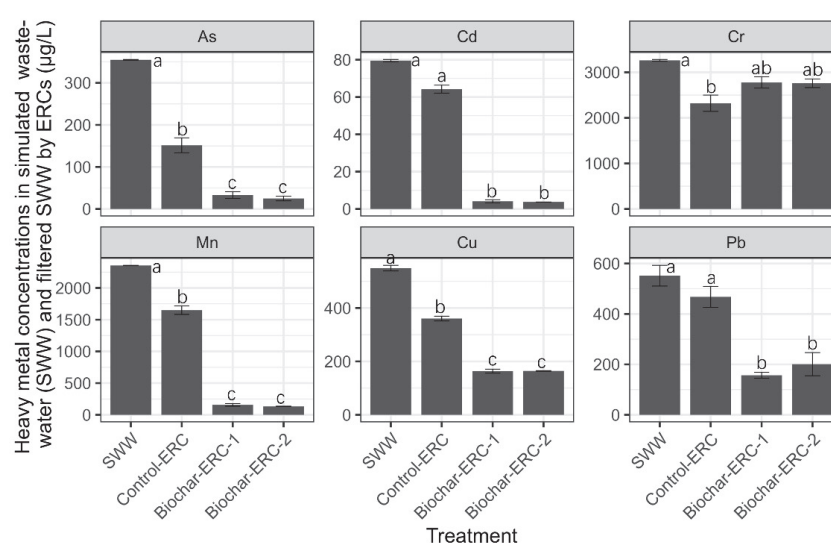


Figure 7. Heavy metal concentrations in the original simulated wastewater effluent (SWW) and the filtrates after filtration using ERCs. Note: Letters a–c denote statistical comparisons between groups; a significant difference is considered when two groups do not share common letters ($p < 0.05$).

Table 2. Heavy metal (HM) concentrations in the solution before filtration and after filtration through ERCs.

Samples	As (µg/L)	Cd (µg/L)	Cr (µg/L)	Mn (µg/L)	Cu (µg/L)	Pb (µg/L)
Simulated wastewater before filtration	355.01 ± 0.84	79.51 ± 0.67	3262.70 ± 20.78	2353.99 ± 3.41	549.11 ± 10.67	551.74 ± 41.15
Filtrates through Control-ERC	151.45 ± 17.86	64.23 ± 2.12	2320.91 ± 178.84	1649.52 ± 66.54	360.42 ± 9.09	467.72 ± 41.63
Filtrates through Biochar-ERC -1	32.893 ± 7.84	4.10 ± 0.81	2777.24 ± 123.983	157.62 ± 21.33	163.57 ± 7.55	156.85 ± 11.73
Filtrates through Biochar-ERC -2	24.935 ± 5.74	3.72 ± 0.05	2760.43 ± 95.54	132.41 ± 3.83	164.53 ± 1.21	200.89 ± 45.85
GB 5084-2021 [30]	50–100 ^a	10	100	none	500–1000 ^a	200

Note: ^a The standard concentrations depend on the crops.

Furthermore, the adsorption performance of HMs from the SWW using different ERCs was evaluated (Figure 8). Specifically, when the SWW was filtered through Biochar-ERC-1 and Biochar-ERC-2 concrete blocks, it resulted in the removal of more than 90% of As, Cd, and Mn, indicating that both treatments were exceptionally effective in eliminating these three HMs. The removal rates for all other HMs were greater than 60%. In contrast, filtering SWW through Control-ERC concrete removed less than 40% of all HMs, except

for As, which was removed by about 60%. Notably, the removal rates of HMs except Cr were significantly lower for Control-ERC compared to the other two concretes containing shell-derived biochar. This suggests that shell-derived biochar exhibits strong adsorption capacity for HMs, which should be attributed to the increased porous structure and rich functional groups of the biochar. This postulation needs to be further verified. The lower removal rate of Cr with Biochar-ERC-1 and Biochar-ERC-2 may be attributed to the presence of Cr-repelling substances within the shell-derived biochar, which also needs to be further verified. In addition, Biochar-ERC-2 demonstrated higher adsorption capacity for HMs (except Pb) compared to Biochar-ERC-1. This suggests that excessive addition of shell-derived biochar can affect the adsorption of Pb to some extent. The removal of Pb in wastewater is not particularly increased with biochar addition, which may be due to the complex existence state of Pb ions in aqueous solution, the selectivity and efficiency limitations of biochar, as well as the influence of other factors in the wastewater [34]. Therefore, in practical applications, we need to integrate multiple treatment methods according to the specific composition and conditions of the wastewater to achieve the best removal efficacy.

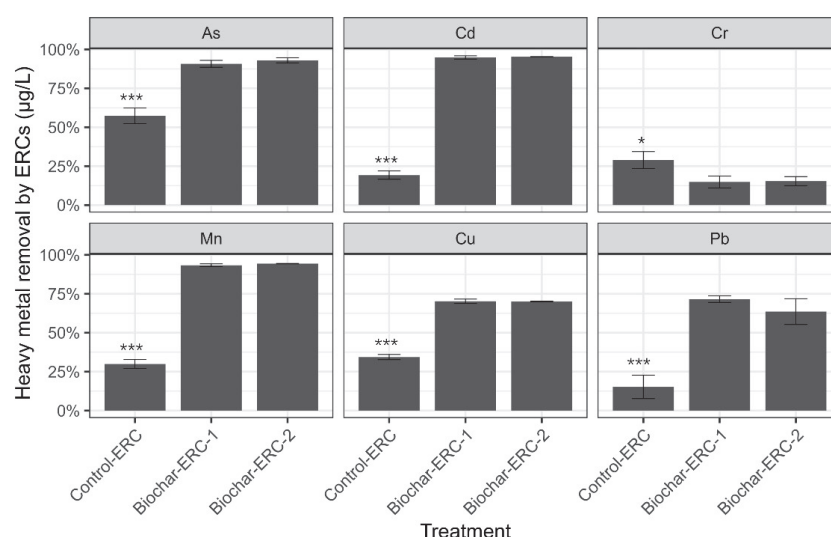


Figure 8. Heavy metal removal by ERCs in the filtration experiment. Note: The symbols * and *** are used to denote statistical comparisons between groups; a significant difference is considered when $p < 0.05$ (*), and a highly significant difference is considered when $p < 0.001$ (***).

Figure 9 illustrates the alterations in pH, DO, and conductivity observed in the filtration experiment. The use of concrete for filtration led to an increase in the effluent's pH, while the incorporation of biochar into the concrete had a negligible impact on the effluent's pH. Additionally, the application of concrete for filtration resulted in an elevation of effluent conductivity and a reduction in DO content. However, the introduction of biochar caused a decrease in both effluent conductivity and DO content.

In regions such as southern China, the southeast coast, and the middle and lower reaches of the Yangtze River, high precipitation leads to the easy leaching of alkaline substances from the soil, ultimately resulting in a predominantly acidic or strongly acidic soil pH level [35]. Concrete filtration can elevate the pH value of the water, making ERCs a promising material for use in these areas. By neutralizing soil acidity, it can improve the local soil environment, which helps optimize the growing conditions for crops and promotes healthy plant growth, ultimately boosting agricultural yield and quality. Overall, eco-recycled concrete with shell-derived biochar exhibits significant effects on the control of heavy metal pollution in water bodies, which is of positive significance for environmental protection and human health.

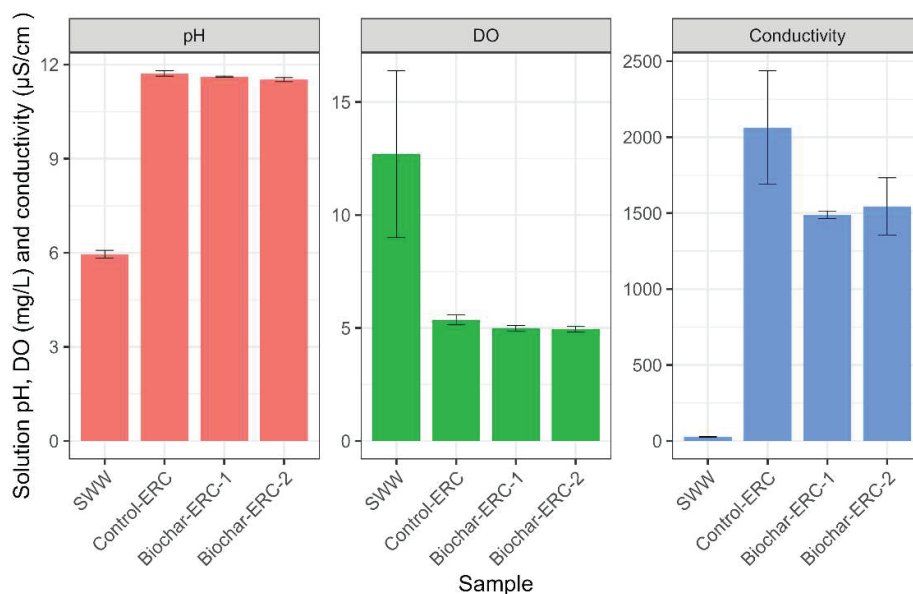


Figure 9. Variation of relevant parameters of solution samples in wastewater filtration experiments with ERCs.

3.4. Limitations of the Preliminary Study

This preliminary study mainly focused on the permeability, porosity, and adsorption efficiency of ERCs. To further enhance its comprehensiveness, additional analyses such as the durability of ERC blocks, their long-term effectiveness, temperature resistance, and potential side effects should be incorporated, especially considering their practical application in different environmental conditions.

4. Conclusions

Shell-derived biochar and aggregate recycled from construction waste were shown to be cost-effective additives in concrete for improving its performance in multiple aspects. The biochar significantly increased the water permeability coefficients and the continuous porosity of the ERCs. It also significantly enhanced the adsorption efficiency of the concrete for removing HMs from wastewater. Furthermore, filtration with ERCs increased the pH and demonstrated a stable performance in maintaining the acid–base balance of water, which is particularly suitable for regions with acidic soils, such as southern China, the southeast coast, and the middle and lower reaches of the Yangtze River. Overall, the addition of shell-derived biochar greatly broadens the application potential of ERCs in the field of water treatment and ecological restoration. As technology advances and the scope of application expands, this innovative material is poised to play an increasingly important role in environmental protection and sustainable development.

Author Contributions: Conceptualization, J.L., S.S., Y.R. and X.L.; methodology, J.L., S.S., Y.R. and X.L.; software, J.L.; validation, Y.R., X.L., J.W., R.L. and S.L.; formal analysis, J.L., Y.R., X.L., X.Y. and J.W.; investigation, J.L., Y.R., X.L., J.W., R.L., S.L. and X.Y.; resources, J.L. and S.S.; data curation, J.L. and S.S.; original draft preparation, J.L., Y.R., X.L., J.W., R.L. and S.L.; writing—review and editing, J.L. and S.S.; visualization, J.L., S.S., Y.R. and X.L. supervision, J.L. and S.S.; project administration, J.L. and S.S.; funding acquisition, J.L. All authors have read and agreed to the published version of the manuscript.

Funding: This work was supported by the Environmental Research Institute Liu Jing Young Scholar Future Plan at Shandong University; project ZR2021QD019 supported by Shandong Provincial Natural Science Foundation; the National Natural Science Foundation of China (42207325), and Shandong University School-Level Innovation Training Project (2023099).

Data Availability Statement: Data are contained within the article.

Acknowledgments: The authors thank Chengjia Zhang and Sen Wang of the Core Facilities for Life and Environmental Sciences, State Key laboratory of Microbial Technology of Shandong University for their help respectively in analyzing the concentrations of heavy metals in solution samples with ICP-MS (NexION 1000G) and surface characterization of biochar with SEM (ZEISS Crossbeam 550, Germany).

Conflicts of Interest: The authors declare no competing financial interests.

References

1. Solecki, W.; Friedman, E. At the Water's Edge: Coastal Settlement, Transformative Adaptation, and Well-Being in an Era of Dynamic Climate Risk. *Annu. Rev. Public Health* **2021**, *42*, 211–232. [CrossRef] [PubMed]
2. Li, Y.; Zhou, Q.; Ren, B.; Luo, J.; Yuan, J.; Ding, X.; Bian, H.; Yao, X. Trends and Health Risks of Dissolved Heavy Metal Pollution in Global River and Lake Water from 1970 to 2017. In *Reviews of Environmental Contamination and Toxicology*; Springer: Berlin/Heidelberg, Germany, 2019; Volume 251, pp. 1–24. [CrossRef]
3. Chen, S.; Zhou, J.; Liu, J.; Bie, Y.; Hu, Q. Sustainable ecological pervious concrete (SEPC) based on modified corn-cob coarse aggregate: Crushing morphology, strength, pore properties, and durability. *Constr. Build. Mater.* **2024**, *426*, 136194. [CrossRef]
4. Shi, Q.; Xiong, Y.; Kaur, P.; Sy, N.D.; Gan, J. Contaminants of emerging concerns in recycled water: Fate and risks in agroecosystems. *Sci. Total. Environ.* **2022**, *814*, 152527. [CrossRef] [PubMed]
5. Sodhi, K.K.; Mishra, L.C.; Singh, C.K.; Kumar, M. Perspective on the heavy metal pollution and recent remediation strategies. *Curr. Res. Microb. Sci.* **2022**, *3*, 100166. [CrossRef]
6. Yang, D.; Yang, Y.; Xia, J. Hydrological cycle and water resources in a changing world: A review. *Geogr. Sustain.* **2021**, *2*, 115–122. [CrossRef]
7. Li, S.; Li, S.; Wen, N.; Wei, D.; Zhang, Y. Highly effective removal of lead and cadmium ions from wastewater by bifunctional magnetic mesoporous silica. *Sep. Purif. Technol.* **2021**, *265*, 118341. [CrossRef]
8. Zhang, Y.; Chen, J.; Ji, H.; Xiao, Z.-G.; Shen, P.; Xu, L.-H. Protective effects of Danshen injection against erectile dysfunction via suppression of endoplasmic reticulum stress activation in a streptozotocin-induced diabetic rat model. *BMC Complement. Altern. Med.* **2018**, *18*, 1–12. [CrossRef]
9. Wang, L.; Deng, J.; Yang, X.; Hou, R.; Hou, D. Role of biochar toward carbon neutrality. *Carbon Res.* **2023**, *2*, 2. [CrossRef]
10. Tang, B.; Xu, H.; Song, F.; Ge, H.; Chen, L.; Yue, S.; Yang, W. Effect of biochar on immobilization remediation of Cd-contaminated soil and environmental quality. *Environ. Res.* **2022**, *204*, 111840. [CrossRef]
11. Liu, Z.; Xu, Z.; Xu, L.; Buyong, F.; Chay, T.C.; Li, Z.; Cai, Y.; Hu, B.; Zhu, Y.; Wang, X. Modified biochar: Synthesis and mechanism for removal of environmental heavy metals. *Carbon Res.* **2022**, *1*, 8. [CrossRef]
12. Zhang, W.; Qiu, X.; Wang, C.; Zhong, L.; Fu, F.; Zhu, J.; Zhang, Z.; Qin, Y.; Yang, D.; Xu, C.C. Lignin derived carbon materials: Current status and future trends. *Carbon Res.* **2022**, *1*, 14. [CrossRef]
13. Kumar, S.S.; Murugesan, R.; Sivaraja, M.; Athijayamani, A. Innovative Eco-Friendly Concrete Utilizing Coconut Shell Fibers and Coir Pith Ash for Sustainable Development. *Sustainability* **2024**, *16*, 5316. [CrossRef]
14. Mahedi, M.; Dayioglu, A.Y.; Cetin, B.; Jones, S. Remediation of acid mine drainage with recycled concrete aggregates and fly ash. *Environ. Geotech.* **2020**, *11*, 15–28. [CrossRef]
15. Senadheera, S.S.; Gupta, S.; Kua, H.W.; Hou, D.; Kim, S.; Tsang, D.C.; Ok, Y.S. Application of biochar in concrete—A review. *Cem. Concr. Compos.* **2023**, *143*, 105204. [CrossRef]
16. Liu, J.; Su, J.; Zhao, Z.; Feng, W.; Song, S. Treatment of Wastewater Effluent with Heavy Metal Pollution Using a Nano Ecological Recycled Concrete. *Water* **2022**, *14*, 2334. [CrossRef]
17. Winters, D.; Boakye, K.; Simske, S. Toward Carbon-Neutral Concrete through Biochar–Cement–Calcium Carbonate Composites: A Critical Review. *Sustainability* **2022**, *14*, 4633. [CrossRef]
18. Revathi, S.; Tania, D.A.E.; Shadin, S.A.; Keerthana, J. Effect of zeolite and bamboo biochar as CO₂ absorbant in concrete. *Carbon Res.* **2024**, *3*, 1–15. [CrossRef]
19. Chen, L.; Zhu, X.; Zheng, Y.; Wang, L.; Poon, C.S.; Tsang, D.C. Development of high-strength lightweight concrete by utilizing food waste digestate based biochar aggregate. *Constr. Build. Mater.* **2023**, *411*, 134142. [CrossRef]
20. Zhang, J.; Guan, K.; Peng, B.; Pan, M.; Zhou, W.; Jiang, C.; Kimm, H.; Franz, T.E.; Grant, R.F.; Yang, Y.; et al. Sustainable irrigation based on co-regulation of soil water supply and atmospheric evaporative demand. *Nat. Commun.* **2021**, *12*, 5549. [CrossRef]
21. Singhal, S. Biochar as a cost-effective and eco-friendly substitute for binder in concrete: A review. *Eur. J. Environ. Civ. Eng.* **2023**, *27*, 984–1009. [CrossRef]
22. Sinyoung, S.; Jeeraro, A.; Udomkun, P.; Kunchariyakun, K.; Kaewlom, P. Transformative innovations in nano-biochar-enhanced porous concrete: Elevating engineering performance and pollutant removal. *Dev. Built Environ.* **2024**, *18*, 100469. [CrossRef]
23. Xu, W.; Zhang, Y.; Li, M.; Qu, F.; Poon, C.S.; Zhu, X.; Tsang, D.C. Durability and micromechanical properties of biochar in biochar-cement composites under marine environment. *J. Clean. Prod.* **2024**, *450*, 141842. [CrossRef]
24. Acarturk, B.C.; Jungclaus, M.A.; Torres, M.; Lash, B.; Srubar, W.V., III. Effect of algal biomass on the properties of calcium sulfoaluminate cement. *ACS Sustain. Chem. Eng.* **2024**, *12*, 8690–8701. [CrossRef]

25. Pahlavan, F.; Kaur, H.; Ackerman-Biegasiewicz, L.K.; Lamanna, A.; Fini, E.H. Application of algal biochar to prevent leachate of heavy metals from mine tailings. *Resour. Conserv. Recycl.* **2024**, *210*, 107810. [CrossRef]
26. Zhang, Y.; Xu, H.; Fang, S.; Li, D.; Xue, W.; Chen, B.; Zhao, L. Biochar as additive for improved building performances and heavy metals solidification of sediment-based lightweight concrete. *Environ. Sci. Pollut. Res.* **2022**, *30*, 4137–4150. [CrossRef]
27. Chen, S.; Wang, Y.; Dai, W.; Yang, H.; Wang, D.; Lv, Y. Recycled aggregate porous concrete: Pore structure, clogging properties and models. *Constr. Build. Mater.* **2024**, *417*, 135344. [CrossRef]
28. GB8978-1996; Integrated Wastewater Discharge Standard. Ministry of Ecology and Environment of the People's Republic of China: Beijing, China, 1996. Available online: <https://www.mee.gov.cn/ywgz/fgbz/bz/bzwb/shjbh/swrwpfbz/199801/W020061027521858212955.pdf> (accessed on 15 December 2024).
29. Tan, K.; Qin, Y.; Du, T.; Li, L.; Zhang, L.; Wang, J. Biochar from waste biomass as hygroscopic filler for pervious concrete to improve evaporative cooling performance. *Constr. Build. Mater.* **2021**, *287*, 123078. [CrossRef]
30. GB 5084-2021; Standard for Irrigation Water Quality. Ministry of Ecology and Environment of the People's Republic of China: Beijing, China, 2021. Available online: <https://www.mee.gov.cn/ywgz/fgbz/bz/bzwb/shjbh/shjzlbz/202102/W020230908393378970360.pdf> (accessed on 15 December 2024).
31. Ukhurebor, K.E.; Aigbe, U.O.; Onyancha, R.B.; Nwankwo, W.; Osibote, O.A.; Paumo, H.K.; Ama, O.M.; Adetunji, C.O.; Siloko, I.U. Effect of hexavalent chromium on the environment and removal techniques: A review. *J. Environ. Manag.* **2021**, *280*, 111809. [CrossRef]
32. GracePavithra, K.; Jaikumar, V.; Kumar, P.S.; SundarRajan, P. A review on cleaner strategies for chromium industrial wastewater: Present research and future perspective. *J. Clean. Prod.* **2019**, *228*, 580–593. [CrossRef]
33. Peng, H.; Guo, J. Removal of chromium from wastewater by membrane filtration, chemical precipitation, ion exchange, adsorption electrocoagulation, electrochemical reduction, electrodialysis, electrodeionization, photocatalysis and nanotechnology: A review. *Environ. Chem. Lett.* **2020**, *18*, 2055–2068. [CrossRef]
34. Wang, Z.; Luo, P.; Zha, X.; Xu, C.; Kang, S.; Zhou, M.; Nover, D.; Wang, Y. Overview assessment of risk evaluation and treatment technologies for heavy metal pollution of water and soil. *J. Clean. Prod.* **2022**, *379*, 134043. [CrossRef]
35. Han, T.-F.; Liu, K.-L.; Huang, J.; Ma, C.-B.; Zheng, L.; Wang, H.-Y.; Qu, X.-L.; Ren, Y.; Yu, Z.-K.; Zhang, H.-M. Spatio-temporal evolution of soil pH and its driving factors in the main Chinese farmland during past 30 years. *J. Plant Nutr. Fertil.* **2020**, *26*, 2137–2149.

Disclaimer/Publisher's Note: The statements, opinions and data contained in all publications are solely those of the individual author(s) and contributor(s) and not of MDPI and/or the editor(s). MDPI and/or the editor(s) disclaim responsibility for any injury to people or property resulting from any ideas, methods, instructions or products referred to in the content.

Article

Sewage Vertical Infiltration Introduced Polygenic Multipollutants into Groundwater

Yihan Dong ¹, Yifan Han ², Xu Han ³, Yaoxuan Chen ^{4,*} and Yuanzheng Zhai ^{2,*}

¹ School of Water Resources and Environment, China University of Geosciences (Beijing), Beijing 100083, China; dongyihan101@163.com

² College of Water Sciences, Beijing Normal University, Beijing 100875, China; 201921470006@mail.bnu.edu.cn

³ Department of Ecology and Environment of Heilongjiang Province, Harbin 150090, China; 18545596886@163.com

⁴ China Institute of Geo-Environmental Monitoring, Beijing 100081, China

* Correspondence: chenyaoyuan92@163.com (Y.C.); zyz@bnu.edu.cn (Y.Z.); Tel.: +86-010-81134888 (Y.C.); +86-010-58802736 (Y.Z.)

Abstract: With the increasing environmental impacts of human activities, the problem of polygenic multipollutants in groundwater has attracted the attention of researchers. Identifying the hydrobiogeochemical characteristics of the surface sewage that replenishes groundwater is crucial to addressing this problem. The input of polygenic multipollutants into groundwater leads to not only the mechanical superposition of pollutants but also the formation of secondary pollutant types. The evolution of polygenic multipollutants is influenced by aquifer characteristics, carbon sources, microbial abundance, etc. Therefore, this study took a sewage leakage point in Northwest China as the research object, carried out a controlled laboratory experiment on the impact of sewage discharge on groundwater, and, combined with long-term field monitoring results, determined the main hydrobiogeochemical processes of polygenic multipollutants and their secondary pollutants. The results showed that the redox environment and the gradient change in pH were identified as the most critical controlling factors. In oxidative groundwater during the early stage of vertical infiltration, sewage carries a substantial amount of NH_4^+ , which is oxidized to form the secondary pollutant NO_3^- . As O_2 is consumed, the reduction intensifies, and secondary pollutants NO_3^- , Mn (IV), and Fe(III) minerals are successively reduced. Compared with the natural conditions of rainwater vertical infiltration, the reaction rates and intensities of various reactions significantly increase during sewage vertical infiltration. However, there is a notable difference in the groundwater pH between sewage and rainwater vertical infiltration. In O_2 and secondary pollutant NO_3^- reduction, a large amount of CO_2 is rapidly generated. Excessive CO_2 dissolves to produce a substantial amount of H^+ , promoting the acidic dissolution of Mn (II) minerals and generation of Mn^{2+} . Sewage provides a higher carbon load, enhancing Mn (II) acidic dissolution and stimulating the activity of dissimilatory nitrate reduction to ammonium, which exhibits a higher contribution to NO_3^- reduction. This results in a portion of NO_3^- converted from NH_4^+ being reduced back to NH_4^+ and retained in the groundwater, reducing the denitrification's capacity to remove secondary NO_3^- . This has important implications for pollution management and groundwater remediation, particularly monitored natural attenuation.

Keywords: polygenic pollution; multipollutant; geogenic pollutant; DNRA; autotrophic reduction

1. Introduction

With the increase in human activities, the issue of groundwater composite pollution caused by pollutants from various sources during the vertical replenishment of surface sewage into aquifers has garnered more attention [1,2]. In this paper, pollutants from different sources (natural and anthropogenic sources) and components (natural and anthropogenic components) are called polygenic multipollutants. The input of polygenic

multipollutants leads to a direct overlay of pollutant components in the groundwater system. Interactions occur among pollutants from different sources, between the aquifer and groundwater, and between the aquifer and pollutants, generating new soluble components and, thus, forming secondary pollutants [3,4]. Groundwater pollution in many regions worldwide has been characterized by polygenic sources [5,6] by primarily focusing on natural sources, namely, Fe, Mn [4], and anthropogenic sources (i.e., NH_4^+ and NO_3^-) [7,8]. The interactions among groundwater, polygenic multipollutants, and aquifer media are very complex and are regulated by factors such as lithology, recharge, environmental conditions, and microbial activity [9]. Identifying the hydrobiogeochemical characteristics of the surface sewage that replenishes groundwater is crucial to addressing this problem.

In the process of localized concentrated vertical infiltration of polygenic multipollutants, the presence of sewage carrying abundant organic carbon, organic nitrogen, and inorganic nitrogen leads to complex hydrogeochemical reactions [10,11]. Water–rock interactions, adsorption processes, and biogeochemical processes primarily govern these reactions. The control factors include the permeability of the aquifer media, the content of humic substances, redox conditions, and acidity [9]. The permeability of aquifer media can influence the retention time of groundwater, affecting the storage capacity of pollutant components in the aquifer media. Prolonged filtration processes result in significant cation exchange adsorption [12,13]. Humic substances in aquifer media can provide a substantial carbon source. During the process of sewage vertical recharge aquifers, the input of organic carbon can influence the diversity and activity of micro-organisms, triggering biogeochemical processes in carbon cycling, such as the degradation of organic matter and nitrogen transformation [14]. Additionally, nitrogen compounds, such as amino acids, may be present in humic substances, participating in nitrogen biogeochemical processes. Micro-organisms can utilize these nitrogen compounds in reactions such as nitrification, denitrification, and dissimilatory nitrate reduction to ammonium (DNRA) [15,16], influencing the morphological transformation of nitrogen [17].

Under natural conditions, with the increase in dissolved oxygen (DO) content in the aquifer medium under oxidation conditions, nitrification plays a leading role, and NH_4^+ is oxidized to NO_3^- , accompanied by the decomposition of organic matter [5,18]. As oxygen is consumed, the system gradually shifts to a reducing environment, and the prominence of denitrification increases, reducing NO_3^- to produce N_2 and NH_4^+ [19]. The acidity (pH) of the aquifer media is a crucial factor controlling the strength of water–rock interactions. Under acidic conditions, water–rock interactions intensify, increasing the concentration of inorganic ions in groundwater. These conditions may also induce the acidic dissolution of metal minerals such as Fe and Mn, increasing their concentrations in groundwater [17,19]. In addition, under natural conditions, along the vertical infiltration direction of water, REDOX conditions, pH, and carbon load form a gradient. Under the action of micro-organisms, carbon sources provide electrons, and O_2 , NO_3^- , Mn(IV), and Fe(III) [14] are successively reduced to form a sequential REDOX zone. However, the introduction of wastewater containing large amounts of COD and NH_4^+ changes the sequential REDOX process. The initial oxidation of NH_4^+ generates NO_3^- , which leads to the increase of NO_3^- concentration and promotes denitrification. The large amount of H^+ produced in this process can change the pH value of the aquifer medium [20,21]. Prolonged nitrification can shift the reaction zone of Mn(IV) and Fe(III) backward [22,23].

Hydrochemical tracing and laboratory simulation inversion are the most commonly used methods for identifying polygenic multipollutants [21,24]. Cao, X. et al. demonstrated through leaching experiments that Flood irrigation increases the release of phosphorus from aquifer sediments into groundwater [25], and Zhai, Y. et al. confirmed through leaching experiments that anthropogenic organic pollutants in groundwater increase the release of Fe and Mn from aquifer sediments [18]. In the field, hydrochemical tracing is used as a basis, and specific experiments are conducted indoors to simulate inversion based on polygenic multipollutants [19]. This approach identifies the main geochemical processes and their impact intensity, providing a scientific basis for the management and remediation

of groundwater. In a specific location in a desert in Northwest China with a concentrated leakage of multiple pollutants, research, based on long-term monitoring, was conducted and revealed interactions between trivalent nitrogen and manganese in groundwater. Sewage discharge significantly affected the types and concentrations of solute components in groundwater. The oxidation of exogenous organic nitrogen triggering the reductive dissolution of manganese was identified as the main mechanism for the increase in Mn^{2+} in groundwater. Additionally, under conditions of $\text{DO} > 2 \text{ mg/L}$, chemolithoautotrophic denitrification and nitrate heterotrophic reduction to ammonium were identified as the main mechanisms for NO_3^- attenuation [10].

To further explore the vertical leakage impact of polygenic multipollutants in the desert on groundwater, this study conducted indoor simulation experiments to (1) simulate the impact of sewage discharge on groundwater through controlled laboratory experiments, (2) supplement and validate previous field observation results based on conclusions drawn from experiments, and (3) analyze the influencing mechanisms from physical and chemical perspectives. The research results provide insights into local groundwater management and remediation planning strategies.

2. Materials and Methods

2.1. Study Area

The study area is located in Northwest China (Figure S1). The topography of the study area slopes from the southwest to the northeast, with slopes ranging from 5 to 9‰ and consisting of relatively flat terrain. The climate of the study area is a temperate continental arid climate, with an average annual precipitation of 160 mm, average annual evaporation of 2000 mm, and 2800 h of sunshine annually. Groundwater types include unconfined aquifers in the south and confined aquifers in the north. The groundwater flow direction is from southeast to northwest, and the main aquifer lithology consists of fine sand, silty fine sand, coarse sand, and sandy gravel from the Middle–Upper Pleistocene. The groundwater depth is about 15 m. Groundwater replenishment around the contamination site is mainly from lateral runoff from the southeast to the northwest. The hydraulic gradient is 3‰, moving from the contaminated site to the downstream northern zone. The permeability coefficient of the aquifer is between 6.44 and 13.0 m/d. Groundwater recharge primarily occurs through surface water infiltration, and fractured water from mountain bedrock serves as lateral replenishment. Groundwater discharge is mainly through lateral outflow, with minimal and dispersed artificial extraction and low water consumption.

2.2. Pollution Incident and Field Monitoring

Based on the field investigation, it was found that from 28 May 2014 to 6 March 2015, 209,800 cubic meters of sewage was discharged through a pipeline, resulting in pollution at three sites of varying sizes (designated as #1, #2, and #3 in Figure S1). The discharge volumes for sites #1, #2, and #3 were 74,700, 129,000, and 6100 cubic meters, respectively [10]. The investigation revealed that the main pollutants in the sewage discharged at the three contaminated sites were biodegradable organic nitrogen (represented by COD_{Mn}) and ammonia nitrogen (measured as $\text{NH}_4^+\text{-N}$), with concentrations ranging from 1956 to 2935 mg/L and 625 to 638 mg/L, respectively [10]. The Mn concentration in the sewage was below the detection limit. Long-term monitoring from 15 June 2015 to 1 June 2021 indicated that the discharge of high COD and ammonia nitrogen sewage severely affected the concentrations of hydrogeochemical components in the groundwater at the three polluted sites, as well as the types of hydrogeochemical components present (Figure 1). Specifically, the COD, NH_4^+ , and NO_2^- levels in the groundwater at the three sites were significantly higher than the background values, while the concentrations of NO_3^- and DO were lower. Mn, which was undetectable in the background groundwater, reached a maximum concentration of 1.64 mg/L in the groundwater at the three polluted sites.

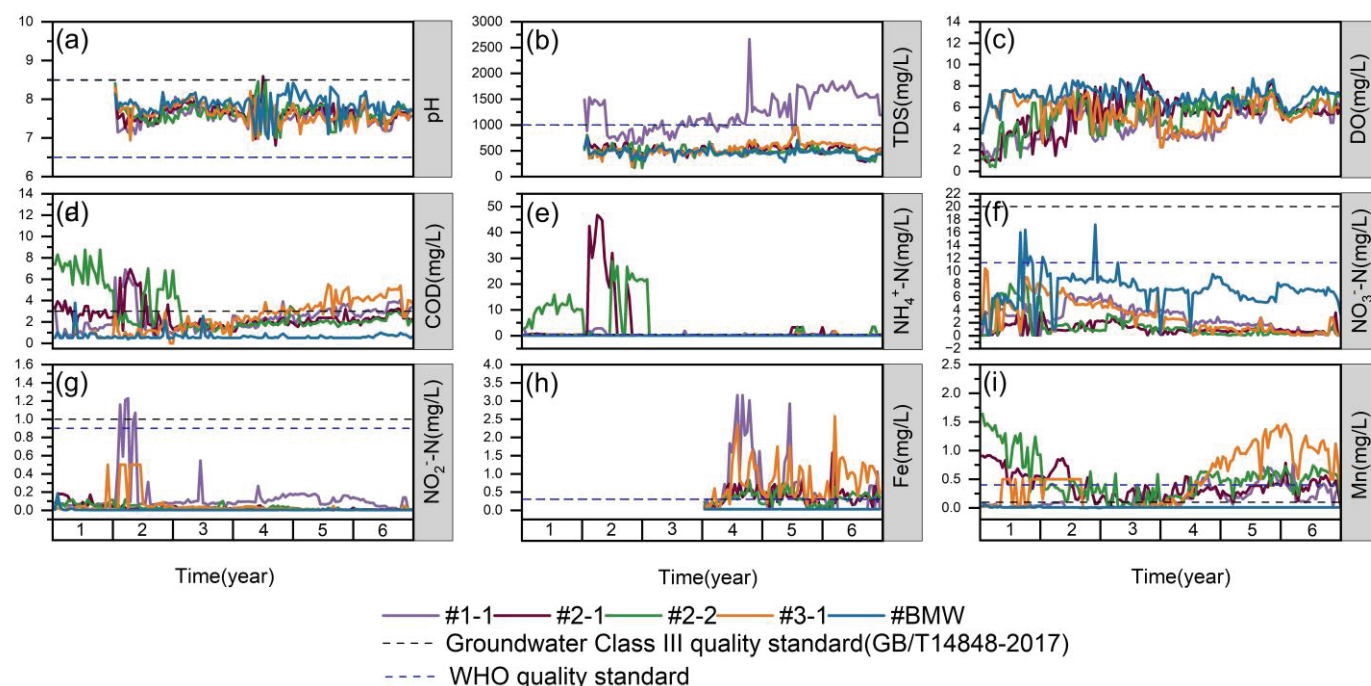


Figure 1. Temporal variations of groundwater monitoring indicators over six years for five wells. (a) pH; (b) TDS; (c) DO; (d) COD; (e) $\text{NH}_4^+\text{-N}$; (f) $\text{NO}_3^-\text{-N}$; (g) $\text{NO}_2^-\text{-N}$; (h) Fe; (i) Mn.

2.3. Laboratory Experiment

2.3.1. Sample Collection and Determination

To further investigate the impact of vertically infiltrating pollutants on groundwater and provide additional insights into the observed field phenomena, laboratory-controlled experiments were conducted to simulate the effects of sewage vertical infiltration on groundwater [24,25]. The soil sample collection and preservation for this experiment strictly followed the China's quality standards (GB/T 36197-2018) [26]. The soil samples, categorized as spatially mixed samples, were collected from the polluted sites (#1, #2, #3 in Figure S1) and uncontaminated background sites (#BMW in Figure S1). The sampling depth is 8–10 m in the unsaturated zone and 18–20 m in the saturated zone. For comparative analysis, two sets of saturated aquifer samples were collected from the polluted sites, and two sets were collected from the uncontaminated background sites, resulting in a total of four sample groups. After collection, the samples were sealed in pre-prepared plastic bags and stored under low-temperature refrigeration conditions before being transported to the laboratory for analysis [5,27].

To improve the understanding of the mineral composition of the saturated aquifer samples and facilitate the analysis of potential biogeochemical processes during sewage leaching, the collected soil samples were air-dried and ground to pass through a 200-mesh sieve [22]. The sieved soil samples were sealed in plastic bags for further use. Using the required procedures, the laboratory pre-treated the samples and determined the metal element composition (Table S1) and mineral components (Figure S2). The elemental content in the samples was determined using inductively coupled plasma atomic emission spectrometry (ICP-AES). Mineral phase analysis was conducted using X-ray diffraction [13,28].

To avoid interference from other chemical components, the water samples used in this experiment were untreated source water samples collected in the study area [10]. For comparative purposes, two types of source water were used in this experiment: sewage from the sewage treatment system of the sewage discharge plant in the study area and local rainwater, with the rainwater samples collected and mixed during months of highest precipitation (Jun–Sep). All water samples were sealed on-site and immediately placed in an insulated box with ice, transported to the laboratory within 1 h, and stored in a refrigerator at 4 °C until testing [24].

To facilitate the comparative analysis of concentration changes in various components during the experiment, the initial concentrations of each chemical component in the experimental water (sewage and rainwater) were measured before the experiment (Table S2) [29]. To accurately and comprehensively characterize the local pollution situation, the selection of detection indicators in the experiment was based on the 'Groundwater Quality Standards (GB/T14848-2017) [30] in China, the WHO quality standard [31] and the current status of groundwater quality in the study area, and other considerations [29]. The overall selection principle covered conventional indicators, macro-soluble components, and "bottleneck" indicators affecting groundwater quality levels, anticipating and emphasizing potentially harmful chemical components. The selected detection indicators included K^+ , Na^+ , Ca^{2+} , Mg^{2+} , SO_4^{2-} , Cl^- , NH_4^+-N , NO_3^--N , NO_2^--N , COD, pH, Al, As, Fe, Mn, P, Zn, and 10 other indicators. The detection of COD, NH_4^+-N , NO_3^--N , NO_2^--N , pH, Fe, and Mn was using the recommended methods in the "Groundwater Quality Standards" (Table S3). Inorganic ion indicators such as K^+ , Na^+ , Ca^{2+} , and Mg^{2+} were tested using ion chromatography, and Al, As, and P were determined using inductively coupled plasma atomic emission spectrometry [30].

2.3.2. Experimental Procedure

Cao, X. et al. demonstrated through leaching experiments that flood irrigation increases the release of phosphorus from aquifer sediments into groundwater [25], and Zhai, Y. et al. confirmed through leaching experiments that anthropogenic organic pollutants in groundwater increase the release of Fe and Mn from aquifer sediments [18]. Therefore, to determine the impact of polygenic multipollutants inputs on the concentration changes in various chemical components in groundwater, leaching experiments were conducted to simulate this process. The leaching experiment was performed in the laboratory by using a conical flask shaking experiment setup (Figure S3). Under dark conditions, with temperature controlled between 10 and 15 °C, sewage samples (or rainwater samples) and groundwater samples were added to a 250 mL conical flask at a water-to-soil ratio of 10:1 [27]. The conical flask was shaken and transferred to a centrifuge, where it was centrifuged at a speed of 4000 rpm for 10 min. After centrifugation, the filtrate was obtained by filtering through a 0.45 μm water-based filter membrane to remove impurities; this filtrate was used for water chemical testing [18]. All glassware used in the experiment was first acid-treated, rinsed with pure water, and air-dried. To achieve the research objectives, four combinations of experiments were conducted. The control experiment combinations and control conditions are shown in Table S4. In each group, 13 conical flasks were used for testing the groundwater samples, equivalent to 13 sampling times, with sampling times at 10 and 30 min and 1, 2, 4, 6, 8, 10, 14, 18, 24, 48, and 72 h. To ensure data quality, parallel sampling was conducted at each sampling point.

To identify the changes in concentration of each component during the experiment, we monitored the concentrations of various components in the leachate at specific times during the experiment [24]. Immediately after sampling, the experimental effluent samples were subjected to water chemical testing. Because of the physicochemical changes that might occur in the leaching experiment, the detection indicators and methods were consistent with the 17 detection indicators in the original water [31]. All analysis procedures fulfilled the quality requirements, with a test conducted for every 26 samples. The error of the indicative standard sample was less than 5%, and the qualification rate was 100%.

3. Results

3.1. Variations in the Concentrations of Nitrogen

The initial concentration of NH_4^+ in rainwater was 2.64 mg/L (Table S2). Under the leaching action of rainwater, the concentration of NH_4^+ in the leachate from the contaminated site samples increased. The rate of increase was initially rapid but plateaued after reaching a certain concentration, indicating a saturated leaching state, and the NH_4^+ concentration in the leachate reached 6.37 ± 0.11 mg/L by the end of leaching. In contrast,

the NH_4^+ concentration in the leachate from the background site samples remained stable throughout the leaching process, showing no significant changes (Figure 2a). The initial NH_4^+ concentration in the wastewater was 86.2 mg/L (Table S2), and the concentration in the leachate from the contaminated site samples exhibited a trend of initially increasing, then decreasing, and increasing again. Throughout the leaching period, the concentration of the leachate was mostly slightly higher than the initial concentration, reaching 89.58 ± 0.44 mg/L at the end of leaching. The concentration of NH_4^+ in the leachate from the background soil layers showed a fluctuating downward trend. It decreased rapidly in the early stages of leaching, continued to fluctuate until it stabilized, and the overall concentration of NH_4^+ in the leachate was lower than the initial concentration, concluding at 79.9 ± 2.50 mg/L at the end of leaching (Figure 2b).

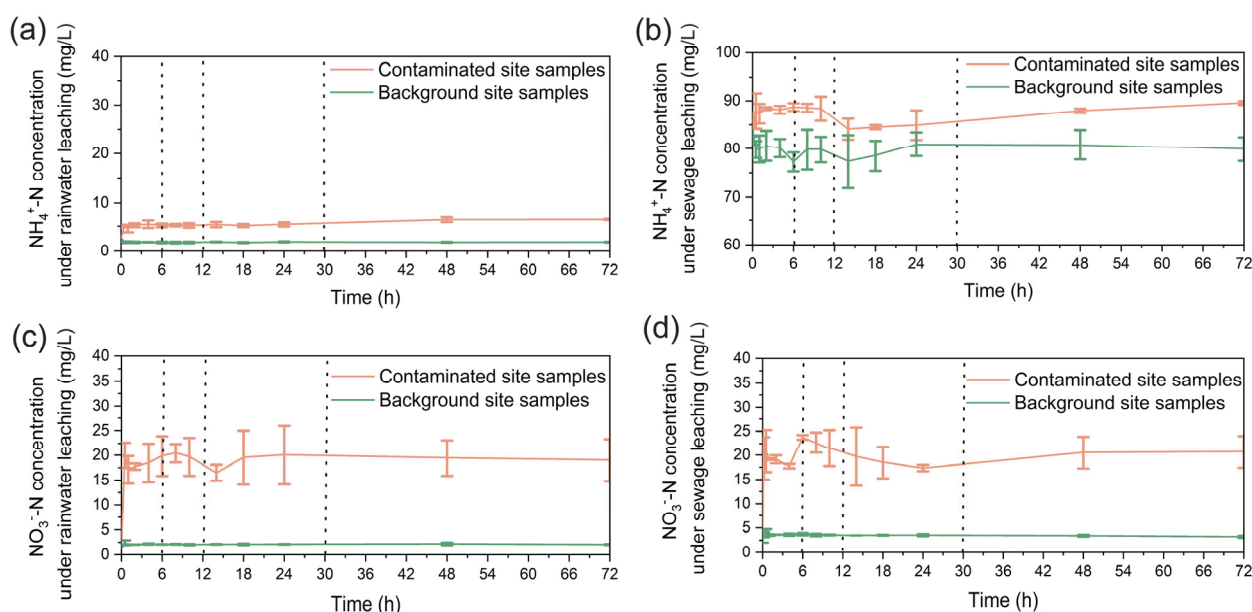


Figure 2. Variations in nitrogen concentrations during the filtration of two types of source water in the contaminated and background environments. (a) Changes in NH_4^+ concentration during rainwater filtration. (b) Variations in NH_4^+ concentration during sewage filtration. (c) Alterations in NO_3^- concentration during rainwater filtration. (d) Changes in NO_3^- concentration during sewage filtration. Each value represented as mean \pm SD, samples size ($n = 4$), * $p < 0.05$. The significance of the grades was calculated with the Kruskal–Wallis test.

The initial concentration of NO_3^- in rainwater was 1.15 mg/L (Table S2). Leaching by rainwater significantly increased the concentration of NO_3^- in the leachate from contaminated site samples, with a substantial rise in the early phase of leaching. As time progressed, the concentration fluctuated within a certain range before eventually stabilizing. In contrast, the increase in NO_3^- concentration in the leachate from the background site samples was minimal, maintaining a stable range between 2 and 2.5 mg/L (Figure 2c). The initial concentration of NO_3^- in wastewater was 2.01 mg/L (Table S2). During the leaching period, the concentration of NO_3^- in the leachate from contaminated site samples rose significantly, whereas the leaching effect in the background site samples was not pronounced. The concentration of NO_3^- in the leachate from the contaminated soil layers fluctuated and overall increased, reaching 20.71 ± 3.31 mg/L by the end of leaching. In the leachate from the background soil layers, the concentration of NO_3^- initially rose slightly and then remained stable, concluding at 3.20 ± 0.19 mg/L at the end of leaching (Figure 2d).

3.2. Variations in the Concentrations of pH/Ca/Mg

The pH of the rainwater was 7.2 (Table S2). When leaching through the contaminated site samples, the pH initially fluctuated significantly before gradually rising to a stable

equilibrium of 7.82 ± 0.13 . The pH trend during leaching at the background site samples was similar to that of the contaminated site samples, but the overall pH was higher, stabilizing at 7.93 ± 0.11 (Figure 3a). The pH of the wastewater was 6.8 (Table S2), showing a similar pattern during leaching through the contaminated site samples: an initial significant fluctuation followed by a gradual rise to a stable equilibrium of 7.53 ± 0.07 . The pH trend during leaching at the background site samples paralleled that of the contaminated site samples, albeit slightly higher, stabilizing at 7.75 ± 0.06 (Figure 3b).

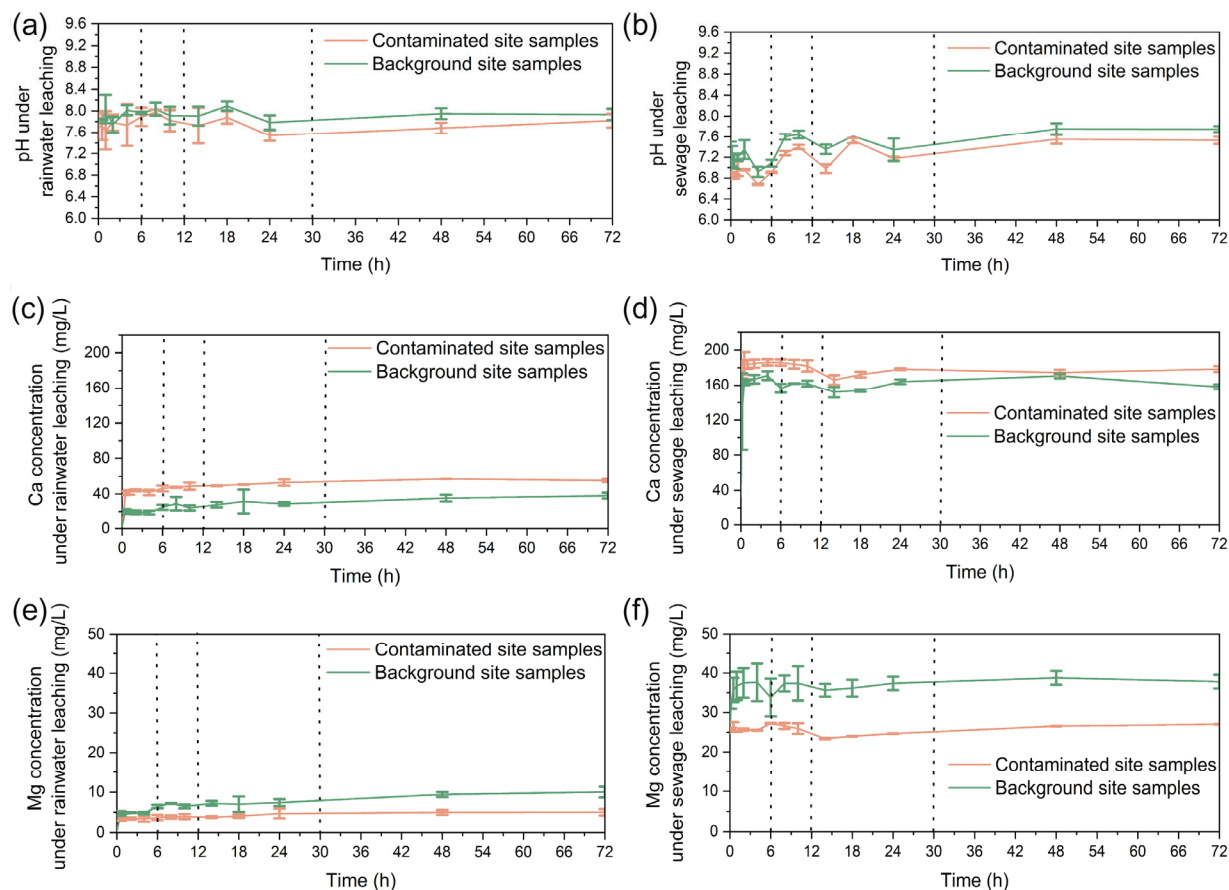


Figure 3. Changes in pH and inorganic ion concentrations during the filtration of two types of source water in the contaminated and background environments. Changes in (a) pH during rainwater filtration; (b) pH during sewage filtration; (c) Ca^{2+} concentration during rainwater filtration; (d) Ca^{2+} concentration during sewage filtration; (e) Mg^{2+} concentration during rainwater filtration; and (f) Mg^{2+} concentration during sewage filtration. Each value represented as mean \pm SD, samples size ($n = 4$), $* p < 0.05$. The significance of the grades was calculated with the Kruskal–Wallis test.

The initial concentration of Ca^{2+} in rainwater was 2.98 mg/L (Table S2). During leaching through the wastewater medium, there was a significant initial increase followed by a slow rise, reaching a steady equilibrium concentration of 55.33 ± 1.87 mg/L. In the background medium, the initial increase was significant, followed by fluctuating rises, and after 24 h, a slow upward trend led to a steady equilibrium of 38.16 ± 13.27 mg/L (Figure 3c). The initial Ca^{2+} concentration in wastewater was 33.25 mg/L (Table S2). Vigorous agitation resulted in substantial leaching of Ca^{2+} from the soil; during leaching through the contaminated medium, the concentration significantly increased within the first 30 min, slightly decreased thereafter, and then rose again to reach a stable equilibrium at 178.52 ± 3.23 mg/L. During leaching through the background medium, the concentration significantly increased in the first 30 min, fluctuated downward, rose again, and then slowly declined over 48 h, settling at 158.25 ± 2.71 mg/L at the end of leaching (Figure 3d).

The initial concentration of Mg^{2+} was 0.33 mg/L in rainwater (Table S2). As leaching progressed, the concentration of Mg^{2+} in the leachate from both contaminated and background site samples continuously increased. At the end of the experiment, the concentrations of Mg^{2+} in the leachate from the contaminated and background site samples were 5.00 ± 0.80 mg/L and 10.02 ± 1.32 mg/L, respectively (Figure 3e). The initial Mg^{2+} concentration in wastewater was 24.63 mg/L (Table S2). During the reaction, the concentration of Mg^{2+} precipitated at the background site samples was higher than at the contaminated site samples. During leaching through the contaminated site samples, there was an initial rise followed by a decrease, then a slow rise after 12 h to reach equilibrium at 27.04 ± 0.05 mg/L. During leaching through the background site samples, the concentration first rose then fell within the first 6 h, fluctuated between 6 and 12 h, then slowly rose and stabilized after 48 h at an equilibrium of 37.80 ± 1.74 mg/L (Figure 3f).

3.3. Variations in the Concentrations of Mn/Fe

In rainwater, both Fe and Mn were below the detection limit (Table S2). During the leaching period, occasional detections of Mn and Fe were observed in the leachate from the background soil layers, but the concentrations were very low, with Mn reaching a maximum concentration of 0.007 ± 0.001 mg/L and Fe peaking at 0.0076 ± 0.003 mg/L. In the leachate from the contaminated soil layers, the concentration of Fe was also low, with a maximum of 0.005 ± 0.002 mg/L. The concentration of Mn was slightly higher than in the leachate from the background site samples and slowly increased over the duration of the leaching process, reaching a concentration of 0.13 ± 0.01 mg/L by the end of leaching (Figure 4).

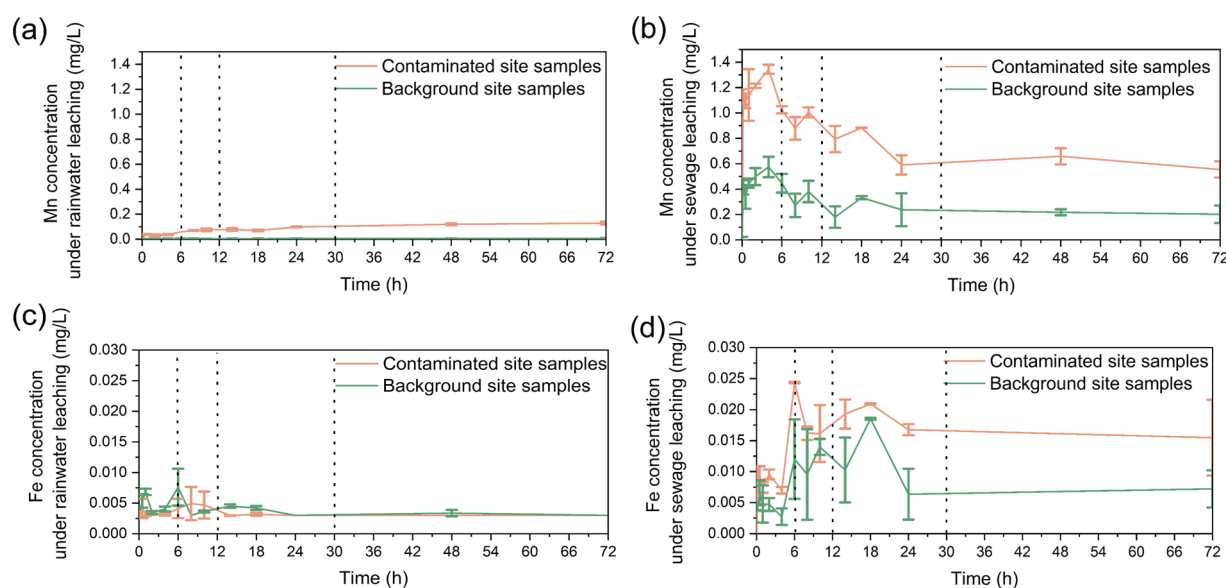


Figure 4. Changes in Mn^{2+} and Fe^{2+} concentrations during filtration of two types of source water in contaminated and background environments. Changes in (a) Mn^{2+} concentration during rainwater filtration, (b) Mn^{2+} concentration during sewage filtration, (c) Fe^{2+} concentration during rainwater filtration, and (d) Fe^{2+} concentration during sewage filtration. Each value represented as mean \pm SD, samples size ($n = 4$), * $p < 0.05$. The significance of the grades was calculated with the Kruskal–Wallis test.

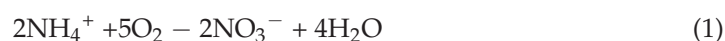
Mn and Fe concentrations in wastewater were very low, only slightly above their respective detection limits (Table S2). Observations during the leaching period showed a clear increase in the concentrations of Mn and Fe in the leachate (Figure 4). The concentration of Mn in the leachate displayed a rapid increase followed by a fluctuating decrease, ultimately reaching a steady state. The concentration of Mn in the leachate was consistently higher than that from rainwater leaching, with a more noticeable increase compared to Fe.

The equilibrium concentrations of Mn in the leachate from the contaminated site samples and background site samples were 0.66 ± 0.06 mg/L and 0.22 ± 0.02 mg/L, respectively. The concentration of Fe in the leachate continued to fluctuate and increase, with the Fe concentration in leachates from all soil layers under wastewater leaching being higher than those from rainwater leaching. The equilibrium concentrations of Fe in the leachate from the contaminated site samples and background site samples were 0.016 ± 0.01 mg/L and 0.07 ± 0.003 mg/L, respectively (Figure 4).

4. Discussion

4.1. Enrichment of the Secondary NO_3^- in Oxidation Zone

During the vertical filtration of surface sewage into aquifers, the initial oxidative source water gradually transitions to a reducing state, forming distinct oxidative and reductive zones [9]. The reduction intensity of O_2 and NO_3^- directly governs the spatial variations between the oxidative and reductive zones. In the natural vertical filtration process of rainwater, the NO_3^- content in source water and groundwater is low, with NH_4^+ in strongly reducing groundwater being the primary inorganic nitrogen form [32]. In the case of sewage with a tendency toward oxidation, the substantial presence of NH_4^+ is attributed to its elevated concentration. Within the oxidative-reductive gradient formed during vertical infiltration, under conditions of oxygen richness and high microbial abundance [33], NH_4^+ undergoes nitrification to produce NO_3^- , as described by Equation (1).



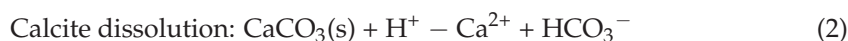
NH_4^+ exhibits strong adsorption characteristics, with a sandstone adsorption capacity (Kd) ranging from 3 to 8 L/kg, reaching adsorption equilibrium within 4–8 h [34,35]. It undergoes significant adsorption during the vertical filtration process. In this experiment, the experimental medium had undergone prolonged percolation filtration (Figure 2b). The concentrations of NH_4^+ in the original water of rain and sewage were 2.639 mg/L and 86.203 mg/L, respectively. Within the 4 h adsorption equilibrium period identified by Chen et al. (2023) [33] the leachate NH_4^+ peak concentrations in the rainwater filtration background medium experimental group and the sewage filtration polluted medium experimental group were (1.97 ± 0.01 mg/L) and (85.86 ± 2.16 mg/L), respectively. These values closely resembled the corresponding original water concentrations, indicating that the experimental medium, under the prolonged influence of rainwater and sewage filtration, had reached thermodynamic adsorption equilibrium for NH_4^+ , rendering the NH_4^+ adsorption effect negligible.

The concentrations of NO_3^- in the original water of rain and sewage were 1.148 mg/L and 2.014 mg/L, respectively (Figure 2c,d). Between 30 and 72 h, the variations in NO_3^- concentrations were minimal, stabilizing at 20.56 ± 3.31 mg/L and 84.51 ± 2.15 mg/L, respectively. At this point, in the background medium experimental group, the NO_3^- concentrations were significantly lower than those in the polluted medium experimental group (Figure 2), suggesting the presence of active nitrogen biogeochemical processes [19]. In the polluted medium experimental group during sewage filtration NH_4^+ content decreased by 5.40 ± 2.16 mg/L within 6 h, and NO_3^- concentration steadily increased by 4.79 ± 1.46 mg/L (Figure 2b). During this initial period of filtration, the environment was oxidative, characterized by abundant COD and O_2 levels, promoting nitrification. However, a consistent trend was observed in the rainwater filtration polluted medium experimental group (Figure 2a,c). The rainwater source water was characterized by no microbial populations, carbon sources, and NH_4^+ , the variation range of NH_4^+ and NO_3^- in rainwater filtration experiments were lower than those observed in sewage filtration experiments, showing that sewage infiltration increased the intensity of nitrification in groundwater compared with rainwater infiltration. Chen et al. (2023) [33] mentioned that nitrification is a first-order kinetic reaction, and its rate is controlled by the concentration of the reactant NH_4^+ . The experiments demonstrate that, within the initial 6 h of the sewage filtration, a

portion of the high concentration of NH_4^+ rapidly transforms into a considerable amount of secondary pollutant NO_3^- .

4.2. Acid Environment Controlled by Rapid Reduction

During rainwater filtration, rapid reduction of O_2 and NO_3^- coupled with the swift production of CO_2 from organic carbon results in an excess of CO_2 dissolved in water. Abedi Koupai et al. (2020) [36] and Chen et al. (2023) [33] inferred that this result promotes the movement of carbonic acid balance in water, producing a certain amount of H^+ and altering groundwater acidity. The impact of this acidity changes on the dissolution equilibrium of carbonate minerals, as shown in Equations (2) and (3), is limited [37,38]. However, there is a substantial presence of O_2 , secondary pollutant NO_3^- , and carbon source COD in the process of vertical filtration of surface sewage. A study by Zhai et al. (2021) [18] on centralized sewage treatment has demonstrated that the rapid reduction in a large amount of NO_3^- promptly produces H^+ , significantly altering the acidity of the groundwater environment.

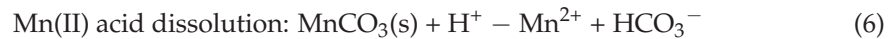


The generation and consumption of H^+ occur simultaneously during filtration, which makes the direct correlation of pH to nitrate reduction less apparent. However, changes in the concentrations of Ca^{2+} and Mg^{2+} can serve as indicators of acid-driven processes [19,39]. In the polluted medium experimental group during sewage filtration, as shown in Figure 3b, the pH value increased from the initial 6.88 ± 0.03 to 6.91 ± 0.01 within 6 h. From 6 to 72 h, the pH gradually decreased and stabilized at the initial level. The concentrations of Ca^{2+} and Mg^{2+} , 33.253 mg/L and 24.63 mg/L in the original water, increased to 185.92 ± 3.59 mg/L and 27.26 ± 0.12 mg/L within 6 h and gradually decreased to the initial level from 6 to 72 h, respectively. The rapid changes in Ca^{2+} and Mg^{2+} concentrations indicate the high activity of H^+ . Within 6–12 h after sewage filtration, the reduction of O_2 and secondary pollutant NO_3^- generates a large amount of H^+ , promoting the dissolution of calcite and dolomite, resulting in increased Ca^{2+} and Mg^{2+} . In the subsequent 6–12 h, the intensity of redox reactions decreased; the consumption of H^+ exceeded the generation; excess Ca^{2+} and Mg^{2+} shifted the balance to the left; and the Ca^{2+} and Mg^{2+} concentrations and pH returned to the initial state. This acidification, induced by the reduction of NO_3^- and CO_2 production, affects the nitrate reduction process. The presence of excess H^+ accelerates the denitrification and DNRA processes, influencing the pathways and rates of nitrogen transformation. Specifically, the acidic conditions promote heterotrophic denitrification, where NO_3^- is reduced to N_2 , and also facilitate DNRA, where NO_3^- is reduced to NH_4^+ . Therefore, the pH changes are indirectly linked to enhanced nitrate reduction, with acidic conditions promoting both the conversion of NO_3^- to N_2 and NH_4^+ . This process obviously influence the acid environment during sewage vertical filtration, compared to that of the rainwater vertical filtration.

4.3. Response of Mn Mineral Release to Acid Condition

The release of Mn^{2+} and Fe^{2+} in groundwater primarily occurs because of the reductive dissolution of Mn(IV)/Fe(III) minerals and the acidic dissolution of Mn(II) minerals in the medium [40]. In the background medium during rainwater vertical infiltration, the release of Mn and Fe is dominated by reductive dissolution, as represented in Equations (4) and (5) [41,42]. However, sewage vertical filtration in an environment with significant production of H^+ from the rapid reduction in secondary NO_3^- promotes the dissolution of MnCO_3 minerals.





The intensity of Mn(IV) and Fe(III) reduction differs between rainwater and sewage filtration. The initial concentrations of Mn^{2+} and Fe^{2+} in rainwater and sewage source water are below 0.001 mg/L (Table S2). After reaching stability in rainwater filtration, Mn^{2+} concentrations in the leachate of the background and polluted medium experimental groups are 0.077 ± 0.01 mg/L and 0.436 ± 0.001 mg/L, respectively (Figure 4a,b), the Fe^{2+} concentrations are 0.003 ± 0.00 mg/L and 0.003 ± 0.001 mg/L, respectively (Figure 4c,d). In sewage filtration, after reaching stability, the Mn^{2+} concentrations in the leachate of the background and polluted medium are 0.22 ± 0.06 mg/L and 0.65 ± 0.02 mg/L, respectively (Figure 4a,b), and the Fe^{2+} concentrations are 0.006 ± 0.01 mg/L and 0.0016 ± 0.002 mg/L, respectively (Figure 4c,d), both lower than that of the rainwater filtration process. As a result of the absence of a carbon source in rainwater filtration process, only a small amount of Mn^{2+} and Fe^{2+} is generated. The sewage carries a significant amount of COD, promoting the reduction in Mn/Fe minerals.

In sewage vertical infiltration, in the background and polluted mediums, the activity of Mn(II) mineral acid dissolution is strong. As shown in Figure 4b, Mn^{2+} concentrations exhibit two peaks in both experimental groups at 0–6 h and 6–30 h. The first peak of Mn^{2+} is affected by pH, per the correlation heat map of water quality parameters in the pollution monitoring wells in Figure 5. There is a significant negative correlation between pH and Mn [20]. The pH dominance map of Mn is consistent, with Mn mainly distributed when $\text{pH} < 8.0$ (Figure 6). The rapid reduction in secondary NO_3^- , generating H^+ , promotes the acidic dissolution of MnCO_3 minerals [27,29]. In the 6–30 h period (Figure 4b), the second peak of Mn^{2+} occurs as the reduction intensity of NO_3^- gradually decreases. Reductive dissolution of Mn(IV) occurs, and with the increasing reductive capacity, Fe^{2+} peaks between 12 and 30 h (Figure 4d), indicating the reduction in Fe(III) [5].

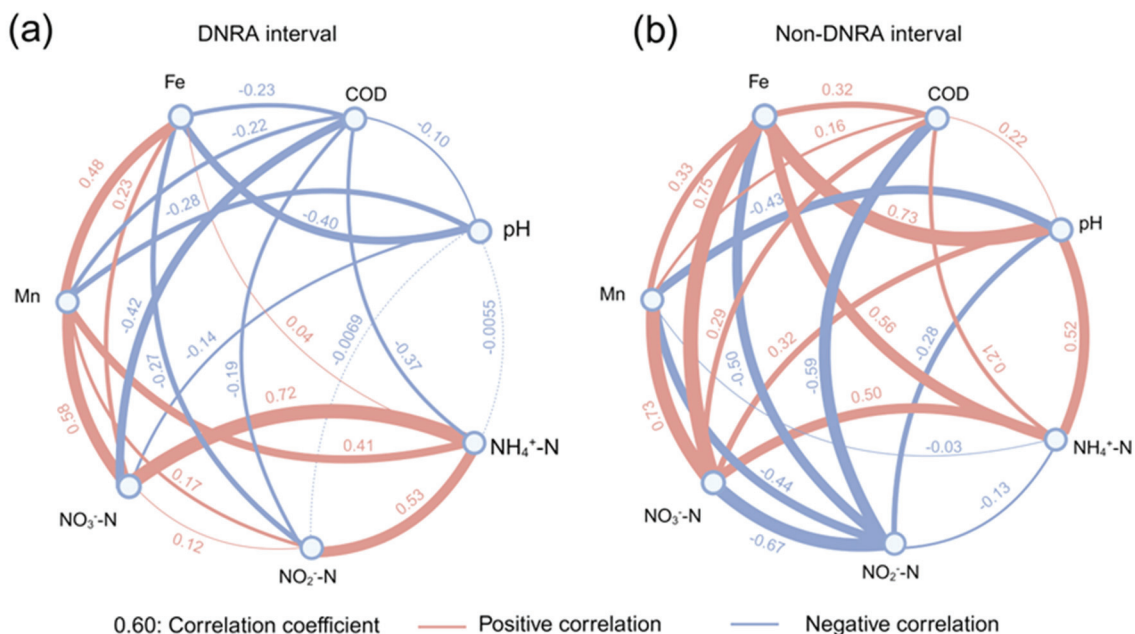


Figure 5. Ion correlation network diagram of (a) DNRA interval and (b) non-DNRA interval.

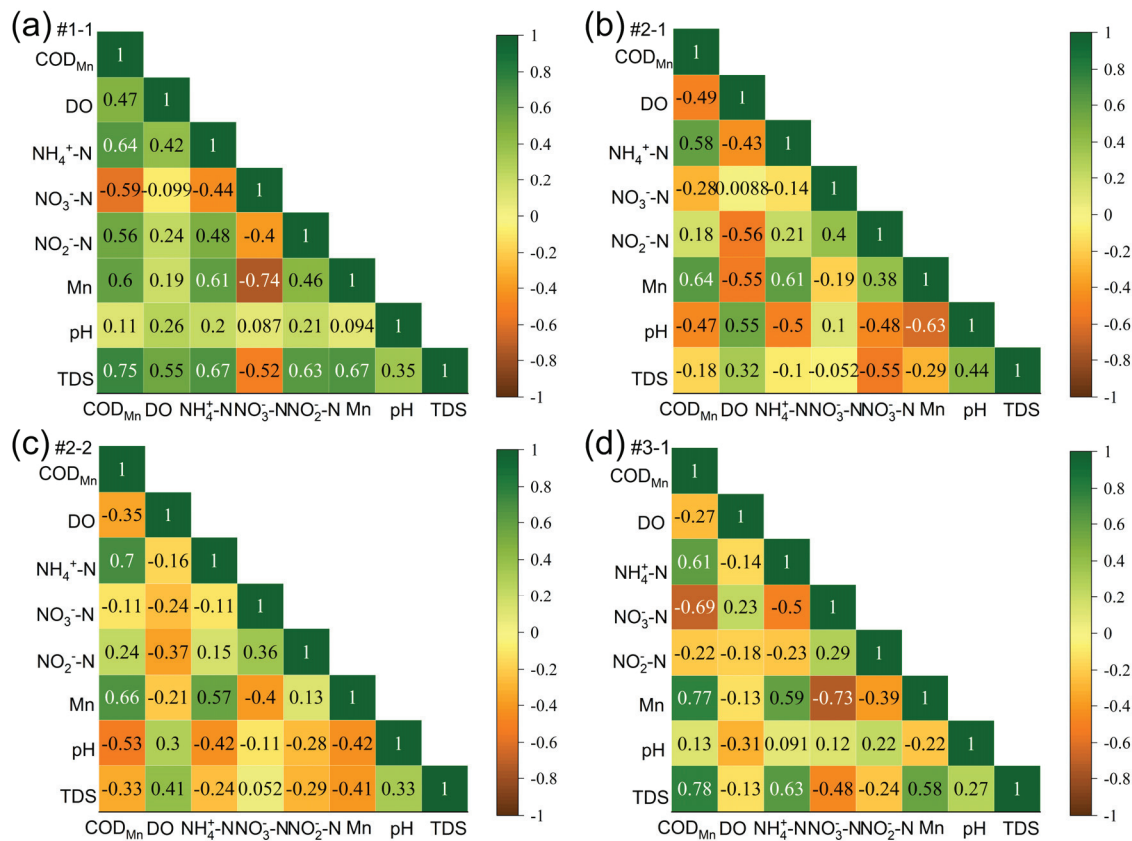
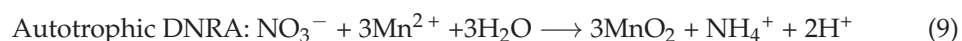
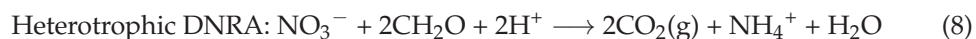
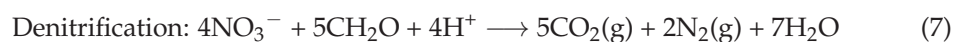


Figure 6. Correlation heat map of water quality parameters in four pollution monitoring wells, (a) #1-1, (b) #2-1, (c) #2-2 and (d) #3-1.

4.4. Active DNRA in High Carbon Load and Mn²⁺ Condition

Under natural conditions, denitrification is the primary process responsible for NO₃⁻ reduction (Equation (7)), resulting in the removal of N₂ from groundwater [18,43]. However, in a strongly reducing environment [19], under conditions of high carbon load [35,44], and elevated concentrations of Mn²⁺/Fe²⁺/HS⁻ ions [14], the reduction of NO₃⁻ is more likely to favor DNRA (Equations (8) and (9)) than denitrification. The active DNRA process generates substantial NH₄⁺, retaining nitrogen in groundwater [28,45]. Although DNRA is rare under natural conditions, it is observed in studies by Li et al. (2023) [46], Dippong et al. (2018) [47], Du et al. (2020) [48], and Abiriga et al. (2021) [6]. It is related to sewage treatment plants and is likely to occur during the continuous vertical filtration of sewage.



The complex carbon load, high H⁺, and high Mn²⁺ environment resulting from vertical filtration enhance the activity of DNRA. In the polluted medium's experimental group for sewage infiltration, within the 6–30 h interval, NH₄⁺ content increases from 84.11 ± 2.16 to 87.90 ± 0.44 mg/L, and NO₃⁻ content decreases from 23.75 ± 0.46 to 17.34 ± 0.63 mg/L (Figure 2b,d). The increase in NH₄⁺ (4.51%) is smaller than the decrease in NO₃⁻ (22.0%), indicating that denitrification is the primary process for nitrate removal, as a significant portion of NO₃⁻ undergoes denitrification, being reduced to N₂ and escaping into the air. Although DNRA also contributes to the reduction process, converting a portion of NO₃⁻ back to NH₄⁺ and retaining it in the groundwater, the data suggests that denitrification plays a more dominant role in nitrate attenuation during sewage infiltration due to the

presence of higher COD and microbial activity levels that favor denitrification kinetics. However, during rainwater infiltration, the changes in NH_4^+ and NO_3^- concentrations are significantly smaller than in the sewage infiltration experiment (Figure 2a,b), and there is no upward trend in NH_4^+ within the 6–30 h interval, indicating the absence of DNRA. Moreover, NH_4^+ shows a positive correlation with NO_2^- during the DNRA interval (Figure 5a) than that of the non-DNRA interval (Figure 5b), where the active NO_2^- is an important symbol of DNRA [33,49]. As denitrification follows first-order kinetics, influenced by reactant concentrations, and DNRA follows zero-order kinetics and is not affected by reactant concentrations [15,16,44], the sewage vertical infiltration enhances the strength of denitrification, increasing the contribution of DNRA to NO_3^- reduction.

The Gibbs free energy of aerobic respiration and denitrification is -125.1 and -118.8 KJ/eq, respectively, higher than the energy of DNRA and Mn(IV) reduction (-84.8 and -81.8 KJ/eq, respectively) and far exceeding the energy of Fe(III) (-28.9 KJ/eq) [50,51]. In the process of vertical filtration under natural conditions, heterotrophic DNRA with carbon as the electron donor is not active. At the same time, NO_3^- in the oxidizing environment and Mn^{2+} in the reducing environment have difficult coexisting in a unified environment, so autotrophic DNRA is not easy to occur [19,33]. However, in high COD sewage vertical filtration, a high carbon load environment is formed [28], which can act as an electron donor [52,53]. During the DNRA interval, NH_4^+ shows a negative correlation with pH and COD, whereas they show a positive correlation during the non-DNRA interval, showing the impact of H^+ and COD on the activity of DNRA (Figure 5). In summary, in the high NH_4^+ and COD sewage vertical filtration, a large amount of secondary NO_3^- is generated. The rapid reduction in secondary NO_3^- produces substantial CO_2 , increasing H^+ levels and causing the acidic dissolution of MnCO_3 . This process releases Mn^{2+} , which then acts as an electron donor for further reduction of NO_3^- . The high carbon load and high Mn^{2+} condition create a favorable condition for DNRA to produce NH_4^+ .

4.5. Novelty, Future Work and Practical Implication

In conclusion, this study unveils several novel insights into the hydrobiogeochemical processes affecting groundwater quality under the influence of polygenic multipollutants. Firstly, it highlights how sewage infiltration introduces substances such as NH_4^+ and COD, which significantly threaten groundwater integrity by facilitating the formation of secondary pollutants like NO_3^- , Mn^{2+} , and Fe^{2+} . Furthermore, the study delineates the interconnected biochemical chain reactions initiated by sewage infiltration—nitrification, denitrification, and dissimilatory nitrate reduction to ammonium (DNRA)—which notably convert part of the secondary NO_3^- back into NH_4^+ in groundwater, differing significantly from natural rainwater infiltration processes. This research also establishes that sewage infiltration intensifies sequential redox reactions, which not only shift the redox potential but also create the acidic conditions necessary for the dissolution of Mn(II). These findings not only contribute new knowledge to our understanding of groundwater pollution dynamics but also have practical implications for the development of more effective groundwater management and remediation strategies. This experiment has demonstrated the existence of the DNRA process, in which carbon sources and Mn^{2+} can be electron donors for DNRA. The ratio of their contributions deserves further exploration and is a promising topic for future research. Such studies can aid groundwater management by identifying key hydrobiogeochemical processes that influence the dynamics of polygenic multipollutants, allowing for targeted remediation strategies. By understanding the interactions between polygenic multipollutants and aquifer conditions, water management authorities can develop more effective policies and practices to mitigate pollution impacts. Additionally, this research can inform the design of natural attenuation and engineered remediation solutions to enhance groundwater quality and protect water resources [54,55].

5. Conclusions

The biogeochemical processes associated with the vertical infiltration of polygenic multipollutants are crucial for understanding the migration and transformation of pollutants, and they hold significant importance for safeguarding groundwater safety and ecological environment protection. Based on field pollution conditions, field media samples were collected, and laboratory experiments were conducted to identify the main biogeochemical processes of polygenic multipollutants and their secondary pollutants. The results indicated that during the early stage of sewage vertical infiltration in oxidative groundwater, the sewage, carrying a large number of NH_4^+ , was oxidized to generate the secondary pollutant NO_3^- . As O_2 was consumed, transforming the groundwater environment into a reducing environment, the secondary pollutants NO_3^- , Mn(IV) , and Fe(III) minerals were sequentially reduced, producing N_2 , NH_4^+ , Fe^{2+} , and Mn^{2+} . Different from rainwater vertical infiltration conditions, sewage vertical infiltration provided many reactive components, leading to a significant increase in the reaction rates and intensities of various reactions during sewage vertical infiltration. In the sewage vertical infiltration process, the high-intensity reactions involving O_2 and secondary pollutant NO_3^- reduction rapidly generated a large amount of CO_2 . Excess CO_2 dissolved to produce a large amount of H^+ , facilitating the acidic dissolution of Mn(II) minerals, leading to the generation of Mn^{2+} . In the studied spatial range, the groundwater had a suitable energy level for DNRA. The environment characterized by high carbon load and high Mn^{2+} promoted DNRA, which had a higher contribution than denitrification to NO_3^- reduction. Although a portion of the NO_3^- produced from the conversion of NH_4^+ in the source pollutants was removed through denitrification, DNRA resulted in the re-reduction of NO_3^- to NH_4^+ , leading to its retention in groundwater. These findings provide valuable insights for planning strategies for local groundwater management and remediation.

Supplementary Materials: The following supporting information can be downloaded at <https://www.mdpi.com/article/10.3390/w16162305/s1>. Table S1: Physical and chemical properties of the aquifer sediments used for the experiment. Each value represented as mean \pm SD, samples size ($n = 4$), * $p < 0.05$. Table S2: Initial concentration of each index in raw water. Table S3: Methods for determining the physicochemical properties of the sediment and the detection limits. Table S4: Control experimental group and control conditions. Figure S1: Overview map of the study area, including three polluted sites (#1, #2, #3) and four monitoring wells (#1-1, #2-1, #2-2, #3-1): modifications of those reported by Zhai et al. (2022). Figure S2: Percentage diagram of mineral content in sediments. Figure S3: Schematic diagram of the leaching experiment.

Author Contributions: Conceptualization, Y.Z.; methodology, Y.D. and Y.H.; software, Y.D.; validation, Y.D.; writing—original draft preparation, Y.D. and Y.H.; writing—review and editing, X.H., Y.C. and Y.Z.; supervision, Y.C. and Y.Z.; project administration, Y.Z.; funding acquisition, Y.Z. All authors have read and agreed to the published version of the manuscript.

Funding: This work was supported by the National Natural Science Foundation of China (Nos. 42077170 and 42377052).

Data Availability Statement: Data are contained within the article.

Conflicts of Interest: The authors declare no conflicts of interest.

References

1. Kabir, M.M.; Akter, S.; Ahmed, F.T.; Mohinuzzaman, M.; Didar-ul-Alam, M.; Mostofa, K.M.G.; Islam, A.R.M.T.; Niloy, N.M. Salinity-induced fluorescent dissolved organic matter influence co-contamination, quality and risk to human health of tube well water, southeast coastal Bangladesh. *Chemosphere* **2021**, *275*, 130053. [CrossRef] [PubMed]
2. Osafo, N.O.-A.; Jan, J.; Porcal, P.; Borovec, J. Contrasting catchment soil pH and Fe concentrations influence DOM distribution and nutrient dynamics in freshwater systems. *Sci. Total Environ.* **2023**, *858*, 159988. [CrossRef]
3. Jang, C.-S.; Chen, J.-S.; Lin, Y.-B.; Liu, C.-W. Characterizing hydrochemical properties of springs in Taiwan based on their geological origins. *Environ. Monit. Assess.* **2012**, *184*, 63–75. [CrossRef]
4. Yang, F.; Yue, S.; Wu, X.; Zhang, C.; Li, D.; Zhu, R. Effects of flood inundation on biogeochemical processes in groundwater during riverbank filtration. *J. Hydrol.* **2023**, *617*, 129101. [CrossRef]

5. Ahmad, H.A.; Ahmad, S.; Gao, L.; Wang, Z.; El-Baz, A.; Ni, S.-Q. Energy-efficient and carbon neutral anammox-based nitrogen removal by coupling with nitrate reduction pathways: A review. *Sci. Total Environ.* **2023**, *889*, 164213. [CrossRef] [PubMed]
6. Abiriga, D.; Vestgarden, L.S.; Klempe, H. Long-term redox conditions in a landfill-leachate-contaminated groundwater. *Sci. Total Environ.* **2021**, *755*, 143725. [CrossRef] [PubMed]
7. Abdullah, T.O.; Ali, S.S.; Al-Ansari, N.A.; Knutsson, S. Hydrogeochemical Evaluation of Groundwater and Its Suitability for Domestic Uses in Halabja Saidiadiq Basin, Iraq. *Water* **2019**, *11*, 690. [CrossRef]
8. Wang, H.; Lu, K.; Shen, C.; Song, X.; Hu, B.; Liu, G. Human health risk assessment of groundwater nitrate at a two geomorphic units transition zone in northern China. *J. Environ. Sci.* **2021**, *110*, 38–47. [CrossRef]
9. Li, X.; Huang, Y.; Liu, H.; Wu, C.; Bi, W.; Yuan, Y.; Liu, X. Simultaneous Fe(III) reduction and ammonia oxidation process in Anammox sludge. *J. Environ. Sci.* **2018**, *64*, 42–50. [CrossRef]
10. Zhai, Y.; Han, Y.; Lu, H.; Du, Q.; Xia, X.; Teng, Y.; Zuo, R.; Wang, J. Interactions between anthropogenic pollutants (biodegradable organic nitrogen and ammonia) and the primary hydrogeochemical component Mn in groundwater: Evidence from three polluted sites. *Sci. Total Environ.* **2022**, *808*, 152162. [CrossRef]
11. Zhao, M.; Jiang, Y.; Jia, Y.; Lian, X.; Feng, F.; Shang, C.; Zang, Y.; Xi, B. Anthropogenic perturbation enhances the release of geogenic Mn to groundwater: Evidence from hydrogeochemical characteristics. *Sci. Total Environ.* **2023**, *891*, 164450. [CrossRef]
12. Kelley, C.J.; Keller, C.K.; Evans, R.D.; Orr, C.H.; Smith, J.L.; Harlow, B.A. Nitrate–nitrogen and oxygen isotope ratios for identification of nitrate sources and dominant nitrogen cycle processes in a tile-drained dryland agricultural field. *Soil Biol. Biochem.* **2013**, *57*, 731–738. [CrossRef]
13. Xiu, W.; Yu, X.; Guo, H.; Yuan, W.; Ke, T.; Liu, G.; Tao, J.; Hou, W.; Dong, H. Facilitated arsenic immobilization by biogenic ferrihydrite-goethite biphasic Fe(III) minerals (Fh-Gt Bio-bi-minerals). *Chemosphere* **2019**, *225*, 755–764. [CrossRef]
14. Lei, X.; Cui, G.; Sun, H.; Hou, S.; Deng, H.; Li, B.; Yang, Z.; Xu, Q.; Huo, X.; Cai, J. How do earthworms affect the pathway of sludge bio-stabilization via vermicomposting? *Sci. Total Environ.* **2024**, *916*, 170411. [CrossRef]
15. Morrissey, J.G.; Currell, M.J.; Reichman, S.M.; Surapaneni, A.; Megharaj, M.; Crosbie, N.D.; Hirth, D.; Aquilina, S.; Rajendram, W.; Ball, A.S. Nitrogen contamination and bioremediation in groundwater and the environment: A review. *Earth-Sci. Rev.* **2021**, *222*, 103816. [CrossRef]
16. Roșca, O.M.; Dippong, T.; Marian, M.; Mihali, C.; Mihalescu, L.; Hoaghia, M.; Jelea, M. Impact of anthropogenic activities on water quality parameters of glacial lakes from Rodnei mountains, Romania. *Environ. Res.* **2020**, *182*, 109136. [CrossRef] [PubMed]
17. Chen, R.; Liu, H.; Zhang, P.; Zhao, L.; Ding, K.; Yuan, S. Attenuation of Fe(III)-reducing bacteria during table fluctuation of groundwater containing Fe²⁺. *Sci. Total Environ.* **2019**, *694*, 133660. [CrossRef] [PubMed]
18. Zhai, Y.; Han, Y.; Xia, X.; Li, X.; Lu, H.; Teng, Y.; Wang, J. Anthropogenic Organic Pollutants in Groundwater Increase Releases of Fe and Mn from Aquifer Sediments: Impacts of Pollution Degree, Mineral Content, and pH. *Water* **2021**, *13*, 1920. [CrossRef]
19. Su, X.; Zheng, Z.; Chen, Y.; Wan, Y.; Lyu, H.; Dong, W. Effects of carbon load on nitrate reduction during riverbank filtration: Field monitoring and batch experiment. *Sci. Total Environ.* **2022**, *845*, 157198. [CrossRef]
20. Hou, Q.; Zhang, Q.; Huang, G.; Liu, C.; Zhang, Y. Elevated manganese concentrations in shallow groundwater of various aquifers in a rapidly urbanized delta, south China. *Sci. Total Environ.* **2020**, *701*, 134777. [CrossRef]
21. Cao, X.; He, W.; Fan, M.; He, W.; Shi, Y.; An, T.; Chen, X.; Zhang, Z.; Liu, F.; Zhao, Y.; et al. Novel insights into source apportionment of dissolved organic matter in aquifer affected by anthropogenic groundwater recharge: Applicability of end-member mixing analysis based optical indices. *Sci. Total Environ.* **2023**, *863*, 160885. [CrossRef] [PubMed]
22. Li, D.; Chang, F.; Zhang, Y.; Duan, L.; Liu, Q.; Li, H.; Hu, G.; Zhang, X.; Gao, Y.; Zhang, H. Arsenic migration at the sediment-water interface of anthropogenically polluted Lake Yangzong, Southwest China. *Sci. Total Environ.* **2023**, *879*, 163205. [CrossRef] [PubMed]
23. Meng, L.; Shi, J.; Zheng, S.; Guo, X.; Wang, J.; Zhai, Y.; Teng, Y.; Zuo, R. Compartmentalization transformation of Fe²⁺, Mn²⁺ and NH⁴⁺ in groundwater: A comparative research containing experimental medium and functional genera profiling derived from experiment data. *J. Water Process Eng.* **2024**, *58*, 104794. [CrossRef]
24. Duan, L.; Song, J.; Yin, M.; Yuan, H.; Li, X.; Zhang, Y.; Yin, X. Dynamics of arsenic and its interaction with Fe and S at the sediment-water interface of the seasonal hypoxic Changjiang Estuary. *Sci. Total Environ.* **2021**, *769*, 145269. [CrossRef] [PubMed]
25. Cao, X.; Han, X.; Chen, Y.; Li, J.; Zhai, Y. Flood irrigation increases the release of phosphorus from aquifer sediments into groundwater. *J. Contam. Hydrol.* **2024**, *261*, 104297. [CrossRef] [PubMed]
26. GB/T 36197-2018[S/OL]; Soil Quality – Guidance on Sampling Techniques. State Administration for Market Regulation, Standardization Administration of the People’s Republic of China. Standards Press of China: Beijing, China, 2018.
27. Lu, C.; Xiu, W.; Guo, H.; Lian, G.; Yang, B.; Zhang, T.; Bi, E.; Shi, Z. Multi-Isotope Based Identification and Quantification of Oxygen Consuming Processes in Uranium Hosting Aquifers with CO₂ + O₂ In Situ Leaching. *Water Resour. Res.* **2023**, *59*, e2022WR033980. [CrossRef]
28. Lu, C.; Xiu, W.; Yang, B.; Lian, G.; Zhang, T.; Bi, E.; Guo, H. Characteristics of Dissolved Organic Matter in Uranium Hosting Aquifers and Potential Molecular Transformation During Neutral In Situ Leaching. *JGR Biogeosciences* **2024**, *129*, e2023JG007851. [CrossRef]

29. Lu, C.; Xiu, W.; Yang, B.; Zhang, H.; Lian, G.; Zhang, T.; Bi, E.; Guo, H. Natural Attenuation of Groundwater Uranium in Post-Neutral-Mining Sites Evidenced from Multiple Isotopes and Dissolved Organic Matter. *Environ. Sci. Technol.* **2024**, *58*, 12674–12684. [CrossRef] [PubMed]
30. GB/T 14848-2017[S/OL]; Groundwater Quality Standard. General Administration of Quality Supervision, Inspection and Quarantine of the People's Republic of China, Standardization Administration of China. Standards Press of China: Beijing, China, 2017.
31. World Health Organization. Guidelines for Drinking-Water Quality. *World Health Organ.* **2011**, *216*, 303–304.
32. Xia, Q.; He, J.; He, B.; Chu, Y.; Li, W.; Sun, J.; Wen, D. Effect and genesis of soil nitrogen loading and hydrogeological conditions on the distribution of shallow groundwater nitrogen pollution in the North China Plain. *Water Res.* **2023**, *243*, 120346. [CrossRef]
33. Chen, Y.; Su, X.; Wan, Y.; Lyu, H.; Dong, W.; Shi, Y.; Zhang, Y. Quantifying the effect of the nitrogen biogeochemical processes on the distribution of ammonium in the riverbank filtration system. *Environ. Res.* **2023**, *216*, 114358. [CrossRef] [PubMed]
34. Tang, M.; Du, R.; Cao, S.; Berry, M.; Peng, Y. Tracing and utilizing nitrogen loss in wastewater treatment: The trade-off between performance improvement, energy saving, and carbon footprint reduction. *J. Environ. Manag.* **2024**, *349*, 119525. [CrossRef] [PubMed]
35. Jia, L.; Zhou, Q.; Li, Y.; Wu, W. Application of manganese oxides in wastewater treatment: Biogeochemical Mn cycling driven by bacteria. *Chemosphere* **2023**, *336*, 139219. [CrossRef] [PubMed]
36. Abedi Koupai, J.; Fatahizadeh, M.; Mosaddeghi, M.R. Effect of pore water pH on mechanical properties of clay soil. *Bull. Eng. Geol. Environ.* **2020**, *79*, 1461–1469. [CrossRef]
37. Zhang, L.-Z.; Xing, S.; Huang, F.-Y.; Xiu, W.; Rensing, C.; Zhao, Y.; Guo, H. Metabolic coupling of arsenic, carbon, nitrogen, and sulfur in high arsenic geothermal groundwater: Evidence from molecular mechanisms to community ecology. *Water Res.* **2024**, *249*, 120953. [CrossRef] [PubMed]
38. Nortjé, G.P.; Laker, M.C. Factors That Determine the Sorption of Mineral Elements in Soils and Their Impact on Soil and Water Pollution. *Minerals* **2021**, *11*, 821. [CrossRef]
39. McMahon, P.B.; Belitz, K.; Reddy, J.E.; Johnson, T.D. Elevated Manganese Concentrations in United States Groundwater, Role of Land Surface–Soil–Aquifer Connections. *Environ. Sci. Technol.* **2019**, *53*, 29–38. [CrossRef] [PubMed]
40. Moore, O.C.; Xiu, W.; Guo, H.; Polya, D.A.; Van Dongen, B.E.; Lloyd, J.R. The role of electron donors in arsenic-release by redox-transformation of iron oxide minerals—A review. *Chem. Geol.* **2023**, *619*, 121322. [CrossRef]
41. Cao, W.; Zhang, Z.; Fu, Y.; Zhao, L.; Ren, Y.; Nan, T.; Guo, H. Prediction of arsenic and fluoride in groundwater of the North China Plain using enhanced stacking ensemble learning. *Water Res.* **2024**, *259*, 121848. [CrossRef]
42. Li, P.; Sabarathinam, C.; Elumalai, V. Groundwater pollution and its remediation for sustainable water management. *Chemosphere* **2023**, *329*, 138621. [CrossRef]
43. Xu, F.; Li, P. Biogeochemical mechanisms of iron (Fe) and manganese (Mn) in groundwater and soil profiles in the Zhongning section of the Weining Plain (northwest China). *Sci. Total Environ.* **2024**, *939*, 173506. [CrossRef] [PubMed]
44. Bai, J.; Yuan, Z.; Su, X. Spatiotemporal distribution patterns of iron, manganese, and arsenic within the river infiltration zone and the potential geochemical activity at key interfaces. *Appl. Geochem.* **2024**, *172*, 106123. [CrossRef]
45. Rivett, M.O.; Buss, S.R.; Morgan, P.; Smith, J.W.N.; Bemment, C.D. Nitrate attenuation in groundwater: A review of biogeochemical controlling processes. *Water Res.* **2008**, *42*, 4215–4232. [CrossRef] [PubMed]
46. Li, Q.; Wang, G.; Wang, H.; Shrestha, S.; Xue, B.; Sun, W.; Yu, J. Macrozoobenthos variations in shallow connected lakes under the influence of intense hydrologic pulse changes. *J. Hydrol.* **2020**, *584*, 124755. [CrossRef]
47. Dippong, T.; Mihali, C.; Năsu, D.; Berinde, Z.; Butean, C. Assessment of Water Physicochemical Parameters in the Strîmtori-Firiza Reservoir in Northwest Romania. *Water Environ. Res.* **2018**, *90*, 220–233. [CrossRef] [PubMed]
48. Du, Y.; Deng, Y.; Ma, T.; Xu, Y.; Tao, Y.; Huang, Y.; Liu, R.; Wang, Y. Enrichment of Geogenic Ammonium in Quaternary Alluvial–Lacustrine Aquifer Systems: Evidence from Carbon Isotopes and DOM Characteristics. *Environ. Sci. Technol.* **2020**, *54*, 6104–6114. [CrossRef] [PubMed]
49. Hu, B.; Song, X.; Lu, Y.; Liang, S.; Liu, G. Fluoride enrichment mechanisms and related health risks of groundwater in the transition zone of geomorphic units, northern China. *Environ. Res.* **2022**, *212*, 113588. [CrossRef] [PubMed]
50. Champ, D.R.; Gulens, J.; Jackson, R.E. Oxidation–reduction sequences in ground water flow systems. *Can. J. Earth Sci.* **1979**, *16*, 12–23. [CrossRef]
51. Stumm, W.; Morgan, J.J. *Aquatic Chemistry: Chemical Equilibria and Rates in Natural Waters*, 3rd ed.; Environmental Science and Technology; John Wiley & Sons, Inc.: Hoboken, NJ, USA, 1996.
52. Li, Y.; Liu, Y.; Feng, L.; Zhang, L. A review: Manganese-driven bioprocess for simultaneous removal of nitrogen and organic contaminants from polluted waters. *Chemosphere* **2023**, *314*, 137655. [CrossRef]
53. Dong, H.; Zeng, Q.; Sheng, Y.; Chen, C.; Yu, G.; Kappler, A. Coupled iron cycling and organic matter transformation across redox interfaces. *Nat. Rev. Earth Environ.* **2023**, *4*, 659–673. [CrossRef]

54. Hu, B.; Teng, Y.; Zhang, Y.; Zhu, C. Review: The projected hydrologic cycle under the scenario of 936 ppm CO₂ in 2100. *Hydrogeol. J.* **2019**, *27*, 31–53. [CrossRef]
55. Xin, J.; Liu, Y.; Chen, F.; Duan, Y.; Wei, G.; Zheng, X.; Li, M. The missing nitrogen pieces: A critical review on the distribution, transformation, and budget of nitrogen in the vadose zone-groundwater system. *Water Res.* **2019**, *165*, 114977. [CrossRef] [PubMed]

Disclaimer/Publisher’s Note: The statements, opinions and data contained in all publications are solely those of the individual author(s) and contributor(s) and not of MDPI and/or the editor(s). MDPI and/or the editor(s) disclaim responsibility for any injury to people or property resulting from any ideas, methods, instructions or products referred to in the content.

Review

Seasonal Variations of Ice-Covered Lake Ecosystems in the Context of Climate Warming: A Review

Qianqian Wang ¹, Fang Yang ^{1,*}, Haiqing Liao ^{1,*}, Weiying Feng ², Meichen Ji ¹, Zhiming Han ³, Ting Pan ¹ and Dongxia Feng ¹

¹ State Key Laboratory of Environmental Criteria and Risk Assessment, Chinese Research Academy of Environmental Sciences, Beijing 100012, China; wangqianqian221@outlook.com (Q.W.); ji.meichen@craes.org.cn (M.J.); panting_2021@sina.com (T.P.); fengdx@craes.org.cn (D.F.)

² School of Materials Science and Engineering, Beihang University, Beijing 100191, China; fengweiying@buaa.edu.cn

³ College of Natural Resources and Environment, Northwest A&F University, Yangling 712100, China; m15029258074@163.com

* Correspondence: yang.fang@craes.org.cn (F.Y.); liaohq@craes.org.cn (H.L.)

Abstract: The period of freezing is an important phenological characteristic of lakes in the Northern Hemisphere, exhibiting higher sensitivity to regional climate changes and aiding in the detection of Earth's response to climate change. This review systematically examines 1141 articles on seasonal frozen lakes from 1991 to 2021, aiming to understand the seasonal variations and control conditions of ice-covered lakes. For the former, we discussed the physical structure and growth characteristics of seasonal ice cover, changes in water environmental conditions and primary production, accumulation and transformation of CO₂ beneath the ice, and the role of winter lakes as carbon sources or sinks. We also proposed a concept of structural stratification based on the differences in physical properties of ice and solute content. The latter provided an overview of the ice-covered period (-1.2 d decade⁻¹), lake evaporation ($+16\%$ by the end of the 21st century), the response of planktonic organisms (earlier spring blooming: 2.17 d year⁻¹) to global climate change, the impact of greenhouse gas emissions on ice-free events, and the influence of individual characteristics such as depth, latitude, and elevation on the seasonal frozen lakes. Finally, future research directions for seasonally ice-covered lakes are discussed. Considering the limited and less systematic research conducted so far, this study aims to use bibliometric methods to synthesize and describe the trends and main research points of seasonal ice-covered lakes so as to lay an important foundation for scholars in this field to better understand the existing research progress and explore future research directions.

Keywords: ice-covered lakes; seasonal variability; climate change; bibliometrics

1. Introduction

The ice-covered period is a significant phenological characteristic of Northern Hemisphere lakes, with nearly 50% of the 117 million lakes larger than 0.002 km² worldwide regularly freezing over. Seasonal ice cover exists in 14,800 lakes larger than 0.1 km² in the Northern Hemisphere [1,2], particularly in the mid-to-high latitudes (30–70° N) [3]. Lakes above 50° N in North America and Asia experience frequent ice cover occurrence (ICO = 100%). Within the latitude range of 50–60° N, the ICO values are almost twice as high as those in European lakes [4]. Under similar latitude conditions, seasonal lake ice is more common in high-altitude regions such as the Qinghai-Tibet Plateau (>4000 m, Asia) and the Rocky Mountains (>2700 m, North America) [3,5,6]. In the southern hemisphere (excluding Antarctica), lake ice cover occurs only at the southern end of the Andes. The lakes in this region have only thin ice cover and short ice duration, and the lake ice is continuing to shrink. By the end of the 21st century, the vast majority of lakes in the region will be virtually ice-free [7].

Seasonally frozen lakes respond uniquely to climate change, such as ice-on/off date, ice duration and spring blooms, and seasonal CO₂ flux [4,8,9], as highly sensitive indicators of regional watershed changes to detect the Earth's response to climate change to some extents [10]. Specifically, variations in lake morphology [11], geographical location [12], and local climatic factors [13] result in significant differences in ice duration, freeze-thaw processes, ice thickness, and spatial coverage in seasonally ice-covered lakes. These differences affect the nutrient status, material cycling, dominant species succession, and ecological conditions within the lakes [6,14,15]. During the frozen period, the trophic status of most lakes is regulated by the solute exclusion processes of ice and sediments [16,17]. Moreover, the CO₂ flux during freeze-thaw events is noteworthy, occasionally surpassing that of other seasons (Buffalo Pound Lake [18]: spring flux contribution: $64\% \pm 20\%$; summer: 43.6%; autumn: 23.3%). Ice phenology has social impacts. The centuries-long records of ice phenology indirectly indicate the social impacts of northern lake ice on human activities and livelihoods. Indigenous communities in northern Canada rely on ice cover for supplies and social interactions [19]. Ice fishing and skating competitions held on lake ice in the United States and Europe promote the development of local infrastructure and winter tourism [20]. Religious practices and ceremonies related to ice phenology are also observed in certain communities. In Japan, Shinto practitioners living near Lake Suwa have been recording ice phenology since 1443 and hold religious purification ceremonies in ice duration [21].

Traditional understanding and practical conditions have historically hindered the study of winter ice-covered lakes [10,22]. Due to the low water temperature and insufficient photosynthetically active radiation (PAR) during the frozen period, it was mistakenly believed that the metabolic and biological activities within the lakes were stagnant, leading to the perception of limited research value [17]. Previous studies on water environmental research and flux estimation often excluded the ice-covered period due to site selection and equipment limitations. However, it is now recognized that lake metabolism continues during the freezing period, with processes such as carbon cycling and nutrient accumulation sometimes exceeding those of the non-ice period. In Qinghai Lake [8], ice season draws large amounts of CO₂ from the atmosphere ($-0.87 \pm 0.38 \text{ g C m}^{-2} \text{ d}^{-1}$), more than twice the CO₂ flux rate during the ice-free period ($-0.41 \pm 0.35 \text{ g C m}^{-2} \text{ d}^{-1}$). In Lake Uliansuhai, the nutrient concentration ratio between the open water and the ice season was 5–10. TDS was 1050–2270 mg L⁻¹ in summer and 2430–5230 mg L⁻¹ in winter; TN was about 2 mg L⁻¹ in summer and increased to 9 mg L⁻¹ in winter [16]. There are still unexplained phenomena and unresolved issues in research on seasonally ice-covered lakes, including the specific mechanisms and processes of carbon sources and sinks in brackish lakes [8,14], the specific categories of solutes excluded and absorbed by lake ice [16,23], and the responsiveness of these lakes to climate change [24,25].

Despite extensive research by scholars from various countries, represented by Matti Leppäranta, Stephanie E. Hampton, Sapna Sharma, Blaize A. Denfeld et al. However, Hampton [26] stated in Eos Special Reports, “Although basic understanding about winter limnology has increased in the past decade, the pace of scientific progress has not kept pace with rates of ecological change”. The research on ice season is relatively limited and scattered compared to the non-ice period. Therefore, we use the Web of Science Core Collection (WOSCC) as the data source and make a bibliometric analysis of internationally published literature related to seasonal freezing lakes. This study provides a comprehensive overview of research progress, highlighting hotspots and trends in this field, and aims to guide future global research on the environmental aspects of seasonally ice-covered lakes.

2. Research History and Frontier Hotspots of Seasonal Ice-Covered Lakes during 1991–2021

We searched the articles of the Web of Science Core Collection (WOSCC) database from 1991 to 2021, using the following search item: TS = ((lake OR reservoir) NOT (*glacial OR permafrost)) AND TS = (ice OR frozen OR freezing) AND TS = (seasonal). The total number of publications found was 1141. Overall, the number of papers on seasonal ice-covered

lake research has been increasing year by year; the growth rate is significantly higher from 2011 to 2021 compared to 1991 to 2010 (Figure 1).

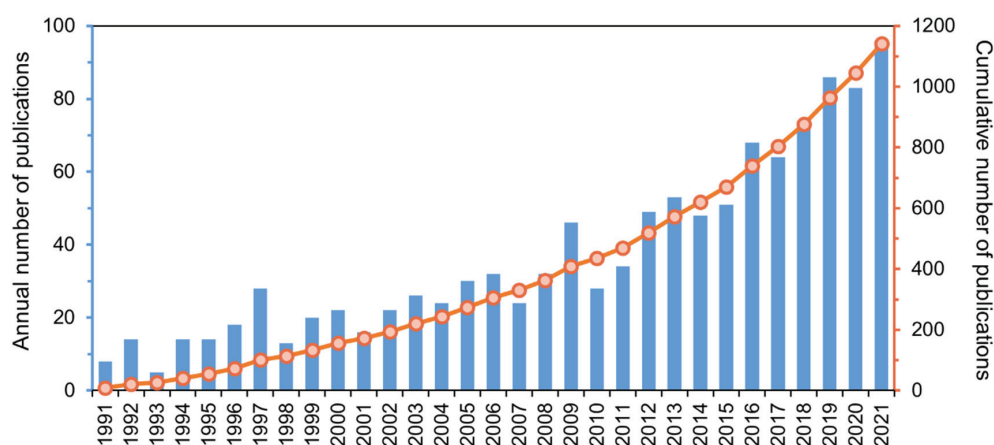


Figure 1. The annual publication volume and cumulative publication volume. A large amount of basic research found seasonal variations in the nutrient status and the dominance of planktonic species in the early stage of research (1991–1998). Starting from 1999, the impact of climate change on the water environment of seasonally frozen lakes has gradually attracted attention.

According to the statistics on the research locations of seasonally ice-covered lakes (Figure 2), 21 major research lakes are concentrated in North America (Lawrence Great Lakes), Europe (Lake Vanajanselkä, Lake Tovel), and China (Lake Uliansuhai, Lake Qinghai) between 30 and 70° N, consistent with the findings of Denfeld (2018). These studies have been conducted in 59 countries. The United States, Canada, and China are the top three countries contributing to publications, accounting for a total publication percentage of 67.69% by 2021 (Table S1). Among the 1285 institutions worldwide that focus on research in this field, the top three institutions with the most publications are the Chinese Academy of Sciences (75 papers), the Russian Academy of Sciences (55 papers), and the University of Helsinki in Finland (36 papers).

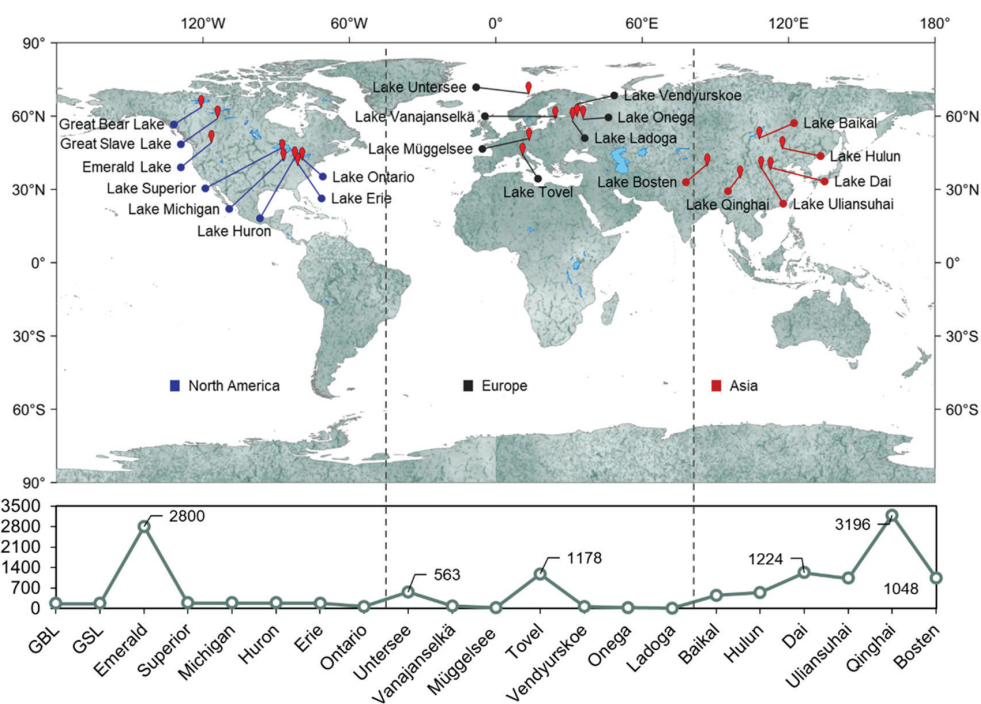


Figure 2. Major seasonally ice-covered lakes (N = 21) and their elevation.

Over the past few years, interdisciplinary studies in physics, chemistry, biology, and geology have intensified the environmental field of seasonally frozen lakes, leading to expanded study areas. This has made research in this field more comprehensive and specific. Under the background of climate warming, an in-depth study on the response of seasonally ice-covered lakes to climate change, combined with large-scale spatial and temporal data, has also promoted cooperation among research countries and institutions [4,11,27]. The exchange and cooperation between countries and institutions show different patterns (Figures S1 and S2). Perhaps the seasonally frozen lakes in Europe are mostly mountain lakes at high altitudes and high latitudes, and European countries tend to cooperate more internally, and the lakes are characterized by certain regional similarities [28].

The links between articles were analyzed by VOSviewer to identify the top 10 keywords as “climate change”, “sediments”, “lake”, “temperature”, “seasonality”, “variability” and “climate change”, “temperature”, “seasonality”, “variability”, “phytoplankton”, “water”, “climate”, “dynamics” (Figure 3). This implies the research focuses on the seasonal dynamics of sediments and water environment (nutrients and phytoplankton) during the ice period and the response of frozen lakes to climate change. This study also investigates the impact of “carbon” and “CO₂” in light of growing concerns about carbon emissions. The average appearance time (keyword link intensity) of these two topics in the four phases (Figure 4) indicates a continuous increase in attention toward “carbon” and “CO₂”, with respective values of 1995.33 (27), 2002.00 (21), 2010.27 (28), 2017.75 (91) and 1997.67 (25), 2001.80 (10), 2010.00 (19), 2018.38 (57).

The visual analysis of keyword activity (Figure 4) describes the research history of seasonally ice-covered lakes. Due to the continuous innovation of techniques and methods, research has evolved from the evolution of the dominant phytoplankton species [29,30] to the diversity of phytoplankton and planktonic microorganisms and their biological effects in winter [31]. It has also shifted from the dynamic changes in water substances [16,32,33] to the seasonal material cycle in the lake ecosystems [8,14,34]. This reveals a transition of indicators from single-factor to multi-factor research in the field of seasonally ice-covered lake water environments and an expansion of research content from the water environment to the integrated study of “hydrology” and “climate”.

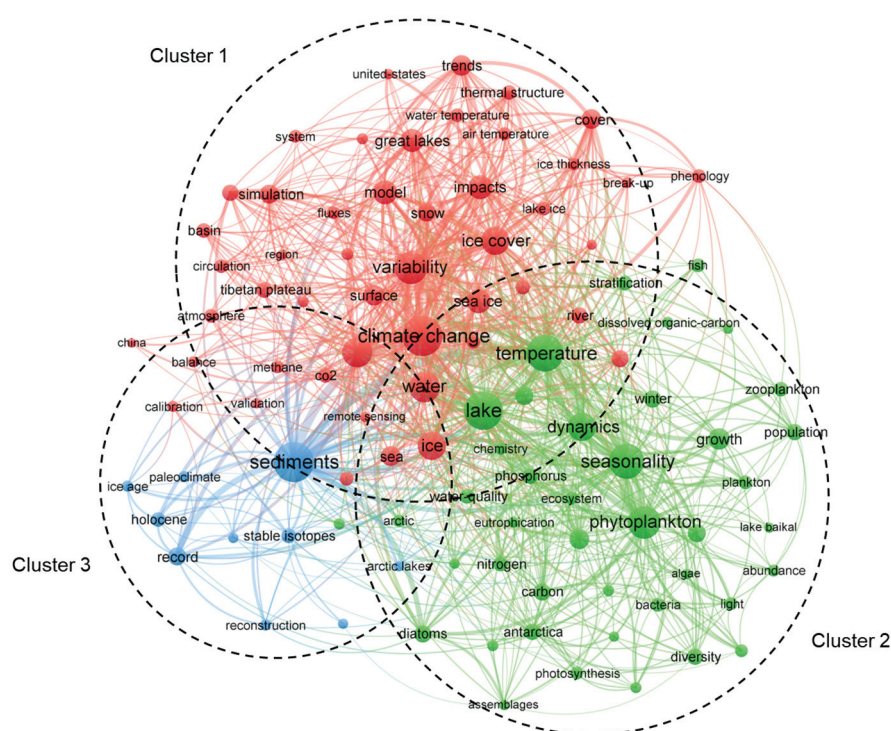


Figure 3. Cluster analysis of research keywords.

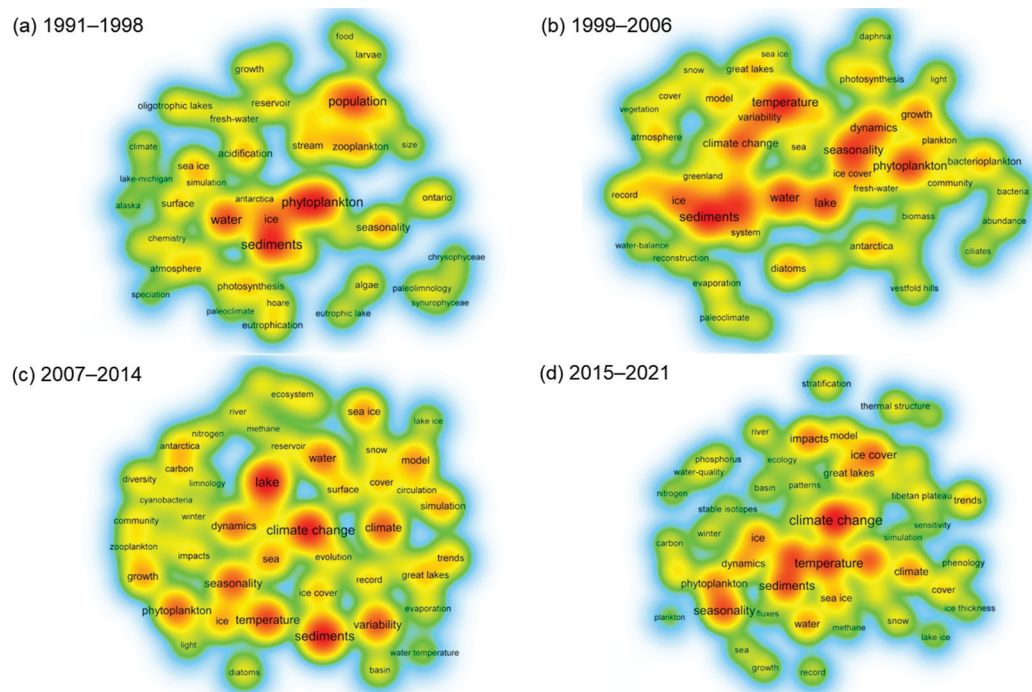


Figure 4. Keyword activity at different stages. The red indicates the keyword has the highest active degree (the research hotspot in this stage).

3. Seasonal Variability of Lakes during the Ice-Covered Period

3.1. Ice Structure and Growth Characteristics

The static lake ice of seasonally ice-covered lakes in the Northern Hemisphere consists of three main layers: primary ice, congelation ice, and superimposed ice (Figure 5). The texture of primary or superimposed ice depends on the meteorological and hydrodynamic conditions during formation. On calm water surfaces, primary ice forms as floating ice grown horizontally within the super-cooled layer, with a thickness of a few millimeters, larger horizontal crystal sizes, and a predominantly vertical c-axis orientation. Under disturbed conditions (turbulent water, windy conditions, or snowfall), primary ice forms from frazil ice crystals or condensed slush, with smaller crystal sizes (<1 mm) and a random orientation of the c-axis, which may be thicker than the former [35,36]. Superimposed ice forms above the primary ice and results from submerging the ice cover with any imaginable water source, such as liquid precipitation or meltwater. It is typically composed of condensed slush (a mixture of snow and liquid water) forming snow ice [35,37,38]. Congelation ice extends from the ice cover into the water column and is the predominant ice type in northern lakes. Its crystal structure is controlled by the primary ice, and the crystal size grows with increasing lake depth [35,39]. When the crystals in the primary ice are vertically oriented, the same pattern will be formed in the congelation ice, resulting in large macroscopic crystals. Otherwise, the congelation ice has a columnar crystal structure with a horizontal rotation of the optic axis [36,40].

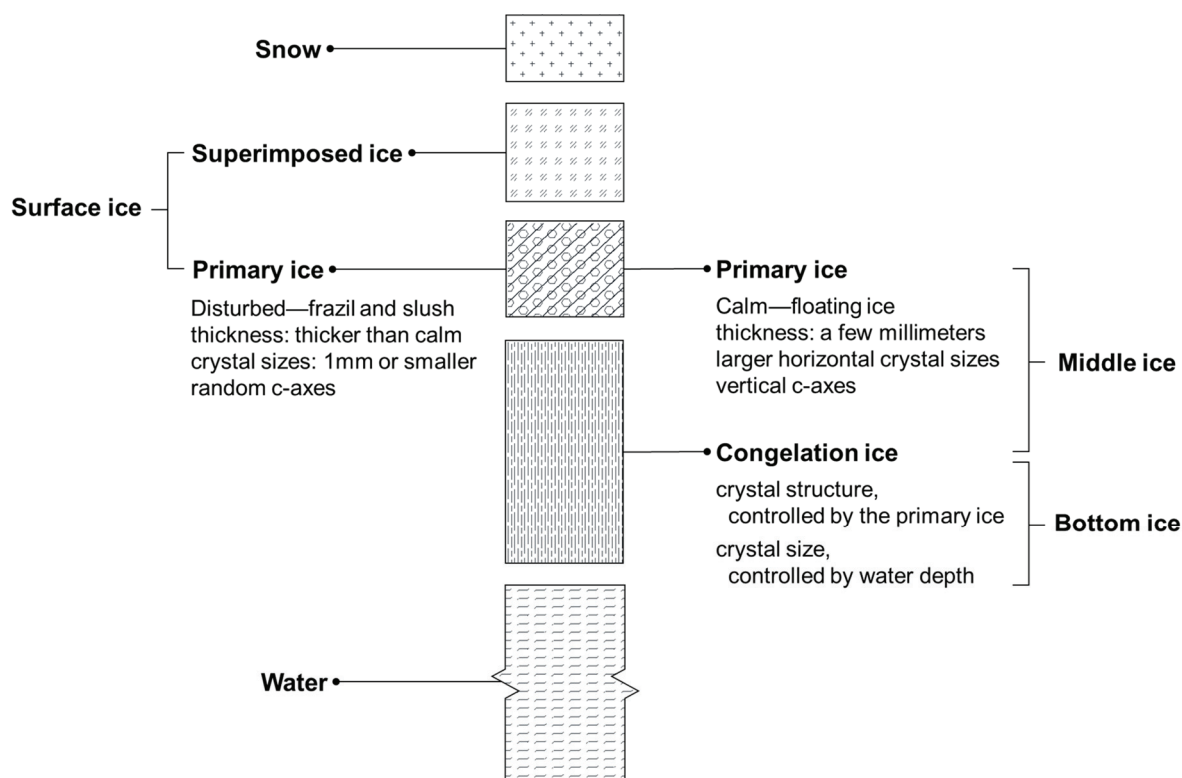


Figure 5. Lake ice structure conceptual diagram. Based on the traditional physical layering, further divisions of ice layers have been made based on the concentration of impurities.

Numerous studies have identified differences in impurity content, such as bubbles and particles in the seasonal lake ice, but they are not specifically stratified. Here, we roughly divide the lake ice into three layers based on the impurity content (Figure 5): surface ice, middle ice, and bottom ice. Surface ice generally contains snow slush and is composed of superimposed ice and primary ice under disturbed conditions, with most impurities likely resulting from water submerging the ice and atmospheric deposition [22,41]. Bottom ice (submerged congelation ice), in contact with the water layer beneath the ice and has a loose, chopsticks-like or horse-teeth shape (also known as horse teeth ice), which could accumulate substances such as chlorophyll-a, phytoplankton, algal fatty acids, and bacteria, regulating primary production by affecting light limitation and modulating dissolved oxygen (DO) and solute concentrations at the ice-water interface (excluding impurities in the ice) [42–44]. During thermodynamic growth, the latent heat released at the bottom of the ice is conducted through the ice to the atmosphere. When the latent heat flux exceeds the heat flux from water to ice, the continuous downward growth of the bottom ice increases the distance of conduction, gradually reducing its growth rate [38,40]. Middle ice mainly consists of primary ice on calm water surfaces and upper congelation ice. It has a higher purity crystal content, slower growth rate, and higher degree of solute exclusion compared to bottom ice. Therefore, the nutrient content in the ice often follows a similar C-shaped distribution pattern: surface > bottom > middle [16,23,44].

3.2. Characteristics of Water Environmental Conditions

The aquatic environment of lakes during the ice-covered period is primarily influenced by factors such as PAR, DO, and organic matter (OM) (Figure 6).

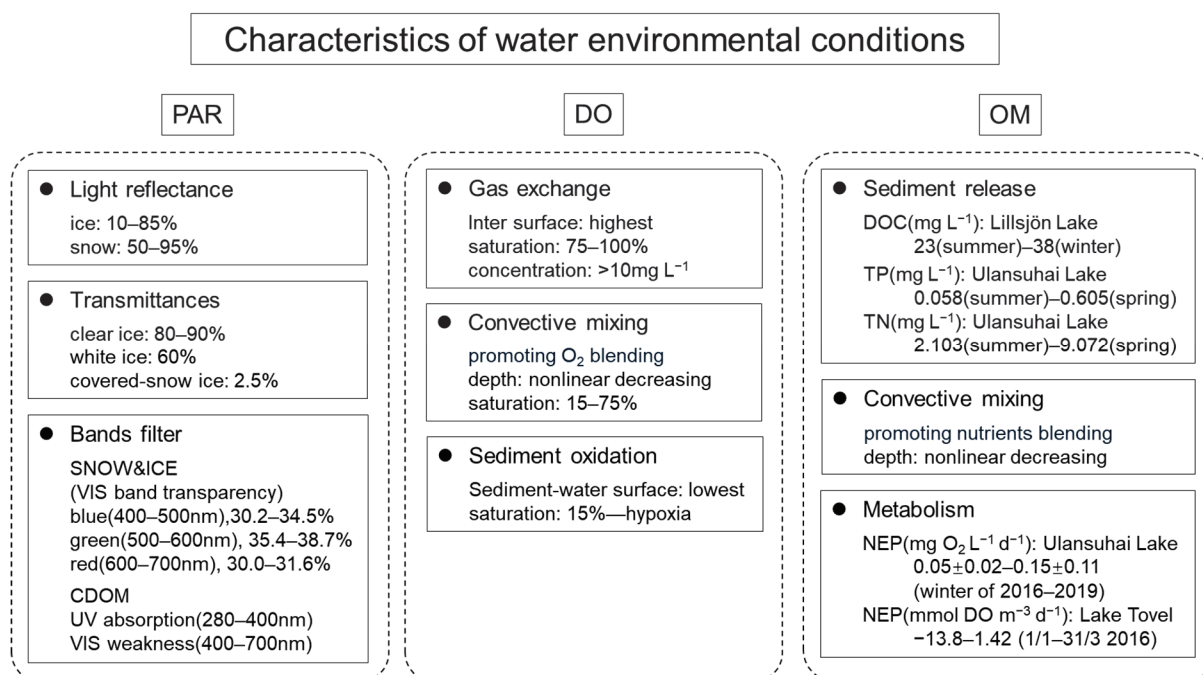


Figure 6. The main variation characteristics of water environmental conditions.

Increased lake ice coverage reduces PAR [20,45]. Light limitation occurs when PAR falls below the critical light intensity threshold for photosynthesis and biomass accumulation [46]. It is primarily caused by ice and snow albedo, ice transmittance coefficient, radiation bands filter, and colored dissolved organic matter (CDOM) in the water. Ice and snow albedo, determined by factors such as ice thickness, humic substances on the ice surface, snow grain size, and water content, affect light reflectance (lake ice: 0.10–0.85, snow: 0.50–0.95) and light attenuation coefficient, which together influence sub-ice radiation [47–49]. According to ice thickness and structure, clear ice transmittance contrasts sharply with snow-covered ice transmittance (clear ice: 80–90% range, white ice: 60%, covered-snow ice: 2.5%) [45]. Moreover, Bolsenga et al. [45] also found that covered snow and ice can filter out a significant portion of visible light, with the green band (500–600 nm) exhibiting the highest transparency (35.4–38.7%), followed by the blue band (400–500 nm, 30.2–34.5%) and the red band (600–700 nm, 30.0–31.6%). CDOM contributes to light limitation beneath the ice by ultraviolet radiation absorption (280–400 nm) and visual light weakness (400–700 nm), reducing the Secchi depth of water [49,50].

DO is another important factor influenced by lake ice during winter. The vertical stability of the water column is enhanced during the ice-covered period compared to the ice-free period, leading to distinct vertical gradients of temperature and DO concentration in the sub-ice water, as density gradient flows are generated due to heat flux from sediments [51]. The formation of ice cover restricts gas exchange and physical disturbance by wind. The exclusion of oxygen from the ice, greater primary production, and convective mixing in the upper water generally result in the highest DO saturation (75–100%) and concentration (>10 mg L⁻¹) near the surface throughout the entire lake [52–54]. As the lake depth increases, the water temperature rises continuously, and enhanced lake metabolism accelerates the consumption of DO, primarily due to biological respiration and chemical oxidation of reduced substances in the bottom sediments, leading to a different decrease in DO at the bottom layer and the lowest DO concentration around the sediment–water interface, creating an anoxic environment [53]. For example, in Eagle Lake of Canada (maximum depth ~31 m), the DO concentration remained relatively stable at all depths (~10 mg L⁻¹, 75% saturation) during pre-winter. At ~30 m depth, it depleted at 0.1 mg L⁻¹ d⁻¹ in winter and down to 4 mg L⁻¹ (31% saturation) by the following spring turnover. Under

the convective mixing and metabolism, the DO remained at $\sim 78 \text{ mg L}^{-1}$ (52% saturation) in the middle layer and ultimately approached hypoxia (15% saturation) at the bottom [54].

In Lake Tovel, a deep, oligotrophic lake at a high altitude in Italy (maximum depth $\sim 39 \text{ m}$), the rate of O_2 consumption varies at different depths [32]. In March 2014–2016, the DO concentration at 5 m depth averaged $\sim 11 \text{ mg L}^{-1}$, with an unstable seasonal pattern influenced by radiation infiltration. At a depth of 25 m, the DO concentration averaged $\sim 8.5 \text{ mg L}^{-1}$, and the pattern of DO was consistently decreasing, with an average rate of decrease of $0.02 \text{ mg L}^{-1} \text{ d}^{-1}$. In shallower lakes, solar radiation intensity can also affect DO by altering entire convective mixing. Transmitted radiation and heat released from sediments jointly influence thermal conduction in the water column, triggering convective turbulent mixing and promoting the uniform distribution of oxygen. In Lake Uliansuhai in Inner Mongolia, China [17], it was observed that during the growth and stable period of ice, local turbulence or turbulence–layer flow mixing can occur in the top or middle layers, promoting heat and oxygen mixing. After the ice melts, convection transports oxygen downward to the near-bottom layer, alleviating or preventing hypoxic conditions. In Lake Vanajanselkä in southern Finland [29], biological metabolism reduction decreases DO in winter. In spring, sunlight penetrates the ice and induces convection, resulting in a more even vertical distribution of DO.

The low-temperature environment and limited light availability result in lower net ecosystem production during the ice duration, such as Lake Ulansuhai, 2016–2019, $0.05 \pm 0.02\text{--}0.15 \pm 0.11 \text{ mg O}_2 \text{ L}^{-1} \text{ d}^{-1}$ [17], and Lake Tovel, spring in 2016: $-13.80\text{--}1.42 \text{ mmol DO m}^{-3} \text{ d}^{-1}$ [32]. Although most of DOM and 90% of the salt excluded in the ice growth process leads to an increase in nutrient concentration at the ice–water interface, the release from sediment is the main reason for increased eutrophication in the entire lake [16,17,49]. The cold anoxic conditions also facilitate the release of large amounts of other reduced substances (hydrogen, methane, acetate, ammonium, etc.) and oxidants (hydrogen peroxide, sulfates, carbon dioxide, etc.) and heavy metals, leading to significant changes in water conductivity and salinity during the ice-covered period and freeze–thaw cycles and altering the thermodynamic properties and convective mixing structure of lakes, thereby affecting their aquatic ecosystems [55–57]. In addition, some studies also proved the limitation of PAR under the ice and higher eutrophication levels could result in weaker convective mixing and a more stable density layer [46].

3.3. The Growth Changes of Primary Producers

Changes in environmental conditions can strongly limit the growth of certain species and remove growth restrictions for others. Light availability is a primary limiting factor, leading to a decrease in overall primary production during the frozen period. In Gossenköllesee Lake, the primary production during the freezing period is 56% lower than in the ice-free season [58]. Although the community structure is influenced by factors such as light conditions and nutrient concentrations of lakes, biodiversity is still present in the ice duration [30,59].

The light conditions in the lake affect the composition of dominant species and community structure of planktonic plants during the ice-covered period. In Lake Balkan, a shallow, large, and nutrient-rich lake [59], the most abundant planktonic plants under the ice layer are *Cyclotella meneghiniana* and *S. uvella* before and after snowfall. In Lake Erie [30], the dominant species of planktonic plants is *Aulacoseira islandica*, with *Cyclotella* spp. as the subdominant species. In Lake Vanajanselkä [29], which is shallow and eutrophic, the most abundant planktonic plant communities consist of cryptophytes (44%), chrysophytes (23%), and chlorophytes (6%) in mid-winter. In comparison, cyanobacteria (39%), cryptophytes (29%), and diatoms (13%) become dominant in late winter. The main reason for the dominance of the former in winter was their ability to adapt to low temperatures and low light conditions, while later, cyanobacteria became the main dominant species due to rapid blooms prompted by warmer temperatures and enhanced light conditions [29]. The ability of these dominant species to continue to flourish under the ice can be attributed to their

unique adaptations under low-light and low-temperature conditions (efficient light energy utilization, buoyancy regulation, ability to move, and tolerance to low temperatures and nutrients) [30,59]. For example, *Cyclotella meneghiniana* has some cold tolerance and is able to maintain metabolic activity at lower temperatures. The species also benefits from its small cell size and ability to regulate buoyancy through changes in lipid content to move through the water column to the optimal light level and utilize the low light through the ice more efficiently.

Furthermore, effective PAR also influences the distribution of planktonic plants in seasonally ice-covered lakes. Studies on lake ice have found that planktonic plants tend to aggregate at the ice-water interface, such as the filamentous diatom community suspended under the ice in Lake Baikal [60] and algal aggregations at the ice-water interface in Lake Saint-Pierre in southern Canada [61]. Lake ice can also absorb some planktonic plant cells. In the freezing Laurentian Great Lakes [42], filamentous diatoms were found to be adsorbed onto the overlying ice through frazil ice. In Simoncouche Lake [44], planktonic plants (*Peridinium* sp., *Cryptomonas* sp., *Synechococcus* sp., etc.) were excluded from lake ice water, while certain populations (*Botryococcus* sp., *Chromulina* sp., *Gymnodinium* sp., etc.) exhibited aggregation within the ice, with their numbers remaining constant or increasing in winter. This proves lake ice can provide stable and potentially beneficial winter habitats for some planktonic plants. When ice cracks, the release of planktonic plant cells promotes spring blooms [44,61]. At this time, the rising of PAR and temperature trigger convective mixing in the water, accelerating the growth of planktonic plants and providing the foundation for spring blooms [29,59]. For some lakes with thicker ice cover and longer ice periods, phytoplankton biomass was correlated with certain nutrient contents. In 28 ice-covered lakes in the Songnen Plain of northeastern China during winter, phytoplankton growth was mainly related to the total nitrogen concentration in the water column and the difference in total phosphorus concentration at the ice–water interface, with contribution rates being, respectively, 25.5–35.0% and 9.2–11.3% [62].

Convective mixing induced by solar radiation has a notable impact on the growth of planktonic plants in freshwater lakes with a low coefficient of expansion ($<3.98\text{ }^{\circ}\text{C}$) [63]. It was found that when there was no convective mixing layer, light conditions were sufficient to support the growth of 50.0% of planktonic plants in four mesotrophic lakes in the northern temperate zone [46]. However, in the presence of convective mixing, only 37.5% of planktonic plants had enough light to increase biomass. This is likely due to the fact that a convective mixing layer can significantly affect the vertical position of non-motile planktonic plants in the upper water column and influence the light intensity they experience during the day. For instance, buoyant planktonic plants can be cycled through the convective mixing layer, providing them with improved light conditions and enhancing their growth and photosynthetic rates [63,64]. Conversely, if positively buoyant or motile planktonic plants are directly beneath the ice, they may have increased opportunities to acquire light, while those within the convective mixing layer may cycle deeper within the water column, reducing their access to light [51].

3.4. Material Circulation

With climate warming, carbon emissions and carbon neutrality have become hot topics of discussion. The carbon cycling process during the freezing period of lakes and its response to climate warming are gradually receiving attention.

During the ice-covered period, the decrease in hydrological inputs (such as surrounding soil, rivers, and groundwater) and hindered gas exchange at the water-air interface constrains the external input of greenhouse gases [65]. Due to higher light limitation and OM, respiration, mineralization, and microbial activity dominate the primary productivity in most lakes, leading to the accumulation of CO_2 [66,67]. At the same time, changes in DO gradients under the ice create environmental conditions for the transformation of CO_2 and CH_4 . Under anoxic conditions, archaea utilize CO_2 and other carbon-containing compounds to produce CH_4 in the bottom layer [68,69], which exists in large amounts at the

sediment-water interface and ice-water interface through diffusion or ebullition (bubble-mediated transport) [70]. The produced CH_4 is then consumed by methane-oxidizing bacteria in the surface sediment or upper layer, with CO_2 as a typical byproduct [71,72]. Furthermore, in terms of lake morphology, sediment metabolism, diffusion, and transformation of CO_2 often result in the highest CO_2 concentrations in the bottom water of most frozen lakes. The overall CO_2 concentration beneath the ice in large, deep lakes may be lower than that in small, shallow lakes [3]. Denfeld et al. [73] divided 506 lakes located in Finland and Sweden into four depth groups and found the average pCO_2 near the surface decreased from $\sim 5000 \mu\text{atm}$ (mean depth $< 2.5 \text{ m}$) to $\sim 2000 \mu\text{atm}$ (mean depth $> 4.5 \text{ m}$). This may be due to incomplete mixing in autumn and faster ice development, which leads to lower oxygen levels and more accumulation of CO_2 and CH_4 during the freezing period. Additionally, small lakes can cool down quickly and are less affected by wind disturbances [74].

Most seasonal frozen lakes have a certain carbon sink effect in winter. It is well-known that the solubility of gases in water increases as temperature decreases. Before the freezing period, the lake can absorb CO_2 from the atmosphere through the water-air interface. Once the freezing period begins, the lake ice blocks most of the gas exchange, and CO_2 mainly accumulates within the lake [8,18]. Changes in ice phenology caused by climate warming reduce the accumulation of CO_2 produced by winter lake metabolism and increase the pH value of the water in spring and summer, diminishing the carbon sink effect [14]. Differences in salinity lead to varying source-sink processes in freshwater lakes and saline lakes in winter. Freshwater lakes mainly achieve CO_2 supersaturation through metabolism and release CO_2 into the atmosphere [75]. With climate warming, the CO_2 emissions decrease because of reduced CO_2 accumulation under the ice.

In contrast, the alkaline conditions (pH 8–11) of saline lakes are influenced by carbonate precipitation or dissolution reactions and the chemical enhancement of the air-water interface CO_2 exchange rate [34,76], primarily determined by the average water pH [14]. When the pH of water exceeds 9.0, CO_2 is converted to HCO_3^- and CO_3^{2-} , promoting carbonate precipitation reactions [76], and CO_2 becomes undersaturated. Consequently, as the water temperature decreases during the freezing process, the salinity and pH of saline lakes increase, pCO_2 decreases, and the total absorption of CO_2 continues to increase [8,14]. During the frozen period, weaker gas exchange at the water-air interface and higher lake metabolism lead to continuous accumulation of CO_2 in the water. As lake ice breaks, the increased gas exchange leads to a decrease in the solubility of gases in water and a reduction in CO_2 flux (depending on the pH of the water at that time, it may be released into the atmosphere). When the temperature rises in spring and solar radiation increases, saline lakes gradually regain their higher primary productivity, fixing a large amount of inorganic carbon stored in the lake from the freezing process and the accumulation during the freezing period, showing a stronger ability to store inorganic carbon than freshwater lakes [34,77,78]. For saline lakes, the reduction in lake water volume caused by climate warming increases water salinity. A shorter ice-covered period results in less accumulation of CO_2 under the ice and higher pH values during spring and summer, which means the seasonal freezing saline lakes emit less CO_2 [14]. Furthermore, studies have shown that high temperatures can lead to autogenic carbonate precipitation, reducing the concentration of Ca^{2+} , which favors CO_2 emissions. That means rising temperatures may cause saline lakes to transition from a carbon sink to a carbon source again [79].

4. Investigation of Factors Affecting Seasonal Ice Duration

4.1. Global Climate Change

Recently, studies comparing time series data have revealed a trend of shorter ice cover duration and thinner ice thickness in lakes across the Northern Hemisphere [11]. Lopez et al. [27] studied 152 lakes located in the Northern Hemisphere and found that 97% of the lakes were shrinking ice cover duration, and the ice breakup dates advanced at a rate of $1.2 \text{ d decade}^{-1}$ during 1951–2014. The ice duration and thickness of five temperate

lakes located in northern Poland decreased at rates of $5.4 \text{ d decade}^{-1}$ and $2.5 \text{ cm decade}^{-1}$ from 1961 to 2017 and are predicted to lose their ice season at a rate between 4.5 and $10.0 \text{ d decade}^{-1}$, and ice thickness will decrease by between 3.0 and $5.0 \text{ cm decade}^{-1}$ during the 21st century (ice thickness $0.12 < R^2 < 0.24$, $p < 0.001$; ice duration $0.14 < R^2 < 0.18$, $p < 0.001$) [80]. The fraction of maximum ice thickness for 402 shallow lakes of the North Slope of Alaska decreased from 51% to 26% during 2000–2011, while their ice cover was thinner by 21–38 cm, and the ice season was shorter by about 24 days in 1950–2011 [81]. A large number of lakes are completely losing their ice cover. Under the background of climate warming, winter surface water temperature plays a crucial role in influencing lake ice phenology, along with factors such as precipitation, solar radiation, and wind. The increase in winter precipitation (snowfall) can control the physical structure and transparency of lake ice cover by suppressing black ice growth and promoting white ice growth, thereby regulating the amount of radiation entering the lake [9]. At the same time, the rise in surface water temperature leads to shorter ice cover duration and thinner lake ice, intensifying the influence of solar radiation and wind on winter lake mixing, resulting in accelerated ice formation in autumn and hastens melting in spring [53,80]. The lack of lake ice coverage (23%) also led to higher evaporation rates (58% increase) and more water loss (natural lakes: $2.1\% \text{ decade}^{-1}$, artificial reservoirs: $5.4\% \text{ decade}^{-1}$) from 1985 to 2018 [82] and the global annual lake evaporation increase by 16% ($R^2 = 0.82$) by the end of the 21st century [83], which can affect regional air humidity and hydrological processes [84]. It is worth noting that higher ice coverage often experiences high autumn evaporation rates (water temperature cooling), but increased evaporation rates in late winter and the following summer and early autumn may also cause lower lake ice coverage (depleting from 90% in 2008–2009 to 31% in 2009–2010), which reflects the complexity and necessity of studies on the interannual climate-seasonal ice phenology-evaporation feedback process [85].

The warming seasonal pattern will also impact the response of planktonic organisms in lake ecosystems to climate change. Due to shorter ice cover duration and higher surface water temperature, the physical conditions and nutrient status of the water have changed (Section 3.2). This inhibits the growth of planktonic organisms adapted to winter's low temperature and hypoxic conditions, while some rapidly growing spring species, such as diatoms and copepods, exhibit a pronounced trend of earlier (2.17 d year^{-1} , 2000–2020) and synchronized blooming [86]. Although some slow-growing, long-living, and more complex summer planktonic species are more affected during crucial developmental stages (e.g., resting stage hatching in cladocerans, *Dreissena* spawning [87], the combined effects of predator–prey relationships and shortened ice cover duration result in a gradual reduction and disappearance of winter phytoplankton blooms in seasonally frozen lakes, with maximum biomass shifting towards summer [88].

In addition, seasonally frozen lakes will gradually lose their lakes in the future, regardless of GHG emissions. Under a climate scenario with substantially lower GHG emissions (RCP 2.6), winter ice thickness and ice period will decrease by 0.1 m and $\sim 15 \text{ d}$, respectively, by 2100, while under a higher emissions scenario (RCP 8.5), ice thickness and ice duration are projected to decrease by 0.17 m and 40 days (RCT, $p > 0.1$) [89]. Therefore, reducing greenhouse gas emissions is crucial for minimizing the loss of seasonally ice-covered lakes and mitigating the associated ecological, cultural, and societal impacts [25].

4.2. Individual Characteristics of Lakes

In recent years, Sharma et al. [2] and Warne et al. [11] analyzed datasets and found that lower altitude, western longitude, and lower latitude deep lakes are more influenced by climate in terms of their ice phenology, which suggests, besides surface temperature trends, individual characteristics of seasonally ice-covered lakes such as surface area, depth, and geographical location can also have an impact on ice phenology.

In winter, as the lake ice forms and temperatures decrease, the lake undergoes vertical density-driven cooling from the water surface downwards. Deeper lakes often have greater

heat storage capacity and require a longer cooling period below the freezing point to freeze [90].

Dimictic lakes undergo complete vertical mixing from top to bottom when they cool or warm and through the maximum density temperature (T_{MD} , 3.984 °C at zero salinity) at the surface pressure [91]. In shallow freshwater lakes during the ice-covered period, stable inverse thermal stratification forms and persists beneath the ice when the water temperature is below the T_{MD} [92]. When the lake ice begins to melt, solar radiation penetrates the ice cover and drives turbulent convection [49] until the overall temperature reaches or exceeds the T_{MD} . For example, in Lake Onega (mean depth: 15 m, max depth: 30 m), higher solar radiation passing through the ice intensifies the daytime activity of the convective mixing layer (reaching depths of 20 m), resulting in a slow overall temperature increase until the end of the ice-covered period [93], promoting the breakup and melting of the ice layer in spring [94]. However, complete sub-ice convective mixing may not occur because of the stratification of salinity in the water. Some of the shallower mid-latitude salt lakes during the freezing period may have a warm intermediate layer formed by salinity stratification, separating the overlying inverse thermal stratification from the underlying positive thermal stratification. For example, in a shallow thermokarst lake in the central part of the Qinghai-Tibet Plateau (mean depth: 120 m, max depth: 150 m), the vertical thermal structure beneath the ice consists of stable, strong inverse thermal stratification and a lower convective layer reaching the lake bottom. The stronger inverse thermal stratification induces horizontal and vertical advection, accelerating ice melting. Meanwhile, a warm layer with gradually increasing thickness and temperature has been present between the two since the middle equilibrium period, accumulating more heat during the ice-covered period, with temperatures rising to 7–9 °C at the end of the frozen period [95].

In deeper seasonally ice-covered lakes, lake ice phenology is typically associated with the upper water column. Since the T_{MD} decreases with increasing pressure in the deeper lake, once the ~4 °C water begins to sink, the interface at the bottom of the upper mixed layer falls below the depth corresponding to the temperature of the T_{MD} at that water depth, resulting in the thermobaric instability being activated and free convection until colder water closer to the T_{MD} curve is encountered at greater depth [96]. Therefore, the upper and lower water masses exhibit distinct temperature profiles and convective mixing patterns with a fuzzy boundary at a certain depth. For example, based on the difference between water temperature and T_{MD} decreases with depth, the Great Slave Lake (max depth: 614 m) in the Mackenzie River Basin of Canada is divided into inverse thermal stratification (<200 m), thermobaric horizon (~200 m), and weakly permanent stratification (>200 m). At the end of the ice duration, solar radiation penetrates the ice, driving convective mixing in the upper layers, deepening the mixed layer, promoting ice breakup and melting, and influencing the timing of spring phytoplankton production [92].

Elevation and latitude have a significant impact on the ice phenology of lakes. Lepäranta and Wen [12] demonstrated through ice phenology time series from 10 Eurasian sites that local temperature (determined by elevation, latitude, and longitude) and solar radiation (determined by latitude) can influence the dates of freezing, thawing, and ice duration. Lakes at higher elevations may also be cooler and less influenced by climate change compared to lakes at lower elevations. For example, during 2000–2016, Qinghai Lake, located on the Tibetan Plateau (3196 m elevation), experienced relatively small fluctuations in freezing, thawing, and ice duration, with values of 20 days, 10 days, and 108 days, respectively [97]. Of the seven alpine lakes (3126–3620 m elevation) in the same region of Colorado, USA, 1981–2014, those at higher elevations demonstrated more consistent freezing and thawing times [98]. Compared to the historical rates of change in northern hemisphere water bodies (1846–1995), the average rate of change for freeze-up and breakup dates in the Great Lakes region was 5.8 times faster and 3.3 times faster, respectively. The average ice duration decreased by 5.3 d decade⁻¹, with the southwest lakes experiencing even faster rates of change in breakup dates and ice duration [99].

Additionally, a clear negative correlation between lake surface area and the start of ice cover, as well as a potential negative correlation with ice duration (Figure 7). Theoretically, larger lakes with greater surface areas often absorb more radiation and have a larger gas exchange interface, facilitating more efficient heat exchange, leading to faster temperature changes in the water during winter and spring, accelerating the freezing and thawing of ice and resulting in earlier ice formation and breakup. However, it should be noted that this could not determine whether the lake area directly influences ice duration or the direction of its impact. Currently, there is a lack of research exploring the relationship and mechanisms between winter lake ice phenology and lake area. Future studies could potentially investigate the response of different types of seasonally ice-covered lakes to climate change by using it as a starting point.

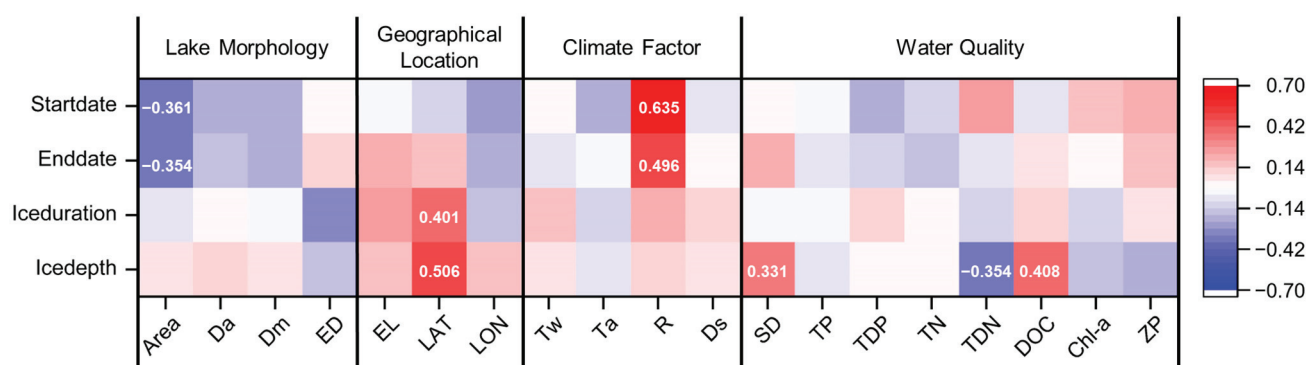


Figure 7. The heat map shows the relationship between ice phenology parameters and influencing factors of seasonally frozen lakes (N = 73). The numbers within the boxes represent Pearson correlation coefficients. The labels on the X-axis represent specific influencing factors, including surface area (Area), lake average depth (Da), lake max depth (Dm), euphotic depth (ED), elevation (EL), station latitude (LAT), station longitude (LON), water temperature (Tw), air temperature (Ta), radiation intensity (R), snow depth (Ds), Secchi depth (SD), total phosphorus (TP), total dissolved phosphorus (TDP), total nitrogen (TN), total dissolved nitrogen (TDN), dissolved organic carbon (DOC), Chlorophylla (Chl-a), zooplankton biomass (ZP).

5. Conclusions and Future Trends

In this study, we discuss the growth characteristics of seasonal ice cover, changes in hydric environmental conditions and primary production, and the accumulation and transformation of carbon dioxide by winter lakes. We also provide an overview of winter lake ice cover periods, evapotranspiration, planktonic responses to global climate change, the effects of greenhouse gas emissions on ice-free events, and the effects of individual characteristics on seasonally frozen lakes. We found that most current studies focus on analyzing water phytoplankton succession, quality changes, and ice phenology in individual seasonal frozen lakes. This existing work provides an important foundation for our continued exploration and study of ice-covered lake ecosystems in the future. In addition, the development of remote sensing has led to the emergence of joint research on multiple lakes with similar or different characteristics at various spatial scales. To comprehensively understand the response of global seasonal frozen lakes to climate change and predict local climate, regression analysis, R, machine learning, and other methods are combined with large datasets containing time series data on lake morphology, geographical location, and climate factors. This helps explore and simulate the impacts of various factors on winter lakes and establish a global-scale frozen lake data model. In addition, the following aspects still need further exploration: future impacts of meteorological/climatic parameters on ice-covered ecosystems, solute changes and carbon emissions in high-altitude lakes and salt lakes in winter, chemical composition and distribution patterns at the ice–water interface, differences in phytoplankton responses among species characteristics, lake types, and regional climates, and rapid stratification methods for measuring solute

content or ice physical properties, the use of sensitivity analyses, and/or multi-criteria methods to determine the impact of analyzed parameters on ice thickness.

Supplementary Materials: The following supporting information can be downloaded at: <https://www.mdpi.com/article/10.3390/w16192727/s1>, Table S1. TOP 10 most productive countries on seasonal ice-covered lakes research during 1991–2021. Figure S1. Research Collaboration between Countries. Figure S2. Global Institutional Collaboration.

Author Contributions: Q.W.: investigation, visualization, writing—original draft. F.Y.: conceptualization, writing—review and editing. W.F., M.J., T.P., D.F. and Z.H.: investigation, data curation, writing—review and editing; H.L.: writing review and editing, funding acquisition, project administration, supervision. All authors have read and agreed to the published version of the manuscript.

Funding: This work was supported by the National Key Research and Development Program (grant ID: 2021YFC3201001) and the Foundation of Important Science & Technology Specific Projects of Ordos (grant ID: ZD20232301).

Data Availability Statement: No new data were created or analyzed in this study.

Acknowledgments: We thank the editors and anonymous reviewers for their excellent comments on the manuscript.

Conflicts of Interest: The authors declare that they have no known competing financial interests or personal relationships that could have appeared to influence the work reported in this paper.

References

1. Verpoorter, C.; Kutser, T.; Seekell, D.A.; Tranvik, L.J. A Global Inventory of Lakes Based on High-Resolution Satellite Imagery. *Geophys. Res. Lett.* **2014**, *41*, 6396–6402. [CrossRef]
2. Sharma, S.; Blagrove, K.; Magnuson, J.J.; O'Reilly, C.M.; Oliver, S.; Batt, R.D.; Magee, M.R.; Straile, D.; Weyhenmeyer, G.A.; Winslow, L.; et al. Widespread Loss of Lake Ice around the Northern Hemisphere in a Warming World. *Nat. Clim. Change* **2019**, *9*, 227–231. [CrossRef]
3. Denfeld, B.A.; Baulch, H.M.; del Giorgio, P.A.; Hampton, S.E.; Karlsson, J. A Synthesis of Carbon Dioxide and Methane Dynamics during the Ice-Covered Period of Northern Lakes. *Limnol. Oceanogr. Lett.* **2018**, *3*, 117–131. [CrossRef]
4. Wang, X.; Feng, L.; Gibson, L.; Qi, W.; Liu, J.; Zheng, Y.; Tang, J.; Zeng, Z.; Zheng, C. High-Resolution Mapping of Ice Cover Changes in over 33,000 Lakes across the North Temperate Zone. *Geophys. Res. Lett.* **2021**, *48*, e2021GL095614. [CrossRef]
5. Yan, F.; Sillanpää, M.; Kang, S.; Aho, K.S.; Qu, B.; Wei, D.; Li, X.; Li, C.; Raymond, P.A. Lakes on the Tibetan Plateau as Conduits of Greenhouse Gases to the Atmosphere. *J. Geophys. Res. Biogeosci.* **2018**, *123*, 2091–2103. [CrossRef]
6. Cohen, A.P.; Melack, J.M. Carbon Dioxide Supersaturation in High-Elevation Oligotrophic Lakes and Reservoirs in the Sierra Nevada, California. *Limnol. Oceanogr.* **2020**, *65*, 612–626. [CrossRef]
7. Huang, L.; Timmermann, A.; Lee, S.-S.; Rodgers, K.B.; Yamaguchi, R.; Chung, E.-S. Emerging Unprecedented Lake Ice Loss in Climate Change Projections. *Nat. Commun.* **2022**, *13*, 5798. [CrossRef]
8. Li, X.; Shi, F.; Ma, Y.; Zhao, S.; Wei, J. Significant Winter CO₂ Uptake by Saline Lakes on the Qinghai-Tibet Plateau. *Glob. Change Biol.* **2022**, *28*, 2041–2052. [CrossRef]
9. Zdrovennova, G.; Palshin, N.; Golosov, S.; Efremova, T.; Belashev, B.; Bogdanov, S.; Fedorova, I.; Zverev, I.; Zdrovennov, R.; Terzhevik, A. Dissolved Oxygen in a Shallow Ice-Covered Lake in Winter: Effect of Changes in Light, Thermal and Ice Regimes. *Water* **2021**, *13*, 2435. [CrossRef]
10. Murfitt, J.; Duguay, C.R. 50 Years of Lake Ice Research from Active Microwave Remote Sensing: Progress and Prospects. *Remote Sens. Environ.* **2021**, *264*, 112616. [CrossRef]
11. Warne, C.P.K.; McCann, K.S.; Rooney, N.; Cazelles, K.; Guzzo, M.M. Geography and Morphology Affect the Ice Duration Dynamics of Northern Hemisphere Lakes Worldwide. *Geophys. Res. Lett.* **2020**, *47*, e2020GL087953. [CrossRef]
12. Leppäranta, M.; Wen, L. Ice Phenology in Eurasian Lakes over Spatial Location and Altitude. *Water* **2022**, *14*, 1037. [CrossRef]
13. Wright, D.M.; Posselt, D.J.; Steiner, A.L. Sensitivity of Lake-Effect Snowfall to Lake Ice Cover and Temperature in the Great Lakes Region. *Mon. Weather Rev.* **2013**, *141*, 670–689. [CrossRef]
14. Finlay, K.; Vogt, R.J.; Bogard, M.J.; Wissel, B.; Tutolo, B.M.; Simpson, G.L.; Leavitt, P.R. Decrease in CO₂ Efflux from Northern Hardwater Lakes with Increasing Atmospheric Warming. *Nature* **2015**, *519*, 215–218. [CrossRef]
15. Sadro, S.; Sickman, J.O.; Melack, J.M.; Skeen, K. Effects of Climate Variability on Snowmelt and Implications for Organic Matter in a High-Elevation Lake. *Water Resour. Res.* **2018**, *54*, 4563–4578. [CrossRef]
16. Yang, F.; Li, C.; Leppäranta, M.; Shi, X.; Zhao, S.; Zhang, C. Notable Increases in Nutrient Concentrations in a Shallow Lake during Seasonal Ice Growth. *Water Sci. Technol.* **2016**, *74*, 2773–2783. [CrossRef]
17. Huang, W.; Zhang, Z.; Li, Z.; Leppäranta, M.; Arvola, L.; Song, S.; Huotari, J.; Lin, Z. Under-Ice Dissolved Oxygen and Metabolism Dynamics in a Shallow Lake: The Critical Role of Ice and Snow. *Water Resour. Res.* **2021**, *57*, e2020WR027990. [CrossRef]

18. Finlay, K.; Vogt, R.J.; Simpson, G.L.; Leavitt, P.R. Seasonality of PCO₂ in a Hard-Water Lake of the Northern Great Plains: The Legacy Effects of Climate and Limnological Conditions over 36 Years. *Limnol. Oceanogr.* **2019**, *64*, S118–S129. [CrossRef]
19. Hori, Y.; Cheng, V.Y.S.; Gough, W.A.; Jien, J.Y.; Tsuji, L.J.S. Implications of Projected Climate Change on Winter Road Systems in Ontario's Far North, Canada. *Clim. Change* **2018**, *148*, 109–122. [CrossRef]
20. Leppäranta, M. *Freezing of Lakes and the Evolution of Their Ice Cover*; Springer Science & Business Media: Berlin/Heidelberg, Germany, 2014; ISBN 9783642290817.
21. Knoll, L.B.; Sharma, S.; Denfeld, B.A.; Flaim, G.; Hori, Y.; Magnuson, J.J.; Straile, D.; Weyhenmeyer, G.A. Consequences of Lake and River Ice Loss on Cultural Ecosystem Services. *Limnol. Oceanogr. Lett.* **2019**, *4*, 119–131. [CrossRef]
22. Salonen, K.; Leppäranta, M.; Viljanen, M.; Gulati, R.D. Perspectives in Winter Limnology: Closing the Annual Cycle of Freezing Lakes. *Aquat. Ecol.* **2009**, *43*, 609–616. [CrossRef]
23. Han, Z.M.; Jia, K.L.; Zhao, S.N.; Sun, B.; Wang, X.Y. Distribution Characteristics of the Nutrients and Ion of Hulun Lake in Frozen and Unfrozen Period. *Ecol. Environ. Sci.* **2017**, *26*, 1201–1209.
24. Woolway, R.I.; Kraemer, B.M.; Lenters, J.D.; Merchant, C.J.; O'Reilly, C.M.; Sharma, S. Global Lake Responses to Climate Change. *Nat. Rev. Earth Environ.* **2020**, *1*, 388–403. [CrossRef]
25. Woolway, R.I.; Sharma, S.; Smol, J.P. Lakes in Hot Water: The Impacts of a Changing Climate on Aquatic Ecosystems. *BioScience* **2022**, *72*, 1050–1061. [CrossRef]
26. Hampton, S.E.; Powers, S.; Devlin, S.; McKnight, D. Big Questions, Few Answers about What Happens under Lake Ice. *EOS* **2020**, *101*. [CrossRef]
27. Lopez, L.S.; Hewitt, B.A.; Sharma, S. Reaching a Breaking Point: How Is Climate Change Influencing the Timing of Ice Breakup in Lakes across the Northern Hemisphere? *Limnol. Oceanogr.* **2019**, *64*, 2621–2631. [CrossRef]
28. George, D.G. (Ed.) *The Impact of Climate Change on European Lakes*; Aquatic Ecology Series; Springer: Dordrecht, The Netherlands, 2010; Volume 4, pp. 1–13.
29. Leppäranta, M.; Heini, A.; Jaatinen, E.; Arvola, L. The Influence of Ice Season on the Physical and Ecological Conditions in Lake Vanajanselkä, Southern Finland. *Water Qual. Res. J.* **2012**, *47*, 287–299. [CrossRef]
30. Twiss, M.R.; McKay, R.M.L.; Bourbonniere, R.A.; Bullerjahn, G.S.; Carrick, H.J.; Smith, R.E.H.; Winter, J.G.; D'souza, N.A.; Furey, P.C.; Lashaway, A.R.; et al. Diatoms Abound in Ice-Covered Lake Erie: An Investigation of Offshore Winter Limnology in Lake Erie over the Period 2007 to 2010. *J. Great Lakes Res.* **2012**, *38*, 18–30. [CrossRef]
31. Butler, T.M.; Wilhelm, A.-C.; Dwyer, A.C.; Webb, P.N.; Baldwin, A.L.; Techtman, S.M. Microbial Community Dynamics during Lake Ice Freezing. *Sci. Rep.* **2019**, *9*, 6231. [CrossRef]
32. Obertegger, U.; Obrador, B.; Flaim, G. Dissolved Oxygen Dynamics under Ice: Three Winters of High-Frequency Data from Lake Tovel, Italy. *Water Resour. Res.* **2017**, *53*, 7234–7246. [CrossRef]
33. Yang, F.; Cen, R.; Feng, W.; Zhu, Q.; Leppäranta, M.; Yang, Y.; Wang, X.; Liao, H. Dynamic Simulation of Nutrient Distribution in Lakes during Ice Cover Growth and Ablation. *Chemosphere* **2021**, *281*, 130781. [CrossRef] [PubMed]
34. Duarte, C.M.; Prairie, Y.T.; Montes, C.; Cole, J.J.; Striegl, R.; Melack, J.; Downing, J.A. CO₂ Emissions from Saline Lakes: A Global Estimate of a Surprisingly Large Flux. *J. Geophys. Res. Biogeosci.* **2008**, *113*, G4. [CrossRef]
35. Michel, B.; Ramseier, R.O. Classification of River and Lake Ice. *Can. Geotech. J.* **1971**, *8*, 36–45. [CrossRef]
36. Bengtsson, L. Spatial Variability of Lake Ice Covers. *Geogr. Ann. Ser. A-Phys. Geogr.* **1986**, *68*, 113–121. [CrossRef]
37. Michel, B. *Properties and Processes of River and Lake Ice*; Université Laval, Laboratoire de mécanique des glaces: Québec, QC, Canada, 1972.
38. Leppäranta, M. Modelling the Formation and Decay of Lake Ice. In *The Impact of Climate Change on European Lakes*; Aquatic Ecology Series; George, G., Ed.; Springer: Dordrecht, The Netherlands, 2010; pp. 63–83.
39. Gow, A.J. Orientation Textures in Ice Sheets of Quietly Frozen Lakes. *J. Cryst. Growth* **1986**, *74*, 247–258. [CrossRef]
40. Gow, A.J.; Langston, D. *Growth History of Lake Ice in Relation to Its Stratigraphic, Crystalline and Mechanical Structure*; Department of Defense, Army, Corps of Engineers, Cold Regions Research and Engineering Laboratory: Hanover, NH, USA, 1977.
41. Leppäranta, M.; Tikkanen, M.; Virkanen, J. Observations of Ice Impurities in Some Finnish Lakes. *Proc. Est. Acad. Sci.* **2003**, *52*, 59–75. [CrossRef]
42. D'souza, N.A.; Kawarasaki, Y.; Gantz, J.D.; Lee Jr, R.E.; Beall, B.F.N.; Shtarkman, Y.M.; Koçer, Z.A.; Rogers, S.O.; Wildschutte, H.; Bullerjahn, G.S.; et al. Diatom Assemblages Promote Ice Formation in Large Lakes. *ISME J.* **2013**, *7*, 1632–1640. [CrossRef]
43. Santibáñez, P.A.; Michaud, A.B.; Vick-Majors, T.J.; D'Andrilli, J.; Chiuchiolo, A.; Hand, K.P.; Prisco, J.C. Differential Incorporation of Bacteria, Organic Matter, and Inorganic Ions into Lake Ice during Ice Formation. *J. Geophys. Res. Biogeosci.* **2019**, *124*, 585–600. [CrossRef]
44. Imbeau, E.; Vincent, W.F.; Wauthy, M.; Cusson, M.; Rautio, M. Hidden Stores of Organic Matter in Northern Lake Ice: Selective Retention of Terrestrial Particles, Phytoplankton and Labile Carbon. *J. Geophys. Res. Biogeosci.* **2021**, *126*, e2020JG006233. [CrossRef]
45. Bolsenga, S.J.; Herdendorf, C.E.; Norton, D.C. Spectral Transmittance of Lake Ice from 400–850 Nm. *Hydrobiologia* **1991**, *218*, 15–25. [CrossRef]
46. Pernica, P.; North, R.L.; Baulch, H.M. In the Cold Light of Day: The Potential Importance of Under-Ice Convective Mixed Layers to Primary Producers. *Inland Waters* **2017**, *7*, 138–150. [CrossRef]
47. Warren, S.G. Optical Properties of Snow. *Rev. Geophys.* **1982**, *20*, 67. [CrossRef]

48. Leppäranta, M.; Terzhevik, A.; Shirasawa, K. Solar Radiation and Ice Melting in Lake Vendyurskoe, Russian Karelia. *Hydrol. Res.* **2010**, *41*, 50–62. [CrossRef]
49. Pulkkanen, M. Under-Ice Temperature and Oxygen Conditions in Boreal Lakes. In *Jyväskylä Studies in Biological and Environmental Science*; University of Jyväskylä: Jyväskylä, Finland, 2013.
50. Belzile, C.; Gibson, J.A.E.; Vincent, W.F. Colored Dissolved Organic Matter and Dissolved Organic Carbon Exclusion from Lake Ice: Implications for Irradiance Transmission and Carbon Cycling. *Limnol. Oceanogr.* **2002**, *47*, 1283–1293. [CrossRef]
51. Vehmaa, A.; Salonen, K. Development of Phytoplankton in Lake Pääjärvi (Finland) during Under-Ice Convective Mixing Period. *Aquat. Ecol.* **2009**, *43*, 693–705. [CrossRef]
52. Yang, B.; Wells, M.G.; Li, J.; Young, J. Mixing, Stratification, and Plankton under Lake-Ice during Winter in a Large Lake: Implications for Spring Dissolved Oxygen Levels. *Limnol. Oceanogr.* **2020**, *65*, 2713–2729. [CrossRef]
53. Cavaliere, E.; Fournier, I.B.; Hazuková, V.; Rue, G.P.; Sadro, S.; Berger, S.A.; Cotner, J.B.; Dugan, H.A.; Hampton, S.E.; Lottig, N.R.; et al. The Lake Ice Continuum Concept: Influence of Winter Conditions on Energy and Ecosystem Dynamics. *J. Geophys. Res. Biogeosci.* **2021**, *126*, e2020JG006165. [CrossRef]
54. Ghane, A.; Boegman, L. The Dissolved Oxygen Budget of a Small Canadian Shield Lake during Winter. *Limnol. Oceanogr.* **2023**, *68*, 265–283. [CrossRef]
55. Sabbe, K.; Hodgson, D.A.; Verleyen, E.; Taton, A.; Wilmotte, A.; Vanhoutte, K.; Vyverman, W. Salinity, Depth and the Structure and Composition of Microbial Mats in Continental Antarctic Lakes. *Freshw. Biol.* **2004**, *49*, 296–319. [CrossRef]
56. Pieters, R.; Lawrence, G.A. Effect of Salt Exclusion from Lake Ice on Seasonal Circulation. *Limnol. Oceanogr.* **2009**, *54*, 401–412. [CrossRef]
57. Boetius, A.; Anesio, A.M.; Deming, J.W.; Mikucki, J.A.; Rapp, J.Z. Microbial Ecology of the Cryosphere: Sea Ice and Glacial Habitats. *Nat. Rev. Microbiol.* **2015**, *13*, 677–690. [CrossRef] [PubMed]
58. Panzenböck, M. Effect of Solar Radiation on Photosynthetic Extracellular Carbon Release and Its Microbial Utilization in Alpine and Arctic Lakes. *Aquat. Microb. Ecol.* **2007**, *48*, 155–168. [CrossRef]
59. Öterler, B. Winter Phytoplankton Composition Occurring in a Temporarily Ice-Covered Lake: A Case Study. *Pol. J. Environ. Stud.* **2017**, *26*, 2677–2688. [CrossRef] [PubMed]
60. Obolkina, L.; Bondarenko, N.A.; Doroshchenko, L.F.; Gorbunova, L.A.; Molozhavaya, O.A. On Finding of Cryophilic Community of Lake Baikal. *Dokl. Akad. Nauk* **2000**, *371*, 815–817.
61. Frenette, J.; Thibeault, P.; Lapierre, J.; Hamilton, P.B. Presence of Algae in Freshwater Ice Cover of Fluvial Lac Saint-Pierre (St. Lawrence River, Canada). *J. Phycol.* **2008**, *44*, 284–291. [CrossRef]
62. Wen, Z.; Song, K.; Shang, Y.; Lyu, L.; Yang, Q.; Fang, C.; Du, J.; Li, S.; Liu, G.; Zhang, B.; et al. Variability of Chlorophyll and the Influence Factors during Winter in Seasonally Ice-Covered Lakes. *J. Environ. Manag.* **2020**, *276*, 111338. [CrossRef]
63. Kelley, D.E. Convection in Ice-Covered Lakes: Effects on Algal Suspension. *J. Plankton Res.* **1997**, *19*, 1859–1880. [CrossRef]
64. Matthews, P.C.; Heaney, S.I. Solar Heating and Its Influence on Mixing in Ice-Covered Lakes. *Freshw. Biol.* **1987**, *18*, 135–149. [CrossRef]
65. Denfeld, B.A.; Klaus, M.; Laudon, H.; Sponseller, R.A.; Karlsson, J. Carbon Dioxide and Methane Dynamics in a Small Boreal Lake during Winter and Spring Melt Events. *J. Geophys. Res. Biogeosci.* **2018**, *123*, 2527–2540. [CrossRef]
66. Larsen, S.; Andersen, T.; Hessen, D.O. The PCO₂ in Boreal Lakes: Organic Carbon as a Universal Predictor? *Glob. Biogeochem. Cycles* **2011**, *25*. [CrossRef]
67. Peter, S.; Isidorova, A.; Sobek, S. Enhanced Carbon Loss from Anoxic Lake Sediment through Diffusion of Dissolved Organic Carbon. *J. Geophys. Res. Biogeosci.* **2016**, *121*, 1959–1977. [CrossRef]
68. Berg, I.A.; Kockelkorn, D.; Ramos-Vera, W.H.; Say, R.F.; Zarzycki, J.; Hügler, M.; Alber, B.E.; Fuchs, G. Autotrophic Carbon Fixation in Archaea. *Nat. Rev. Microbiol.* **2010**, *8*, 447–460. [CrossRef] [PubMed]
69. Saini, R.; Kapoor, R.; Kumar, R.; Siddiqi, T.O.; Kumar, A. CO₂ Utilizing Microbes—A Comprehensive Review. *Biotechnol. Adv.* **2011**, *29*, 949–960. [CrossRef] [PubMed]
70. Sepulveda-Jauregui, A.; Walter Anthony, K.M.; Martinez-Cruz, K.; Greene, S.; Thalasso, F. Methane and Carbon Dioxide Emissions from 40 Lakes along a North–South Latitudinal Transect in Alaska. *Biogeosciences* **2015**, *12*, 3197–3223. [CrossRef]
71. Denfeld, B.A.; Canelhas, M.R.; Weyhenmeyer, G.A.; Bertilsson, S.; Eiler, A.; Bastviken, D. Constraints on Methane Oxidation in Ice-Covered Boreal Lakes. *J. Geophys. Res. Biogeosci.* **2016**, *121*, 1924–1933. [CrossRef]
72. Kalyuzhnaya, M.G.; Gomez, O.A.; Murrell, J.C. The Methane-Oxidizing Bacteria (Methanotrophs). In *Taxonomy, Genomics and Ecophysiology of Hydrocarbon-Degrading Microbes*; Springer: Cham, Switzerland, 2019; pp. 245–278. [CrossRef]
73. Denfeld, B.A.; Kortelainen, P.; Rantakari, M.; Sobek, S.; Weyhenmeyer, G.A. Regional Variability and Drivers of below Ice CO₂ in Boreal and Subarctic Lakes. *Ecosystems* **2015**, *19*, 461–476. [CrossRef]
74. Huotari, J.; Ojala, A.; Peltomaa, E.; Nordbo, A.; Launiainen, S.; Pumpanen, J.; Rasilo, T.; Hari, P.; Vesala, T. Long-Term Direct CO₂ flux Measurements over a Boreal Lake: Five Years of Eddy Covariance Data. *Geophys. Res. Lett.* **2011**, *38*. [CrossRef]
75. Cole, J.J.; Caraco, N.F.; Kling, G.W.; Kratz, T.K. Carbon Dioxide Supersaturation in the Surface Waters of Lakes. *Science* **1994**, *265*, 1568–1570. [CrossRef]
76. Anderson, L.G. Enhanced Uptake of Atmospheric CO₂ during Freezing of Seawater: A Field Study in Storfjorden, Svalbard. *J. Geophys. Res.* **2004**, *109*. [CrossRef]

77. Hammer, U.T. Primary Production in Saline Lakes. In *Salt Lakes*; Williams, W.D., Ed.; Springer: Dordrecht, The Netherlands, 1981; Volume 5, pp. 47–57, ISBN 9789400986671.
78. Shadrin, N. Peculiarities of Structure, Functioning and Dynamics of the Salt Lake Ecosystems. In *Introduction to Salt Lake Sciences*; Science Press: Beijing, China, 2017; pp. 179–188.
79. Jin, Z.; You, C.-F.; Wang, Y.; Shi, Y. Hydrological and Solute Budgets of Lake Qinghai, the Largest Lake on the Tibetan Plateau. *Quat. Int.* **2010**, *218*, 151–156. [CrossRef]
80. Bartosiewicz, M.; Ptak, M.; Iestyn Woolway, R.; Sojka, M. On Thinning Ice: Effects of Atmospheric Warming, Changes in Wind Speed and Rainfall on Ice Conditions in Temperate Lakes (Northern Poland). *J. Hydrol.* **2020**, *597*, 125724. [CrossRef]
81. Surdu, C.M.; Duguay, C.R.; Brown, L.C.; Fernández Prieto, D. Response of Ice Cover on Shallow Lakes of the North Slope of Alaska to Contemporary Climate Conditions (1950–2011): Radar Remote-Sensing and Numerical Modeling Data Analysis. *Cryosphere* **2014**, *8*, 167–180. [CrossRef]
82. Zhao, G.; Li, Y.; Zhou, L.; Gao, H. Evaporative Water Loss of 1.42 Million Global Lakes. *Nat. Commun.* **2022**, *13*, 3686. [CrossRef] [PubMed]
83. Wang, W.; Lee, X.; Xiao, W.; Liu, S.; Schultz, N.; Wang, Y.; Zhang, M.; Zhao, L. Global Lake Evaporation Accelerated by Changes in Surface Energy Allocation in a Warmer Climate. *Nat. Geosci.* **2018**, *11*, 410–414. [CrossRef]
84. Xiao, K.; Griffis, T.J.; Baker, J.M.; Bolstad, P.V.; Erickson, M.; Lee, X.; Wood, J.J.; Hu, C.; Nieber, J.L. Evaporation from a Temperate Closed-Basin Lake and Its Impact on Present, Past, and Future Water Level. *J. Hydrol.* **2018**, *561*, 59–75. [CrossRef]
85. Blanken, P.D.; Spence, C.; Hedstrom, N.; Lenters, J.D. Evaporation from Lake Superior: 1. Physical Controls and Processes. *J. Great Lakes Res.* **2011**, *37*, 707–716. [CrossRef]
86. Ma, J.; Loisel, S.; Cao, Z.; Qi, T.; Shen, M.; Luo, J.; Song, K.; Duan, H. Unbalanced Impacts of Nature and Nurture Factors on the Phenology, Area and Intensity of Algal Blooms in Global Large Lakes: MODIS Observations. *Sci. Total Environ.* **2023**, *880*, 163376. [CrossRef] [PubMed]
87. Adrian, R.; Wilhelm, S.; Gerten, D. Life-History Traits of Lake Plankton Species May Govern Their Phenological Response to Climate Warming. *Glob. Change Biol.* **2006**, *12*, 652–661. [CrossRef]
88. Wollrab, S.; Izmet'yeva, L.; Hampton, S.E.; Silow, E.A.; Litchman, E.; Klausmeier, C.A. Climate Change-Driven Regime Shifts in a Planktonic Food Web. *Am. Nat.* **2020**, *197*, 281–295. [CrossRef]
89. Grant, L.; Vanderkelen, I.; Gudmundsson, L.; Tan, Z.; Perroud, M.; Stepanenko, V.M.; Debolskiy, A.V.; Droppers, B.; Janssen, A.B.G.; Woolway, R.I.; et al. Attribution of Global Lake Systems Change to Anthropogenic Forcing. *Nat. Geosci.* **2021**, *14*, 849–854. [CrossRef]
90. Benson, B.J.; Magnuson, J.J.; Jensen, O.P.; Card, V.M.; Hodgkins, G.; Korhonen, J.; Livingstone, D.M.; Stewart, K.M.; Weyhenmeyer, G.A.; Granin, N.G. Extreme Events, Trends, and Variability in Northern Hemisphere Lake-Ice Phenology (1855–2005). *Clim. Change* **2011**, *112*, 299–323. [CrossRef]
91. Vincent, W.F. Effects of Climate Change on Lakes. *Encycl. Inland Waters* **2009**, 55–60. [CrossRef]
92. Carmack, E.; Vagle, S. Thermobaric Processes Both Drive and Constrain Seasonal Ventilation in Deep Great Slave Lake, Canada. *J. Geophys. Res. Earth Surf.* **2021**, *126*, e2021JF006288. [CrossRef]
93. Bouffard, D.; Zdorovenov, R.E.; Zdorovenova, G.E.; Pasche, N.; Wüest, A.; Terzhevik, A.Y. Ice-Covered Lake Onega: Effects of Radiation on Convection and Internal Waves. *Hydrobiologia* **2016**, *780*, 21–36. [CrossRef]
94. Yang, B.; Wells, M.G.; McMeans, B.; Dugan, H.A.; Rusak, J.A.; Weyhenmeyer, G.A.; Brentrup, J.A.; Hrycik, A.R.; Laas, A.; Pilla, R.M.; et al. A New Thermal Categorization of Ice-Covered Lakes. *Geophys. Res. Lett.* **2021**, *48*, e2020GL091374. [CrossRef]
95. Huang, W.; Zhang, J.; Leppäranta, M.; Li, Z.; Cheng, B.; Lin, Z. Thermal Structure and Water-Ice Heat Transfer in a Shallow Ice-Covered Thermokarst Lake in Central Qinghai-Tibet Plateau. *J. Hydrol.* **2019**, *578*, 124122. [CrossRef]
96. Farmer, D.M.; Carmack, E.C. Wind Mixing and Restratification in a Lake near the Temperature of Maximum Density. *J. Phys. Oceanogr.* **1981**, *11*, 1516–1533. [CrossRef]
97. Qi, M.; Yao, X.; Li, X.; Duan, H.; Gao, Y.; Liu, J. Spatiotemporal Characteristics of Qinghai Lake Ice Phenology between 2000 and 2016. *J. Geogr. Sci.* **2019**, *29*, 115–130. [CrossRef]
98. Preston, D.L.; Caine, N.; McKnight, D.M.; Williams, M.W.; Hell, K.; Miller, M.P.; Hart, S.J.; Johnson, P.T.J. Climate Regulates Alpine Lake Ice Cover Phenology and Aquatic Ecosystem Structure. *Geophys. Res. Lett.* **2016**, *43*, 5353–5360. [CrossRef]
99. Jensen, O.P.; Benson, B.J.; Magnuson, J.J.; Card, V.M.; Futter, M.N.; Soranno, P.A.; Stewart, K.M. Spatial Analysis of Ice Phenology Trends across the Laurentian Great Lakes Region during a Recent Warming Period. *Limnol. Oceanogr.* **2007**, *52*, 2013–2026. [CrossRef]

Disclaimer/Publisher's Note: The statements, opinions and data contained in all publications are solely those of the individual author(s) and contributor(s) and not of MDPI and/or the editor(s). MDPI and/or the editor(s) disclaim responsibility for any injury to people or property resulting from any ideas, methods, instructions or products referred to in the content.

Article

Evaluating the Influence of Water Quality on Clogging Behavior in Drip Irrigation Emitters: A CT Imaging Study

Yuqian Yao ¹, Yang Xiao ^{1,*}, Peng Hou ² and Shuqin Li ¹

¹ College of Water Resources and Civil Engineering, China Agricultural University, Beijing 100083, China; yaoyuqian2022@163.com (Y.Y.); lishuqin@cau.edu.cn (S.L.)

² School of Water Conservancy and Transportation, Zhengzhou University, Zhengzhou 450000, China; houpeng1121@126.com

* Correspondence: xiaoyang@cau.edu.cn

Abstract: Applying poor-quality water in drip irrigation has become increasingly common to address agricultural water scarcity. However, emitter clogging remains a critical challenge that limits the widespread adoption of this technology. Currently, the mechanism of emitter clogging under poor-quality water conditions remains insufficiently explored. This study investigates the distribution and accumulation of clogging substances within drip irrigation emitters under three water conditions: saline water, Yellow River water, and a 1:1 mixture of both, at clogging degrees of 5%, 20%, and 50% (i.e., the flow rate reaches 95%, 80%, 50% of the rated flow). The results showed that when clogging reached 20%, Yellow River water led to the highest clogging volume (i.e., the total volume of clogging substance in the flow channel, 1.77 mm³), while at 50%, saline water resulted in the highest clogging volume (5.11 mm³), while the use of blended water improved the clogging situation. Under different water conditions, clogging substances mainly formed on the upstream and downstream faces of the flow channel, accounting for 23.9–31.8% and 9.3–32.4% of the total volume, respectively. With higher clogging levels, the proportion of clogging substances on the downstream face increased significantly, while other areas showed minimal change. The volume of clogging substances was more pronounced at the front of the flow channel than at the back across the entire length, except at the 20% clogging degree for Yellow River water. At 5% clogging, the largest difference in clogging volume was observed with Yellow River water, while at 50%, the largest difference occurred with blended water. This research provides critical insights into the impact of poor-quality water on emitter clogging and suggests that the use of blending water, gradually varying channel structure, and increasing the arc of clogging faces can effectively alleviate clogging and enhance drip irrigation efficiency.

Keywords: drip irrigation; emitter clogging; industrial computed tomography; saline water; Yellow River water

1. Introduction

Global freshwater resources are depleting due to poor water management and pollution, and water quality is declining, failing to meet the rising demand for agricultural use [1]. Consequently, the utilization of unconventional water sources, including saline water, reclaimed water, and high-sediment water, is becoming increasingly prevalent to fulfill agricultural water demand [2–4]. The sixth longest river in the world is the Yellow River. The region is characterized by a scarcity of freshwater resources, with high-sediment and saline waters also being widely distributed. Efficient use of these unconventional

sources is key to addressing regional water shortages [5,6]. Drip irrigation is among the most effective methods for utilizing unconventional water sources in agriculture [7].

As a core component of drip irrigation system, emitters feature narrow flow channels (0.5–1.2 mm) and complex structures make them vulnerable to clogging from impurities like particles, microorganisms, and ions in poor-quality water [8–11]. Developed countries often have better water quality, resulting in relatively less research on irrigation using high-sand water. In China, the Yellow River is characterized by high sediment concentration, fine particle size and slow sedimentation rate, making the implementation of sedimentation and filtration techniques challenging and expensive [12,13]. Even with filtration and sedimentation measures, fine particles from high-sand water like the Yellow River water can still enter the flow channels, so they can be discharged directly through the emitter flow channels [14,15]. Furthermore, the Yellow River Basin contains over 13 billion m³ of saline water suitable for agricultural irrigation [16,17]. However, using saline water in agricultural irrigation may cause soil secondary salinization and contamination of groundwater [18]. Long-term use may increase maintenance costs, lead to soil hardening, etc. [19,20].

Numerous academics have conducted extensive research on water source filtration, clogging substances composition analysis, the control of electromagnetic fields, and the use of nanobubbles, etc., but the clogging still exists. The core to resolving this issue lies in optimizing flow channel design [15,21–26]. Comprehending the location of clogging in the emitter is essential for such optimization. With the rapid development of modern precision measurement techniques, many scholars have visualized the flow channels of irrigation using advanced measurement methods such as the vertical scanning white-light interference profilometer, Fourier-transform infrared spectroscopy, and field emission scanning electron microscopes (FESEM) to visualize the flow channels of emitters [27–29]. Nevertheless, these techniques only capture local details and often require destructive sampling, which could affect the distribution and structure of clogging substances [26,30]. Industrial Computed Tomography (ICT), with its high-resolution and non-destructive imaging characteristics, has been successfully applied to the imaging of clogging substances in the flow channels of different types of emitters and emitters at different lateral positions in drip irrigation system [31–34], which has the ability to solve the in situ characterization of the flow channels of emitters. However, ICT technology still faces challenges of high costs and cumbersome sample staining processes at present.

However, due to the fact that the spatial distribution of clogging substances in the emitter under different water source conditions is still unknown. Therefore, industrial computed tomography (ICT) was employed in this study to scan emitters with three types of water sources and three degrees of clogging, and to acquire the locational distribution of clogging substances. The study clarified the distribution of clogging substances on several faces and across the flow channels' whole length under different water source conditions. This study offers theoretical guidance for managing clogging in drip irrigation systems that cause clogging and for applying saline water, Yellow River water, and blending water in agricultural drip irrigation.

2. Materials and Methods

2.1. Water Quality Testing and Experimental Setup

2.1.1. Water Source Conditions

The compound clogging experiment of drip irrigation system emitters was carried out at the Ulanbuhe Irrigation Experiment Station, Dengkou, Bayannur, Inner Mongolia, China. This study considered mixing saline water and Yellow River water in a 1:1 ratio as irrigation water source (named Blending Water) can reduce sediment concentration and salt concentration, improve soil permeability, enhance soil moisture retention, and improve

the ability of crop roots to absorb moisture [17,35]. The water sources were the Yellow River water from the Wushen Canal in Inner Mongolia's Hetao Irrigation District (named YR), local saline water at the experimental station (named SW), and the blending water (named BW). Measured water quality parameters are detailed below in Table 1.

Table 1. Water quality parameters during the experiment in the Yellow River basin.

Water Source	pH	Suspended Solids mg/L	Specific Conductance $\mu\text{m/cm}$	Mineralization of Water mg/L	COD _{Cr} mg/L	BOD ₅ mg/L	Total Phosphorus mg/L	Total Nitrogen mg/L	Calcium mg/L	Magnesium mg/L
SW	9.2	<5	9460	4760	24.8	4.2	0.16	2.04	321	127
YR	7.7	41	796	483	6.8	1.7	0.06	1.48	54.7	25.7

2.1.2. Experimental Setup

A sand filter and disk filter combination were installed at the system's head. The system operated at 0.1 MPa pressure. The laterals were laid over 15 m, with a lateral flushing device installed at the system's endpoint. The system operated for 9 h daily, flushed every 60 h at 0.45 m/s velocity. The experiment ran for a total of 840 h (Figure 1a).

The emitters used in the drip irrigation clogging experiments adopted non-pressure compensating labyrinth flow channel emitters, with a drip irrigation tape diameter of 16 mm. The distance between emitters on the lateral tubes was set at 30 cm. The internal dimensions of the emitters' flow channels were 22.4 mm \times 0.7 mm \times 0.61 mm (length \times width \times depth), with a 1.6 L/h flow rate. When the "entire lateral" drip irrigation emitter's flow rate decreased to 95%, 80%, and 50% of the rated flow rate, the lateral section containing the emitter under test was cut from the middle of the lateral tube. Additionally, the flow channels were segmented into some structural units (Figure 1a) to better analyze the distribution of clogging substances in the emitter flow channels, with each unit categorized into five surfaces: the top (TF), substrate (SF), upstream (UF), downstream (DF), and root face (RF) (Figure 1b). Meanwhile, along the internal water flow path of the emitters, the 1–4 structural units of the flow channels were defined as the front (F), and the 5–8 structural units were defined as the back (B). The areas of different faces are listed in Table 2.

Table 2. The areas of different faces within emitter.

The Top Face	The Substrate Face	The Upstream Face	The Downstream Face	The Root Face
2.2248 mm ²	2.2248 mm ²	0.561 mm ²	0.561 mm ²	0.3876 mm ²

2.2. Industrial Computed Tomography (ICT) Technology

Industrial computed tomography (ICT) was used in this study to analyze clogging distribution in emitter flow channels. ICT involves irradiating an object with energy waves (X-rays, gamma rays, etc.) to produce a series of cross-sectional images. By measuring the energy values after passing through the object and utilizing post-processing computer software (VGStudio MAX 2.2) to generate an undistorted 3D model of the object [36]. Since the materials of the emitters and the clogging substances exhibit similar X-ray absorption properties, requiring staining of the clogging substances is required before scanning to distinguish clearly between the two to achieve high-quality imaging. As described by Davit [37], a contrast agent was introduced into the emitters' samples by injecting a staining solution (contrast agent mixed with BaSO₄ suspension (0.33 g/mL) and KI solution (0.1 g/mL)). After staining, the clean water flushed the emitters' samples. Subsequently, the flushed emitters' samples were air-dried and stored in isolation (Figure 1c).

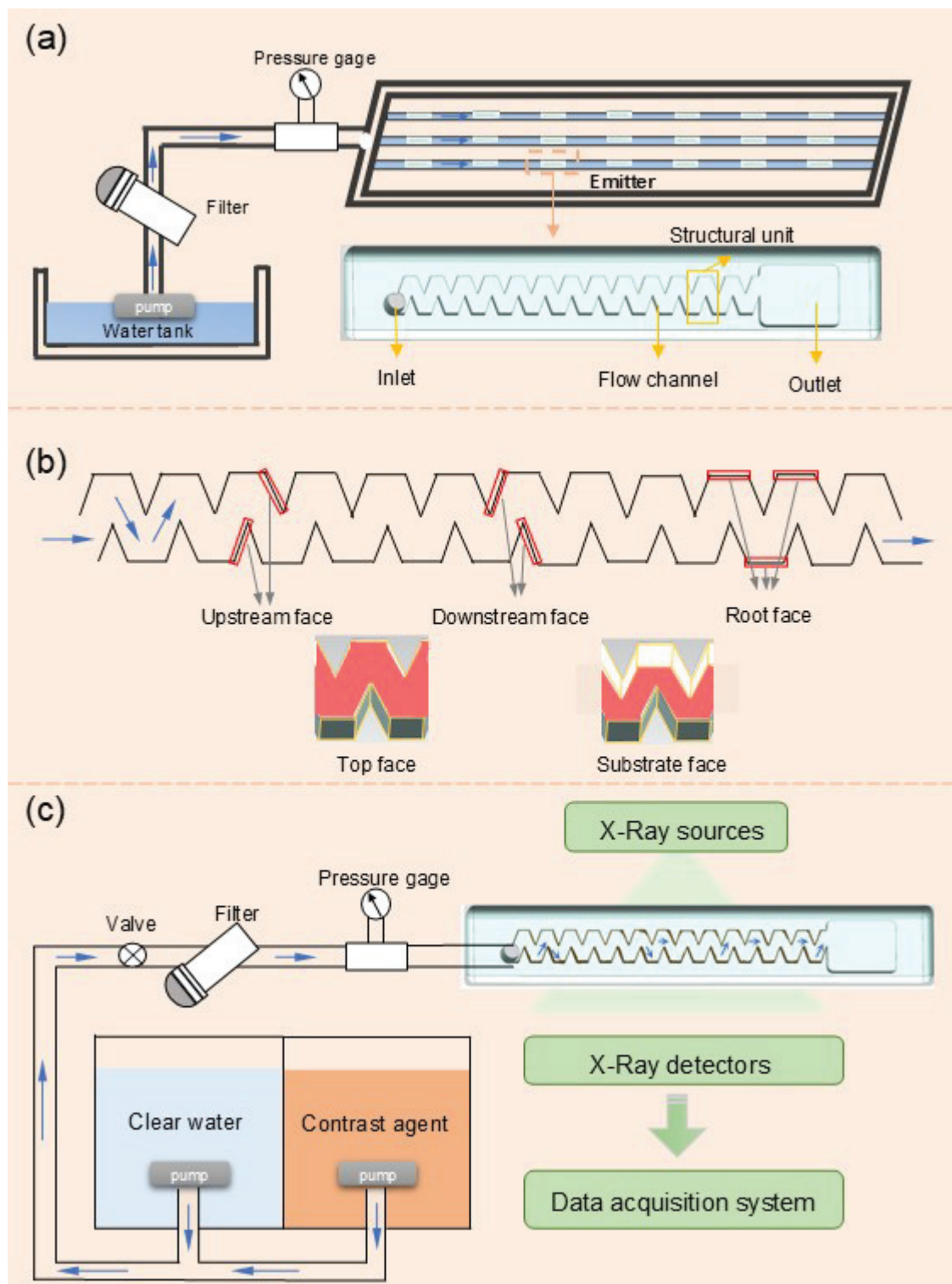


Figure 1. Non-destructive clogging substance observations and emitter structural representation. (a) Drip irrigation emitter clogging experimental device and the structure of the emitter. Different water sources were injected into the water tank for clogging experiments to obtain samples under different water source conditions, and the structure of the emitter was divided into similar structural units. Blue arrows in the emitter channel indicate flow direction of water. (b) The red regions refer to the five faces in the structural unit. (c) Non-destructive clogging substances observation in emitters imaged by industrial computed tomography, with the brown portion in the emitter flow channels representing the attached clogging substances. The entire system involves the staining of clogging substances inside the emitters and the ICT imaging process.

Afterwards, the emitter samples were positioned at the center of the ICT scanner (Xview X5000 | X-ray; Producer, NSI; South Diamond Lake, MN, USA), with the following specific parameters as follows: tube voltage: 25 kV to 225 kV; tube current: 0 mA to 3 mA; tube voltage regulation division 0.1 kV; tube current regulation division 0.1 mA; microfocus $\geq (6 \times 6) \mu\text{m}$; collimator manually or electrically adjustable to meet the needs of CT scanning and VCT scanning for radiation beams; slice thickness collimator (0–5 mm) manually or electrically adjustable; minimum FOD 6.5 mm; minimum detection capability $< 3 \mu\text{m}$. The obtained ICT images were input into the computer, and the ICT images of the samples were reconstructed using VGStudio MAX 2.2, generating a 3D model of the emitters. By adjusting the grayscale threshold of the emitters' sample models, segmented the emitters, clogging substances and air, and the volume of the clogging substances in the 3D emitter models was quantified.

2.3. Evaluation Indicators for the Spatial Distributions of Clogging Substances

Using VGStudio Max 2.2, clogging volume in emitter flow channels under varying water sources can be measured. Other evaluation parameters include (1) the mean thickness of clogging substances on the face, denoted as T ; (2) volume fraction of clogging substances, denoted as Φ_V ; (3) clogging substance ratio on various faces, denoted as W . Within a structural unit of the flow channel, there are 5 faces (Figure 1c), including a top face, a substrate face, two upstream faces, two downstream faces, and two root faces.

2.3.1. Mean Thickness of Clogging Substances T

Taking the upstream face of i -th structural unit as an example, the T of clogging substances on the top face is determined by Equation (1):

$$T_{u_i} = \frac{V_{u_i}}{S_{u_i}} \quad (1)$$

where T_{u_i} is the mean thickness of clogging substances on the upstream face of i -th structural unit in the emitter sample, measured along the water flow direction;

T_{u_i} represents the average clogging thickness on the upstream face of the i -th structural unit, measured along the flow direction;

V_{u_i} denotes the clogging substances volume on the upstream face of the i -th structural unit;

S_{u_i} denotes the upstream face area of the i -th unit.

The thickness of a specific face (e.g., upstream face) across the entire flow channel (including all structural units) is evaluated by the weighted average of the thicknesses of each face, as shown in Equation (2):

$$T_u = \frac{T_{u_1} \times S_{u_1} + T_{u_2} \times S_{u_2} \dots + T_{u_l} \times S_{u_l}}{S_{u_1} + S_{u_2} \dots + S_{u_l}} \quad (2)$$

where T_u is the weighted mean thickness of clogging substances on the upstream face of each structural unit;

T_{u_1} , T_{u_2} , T_{u_l} and S_{u_1} , S_{u_2} , S_{u_l} represent the mean thicknesses and the surface areas of clogging substances on the upstream face within the first, second and final units, respectively.

2.3.2. Volume Fraction of Clogging Substances Φ_V

The volume fraction Φ_{V_i} of the i -th unit is determined by the following Equation (3):

$$\Phi_{V_i} = \frac{V'_i}{V_i} \times 100\% \quad (3)$$

where Φ_{V_i} represents the clogging volume fraction in the i -th unit;

V'_i and V_i are the clogging substance volume and the structural unit volume, respectively, along the flow direction in the i -th unit.

The volume fraction over multiple units is a weighted average, as shown in Equation (4):

$$\Phi_V = \frac{\Phi_{V_1} V_1 + \Phi_{V_2} V_2 \dots + \Phi_{V_l} V_l}{V_1 + V_2 + V_3 \dots + V_l} \quad (4)$$

where Φ_V represents the clogging volume fraction across multiple units; Φ_{V_1} , Φ_{V_2} , Φ_{V_l} and V_1 , V_2 , V_l represent the clogging volume fractions and the volumes in the first, second, and final units, respectively.

2.3.3. Ratio of Clogging Substances W

The clogging ratio on different faces is given as the percentage of the clogging volume on a specific face relative to the total clogging volume within the entire flow channel. This ratio quantifies the distribution of clogging across different faces of the flow channel.

It is calculated as the ratio of a given face's clogging volume relative to the total clogging volume across all faces in the flow channel, as shown in Equations (5) and (6):

$$W_{V_u} = \frac{V_u}{V'} \times 100\% \quad (5)$$

$$V' = V_t + V_s + V_u + V_d + V_r \quad (6)$$

where W_{V_u} represents the clogging ratio on the upstream face, with similar methods applied to other faces; V' denotes the clogging volume in the entire area; V_t , V_s , V_u , V_d , and V_r denote the total clogging volumes on the top, substrate, upstream, downstream, and root face of flow channel.

3. Results and Analysis

3.1. Apparent Morphology of Clogging Substances in Emitter Flow Channels

The spatial distribution of clogging in SW, YR, and BW shows a clear increase with clogging severity increases. At 5% clogging severity, the clogging substances of the emitter within the SW-based drip irrigation system were distributed unevenly along the flow channel, primarily accumulating at the front, while YR and BW were distributed uniformly. In addition, at 50% clogging severity, the clogging substances with SW and YR had a main flow area throughout the flow channel length (Figure 2). For different faces, at clogging severities of 5% and 20%, clogging substances mainly gathered on the upstream and root faces of the flow channel. While the degree of clogging reached 50%, clogging substances mainly accumulated on the downstream and root faces. As the clogging degree increased from 20% to 50%, there was a more rapid increase in clogging substances on the downstream face.

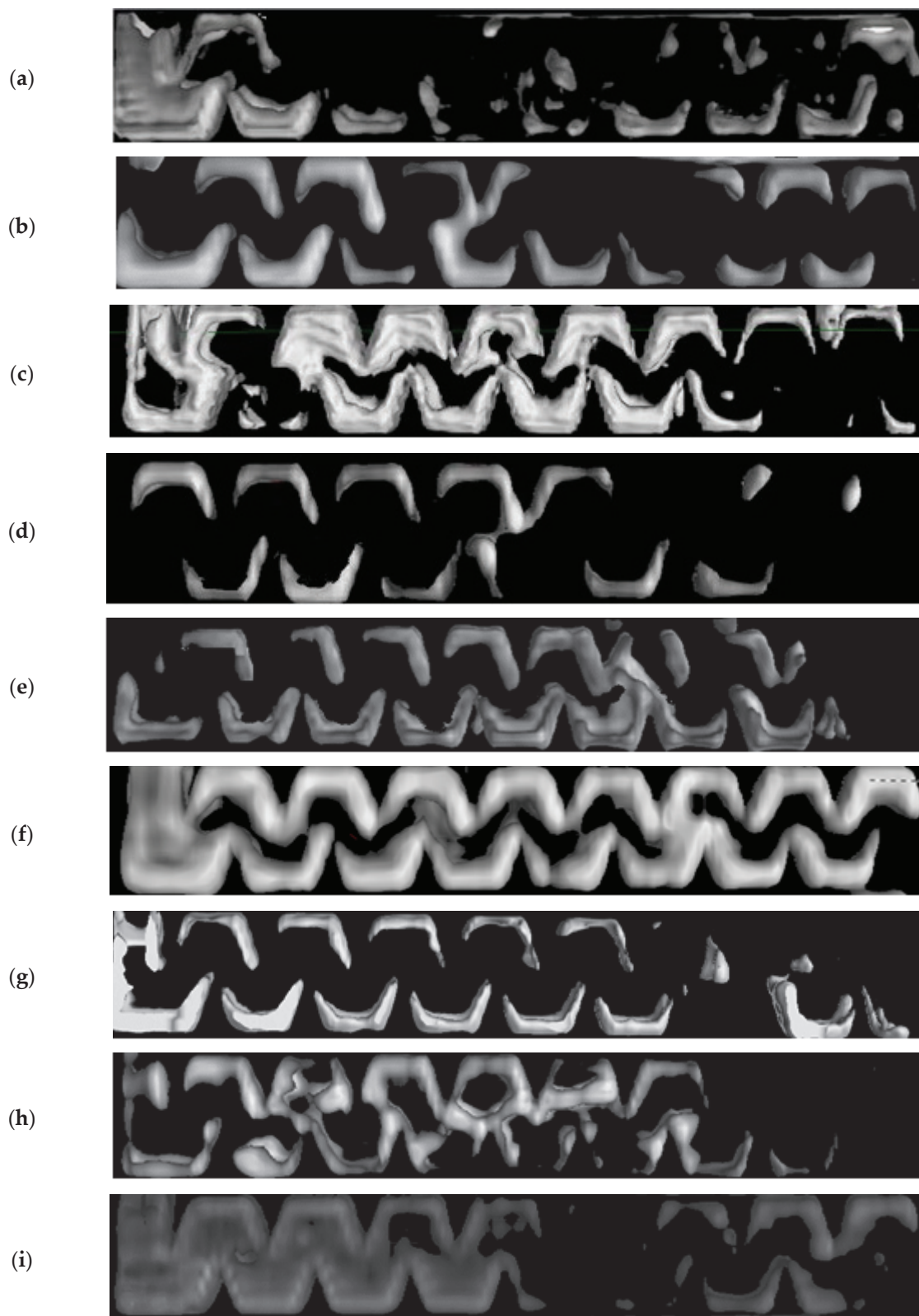


Figure 2. Three-dimensional morphology of clogging substances in the emitter flow channel. (a–c) represent the results in the saline water for 5%, 20% and 50% of clogging degree, respectively. (d–f) represent the results in the Yellow River water for 5%, 20%, and 50% of clogging degree, respectively. (g–i) represent the results in the blending water for 5%, 20%, and 50% of clogging degree, respectively.

3.2. Distribution of Clogging Substances Under Different Water Sources

3.2.1. Distribution of Clogging Substances Within Structural Units of Emitter Flow Channels

Overall, there was an increase in both the volume and mean thickness of clogging substances with increasing clogging severity under different water sources. As clogging severity increased, the total clogging volumes within the emitter flow channels for SW, YR and BW were 1.40 mm³, 2.27 mm³, and 5.11 mm³ (for SW); 1.77 mm³, 3.17 mm³, and 4.24 mm³ (for YR); 1.21 mm³, 2.95 mm³, and 4.91 mm³ (for BW), respectively. The clogging volume fractions in the flow channels were 12.89%, 20.91%, and 47.05% (for SW); 16.28%, 29.23%, and 39.05% (for YR); and 11.11%, 27.19%, and 45.26% (for BW), respectively.

The degree of clogging ranged from 5% to 20%, and the total clogging volumes in emitter flow channels under SW, YR, BW increased by 62.14%, 79.54%, and 144.77%, respectively. For the degree of clogging ranging from 20% to 50%, the total clogging volumes under SW, YR and BW increased by 125.02%, 33.60%, and 66.48%, respectively. It was observed that with increasing clogging severity, the volume increment of clogging substances within emitters of drip irrigation systems using SW was larger, while the volume increments for YR and BW were smaller. At clogging severities of 5%, 20%, and 50%, the volume of clogging substances within each structural unit of emitter flow channels under SW, YR, and BW ranged from 0.02 to 0.90 mm³, 0.02 to 0.69 mm³, and 0.03 to 1.04 mm³, respectively. The mean thickness varied between 2.68 µm and 120.76 µm, 2.65 µm and 91.91 µm, 3.62 µm and 139.63 µm, respectively. No significant differences were found in clogging volume among the three water sources, but the volume of clogging substances at 50% clogging degree was significantly higher than those at 5% and 20% ($p < 0.05$, Figure 3).

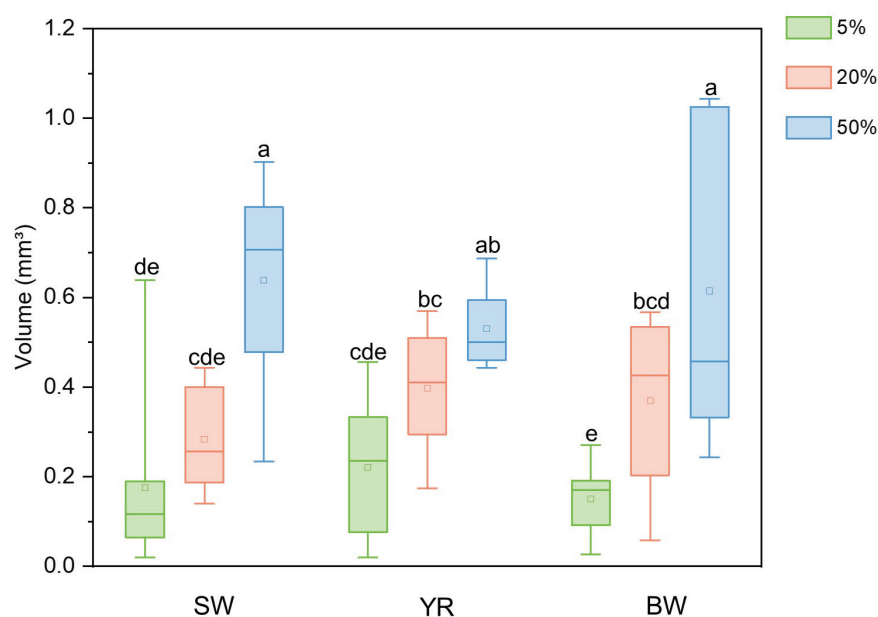


Figure 3. The total volume of clogging substances under different water sources at different degrees of clogging. The letters above the boxplots indicate significant analysis, and the letters a–e represent the average values from small to large. Groups that did not have the same letter indicate that there were significant differences between the groups ($p < 0.05$), whereas groups that had the same letter indicate that the differences were not significant. In the box, the transverse line represents the median value line, and the square represents the average value. The up and down transverse line represent the maximum and minimum values, respectively.

3.2.2. Distribution of Clogging Substances of Emitter Flow Channels on Different Faces

In general, SW, YR, and BW showed consistent patterns for different surfaces of the internal emitter flow channels. With the increase in clogging degree, there was a certain increase in clogging substances on each face, especially the clogging mean thickness on the downstream face. The maximum clogging volumes accumulated on the upstream face and downstream face, while the maximum mean thickness mostly appeared on the root face. The minimum volume and mean thickness of clogging substances were mainly found on the top and substrate face.

At 5% clogging severity, the three water sources all showed the highest clogging volume on the upstream face, with values of 0.049 mm^3 , 0.062 mm^3 , and 0.048 mm^3 , respectively. SW had the minimum volume on the top face and substrate face, and YR and BW had the minimum volumes on the downstream face, which were below 0.030 mm^3 . At 20% clogging severity, the three water sources all exhibited relatively large volumes on the upstream face and downstream face, varying between 0.072 mm^3 and 0.108 mm^3 . A reduced amount of clogging substances was found on the top and substrate faces, which were below 0.060 mm^3 . At 50% clogging severity, the situation was similar to that at 20%, the largest volume of clogging substances under three kinds of water quality appeared in the downstream face, upstream face, and upstream face, respectively, ranging from 0.155 to 0.207 mm^3 . While a smaller volume of clogging substances was observed on the top and substrate faces, which was below 0.110 mm^3 ($p < 0.05$, Figure 4). At 50% clogging severity, the clogging volume on all surfaces under SW and BW were significantly higher than those at the degree of 5%, while there was no significant difference between the volume of clogging substances on each face under different clogging degrees ($p < 0.05$, Figure 4).

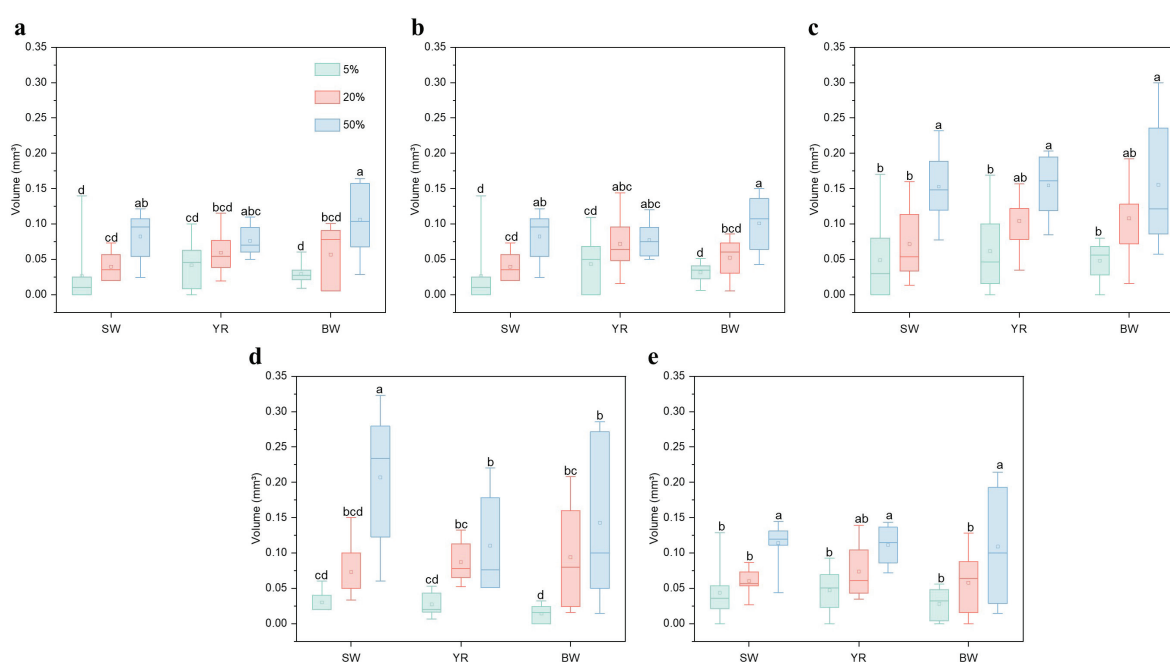


Figure 4. (a–e) represent the clogging substances volume in various faces under different water sources for 5%, 20%, and 50% of clogging degree, respectively. (a–e) represent the top face, substrate face, upstream face, downstream face, and root face of the emitter, respectively. SW, YR, and BW represent the saline water, Yellow River water, and blending water. The letters above the boxplots indicate significant analysis, and the letters a–d represent the average values from small to large. Groups that did not have the same letter indicate that there were significant differences between the groups ($p < 0.05$), whereas groups that had the same letter indicate that the differences were not significant. In the box, the transverse line represents the median value line, and the square represents the average value. The up and down transverse line represent the maximum and minimum values, respectively.

For SW, YR, and BW, the larger volumes of clogging substances were all located on the upstream face, accounting for 23.9–31.8% of the total volume of clogging substances on the five faces. Therefore, it was crucial to prioritize controlling the buildup of clogging substances on the upstream face. With increasing clogging severity, the clogging volume ratio on downstream face increased to a certain extent under the three water sources. When the degree of clogging was 5%, the clogging volume ratio on the downstream face ranging from 9.29% to 17.14%. At clogging severities of 20% and 50%, the ratio ranging from 20.79% to 32.41%. In contrast, the clogging volume ratios on the top face and substrate faces were relatively lower, ranging from 12.91% to 19.40% and 12.91% to 20.90%, respectively. At 50% clogging severity, the volume of clogging substances on the downstream face under SW was notably greater than that observed under YR and BW ($p < 0.05$, Figure 4d), whereas the clogging substances volume showed no significant differences on each face among other water sources ($p < 0.05$, Figure 4).

As for the mean thickness of clogging substances (Figure 5), all water sources exhibited larger thicknesses of clogging substances on the upstream face and root face when the degree of clogging reached 5%, ranging from 43.45 to 56.44 μm (for SW), 54.85 to 61.03 μm (for YR), 42.78 to 36.12 μm (for BW), respectively. Smaller thicknesses were observed on the top, substrate and downstream faces, all below 27 μm . At 20% clogging severity, all water sources showed larger thicknesses on the upstream, downstream and root faces, with maximum values appearing on the root face (SW, 77.40 μm), root face (YR, 95.35 μm), and upstream face (BW, 96.26 μm), respectively. While smaller thicknesses were distributed on the top face and substrate face, all below 35 μm . At 50% clogging severity, the thicknesses on the upstream, downstream, and root faces were still larger, with maximum values appearing on the downstream face (SW, 184.47 μm), root face (YR, 143.60 μm), and root face (BW, 140.52 μm), respectively. Smaller thicknesses were observed on the top face and substrate face, all below 50 μm . At 50% clogging severity, the mean thicknesses of clogging substances on all five faces under SW and BW were significantly higher than those at clogging degree of 5%. And there was no significant difference in the mean thickness of clogging substances on each face under different clogging degrees ($p < 0.05$, Figure 5).

Under the conditions of SW and YR, the maximum mean thicknesses of clogging substances were observed on the downstream face and root face, ranging from 56.44 to 184.47 μm and 61.03 to 143.60 μm , respectively. The minimum thicknesses were observed on the top face and substrate face, ranging from 11.80 to 37.04 μm and 18.73 to 34.83 μm , respectively. Under the condition of BW, the maximum thickness occurred on the upstream face at the clogging degrees of 5% and 20%, and on the root face at the clogging degree of 50%. The minimum thickness initially occurred on the downstream face, and it occurred on the top face and substrate face at 20% clogging severity. During the whole clogging experiment period, the mean thickness of the root face was relatively large, and the volume value was medium. This was due to the small face area of the root face, resulting in a smaller volume occupied by a certain thickness of clogging substances (Table 2). Additionally, the clogging mean thickness on the downstream face under the condition of SW at a clogging degree of 50% was significantly higher than that under YR and BW ($p < 0.05$, Figure 5d). No significant difference was found in the mean thickness of clogging substances on each face among different water sources ($p < 0.05$, Figure 5).

Figure 6 shows the proportion of clogging substance volume on the five faces under different water sources. It was evident that as clogging severity increased, the proportion of the downstream face had a significant increase. The volume proportion of the upstream face was larger, accounting for 23.93–31.84%, and the volume proportions of the top face and substrate face were smaller, accounting for 12.91–20.90%. At 5% clogging severity, clogging

substances were primarily located in the upstream and root faces, and the distribution on the downstream face increases with the increase in the clogging degree.

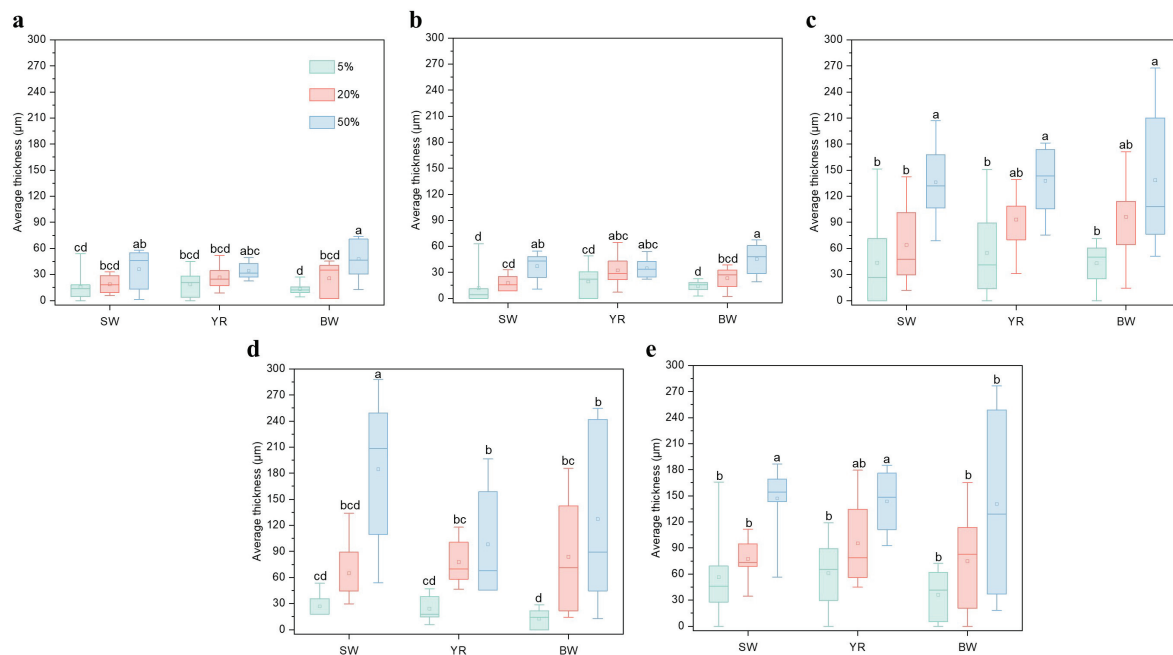


Figure 5. (a–e) represent the clogging substances mean thickness in various faces under different water sources for 5%, 20%, and 50% of clogging degree, respectively. (a–e) represent the top face, substrate face, upstream face, downstream face, and root face of the emitter, respectively. SW, YR, and BW represent the saline water, Yellow River water and blending water. The letters above the boxplots indicate significant analysis, and the letters a–d represent the average values from small to large. Groups that did not have the same letter indicate that there were significant differences between the groups ($p < 0.05$), whereas groups that had the same letter indicate that the differences were not significant. In the box, the transverse line represents the median value line, and the square represents the average value. The up and down transverse line represent the maximum and minimum values, respectively.

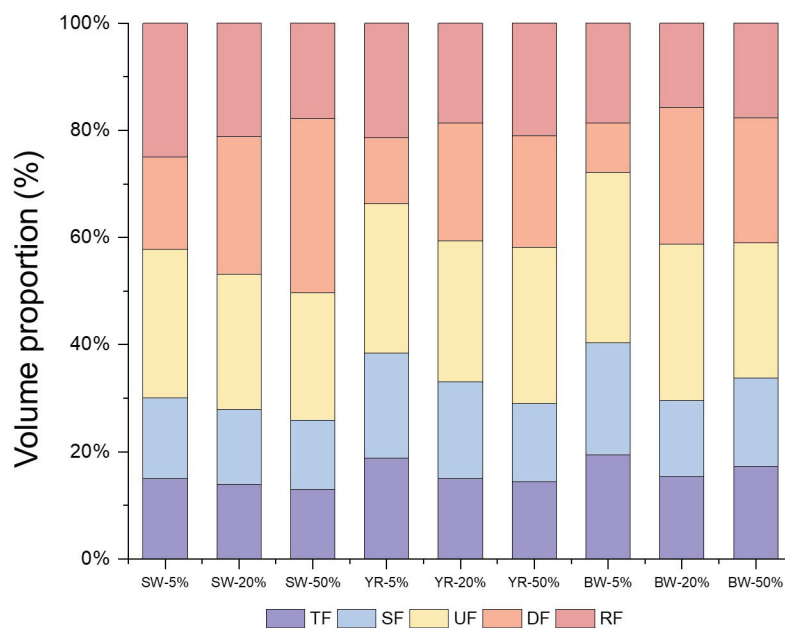


Figure 6. Volume proportion of clogging substances in different faces. SW, YR, and BW represent the saline water, Yellow River water, and blending water. TF, SF, UF, DF, and RF represent the top face, the substrate face, the upstream face, the downstream face, and the root face.

3.3. The Distribution of Clogging Substances in the Direction of Water Flow

Figure 7 presents the clogging average volume within flow channel structural units with different clogging degrees under SW, YR, and BW with increasing flow channel length. A clear upward trend was observed in the clogging volume in the structural units for SW, YR, and BW. Moreover, the clogging volume at the front of the flow channel was mostly greater than that at the back, ranging from 51.4% to 113.8% (for SW), -12.8% to 284.0% (for YR), and 88.0% to 184.4% (for BW), respectively. At 20% clogging severity, the volume of the YR was an exception, and the front of the volume was smaller than the back, but the difference was not large.

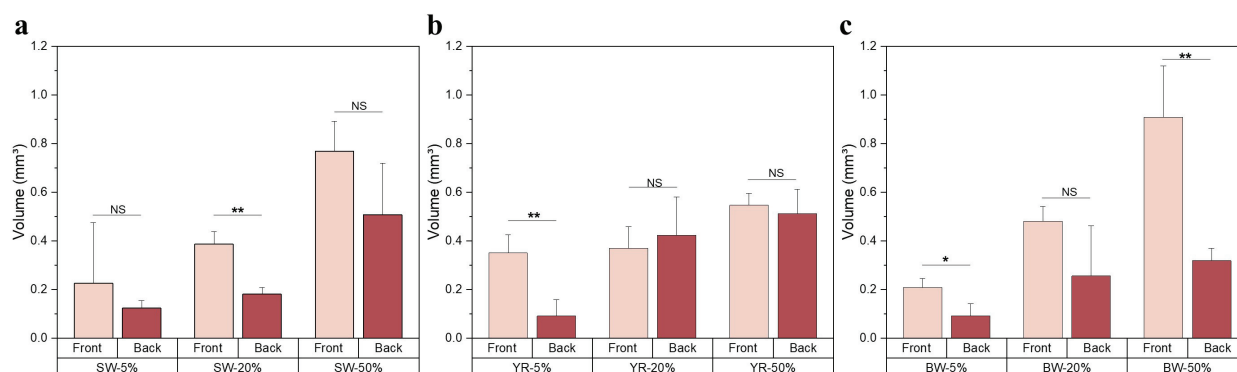


Figure 7. Distribution of clogging substances with the water flow direction. (a–c) represent the volume of clogging substances under the saline water (SW), Yellow River water (YR), and blending water (BW). The 1–4 structural units of the flow channels were defined as the front and the 5–8 structural units were defined as the back. * and ** represent significant ($p < 0.05$) and extremely significant ($p < 0.01$); and NS indicates not significant.

With the clogging degree increases, the clogging volume increment at the front edge of the flow channel had been increasing compared with that at the back under the conditions of SW and BW. However, when the degree of clogging was 20% and 50%, there was no significant variation accumulation in clogging volume between the front and back under YR.

For different water sources, the difference between the front and back regions of flow channel under SW was more obvious. At a clogging degree of 20%, the clogging volume in the front was considerably higher than back ($p < 0.05$, Figure 7a). For YR, the difference was relatively uniform, with the volume at the front significantly higher than that at the back under clogging degree of 5% ($p < 0.05$, Figure 7b). The difference between the front and back of the emitter under BW was obvious, and the clogging volume in the front was considerably higher than in the back when the clogging degree reached 5% and 50% ($p < 0.05$, Figure 7c).

4. Discussion

Nowadays, freshwater resources are extremely limited, and the widespread use of SW and YR can effectively mitigate freshwater scarcity [17]. However, Yellow River water is characterized by fine sediment particle size and high viscosity, and the biofilm is attached to the majority of sediment particles [37]. Saline water is rich in calcium ions, magnesium ions, and other substances that are prone to form chemical precipitation and cause clogging [38,39]. Blending water can reduce the sediment concentration and mineralization degree in the water and can effectively alleviate the formation of clogging substances [17]. Therefore, this study conducted in situ nondestructive testing of clogging substances in the flow channels of drip irrigation emitters under three water conditions. The clogging spatial distribution under different water source conditions was obtained in this study. It can be revealed intuitively that the distribution pattern of clogging substances

along the flow channel was less uniform under the condition of saline water and there were obvious scour traces of the main flow area. Conversely, the clogging distribution throughout the flow channel was more uniform under the condition of Yellow River water and there were obvious scour traces of the main flow area as well. Meanwhile, under the condition of blending water, the clogging substances distribution along the flow channel was less uniform.

When the clogging degree was 5%, both the total volume and maximum thickness of clogging substances in BW were lower than those in YR and SW. When the clogging degree was 20%, the volume value was shown as follows: $SW < BW < YR$. When the degree of clogging reached 50%, the volume value was shown as follows: $YR < BW < SW$. It can be seen that BW at the initial stage of clogging can effectively reduce the clogging volume. In the later stage of clogging, the drawbacks of the two water sources could be balanced at a middle level, which was better than the worst case (Figure 4). Clogging accumulation at the front of flow channels was more pronounced under the conditions of Yellow River and blending water conditions. This is attributed to the higher concentration of suspended particles in Yellow River water and the blending water conditions, which rapidly settle in the vortex area (i.e., the area between upstream face and the root face of emitter) of several units located at the front of the flow channel after entering the emitter [13]. The clogging substances under the different water sources were concentrated at the upstream face, root face, and corners, then gradually growing into other areas. This is similar to previous research that a higher clogging concentration was detected around the corners of emitter flow channels [40,41]. Some scholars propose removing these corners while preserving only the main channel area [42]. While this method effectively controls clogging substances, it decreases the vortex region and labyrinth flow channel's dissipation capacity [21]. Moreover, this study also observed that the severity of emitter clogging tends to alleviate with the direction of water flow. Under different conditions of water source, the distributions were consistent, showing that there was a greater clogging accumulation at the front of the flow channel compared to the back. The clogging volume difference between the front and back grew as the clogging degree increased. This phenomenon may be attributed to the movement of solid particles, mineral components, and other impurities in poor-quality water, which affects the growth of clogging substances [43,44]. With the direction of the water flow, the probability of contact between water impurities and the structural units is observably decreased, leading to a higher abundance of clogging substances at the front of the flow channel [32,45]. However, the formation and removal of clogging substances were frequent, and they are prone to move to subsequent structural units, resulting in certain randomness in the volume of clogging substances within each structural unit.

Across different faces, the volume and mean thickness of clogging substances exhibited consistent patterns across the three water sources. It was shown that with the increase in clogging degree, both the volume and mean thickness of clogging substances on each face had a certain increase. A higher accumulation of clogging substances was observed on the upstream, downstream, and root faces, while less on the top face and substrate face. The clogging volume on the top and substrate faces was relatively low, showing minor fluctuations. This phenomenon is likely due to the relatively small width-depth ratio of the emitter. It can be found from the direct morphology that most areas on the top face and substrate face were located within the main flow area, making it difficult to deposit clogging substances. Because the distribution of clogging substances on the top face and substrate face mainly occurred outside the main flow zone and the position of the main flow zone changed little with the change in time, the distribution of clogging substances changed little as well. Conversely, the volume of clogging substances on the downstream face was

medium but the mean thickness was large, which is caused by the small surface area of the downstream face. The increase in clogging substance volume on the downstream face was the most obvious, and the volume ratio value of clogging substances on the downstream face was low but later increased. This is because the downstream face experiences relatively less shear force from nearby faces, which faster growth of clogging substances on this face. Additionally, the volume ratio value of clogging substances on the upstream face was highest and relatively stable (Figure 6). This is primarily due to more intense collisions between particles inside the emitter flow channel and the upstream face, leading to a more abundant formation of clogging substances on this face.

However, due to the complex characteristic of emitter flow channel, which involves turbulence, particle deposition, and shear forces. It is difficult to fully reveal the clogging mechanism through ICT imaging alone, and different types of emitters may have their own unique clogging mechanisms [34]. Therefore, combined with numerical simulation, the hydraulic characteristics in the flow channel can be studied more deeply and the flow channel design can be optimized. In recent years, there have been studies using the method of combining experiment and numerical simulation to analyze the flow characteristics and clogging mechanism of drip irrigation emitters [31,33]. The combination of the two methods provides a reliable basis for the flow channel design. In the future, our research can be further extended to various flow channel structures, utilizing a combination of experiments and simulations to explore the effects of different design parameters and operating conditions on anti-clogging, thereby optimizing emitter design and enhancing the operational efficiency of drip irrigation systems.

In general, the emitter exhibits more clogging on the front of the flow channel, the downstream, upstream and root faces, leading to greater uncertainty in emitter clogging, which negatively affects irrigation uniformity in the drip irrigation system. These areas also have a pivotal function in dissipating energy within labyrinth-type emitter flow channels. In the design process of the emitter flow channel, a gradually varying channel structure can be considered to reduce the accumulation of clogging substances in the front section (from large to small along the direction of the flow). Additionally, it can be considered to increase the arc of the upstream and downstream faces to form a vortex, which helps clean the flow channel and consequently reduces the deposition of clogging substances.

5. Conclusions

Industrial computed tomography was used in this study to characterize the spatial distribution of clogging substances in drip irrigation emitters under saline water, Yellow River water, and blending water conditions. The findings indicate that blending water significantly reduced clogging volume in the early stages of clogging and continued to mitigate clogging as severity increased. The upstream and downstream faces exhibited the greatest clogging volume, while the root face showed the largest thickness. The least clogging occurred on the top and substrate faces. With the increase in clogging severity, the clogging volume on the downstream face rose significantly, while the volume on the upstream face remained relatively stable. Additionally, the study found that the clogging volume decreased as the length of the flow channel increased. Therefore, this study suggests that using blending water, incorporating a gradually varying channel structure, and increasing the arc of the upstream and downstream faces can help reduce the accumulation of clogging substances in the emitter. This research provides valuable insights into clogging behavior under different water qualities and supports the application of saline and high-sediment water in agricultural drip irrigation systems.

Author Contributions: Conceptualization, Y.X. and P.H.; methodology, Y.X. and P.H.; software, Y.Y.; formal analysis, S.L.; data curation, Y.Y. and Y.X.; writing—original draft preparation, Y.Y.; writing—review and editing, Y.Y., Y.X., P.H. and S.L.; visualization, Y.Y.; supervision, Y.X. and S.L.; project administration, Y.X. and S.L. All authors have read and agreed to the published version of the manuscript.

Funding: This study research was funded by the National Key Research Project (2023YFD1900803) and the National Natural Science Foundation of China (U2443211, 52209074).

Data Availability Statement: The raw data supporting the conclusions of this article will be made available by the authors on request.

Acknowledgments: We thank the anonymous reviewers for their constructive comments.

Conflicts of Interest: The authors declare no conflicts of interest.

Abbreviations

The following abbreviations are used in this manuscript:

ICT	Industrial Computed Tomography
SW	saline water
YR	Yellow River water
BW	blending water
F	front
B	back

References

1. Boretto, A.; Rosa, L. Reassessing the projections of the world water development report. *NPJ Clean Water* **2019**, *2*, 15. [CrossRef]
2. Gosling, S.N.; Arnell, N.W. A global assessment of the impact of climate change on water scarcity. *Clim. Change* **2016**, *134*, 371–385. [CrossRef]
3. Yazdandoost, F.; Noruzi, M.M.; Yazdani, S.A. Sustainability assessment approaches based on water-energy Nexus: Fictions and nonfictions about non-conventional water resources. *Sci. Total Environ.* **2021**, *758*, 143703. [CrossRef]
4. Karimidastenaie, Z.; Avellán, T.; Sadegh, M.; Kløve, B.; Haghighi, A.T. Unconventional water resources: Global opportunities and challenges. *Sci. Total Environ.* **2022**, *827*, 154429. [CrossRef]
5. Skaggs, R.K. Drip irrigation in the desert: Adoption, implications, and obstacles. *Agric. Water Manag.* **2000**, *43*, 125–142. [CrossRef]
6. Qiu, X.; Wang, J.; Wang, H.; Wang, C.; Sun, Y.; Li, G. Elimination of clogging of a biogas slurry drip irrigation system using the optimal acid and chlorine addition mode. *Agriculture* **2022**, *12*, 777. [CrossRef]
7. Wan, S.; Kang, Y.; Wang, D.; Liu, S.P.; Feng, L.P. Effect of drip irrigation with saline water on tomato (*Lycopersicon esculentum* Mill) yield and water use in semi-humid area. *Agric. Water Manag.* **2007**, *90*, 63–74. [CrossRef]
8. Nakayama, F.S.; Bucks, D.A. Water quality in drip/trickle irrigation: A review. *Irrig. Sci.* **1991**, *12*, 187–192. [CrossRef]
9. Liu, L.; Niu, W.; Guan, Y.; Wu, Z.; Ayantobo, O.O. Effects of urea fertigation on emitter clogging in drip irrigation system with muddy water. *J. Irrig. Drain. Eng.* **2019**, *145*, 04019020. [CrossRef]
10. Wang, H.; Ling, G.; Wang, W.; Hu, X.; Gao, X. A Prediction Model of Labyrinth Emitter Service Duration (ESD) under Low-Quality (Sand-Laden Water) Irrigation. *Water* **2022**, *14*, 1690. [CrossRef]
11. Pei, Y.; Li, Y.; Liu, Y.; Zhou, B.; Shi, Z.; Jiang, Y. Eight emitters clogging characteristics and its suitability Under on-site reclaimed water drip irrigation. *Irrig. Sci.* **2014**, *32*, 141–157. [CrossRef]
12. Puig-Bargués, J.; Lamm, F.R. Effect of flushing velocity and flushing duration on sediment transport in microirrigation driplines. *Trans. ASABE* **2013**, *56*, 1821–1828. [CrossRef]
13. Zhang, W.; Lv, C.; Zhao, X.; Dong, A.; Niu, W. The influence mechanism of the main suspended particles of Yellow River sand on the emitter clogging—An attempt to improve the irrigation water utilization efficiency in Yellow River basin. *Agric. Water Manag.* **2021**, *258*, 107202. [CrossRef]
14. He, X.; Wu, P.; Zhang, L.; Wei, Y.; Liu, X.; Yang, F.; Zhou, W. Microporous ceramic emitter: A drip irrigation emitter suitable for high-sediment water. *J. Water Process Eng.* **2024**, *67*, 106169. [CrossRef]
15. Li, Y.K.; Zhou, B.; Yang, P. Research advances in drip irrigation emitter clogging mechanism and controlling methods. *J. Hydraul. Eng.* **2018**, *49*, 103–114. [CrossRef]
16. Chen, S.F.; He, X.L.; Wang, Z.F. Development of research on drip irrigation of saline water. *Water Sav Irrig.* **2010**, *2*, 6–9. (In Chinese with English Abstract)


17. Wang, T.; Guo, Z.; Kuo, C.T. Effects of mixing Yellow River water with brackish water on the emitter's clogging substance and solid particles in drip irrigation. *SN Appl. Sci.* **2019**, *1*, 1269. [CrossRef]
18. Ding, B.; Bai, Y.; Guo, S.; He, Z.; Wang, B.; Liu, H.; Zhai, J.; Cao, H. Effect of irrigation water salinity on soil characteristics and microbial communities in cotton fields in Southern Xinjiang, China. *Agronomy* **2023**, *13*, 1679. [CrossRef]
19. Slama, F.; Zemni, N.; Bouksila, F.; De Mascellis, R.; Bouhlila, R. Modelling the impact on root water uptake and solute return flow of different drip irrigation regimes with brackish water. *Water* **2019**, *11*, 425. [CrossRef]
20. Qadir, M.; Quill  rou, E.; Nangia, V.; Murtaza, G.; Singh, M.; Thomas, R.J.; Drechsel, P.; Schmid, E.; Donaj, D.; Noble, A.D. Economics of salt-induced land degradation and restoration. *Nat. Resour. Forum.* **2014**, *38*, 282–295. [CrossRef]
21. Feng, J.; Li, Y.; Wang, W.; Xue, S. Effect of optimization forms of flowpath on emitter hydraulic and anti-clogging performance in drip irrigation system. *Irrig. Sci.* **2018**, *36*, 37–47. [CrossRef]
22. Lv, C.; Zhang, E.; Gan, H.; Niu, W.; Ali, S.; Dong, A.; Zhang, W.; Sun, D. Aerated drip irrigation increased the emitter clogging risk of the Yellow River water drip irrigation. *Irrig. Drain.* **2023**, *72*, 3–20. [CrossRef]
23. Zaiyu, L.; Yan, M.; Hao, G.; Shihong, G.; Yanqun, Z.; Guangyong, L.; Feng, W. The hydraulic performance and clogging characteristics of a subsurface drip irrigation system operating for five years in the North China plain. *Agric. Water Manag.* **2025**, *307*, 109217. [CrossRef]
24. Benlouali, H.; Karmal, I.; Cherif Harrouni, M.; Ghanbaja, J.; Frascari, D.; Hamdani, M.; Choukr-Allah, R. Characterization of clogging deposits in an irrigation pipeline and effect of post-aeration on clogging potential of tertiary-treated wastewater. *Water Sci. Technol.* **2021**, *83*, 309–321. [CrossRef]
25. Shi, K.; Zhangzhong, L.; Han, F.; Zhang, S.; Guo, R.; Yao, X. Reducing emitter clogging in drip fertigation systems by magnetization technology. *Sustainability* **2023**, *15*, 3712. [CrossRef]
26. Petit, J.; Ait-Mouheb, N.; Garc  a, S.M.; Metz, M.; Molle, B.; Bendoula, R. Potential of visible/near infrared spectroscopy coupled with chemometric methods for discriminating and estimating the thickness of clogging in drip-irrigation. *Biosyst. Eng.* **2021**, *209*, 246–255. [CrossRef]
27. Li, G.B.; Li, Y.K.; Xu, T.W.; Liu, Y.Z.; Jin, H.; Yang, P.L.; Zhang, F.S.; Tian, Z.F. Effects of average velocity on the growth and surface topography of biofilms attached to the reclaimed wastewater drip irrigation system laterals. *Irrig. Sci.* **2012**, *30*, 103–113. [CrossRef]
28. Yuan, H.; Wang, Y.; Sun, Z.; Shi, N.; Li, B.; Ma, C.; Xiao, Y.; Li, Q.; Li, Y. Increasing iron use efficiency by controlling emitter clogging in drip irrigation systems. *Agric. Water Manag.* **2023**, *290*, 108601. [CrossRef]
29. Ribeiro, M.D.; Azevedo, C.A.D.; Santos, D.B.D.; Szkut, F.D.; Klein, M.R.; Reis, C.F. Optical microscopy and SEM for identifying clogging material in a drip irrigation system. *Rev. Coatinga* **2018**, *31*, 997–1007. [CrossRef]
30. Petit, J.; Garc  a, S.M.; Molle, B.; Bendoula, R.; Ait-Mouheb, N. Methods for drip irrigation clogging detection, analysis and understanding: State of the art and perspectives. *Agric. Water Manag.* **2022**, *272*, 107873. [CrossRef]
31. Yao, Y.; Shen, Y.; Ma, C.; Zhang, K.; Li, J.; Xiao, Y.; Li, Y. Spatial distribution of clogging substances in drip irrigation emitters fed with reclaimed water. *Irrig. Sci.* **2024**, *42*, 239–251. [CrossRef]
32. Ma, C.; Li, M.; Hou, P.; Wang, X.; Sun, Z.; Li, Y.; Zhang, K.; Yao, Y.; Li, Y. Biofilm dynamic changes in drip irrigation emitter flow channels using reclaimed water. *Agric. Water Manag.* **2024**, *291*, 108624. [CrossRef]
33. Ramachandrupa, V.R.; Kasa, R.R.; Torris, A. Micro-Computed Tomography (μ CT) Study of Clogging in Long-Used Strip and Cylindrical Drip Emitters. *J. Inst. Eng. India Ser. A* **2023**, *104*, 167–174. [CrossRef]
34. Chiffre, L.; Carmignato, S.; Kruth, J.; Schmitt, R.; Weckenmann, A. Industrial applications of computed tomography. *CIRP Ann. Manuf. Technol.* **2014**, *63*, 655–677. [CrossRef]
35. Wang, T.; Dai, X.; Zhang, T.; Xin, C.; Guo, Z.; Wang, J. Formation and microbial composition of biofilms in drip irrigation system under three reclaimed water conditions. *Water* **2022**, *14*, 1216. [CrossRef]
36. Davit, Y.; Debenest, G.; Quintard, M. Multiple-scale analysis of transport in porous media with biofilms. In *AIP Conference Proceedings*; American Institute of Physics: College Park, MD, USA, 2010; Volume 1254, Issue 1, pp. 175–180. [CrossRef]
37. Wang, W.; Xu, F.; Zhou, B.; Feng, J.; Li, Y. Structural and fractal characteristics of biofilm attached on surfaces of sediments in Yellow River for drip irrigation. *J. Drain Irrig. Mach. Eng.* **2014**, *32*, 914–920. (In Chinese with English Abstract) [CrossRef]
38. Zhou, L.; Wei, C.; Yang, P.; Li, Y.; Zhangzhong, L.; Su, Y.; Ren, S.; He, X. Effects of saline water with different concentrations of calcium and magnesium ions on emitter clogging in drip irrigation integrated water–fertilizer system. *Irrig. Drain.* **2024**, *73*, 16–28. [CrossRef]
39. Zhangzhong, L.; Yang, P.; Ren, S.; Li, Y.; Liu, Y.; Xia, Y. Chemical clogging of emitters and evaluation of their suitability for saline water drip irrigation. *Irrig. Drain.* **2016**, *65*, 439–450. [CrossRef]
40. Lequette, K.; Ait-Mouheb, N.; W  ry, N. Hydrodynamic effect on biofouling of milli-labyrinth channel and bacterial communities in drip irrigation systems fed with reclaimed wastewater. *Sci. Total Environ.* **2020**, *738*, 139778. [CrossRef]
41. Qian, J.; Horn, H.; Tarchitzky, J.; Chen, Y.; Katz, S.; Wagner, M. Water quality and daily temperature cycle affect biofilm formation in drip irrigation devices revealed by optical coherence tomography. *Biofouling* **2017**, *33*, 211–221. [CrossRef]

42. Li, Y.; Liu, H.; Yang, P.; Wu, D. Analysis of tracing ability of different sized particles in drip irrigation emitters with computational fluid dynamics. *Irrig. Drain.* **2013**, *62*, 340–351. [CrossRef]
43. Shen, Y.; Puig-Bargués, J.; Li, M.; Xiao, Y.; Li, Q.; Li, Y. Physical, chemical and biological emitter clogging behaviors in drip irrigation systems using high-sediment loaded water. *Agric. Water Manag.* **2022**, *270*, 107738. [CrossRef]
44. Yang, B.; Wang, F.; Wang, J.; Wang, C.; Qiu, X. Numerical simulation and optimization of the inlet structure of dentiform emitters in drip-irrigation systems. *Biosyst. Eng.* **2024**, *246*, 183–190. [CrossRef]
45. Wang, H.; Wang, J.; Wang, C.; Wang, S.; Qiu, X.; Sun, Y.; Li, G. Characterization of labyrinth emitter-clogging substances in biogas slurry drip irrigation systems. *Sci. Total Environ.* **2022**, *820*, 153315. [CrossRef]

Disclaimer/Publisher’s Note: The statements, opinions and data contained in all publications are solely those of the individual author(s) and contributor(s) and not of MDPI and/or the editor(s). MDPI and/or the editor(s) disclaim responsibility for any injury to people or property resulting from any ideas, methods, instructions or products referred to in the content.

Article

A Deep Learning Method Coupling a Channel Attention Mechanism and Weighted Dice Loss Function for Water Extraction in the Yellow River Basin

Jichang Yang ^{1,2}, Yuncong Lu ^{1,3}, Zhiqiang Zhang ⁴, Jieru Wei ^{1,2}, Jiandong Shang ^{1,2,*}, Chong Wei ^{4,*}, Wensheng Tang ^{1,2}  and Junjie Chen ^{1,2}

¹ The School of Computer and Artificial Intelligence, Zhengzhou University, Zhengzhou 450000, China; nscczyjc@gs.zzu.edu.cn (J.Y.); luyuncong@rpc.edu.cn (Y.L.); weijr0117@gs.zzu.edu.cn (J.W.); tangwensheng@gs.zzu.edu.cn (W.T.); c17538273356@gs.zzu.edu.cn (J.C.)

² National Supercomputing Center in Zhengzhou, Zhengzhou University, Zhengzhou 450000, China

³ Department of Image and Network Investigation, Zhengzhou Police University, Zhengzhou 450000, China

⁴ College of Surveying and Geo-Informatics, North China University of Water Resources and Electric Power, Zhengzhou 450046, China; zhangzhiqiang@ncwu.edu.cn

* Correspondence: sjd@zzu.edu.cn (J.S.); weic85@ncwu.edu.cn (C.W.)

Abstract: The extraction of small water bodies in the Yellow River Basin has always been a key issue of concern in the fields of remote sensing technology application, water resource management, environmental science, and geographic information systems. Due to factors such as water bodies, human activities, and cloud cover, water body extraction becomes difficult. In addition, convolutional neural networks are prone to losing small water body feature information during the process of extracting local features, which can cause more imbalance between positive and negative samples of water bodies and non-water bodies. In response to these issues, this study focused on a specific research area—the middle and lower reaches of the Yellow River. We processed and analyzed high-resolution optical satellite images collected from the Yellow River Basin and other areas, with a particular emphasis on precise identification of small water bodies, and proposed a network structure, the SE-Attention-Residual-Unet (SE-ResUnet), for water extraction tasks. The main contributions of this article are threefold: (1) Introducing a channel attention mechanism with residual structure in the down-sampling process, and learning Unet's skipping structure for multi-scale feature extraction and compensation, thereby enhancing the feature extraction ability of small water bodies, including rivers, lakes, and reservoirs. (2) Introducing a weighted-Dice (W-Dice) loss function to balance positive and negative samples and enhance the generalization of the model. (3) In comparative experiments on improving the Unet model with semantic segmentation networks such as Unet, PSPNet, Deeplabv3+ on a self-built dataset and remote sensing interpretation public dataset, excellent performance and results were achieved on the mIoU, OA, and F1-score metrics. On the self-built dataset, compared with Unet, the mIoU, OA, and F1-score improved by 0.38%, 0.12%, and 0.08%, respectively. On the publicly available dataset, for remote sensing interpretation of water extraction, the mIoU, OA, and F1-score improved by 0.63%, 0.26%, and 0.25%, respectively. The experimental results demonstrate that a strategy combining an attention mechanism and a weighted loss function has a significant effect on the effectiveness of the collaborative improvement of neural network models in water extraction tasks.

Keywords: improved Unet; semantic segmentation; channel attention; water extraction; remote sensing images; weighted loss function

1. Introduction

The use of remote sensing technology, namely, optical remote sensing images, is becoming important in the extraction of water bodies due to its wide coverage, abundant information, and fast update rate. Remote sensing imagery provides efficient and accurate data on water bodies, offering significant assistance for related research and applications [1]. Water body extraction technology is founded on the capacity to identify, classify, and retrieve data pertaining to water bodies from remote sensing methods. This procedure utilizes technologies and knowledge from various domains, such as image processing, pattern recognition, geographic information systems, and others [2]. Water bodies typically exhibit distinct spectral and spatial properties, such as reflectivity, texture, shape, etc. By analyzing and using these attributes, we may efficiently gather information about water bodies. In recent years, the progress in computer and remote sensing technologies has resulted in notable improvements in water body extraction technology [3].

The water body index and image classification method are the two main conventional techniques employed for extracting water bodies from high-resolution optical remote sensing images. Several scholars have developed a variety of indicators for extracting information about water bodies. McFeeter proposed using the Normalized Differential Water Index (NDWI) for the green and near-infrared bands [4]. Nevertheless, the presence of buildings causes substantial interference with NDWI, hence posing difficulties in accurately identifying water bodies in such areas. In order to overcome the limitations of the NDWI, Xu et al. proposed the Modified Normalized Differential Water Index (MNDWI) [5], which replaces the near-infrared band with the short-wave infrared band in NDWI [5]. Yan et al. introduced the Enhanced Water Index (EWI) by merging NDWI and MNDWI [6]. Feyisa et al. developed the Automated Water Extraction Index (AWEI) [7] to reduce noise in mountainous and urban regions. Zhang et al. [8] combined a suspended particulate matter concentration and water index to reveal the multi-scale variation pattern of the surface water area in the Yellow River Basin. They used various bands (1, 2, 4, 5, and 7) of Landsat 5 TM. Other, less prevalent water indices encompass the shadow water index, pseudo-NDWI, Gaussian NDWI, MNDWI, and the new water index. However, the majority of water index techniques are unsuitable due to the limited number of spectral bands found in high-resolution images, often consisting of only four bands: blue, green, red, and near infrared.

In order to overcome the shortcomings of the water index method and make use of the spatial information of high-resolution optical remote sensing images, various image classification methods have been proposed. Image classification performs water extraction by combining spectral, shape, and texture features and using various classifiers in machine learning. Commonly used classifiers include decision tree [9], random forest [10], support vector machine [11–13], etc. Although image taxonomies can make use of a variety of features to achieve better results than water index methods, they require these features to be manually constructed for specific water extraction tasks. This will greatly reduce the efficiency and prolong the extraction time. In addition, the application scope of these artificially constructed features is limited, and it is difficult to extract water bodies in different regions [14].

Convolutional Neural Networks (CNNs) [15] have gained popularity in the fields of semantic segmentation, object identification, and scene categorization due to their ability to efficiently learn multiple layers of automated features. Water body extraction is a specific task in semantic segmentation that is commonly addressed by CNN models [16]. Chen et al. introduced an adaptive water extraction pooling layer [17] to reduce the loss of features during pooling. Most existing methods fail to meet the extraction requirements of water bodies of different sizes [18]. In addition, as features are extracted sequentially, the

size of the feature map will decrease, potentially leading to the omission of small water bodies with subtle characteristics, resulting in biased outcomes. Thus, it is necessary to employ multi-layer and multi-scale characteristics in order to address these challenges. Multi-layer features refer to features that have been extracted from different convolutional neural network (CNN) layers [19,20]. Several multi-scale feature extraction modules have been developed as a result of semantic segmentation, such as Spatial Pyramid Pooling (SPP), Pyramid Pooling Module (PPM) in PSPNet [21], and Atrous Spatial Pyramid Pooling (ASPP) in DeepLabv2. Unfortunately, data loss occurs due to the absence of multi-layer settings in these multi-scale feature extraction modules, which primarily execute pooling on feature maps. And Sun et al. [22] improved the Deeplabv3+ network to extract water bodies and attempted to combine DEM data with remote sensing image data to extract small water bodies [23]. Cao et al. [24] extracted water bodies from high-resolution remote sensing images by enhancing Unet networks and multi-scale information fusion. Yan et al. [25] used a novel water body extraction method to automate water body extraction from Landsat 8 OLI images. Cheng et al. [26] proposed a water body extraction method based on spatial partitioning and feature decoupling. Zhao et al. [27] proposed an unsupervised water body extraction method by combining the estimated probabilities of historical, neighboring, and neighborhood prior information using Bayesian model averaging. Chen et al. [28] refined the feature information by introducing dynamic semantic kernels to achieve high-precision extraction of lake water bodies. Mishra et al. [29] used principal component analysis to fuse panchromatic and infrared bands to classify the fused images into surface types. Wang et al. [30,31] incorporated a mixed-domain attention mechanism into the decoder structure to fully exploit the spatial and channel features of small water bodies in the image.

Traditional water extraction methods, such as the threshold method, spectral index method, object-oriented method, and machine learning classification method, mainly rely on manual statistical features and expert experience, which may not be effective in dealing with complex backgrounds or diverse water bodies. In addition, traditional methods often struggle to achieve a high degree of automation, which increases the complexity and time cost of operations. Interference factors such as shadows and buildings can also limit the accuracy of water extraction, and traditional methods may not be flexible and accurate enough in dealing with these interferences. Deep learning methods can automatically learn and extract useful features from input data without the need for manual feature selection and extraction, greatly improving the efficiency and accuracy of water extraction. Deep learning models can learn complex features and the intrinsic laws of water bodies by training on large amounts of data, thus having good generalization ability to unknown data. Furthermore, deep learning models have strong robustness to noise and interference, and can handle water extraction tasks in complex backgrounds. Deep learning models have transferability and can be applied to water extraction tasks in different regions and data sources. Moreover, with the continuous development of technology, deep learning models can be continuously optimized and expanded to meet more complex water extraction needs.

In light of this, the current study constructs a feature extraction network that utilizes the Unet's multi-scale feature architecture and jumping structure [32] to extract water body features at several layers and scales. The water body extraction task involves only two categories: background and water body. To ensure a balanced representation of positive and negative data during training, the W-Dice loss function is incorporated. To be more precise, the model minimizes unnecessary computation usage while accurately extracting the crucial information from the data by combining the optimization guidance of the loss function with the focusing ability of the attention mechanism [33]. This enhances the model's cognitive process and augments the precision of its predictions. The W-Dice loss function offers a distinct optimization objective for the model, while the SE channel

attention mechanism effectively captures the complex relationships among several channels in remote sensing images. To achieve the desired outcomes, this combination enables the model to consistently improve its performance and optimize the utilization of river features in remote sensing images [34].

The main contents of this paper are as follows:

- (1) The down-sampling approach integrates the SE attention mechanism with a residual structure, and learns the jumping structure of the Unet for multi-scale feature extraction and compensation. This enhances the capability to extract the characteristics of small water bodies, including rivers, lakes, and reservoirs.
- (2) In order to enhance the model's generalization and to ensure that both positive and negative samples are given equal importance, the W-Dice loss function is incorporated into the loss calculation during the training phase.
- (3) The enhanced network model is compared and evaluated with semantic segmentation networks like PSPNet and Deeplabv3+ on both a self-built remote sensing image dataset and another public remote sensing interpretation dataset. The effectiveness of water body extraction is assessed using the mIoU as a crucial metric.

2. Materials and Methods

2.1. SE-ResUnet

The network configuration described in this paper, illustrated in Figure 1, is referred to as the SE-ResUnet. The coding layer is predominantly situated on the left side of the diagram, whereas the decoding layer is positioned on the right. The input image is reconstructed at the decoder stage after passing through the convolutional structure's feature extraction backbone network. To address the presence of features, the output feature images from several down-sampling layers are combined and overlaid using a hierarchical structure. An SE attention mechanism is incorporated into the third down-sampling layer of the ResnetBottleNeck [35] module within the residual structure. The primary distribution of the residual structure with the SE attention mechanism in the structure diagram of the SE-ResUnet is in the feature extraction backbone network, which is referred to as the "SRBlock".

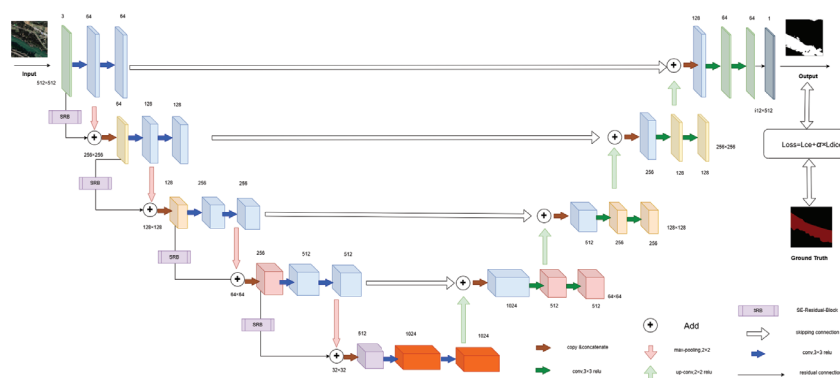


Figure 1. SE-ResUnet network structure.

Convolutional neural networks have advantages in extracting local feature information from remote sensing images, including remote sensing water body images. However, for small water bodies in the distribution of remote sensing images, they are easily lost during the down-sampling process, and the retained small water bodies pixels are more difficult to capture due to the small number of samples. Therefore, we introduce a residual structure with a channel attention mechanism on the basis of the Unet network to compensate for the lost small water bodies features during the down-sampling process. In addition, we coupled the weighted Dice loss function to balance positive and negative samples, thereby

reducing the impact of insufficient positive samples in small water bodies. Shown in Figure 2 is the improved flow chart of the SE-ResUnet model.

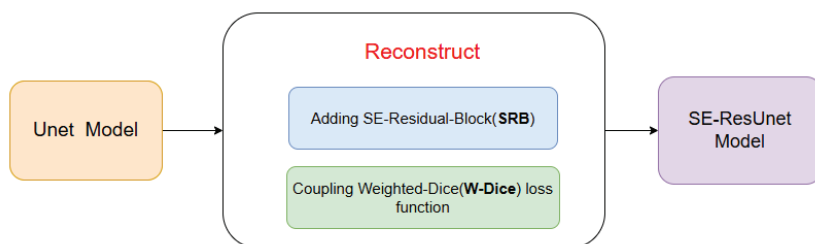


Figure 2. Flow chart of the SE-ResUnet model.

2.2. Squeeze-Excitation Residual Block Module

A unique architectural unit, called the Squeeze-Excitation Residual Block (SRB) module, is intended to improve the network representation capabilities by means of dynamic channel feature recalibration. The structure of the SRB module and ResBlock are comparable in that they both have residual connections, as seen in Figure 3. The SRB module's rightmost branch, in contrast to the typical ResBlock, further includes functions like global pooling, a fully connected layer, a ReLU activation function, and a sigmoid function. These functions, in turn, transform, compress, and excite images with input size $H \times W \times C$. It is easy to see how the image's width, height, and channel change during this procedure. In order to produce the attention mechanism effect, the final step involves performing feature fusion with the left branch after restoring the image to an $H \times W \times C$ tensor of the same size as the input through the zoom operation.

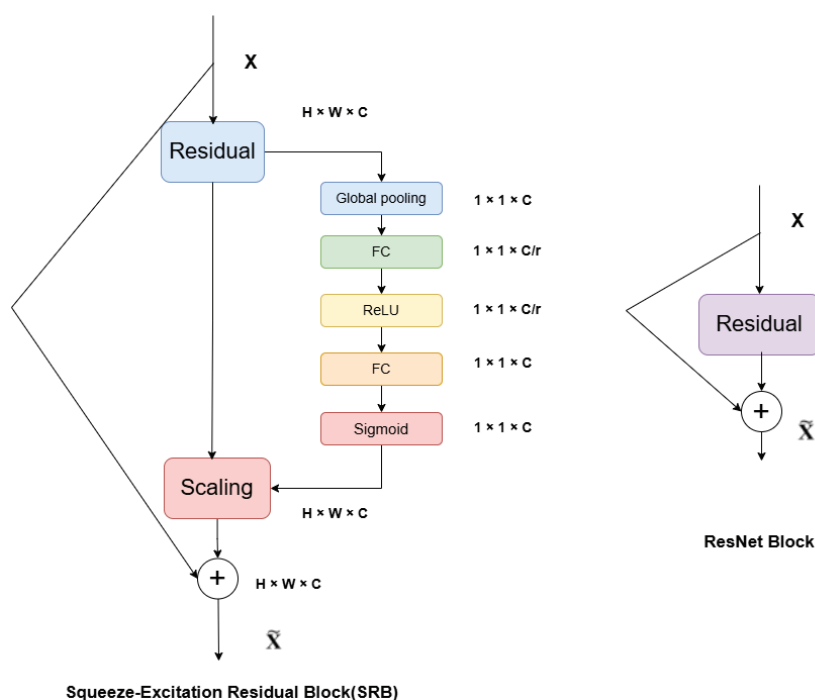


Figure 3. SRB structure.

We built the modified SE-ResUnet by first reconstructing the original Unet, adding the SE attention mechanism, and replacing the original loss function with the W-Dice loss function and the CE cross-entropy loss function. The modified SE-ResUnet is then applied to the remote sensing satellite images for water body extraction.

By explicitly modeling the interdependencies between convolutional feature channels, the Squeeze-and-Excitation technique [36] can enhance the network's representation ca-

capacity. This strategy enables the network to dynamically recalibrate features by selectively stressing desirable ones and suppressing undesirable ones, hence facilitating the learning of global information.

The SE module has three essential actions for recalibrating the input X feature channel, as depicted in Figure 4. After a number of convolutions and transformations, a feature with a specific number of feature channels, denoted as $C2$, is produced. This is based on the assumption that the input X has a certain number of feature channels, denoted as $C1$. F_{tr} represents the standard convolution operation, which transforms the feature map X into the feature map U , and F_{sq} represents the compression operation, specifically using global average pooling of channels to compress global spatial information into a channel descriptor. F_{ex} scales the channel dimension by a fixed coefficient to fully capture channel dependencies in order to utilize the information gathered during compression operations. F_{scale} weights the attention weights obtained earlier onto the features of each channel to obtain the final output of the module \tilde{X} .

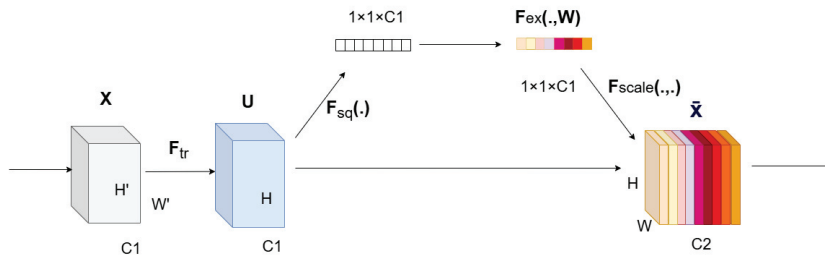


Figure 4. The Squeeze-Excitation module.

The first operation, known as squeezing, is responsible for feature compression in the spatial dimension. It turns each two-dimensional feature channel into a single real number, so creating a somewhat global receptive field. The output dimension is equal to the number of input feature channels, denoted as $C1$. It is highly beneficial in various activities as it represents the worldwide distribution of the response on the feature channel and allows the layers close to the input to also obtain the global receptive field. The second operation is excitation, which is analogous to the gating process seen in recurrent neural networks. The parameter w assigns weights that explicitly represent the relationship between the feature channels for each individual feature channel. The final step in re-calibrating the original features in the channel dimension is the reweighting operation. This operation utilizes the output weight of the excitation operation as a crucial indicator for each feature channel. It then applies this weight to the previous feature channels through multiplication, one channel at a time. The attention mechanism [37] is achieved through two crucial steps: the fully connected layer and feature multiplication fusion. Assuming that a fully connected layer and global pooling are employed, the input image with dimensions $H \times W \times C1$ is extended to a $1 \times 1 \times C1$ size. The initial image is subsequently multiplied to allocate weights to each channel.

2.3. Loss Function

Cross-entropy loss is a metric for calculating the discrepancy between the actual and predicted maps. The cross-entropy loss function allows the network to have a faster gradient descent process during the first training stage, preventing gradient disappearance, when compared to other loss functions, like the mean square error and the L1 loss [38]. As shown in Formula (1), the divergence between the two probability distributions, j and k (j)

representing the actual distribution and k representing the predicted distribution) is known as the cross-entropy in information theory. One can obtain the cross-entropy loss L_{CE} by:

$$L_{CE}(j, k) = - \sum_{i=1}^n j(x_i) \log(k(x_i)) \quad (1)$$

In the water body extraction task, $j(x_i)$ is the ground truth label and $k(x_i)$ is the predicted water body map, as shown in Formula (2). In the binary classification task (e.g., water body extraction), one can obtain the cross-entropy loss by:

$$L_{CE}(j, k) = -[j \log k + (1 - j) \log(1 - k)] \quad (2)$$

To process the resulting feature map, the Softmax function and cross-entropy loss function are typically employed. The cross-entropy loss is computed after adding the predicted values of all the classes to one. The model's prediction improves with a decreasing cross-entropy value [39]. The dice coefficient, a commonly used set similarity measure function, is employed to assess the similarity between two samples. This coefficient ranges from 0 to 1 in Formula (3), as follows:

$$DiceCoefficient = \frac{2 |X \cap Y|}{|X| + |Y|} \quad (3)$$

where $|X \cap Y|$ represents the intersection of the $|X|$ and $|Y|$ sets, and $|X|$ and $|Y|$ represent the number of its elements, respectively. In the segmentation task, $|X|$ and $|Y|$ represent the segmented ground truth and the predict mask in Formula (4). Furthermore, the formula of the Dice loss is as follows:

$$DiceLoss = 1 - \frac{2 |X \cap Y|}{|X| + |Y|} \quad (4)$$

The enhanced model training incorporates the W-Dice loss, and the parameter is used to modify the Dice loss weight during backpropagation. The W-Dice loss and cross-entropy loss make up the two components of the overall model loss in Formula (5). In this experiment, we set the parameter value to 0.5, meaning that the optimal water body extraction effect is achieved when the ratio of the cross-entropy loss to the Dice loss is 2:1.

$$Loss = L_{CE} + \partial L_{Dice} \quad (5)$$

2.4. Evaluation Metrics

To assess our model's performance, we utilized three commonly-used evaluation metrics: the F1-score, Overall Accuracy (OA), and Mean Intersection over Union (mIoU). True positive (TP), false positive (FP), true negative (TN), and false negative (FN) are the elements of the confusion matrix from which the recall rate (Recall) and the precision indicator (Precision) can be obtained, as shown in Formulas (6)–(8). The F1-score can be obtained as:

$$Precision = \frac{TP}{TP + FP} \quad (6)$$

$$Recall = \frac{TP}{TP + FN} \quad (7)$$

$$F1 - score = 2 \times \frac{Precision \times Recall}{Precision + Recall} \quad (8)$$

The ratio of the results that the model properly predicts on all test sets to the total dataset is known as the overall precision in Formula (9). OA is best defined as:

$$OA = \frac{TP}{TP + FP + TN + FN} \quad (9)$$

The Intersection over Union (IoU) ratio between the prediction map and the ground truth map for each class can be calculated as follows:

$$IoU = \frac{TP}{TP + FP + FN} \quad (10)$$

In the water body extraction task, as shown in Formula (10), TP denotes that the number of pixels in the water body is the same as the ground truth value and the prediction result, while TP + FP + FN denotes the number of pixels in their union region [40]. Furthermore, the average IoU value obtained from all classes of the remote sensing images is referred to as the mIoU.

We use the weight file size obtained after model training as an indicator to measure the number of model parameters, and GFLOPS as an indicator to measure the speed of model training and inference. That is, the size of the weight file obtained after SE-ResUnet training is used to evaluate the number of model parameters, measured in MB. The smaller the space occupied, the lighter the model parameters, and GFLOPS are used to evaluate the efficiency of model training and inference. GFLOPS is the Giga Floating Point Operations Per Second, which means 1 billion floating-point operations per second. The larger the GFLOPS, the faster the model training and inference speed.

2.5. Dataset Description

The first self-built dataset used for the experiment consists of four main components of remote sensing images data. The UC-Merced Land-Use dataset is where the first component is taken from, including 99 images in total, each measuring 256 by 256 pixels and having a resolution of 0.3 m. The UC-Merced Land-Use dataset comprises 100 distinct image categories, providing a comprehensive collection of 21 levels of land use remote sensing data. The river images that were taken from the WHU-RS19 dataset make up the second component, including 56 images in total, each measuring 600 by 600 pixels and having a resolution of 0.5 m. The river images, extracted from the AID dataset, constitute the third component, including 410 images in total, each having a resolution of 0.5–8 m and measuring 600 by 600 pixels. The remote sensing image dataset AID was released by the Wuhan University and Huazhong University of Science and Technology in 2017, and contains a total of 30 categories of images, each containing 220–420 images and totaling 10,000 images. The remote sensing image data of the Yellow River Basin are mainly collected from the Gaofen-2 satellite, with a total of 1000 sample images. The image of one scene measures 6920 by 7300 pixels and the resolution is 3 m. In order to facilitate model training, the collected multi-scene images are segmented into small blocks, which measure 256 by 256 pixels. In the early stage of the experiment, the visual interpretation method and the ‘labelme’ tool were used to uniformly annotate and name these images, so as to produce images and labels for subsequent model training. The river semantic annotation format follows the specification of the VOC dataset, and is uniformly called Dataset1 in the study, as shown in Figure 5.

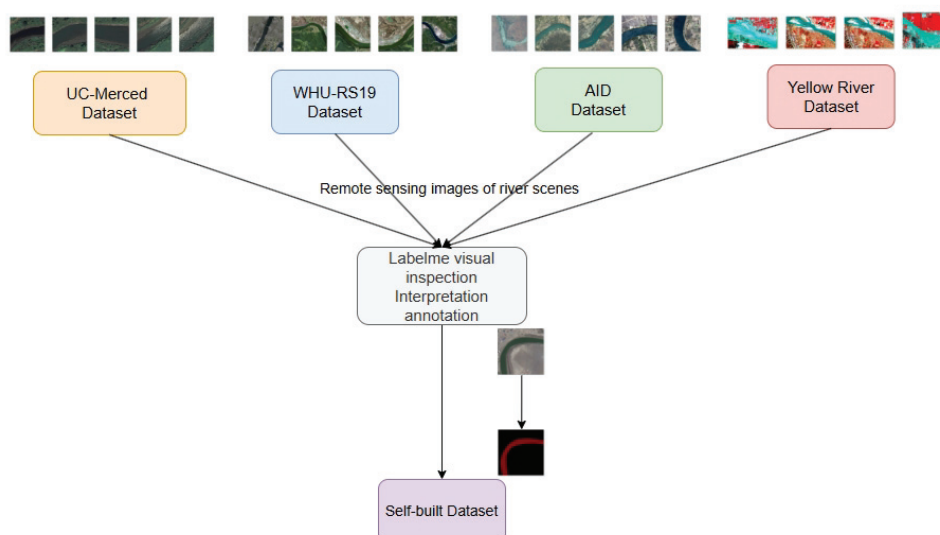


Figure 5. Dataset1 remote sensing image data collection and labeling procedure.

The Kaggle Remote Sensing Interpretation Public Dataset provides a second remote sensing image dataset for model training and generalization. The optical remote sensing image in question is part of a resource series and possesses a high resolution of 2 m. It is used to extract the water surface within the study area and is mostly directed towards domestic complicated water bodies. There are two categories in the dataset: background and water body. Each sample consists of two PNG files, Image and Label, that have identical file names. The Label file is in the single-channel 8-bit format, with a background pixel value of 0 and a water surface information value of 255, and the sample Image file is in 3-channel PNG format. The image size is 1024×1024 pixels, and the dataset contains a total of 2000 sets of data. All references to this dataset in the research are to Dataset2, as shown in Table 1.

Table 1. The spatial resolution, size, and quantity information of the datasets used in the experiment, Dataset2 denotes the Kaggle Remote Sensing Interpretation Public Dataset.

Dataset Name	Spatial Resolution	Size	Number
UC-Merced	0.3	256×256	99
WHU-RS19	0.5	600×600	56
AID	0.5–8	600×600	410
Yellow River	0.8	256×256	1000
Dataset2	2	1024×1024	2000

The design of the SE-ResUnet model takes into account the problem of adapting to the input of different image sizes. For the input of images of different sizes, the patch will be uniformly adjusted to the standard size of 512×512 . If the input image size is larger than the standard size, the data preprocessing will slide-crop the image, and then train the cropped fragment in batches. If the input image is smaller than the standard size, it is filled to reach the standard patch size and then input to the network for training.

2.6. Data Enhancement

Figure 6 displays the samples and mask labels from Dataset1; Figure 7 displays the 2000 sets of samples and mask labels from Dataset2. We expanded Dataset1 by arbitrarily cropping, rotating, and mirroring images to fulfill the requirements of the deep learning model training. In the data preprocessing code section of the model, we use the Augmentor

library to perform data augmentation operations, such as cropping, rotating, and mirroring on the input source data, and expand the self-built dataset Dataset1 by controlling the number of remote sensing images used for training through parameter control. This study aimed to improve the model's generalizability by using geometric and color data enhancement approaches. Geometric data enhancement includes operations such as horizontal, vertical, and mixed flipping, while color data enhancement includes operations such as photometric distortion [41]. Photometric distortion adds noise to an image while adjusting its brightness, chroma, contrast, and saturation. The entire dataset covers a variety of water body types, such as lakes, rivers, canals, ponds and reservoirs, etc., as seen in Figures 6 and 7.

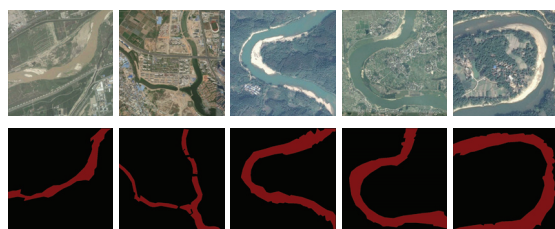


Figure 6. Original Dataset1 images and visual interpretation label images.

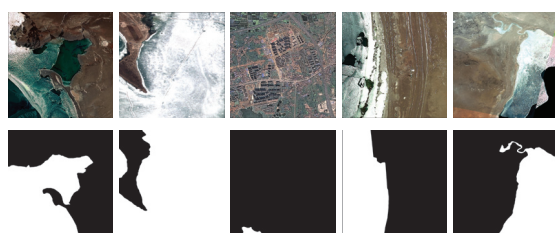


Figure 7. Original Dataset2 images and mask label images.

3. Results

3.1. Environment Settings

Our experiments were performed in a server environment (Intel Core w2223 quad core CPU and NVIDIA RTX 4070Ti GPU). The deep learning frameworks PyTorch 1.10.1 and Python 3.7 were used for all experiments, and CUDA 11.3 and CUDNN8.0 were used to speed up the training and inference process. The Adam optimizer was employed for training, with an initial learning rate of $1e-4$, a momentum parameter of 0.9, and a learning rate reduction strategy that optimizes the objective function using the cosine annealing descent method. There are 1000 training iterations in total. In the first 300 iterations, the backbone network's training parameters were retrieved by freezing features, and in the final 700 iterations, the training parameters were unfrozen. After data enhancement, we obtained two water body datasets, namely, Dataset1 and Dataset2, which contained a total of 3000 sets of original images and mask samples. The dataset was divided into a training set, validation set, and test set at a ratio of 7:2:1. Subsequent contrast experiments with different models and ablations will be performed on these two datasets. The software and hardware environments used for specific experiments are given in Tables 2 and 3.

Table 2. Hardware environment.

Hardware Environment	
Operating System	Ubuntu20.04LTS
CPU	Intel-w2223 Quad Core 3.6 Ghz
GPU	NVIDIA GeForce RTX4070Ti (12,288 MB)
RAM	64 GB

Table 3. Software environment.

Software Environment	Version
PyTorch/torchvision	1.10.1/0.11.2
CUDA/CUDNN	11.3/8.0
python	3.7.13
Opencv-python	4.1.2.30
pillow	8.2.0
pyYAML	5.4.1
scipy	1.2.1
tqdm	4.60.0
numpy	1.17.0
matplotlib	3.1.2
setuptools	65.6.3
tensorboard	2.11.2

3.2. Ablation Study

We conducted a comparative analysis between the SE-ResUnet and the original Unet model in order to assess their performance in large-scale water body extraction tasks. Furthermore, a sequence of ablation tests were conducted to confirm the efficacy of including the SRB module and the weighted Dice loss function [15]. In particular, training was performed on the two previously introduced datasets using the original Unet feature extraction network as the baseline network, introducing the SRB module and the W-Dice loss in turn. The dataset is labeled and divided before being introduced into the model in batches for training. Tables 4 and 5 display the comparison results.

Table 4. Evaluation metrics from the ablation study on Dataset1 (SRB represents the residual structure with channel attention, and W-Dice represents the weighted Dice loss function).

Dataset1	mIoU	OA	F1-Score
Unet	94.44	98.41	97.82
+SRB	94.60	98.40	97.70
+W-Dice	94.17	98.34	97.62
+W-Dice + SRB	94.82	98.53	97.90

Table 5. Evaluation metrics from the ablation study on Dataset2 (SRB represents the residual structure with channel attention, and W-Dice represents the weighted Dice loss function).

Dataset2	mIoU	OA	F1-Score
Unet	96.67	98.31	98.31
+SRB	96.72	98.34	98.35
+W-Dice	96.22	98.09	98.10
+W-Dice + SRB	97.02	98.50	98.51

Tables 4 and 5 show the ablation experiment results on Dataset1 and Dataset2. SRB represents the experimental results of introducing residual structures with attention. +W-

DICE represents the experimental results obtained by introducing the weighted Dice loss function. +W-DICE + SRB represents the experimental results of introducing both simultaneously. Upon careful examination of the results, it can be seen that introducing only one optimization strategy results in limited improvement on the model, even resulting in negative optimization when only the weighted Dice loss function is introduced. Introducing two optimizations simultaneously achieved the best water extraction effect, proving that the joint weighted Dice loss function and the residual structure with attention are effective in improving the model. The training phase statistics show that using just the original Unet network with Resnet as the backbone and adding the W-Dice loss function has a poor training effect. The tables show that the three metrics, mIoU, OA, and F1-score, dramatically decrease after the W-Dice loss is introduced to the Unet, whether on Dataset1 or Dataset2. There is a clear improvement in the training effect after SRB is added to the network. Compared to the original Unet, mIoU has a 0.1–0.2% improvement on both datasets. It is noteworthy that the training effect is greatly enhanced upon simultaneous introduction of the SRB module and the weighted Dice loss function. The model achieved the best mIoU on both datasets. This study confirms the efficacy of integrating SE attention and the weighted Dice loss function to enhance the accuracy of water body extraction in the model. Furthermore, it suggests that this combination is a promising approach for optimizing the model.

The inference results of some images from the ablation study on Dataset1 and Dataset2, GroundTruth, Unet, Unet + SRB, Unet + W-Dice and Unet + SRB + W-Dice are shown in Figures 8 and 9 from left to right, respectively. (a), (b), (c), (d), (e), and (f), respectively, represent Raw-Images, GroundTruth, Unet, Unet + SRB, Unet + W-Dice and Unet + SRB + W-Dice.

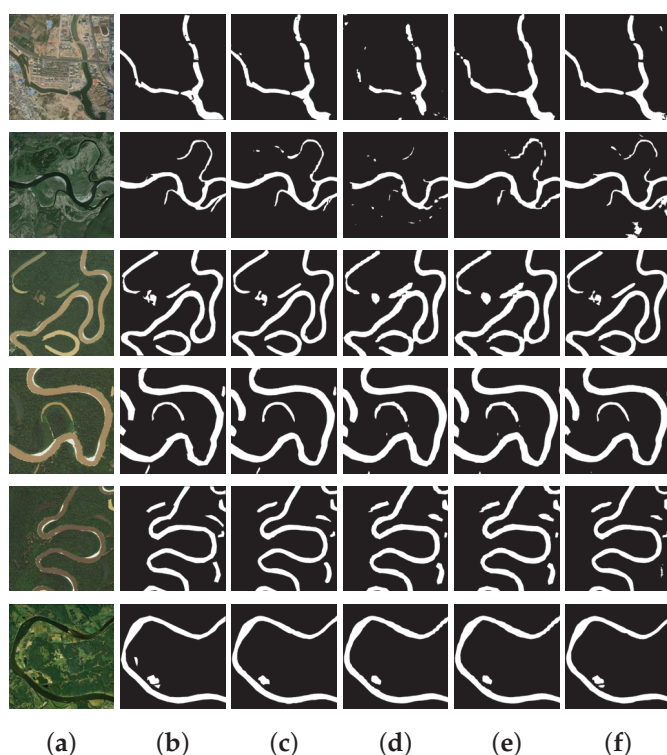


Figure 8. Ablation study on Dataset1. (a–f), respectively, represent Raw-Images, GroundTruth, Unet, Unet + SRB, Unet + W-Dice and Unet + SRB + W-Dice.

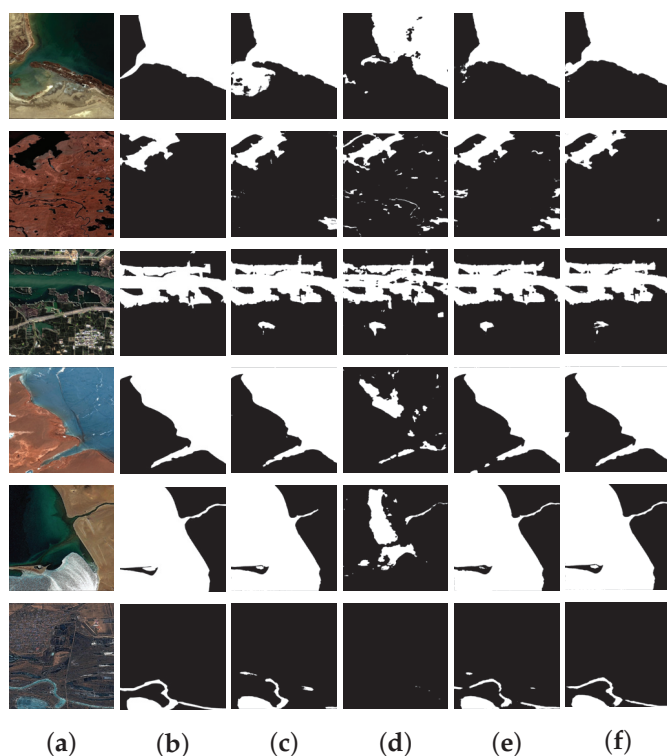


Figure 9. Ablation study on Dataset2. (a–f), respectively, represent Raw-Images, GroundTruth, Unet, Unet + SRB, Unet + W-Dice and Unet + SRB + W-Dice.

It is easy to see the results of the ablation experiment on Dataset 1 and Dataset 2. The introduction of the SRB module significantly improves the extraction effect of rivers compared to Unet. However, when only the W-Dice module is introduced, the water bodies at the end of the river branches cannot be extracted well. After introducing both the SRB module and the W-Dice mechanism, not only are the extracted river edges smoother, but the water bodies at the center of the river can also be identified well.

3.3. Contrast Experiment

To confirm that the model's performance had indeed improved when compared to other models, we trained SE-ResUnet and HRnet, Deeplabv3+, PSPnet, and the original Unet model [42] on two datasets and compared the results, as shown in Tables 6 and 7. The SE-ResUnet obtained the best evaluation metrics, indicating that it is more effective in water body extraction.

Table 6. Evaluation metrics from model performance comparison on Dataset1.

Dataset1	mIoU	Accuracy	F1-Score
HRnet	94.06	98.30	97.58
Deeplabv3+	94.05	98.30	97.58
Unet	94.44	98.41	97.82
PSPnet	93.39	98.10	97.30
SE-ResUnet	94.82	98.53	97.90

Table 5 displays the evaluation metrics of various models on Dataset 1 following 1000 training rounds. With a maximum mIoU of 94.82%, SE-ResUnet outperformed the original Unet semantic segmentation model by about 0.4%. Furthermore, SE-ResUnet's OA value of 98.53% was greater than the PSPNet model's OA value of 98.10%. At 97.9%, SE-ResUnet outperformed the Deeplabv3+ and HRNet models on the F1-score. These

findings demonstrate the effectiveness of the Unet improvement performed in this study, as well as the superior extraction effect on this water body dataset when compared to other semantic segmentation methods.

Figure 10 displays the outcomes of the model performance evaluation on Dataset1, including GroundTruth, Deeplabv3+, HRNet, PSPNet, and SE-ResUnet. (a), (b), (c), (d), (e), and (f), respectively, represent Raw-Images, GroundTruth, Deeplabv3+, HRNet, PSPNet, and SE-ResUnet.

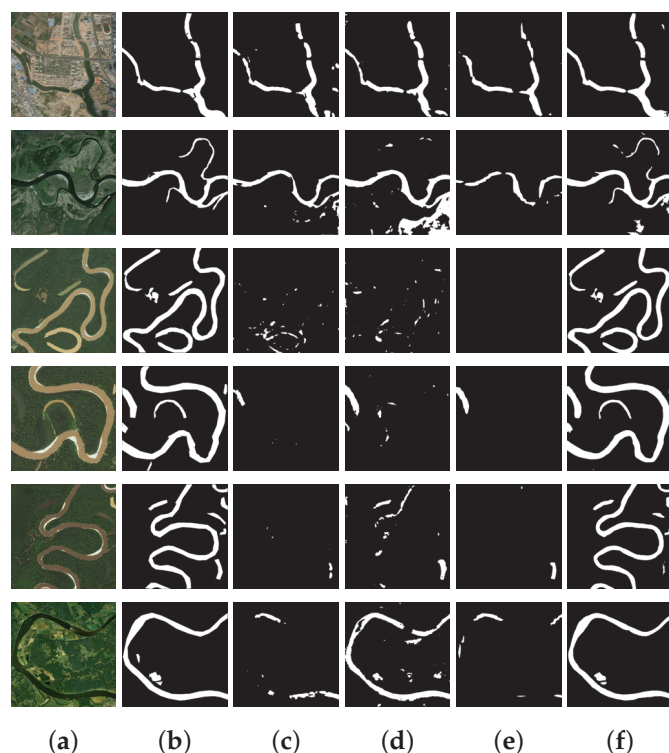


Figure 10. Contrast experiment on Dataset1. (a–f), respectively, represent Raw-Images, GroundTruth, Deeplabv3+, HRNet, PSPNet, and SE-ResUnet.

We can see from the comparative experiments on Dataset1 that compared with Ground Truth, Deeplabv3+, HRNet, and PSPNet, SE-ResUnet cannot extract the river center water body completely, and there is a different degree of missing extraction and over-extraction of the water body at the edge of the image. However, SE-ResUnet can extract the river edge more smoothly and the river center water body can be well recognized because it introduces the SRB module and W-Dice mechanism simultaneously, and the attention mechanism can pay more attention to the water body information between channels, as shown in Figure 9.

Table 7. Evaluation metrics from model performance comparison on Dataset2.

Dataset2	mIoU	Accuracy	F1-Score
HRnet	97.05	98.51	98.52
Deeplabv3+	96.64	98.30	98.31
Unet	96.67	98.31	98.31
PSPnet	94.94	97.42	97.44
SE-ResUnet	97.30	98.57	98.56

It was previously stated in the dataset description section that Dataset2 has a larger data volume than Dataset1. The training effect on Dataset2 is superior to that on Dataset1 from a variety of data indicator perspectives, and the three evaluation metrics (i.e., mIoU,

OA, and F1-score) have increased numerically. To be more precise, SE-ResUnet scored 97.3%, 98.57%, and 98.56% for each of the mIoU, OA, and F1-score metrics. The mIoU, OA, and F1-score of the modified Unet increased by 0.63%, 0.26%, and 0.25%, respectively, compared to the original Unet. They grew by 2.36%, 1.15%, and 1.12%, respectively, compared to PSPNet; 0.25%, 0.06%, and 0.04% compared to HRNet; and 0.66%, 0.27%, and 0.25% compared to Deeplabv3+. It follows that the Unet network with the SRB module performs better in extracting the water body's semantic information, and the weighted Dice loss function speeds up the entire training process to the point of convergence.

The results of the model performance comparison on Dataset2, including GroundTruth, Deeplabv3+, HRNet, PSPNet, and SE-ResUnet are shown in Figure 11 in left to right order. (a), (b), (c), (d), (e), and (f), respectively, represent Raw-Images, GroundTruth, Deeplabv3+, HRNet, PSPNet, and SE-ResUnet.

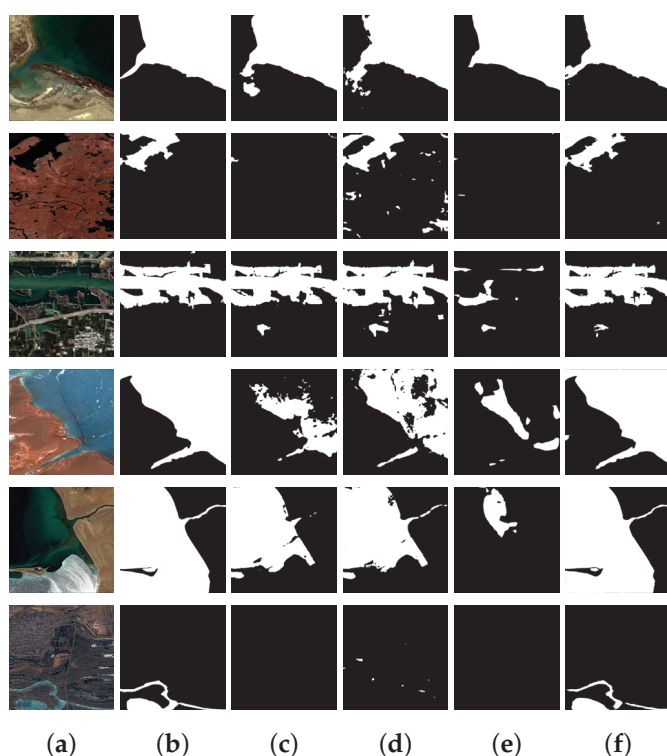


Figure 11. Contrast experiment on Dataset2. (a–f), respectively, represent Raw-Images, GroundTruth, Deeplabv3+, HRNet, PSPNet, and SE-ResUnet.

From the comparative experiments on Dataset2, we can see that compared with Ground Truth, PSPNet cannot extract the edge protruding type water body completely, and Deeplabv3+ and HRNet have a different degree of missing extraction and over-extraction of the water body at the edge of the image, and the main trunk of the extracted water body is also rough, as shown in Figure 11. However, SE-ResUnet can extract the river edge more smoothly and the river center water body can be well recognized because it introduces the SRB module and W-Dice mechanism simultaneously, and the weighted Dice loss function can pay more attention to the important water body information between channels. The river edge extracted is more smooth, and the water body at the edge protrusion and the river center can be well extracted.

Table 8 illustrates that after training, SE-ResUnet has the largest number of parameters, the largest weight file (177.5 MB), and the fastest inference speed (252.31 GFLOPS).

Table 8. Parameters and calculation speed of models involved in performance comparison.

	Param (MB)	GFLOPS (G)
HRNet	37.5	80.18
Deeplabv3+	22.4	52.87
Unet	167.9	200.57
PSPNet	25.5	55.6
SE-ResUnet	177.5	252.31

4. Discussion

This paper proposes the SE-ResUnet method for water extraction from satellite images. This method uses Unet's skipping structure for multi-scale feature extraction and compensation, the SE attention mechanism with residual structure for down-sampling, and the W-Dice loss function for loss calculation during training [35]. We conducted numerous performance comparison experiments and ablation studies on two datasets. The experiments demonstrated that, while adjusting the imbalance between water bodies and background distribution in some sample data, we can effectively acquire the semantic information of the river center and marginal water bodies in high-resolution remote sensing images.

The performance of SE-ResUnet was evaluated by comparing it with other semantic segmentation networks, such as Unet, PSPNet, HRNet, and Deeplabv3+. The evaluation was conducted using a self-built dataset and a publicly available remote sensing interpretation water body dataset. The comparison results demonstrated that SE-ResUnet shows superior water body extraction performance. The mIoU, OA, and F1-score of SE-ResUnet are improved by 0.38%, 0.12%, and 0.08%, respectively, on the generated dataset, while that on the public remote sensing dataset showed enhancements of 0.63%, 0.26%, and 0.25%, respectively, when compared with the original Unet. Based on the results displayed in Figures 10 and 11, SE-ResUnet was able to effectively extract target water bodies from those images containing spectral noise and other shadow interference, while fully extracting water bodies that are challenging to identify at the river's edge and center. The edge and ground truth also matched very well. The ablation study results, depicted in Figures 8 and 9, indicate a significant imbalance in the distribution of positive and negative samples between the water body and background in narrow rivers. Additionally, the SE-ResUnet model performs effectively on these specific test sets. The smoothness of the extracted water body's edge indicates that the SE channel attention mechanism with residual structure is more effective in capturing the relationship between different channels, especially the information at the image edge. However, solely using the W-Dice loss function is not enough to adequately supervise and focus on the features across channels. The comparison results and ablation study findings on the two datasets suggest that the weighted loss function can enhance the model's generalization, and help the SE-ResUnet model perform end-to-end water body extraction from multi-resolution remote sensing satellite images.

Our ablation experiment verified the feasibility of combining an attention mechanism and weighted loss function to optimize water extraction tasks, and achieved good experimental results on the two datasets used in the paper experiment. In the future, we will consider conducting experiments on more remote sensing image datasets and tasks to expand the application scope of this optimization strategy.

At the same time, it should be noted that there is still room for further experimentation with the Resnet backbone network selected by our proposed model. Additionally, the number and types of datasets are still limited, and there are not enough ways to enhance the data. This may result in poor generalization of our model on other datasets. However, based on our experimental results, our optimization strategy has shown good performance.

Despite achieving a good segmentation performance on Dataset1 and Dataset2, our suggested SE-ResUnet method still has significant limitations that will direct our future studies. First, there are a lot of parameters in the Unet model that are introduced into the SE attention mechanism, which means that training and deployment will be very expensive. We intend to use model pruning and distillation approaches to lower the model's complexity and processing requirements in order to increase efficiency in our follow-up research. The paper by Pandey et al. [43] includes a list of other performance metrics that we will attempt to use in other models to describe model performance and training effectiveness. Second, the left single CNN structure is not sensitive enough to fine features, especially when dealing with water body boundaries. The main reason is that this mode is an encoder-decoder network, which might result in less smooth water body boundary lines. Finally, a parameter is introduced to achieve a balance between the cross-entropy loss and Dice loss when computing the objective function using the W-Dice loss function. However, it is important to note that this parameter is not trained automatically. Due to the expense of training time, the experiment achieves its nearly optimal water extraction effect at a value of 0.5 after multiple manual adjustments. Subsequently, we can attempt to fine-tune it to the hyper-parameter of the network, and through the utilization of the training data, it will autonomously learn to reach a parameter threshold that is nearly optimal. Ozdemir et al. [44] used the automatic mask generator method of SAM to segment images and zero shot classification of fragments using CLIP. The proposed method accurately depicts water bodies under complex environmental conditions. In the future, combining SAM with massive remote sensing image data to complete segmentation and extraction tasks will be a research direction.

5. Conclusions

This paper proposes a new network structure, SE-ResUnet, which is used to extract small water bodies in the Yellow River Basin. Our experiments show that it has good generalization ability for water extraction tasks in large areas such as rivers, lakes, and reservoirs. We have derived the following conclusions:

- (1) The distinguishing characteristic of SE-ResUnet is the incorporation of the SE attention mechanism with the residual structure during the down-sampling process. This allows for the learning of the Unet's jumping structure, which facilitates multi-scale feature extraction and compensation.
- (2) SE-ResUnet enhances the ability to extract features from small water bodies in the Yellow River Basin, including large areas of water, such as rivers, lakes, and reservoirs. The W-Dice loss function was included in the training procedure.
- (3) On a generated dataset and a public remote sensing interpretation water body dataset, SE-ResUnet was compared with semantic segmentation networks, including Unet, PSPNet, HRNet, and Deeplabv3+. The comparison results demonstrated that the SE-ResUnet shows superior water body extraction performance and generalization.
- (4) SE-ResUnet's inference time cost is similar to the conventional Unet, demonstrating the high accuracy and high efficiency of our method. This suggests that the utilization of the channel attention mechanism in conjunction with the weighted Dice loss function is highly effective in enhancing the algorithm.

Author Contributions: Conceptualization, J.Y. and J.W.; methodology, J.Y., J.W., J.S., Y.L. and C.W.; software, J.Y., Y.L. and W.T.; validation, J.Y., W.T., J.C., J.S. and Z.Z.; formal analysis, J.Y.; investigation, J.Y., Z.Z. and C.W.; resources, J.Y., C.W., Y.L. and Z.Z.; data curation, J.Y., W.T., J.C., Z.Z. and J.W.; writing—original draft preparation, J.Y. and J.W.; writing—review and editing, J.Y., J.W. and J.S.; visualization, J.Y.; supervision, J.Y., Z.Z. and C.W.; project administration, J.Y., W.T., J.S. and Z.Z.; funding acquisition, J.S. All authors have read and agreed to the published version of the manuscript.

Funding: It should be noted that this research was funded by Science and Technology Innovation 2030 (2023ZD0120600), major science and technology project of Henan Province, China [221100210600], Higher Education Teaching Reform Research and Practice Project of NCWU (2024XJGXM061), Henan province water conservancy science and technology research projects (GG202404 GG202405, GG202338).

Data Availability Statement: The datasets that support the findings of this study are available on request from the corresponding author upon reasonable request.

Acknowledgments: We thank the laboratory for providing experimental equipment, including GPUs, and experimental datasets and for their support.

Conflicts of Interest: The authors declare that they have no known competing financial interests or personal relationships that could have appeared to influence the work reported in this paper.

References

1. Zhang, Z.; Wang, W.; Zhang, X.; Zhang, H.; Yang, L.; Lv, X.; Xi, X. A Harmony-Based Approach for the Evaluation and Regulation of Water Security in the Yellow River Water-Receiving Area of Henan Province. *Water* **2024**, *16*, 2497. [CrossRef]
2. Duan, M.; Qiu, Z.; Li, R.; Li, K.; Yu, S.; Liu, D. Monitoring Suspended Sediment Transport in the Lower Yellow River using Landsat Observations. *Remote Sens.* **2024**, *16*, 229. [CrossRef]
3. Nagaraj, R.; Kumar, L.S. Extraction of Surface Water Bodies using Optical Remote Sensing Images: A Review. *Earth Sci. Inform.* **2024**, *17*, 893–956. [CrossRef]
4. McFeeters, S.K. The use of the Normalized Difference Water Index (NDWI) in the delineation of open water features. *Int. J. Remote Sens.* **1996**, *17*, 1425–1432. [CrossRef]
5. Xu, H. Modification of normalised difference water index (NDWI) to enhance open water features in remotely sensed imagery. *Int. J. Remote Sens.* **2006**, *27*, 3025–3033. [CrossRef]
6. Yan, P.; Zhang, Y. A Study on Information Extraction of Water System in Semi-arid Regions with the Enhanced Water Index (EWI) and GIS Based Noise Remove Techniques. *Remote Sens. Inf.* **2007**, *6*, 62–67.
7. Feyisa, G.L.; Meilby, H.; Fensholt, R.; Proud, S.R. Automated Water Extraction Index: A new technique for surface water mapping using Landsat imagery. *Remote Sens. Environ.* **2014**, *140*, 23–35. [CrossRef]
8. Zhang, Z.; Guo, X.; Cao, L.; Lv, X.; Zhang, X.; Yang, L.; Zhang, H.; Xi, X.; Fang, Y. Multi-Scale Variation in Surface Water Area in the Yellow River Basin (1991–2023) Based on Suspended Particulate Matter Concentration and Water Indexes. *Water* **2024**, *16*, 2704. [CrossRef]
9. Quinlan, J.R. Induction of decision trees. *Mach. Learn.* **1986**, *1*, 81–106. [CrossRef]
10. Belgiu, M.; Drăguț, L. Random forest in remote sensing: A review of applications and future directions. *ISPRS J. Photogramm. Remote Sens.* **2016**, *114*, 24–31. [CrossRef]
11. Cortes, C.; Vapnik, V. Support-Vector Networks. *Mach. Learn.* **1995**, *20*, 273–297. [CrossRef]
12. Huang, X.; Hu, T.; Li, J.; Wang, Q.; Benediktsson, J.A. Mapping Urban Areas in China Using Multisource Data with a Novel Ensemble SVM Method. *IEEE Trans. Geosci. Remote Sens.* **2018**, *56*, 4258–4273. [CrossRef]
13. Koda, S.; Zeggada, A.; Melgani, F.; Nishii, R. Spatial and Structured SVM for Multilabel Image Classification. *IEEE Trans. Geosci. Remote Sens.* **2018**, *56*, 5948–5960. [CrossRef]
14. Kittler, J.; Hatef, M. On combining classifiers. *IEEE Trans. Pattern Anal. Mach. Intell.* **1998**, *20*, 226–239. [CrossRef]
15. Chen, L.C.; Papandreou, G.; Kokkinos, I.; Murphy, K.; Yuille, A.L. DeepLab: Semantic Image Segmentation with Deep Convolutional Nets, Atrous Convolution, and Fully Connected CRFs. *IEEE Trans. Pattern Anal. Mach. Intell.* **2018**, *40*, 834–848. [CrossRef]
16. Wu, P.; Fu, J.; Yi, X.; Wang, G.; Mo, L.; Maoponde, B.T.; Liang, H.; Tao, C.; Ge, W.Y.; Jiang, T.T. Research on water extraction from high resolution remote sensing images based on deep learning. *Front. Remote Sens.* **2023**, *4*, 1283615. [CrossRef]
17. Chen, L.C.; Zhu, Y.; Papandreou, G.; Schroff, F.; Adam, H. Encoder-Decoder with Atrous Separable Convolution for Semantic Image Segmentation. In Proceedings of the European Conference on Computer Vision, Munich, Germany, 8–14 September 2018.
18. Walker, G.; Prowse, T.D.; Dibike, Y.B.; Bonsal, B.R. Climate Change Impacts on Precipitation Patterns and Water Storage in the High-latitude Dry Interior Climate of Northern Alberta, Canada. In Proceedings of the Agu Fall Meeting, San Francisco, CA, USA, 3–7 December 2012.
19. Wang, J.; Sun, K.; Cheng, T.; Jiang, B.; Xiao, B. Deep High-Resolution Representation Learning for Visual Recognition. *IEEE Trans. Pattern Anal. Mach. Intell.* **2020**, *43*, 3349–3364. [CrossRef]
20. Miao, Z.; Fu, K.; Sun, H.; Sun, X.; Yan, M. Automatic Water-Body Segmentation from High-Resolution Satellite Images via Deep Networks. *IEEE Geosci. Remote Sens. Lett.* **2018**, *15*, 602–606 [CrossRef]

21. Zhao, H.; Shi, J.; Qi, X.; Wang, X.; Jia, J. Pyramid Scene Parsing Network. In Proceedings of the IEEE Conference on Computer Vision and Pattern Recognition (CVPR), Honolulu, HI, USA, 21–26 July 2017.
22. Sun, D.; Gao, G.; Huang, L.; Liu, Y.; Liu, D. Extraction of water bodies from high-resolution remote sensing imagery based on a deep semantic segmentation network. *Sci. Rep.* **2024**, *14*, 14604. [CrossRef]
23. Sun, Q.; Li, J. A method for extracting small water bodies based on DEM and remote sensing images. *Sci. Rep.* **2024**, *14*, 760. [CrossRef] [PubMed]
24. Cao, H.; Tian, Y.; Liu, Y.; Wang, R. Water body extraction from high spatial resolution remote sensing images based on enhanced U-Net and multi-scale information fusion. *Sci. Rep.* **2024**, *14*, 16132. [CrossRef]
25. Yan, P.; Fang, Y.; Chen, J.; Wang, G.; Tang, Q. Automated Extraction for Water Bodies Using New Water Index from Landsat 8 OLI Images. *Acta Geod. Cartogr. Sin.* **2023**, *6*, 59–75.
26. Cheng, X.; Han, K.; Xu, J.; Li, G.; Xiao, X.; Zhao, W.; Gao, X. SPFDNet: Water Extraction Method Based on Spatial Partition and Feature Decoupling. *Remote Sens.* **2024**, *16*, 3959. [CrossRef]
27. Zhao, B.; Wu, J.; Han, X.; Tian, F.; Liu, M.; Chen, M.; Lin, J. An improved surface water extraction method by integrating multi-type priori information from remote sensing. *Int. J. Appl. Earth Obs. Geoinf.* **2023**, *124*, 103529. [CrossRef]
28. Chen, C.; Wang, Y.; Yang, S.; Ji, X.; Wang, G. A K-Net-based hybrid semantic segmentation method for extracting lake water bodies. *Eng. Appl. Artif. Intell.* **2023**, *126*, 106904. [CrossRef]
29. Mishra, V.K.; Chaudhary, P.K.; Pant, T. Image fusion based approach of water extraction from spectrally mixed water regions belonging to the sources of varying nature. *Multimed. Tools Appl.* **2023**, *82*, 39783–39795. [CrossRef]
30. Wang, Y.; Li, Y.; Wang, D. Extraction of small water body information based on Res2Net-Unet. In Proceedings of the 2023 17th International Conference on Ubiquitous Information Management and Communication (IMCOM), Seoul, Republic of Korea, 3–5 January 2023; pp. 1–5.
31. Shihao, A.; Xiaoping, R. A High-Precision Water Body Extraction Method Based on Improved Lightweight U-Net. *Remote Sens.* **2022**, *14*, 4127. [CrossRef]
32. Ronneberger, O.; Fischer, P.; Brox, T. U-Net: Convolutional Networks for Biomedical Image Segmentation. In *Medical Image Computing and Computer-Assisted Intervention—MICCAI 2015*; Springer International Publishing: Cham, Switzerland, 2015; pp. 234–241.
33. Moknati, M. Spatiotemporal Water Body Change Detection Using Multi-temporal Landsat Imagery: Case Studies of Lake Enriquillo and Lake Azuei. In Proceedings of the AGU Fall Meeting, San Francisco, CA, USA, 14–18 December 2015.
34. Tong, X.Y.; Xia, G.S.; Lu, Q.; Shen, H.; Zhang, L. Land-cover classification with high-resolution remote sensing images using transferable deep models. *Remote Sens. Environ.* **2020**, *237*, 111322. [CrossRef]
35. He, K.; Zhang, X.; Ren, S.; Sun, J. Deep Residual Learning for Image Recognition. In Proceedings of the IEEE Conference on Computer Vision and Pattern Recognition (CVPR), Las Vegas, NV, USA, 27–30 June 2016.
36. Hu, J.; Shen, L.; Sun, G.; Albanie, S. Squeeze-and-Excitation Networks. *IEEE Trans. Pattern Anal. Mach. Intell.* **2017**.
37. Vaswani, A.; Shazeer, N.; Parmar, N.; Uszkoreit, J.; Jones, L.; Gomez, A.N.; Kaiser, L.; Polosukhin, I. Attention Is All You Need. *arXiv* **2017**, arXiv:1706.03762.
38. Wang, L.; Lee, C.Y.; Tu, Z.; Lazebnik, S. Training Deeper Convolutional Networks with Deep Supervision. *arXiv* **2015**, arXiv:1505.02496.
39. Yuan, K.; Zhuang, X.; Schaefer, G.; Feng, J.; Fang, H. Deep-Learning-Based Multispectral Satellite Image Segmentation for Water Body Detection. *IEEE J. Sel. Top. Appl. Earth Obs. Remote. Sens.* **2021**, *14*, 7422–7434. [CrossRef]
40. Yu, L.; Wang, Z.; Tian, S.; Ye, F.; Ding, J.; Kong, J. Convolutional Neural Networks for Water Body Extraction from Landsat Imagery. *Int. J. Comput. Intell. Appl.* **2017**, *16*, 1750001. [CrossRef]
41. Nie, C. Rich CNN Features for Water-Body Segmentation from Very High Resolution Aerial and Satellite Imagery. *Remote Sens.* **2021**, *13*, 1912. [CrossRef]
42. Duan, Y.; Zhang, W.; Huang, P.; He, G.; Guo, H. A New Lightweight Convolutional Neural Network for Multi-Scale Land Surface Water Extraction from GaoFen-1D Satellite Images. *Remote Sens.* **2021**, *13*, 4576. [CrossRef]
43. Pandey, M.; Arora, A.; Arabameri, A.; Shukla, U. Flood Susceptibility Modeling in a Subtropical Humid Low-Relief Alluvial Plain Environment: Application of Novel Ensemble Machine Learning Approach. *Front. Earth Sci.* **2021**, *9*, 659296. [CrossRef]
44. Ozdemir, S.; Akbulut, Z.; Karsli, F.; Kavzoglu, T. Extraction of Water Bodies from High-Resolution Aerial and Satellite Images Using Visual Foundation Models. *Sustainability* **2024**, *16*, 2995. [CrossRef]

Disclaimer/Publisher’s Note: The statements, opinions and data contained in all publications are solely those of the individual author(s) and contributor(s) and not of MDPI and/or the editor(s). MDPI and/or the editor(s) disclaim responsibility for any injury to people or property resulting from any ideas, methods, instructions or products referred to in the content.

MDPI AG
Grosspeteranlage 5
4052 Basel
Switzerland
Tel.: +41 61 683 77 34

Water Editorial Office
E-mail: water@mdpi.com
www.mdpi.com/journal/water



Disclaimer/Publisher's Note: The title and front matter of this reprint are at the discretion of the Guest Editors. The publisher is not responsible for their content or any associated concerns. The statements, opinions and data contained in all individual articles are solely those of the individual Editors and contributors and not of MDPI. MDPI disclaims responsibility for any injury to people or property resulting from any ideas, methods, instructions or products referred to in the content.



Academic Open
Access Publishing

mdpi.com

ISBN 978-3-7258-6058-6